Nonlinear Terahertz Spectroscopy of the 3D Dirac Material Cd_3As_2

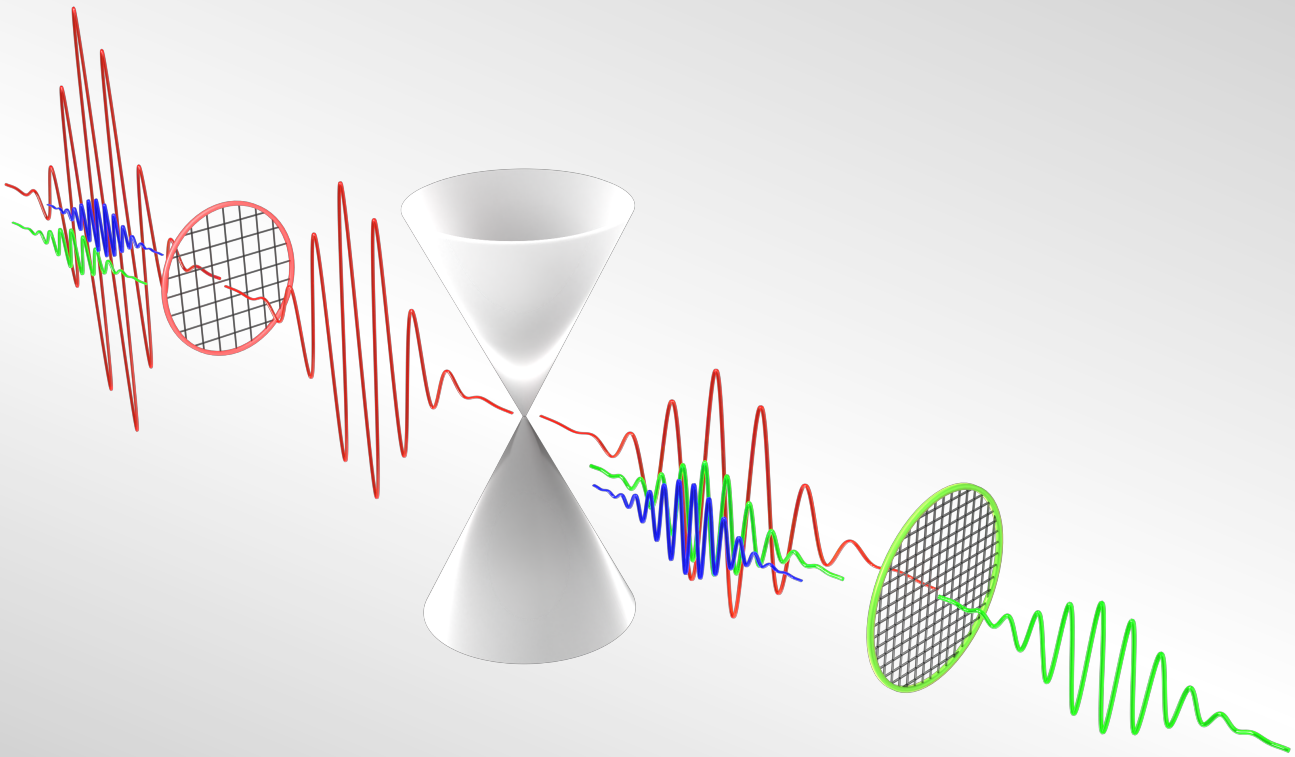

Semen Germanskiy

Cologne, 2025

Nonlinear Terahertz Spectroscopy of the 3D Dirac Material Cd_3As_2

Inaugural-Dissertation
zur
Erlangung des Doktorgrades
der Mathematisch-Naturwissenschaftlichen Fakultät
der Universität zu Köln

vorgelegt von
Semen Germanskiy
geboren in Nowokusnezk, Russland

Köln
December 2024

Gutachter:	Prof. Dr. Ir. Paul H. M. van Loosdrecht
Gutachter:	Prof. Dr. Andrei Pimenov
Vorsitzender der Prüfungskommission:	Prof. Dr. Malte Gather

Tag der mündlichen Prüfung: 18. Februar 2025

This thesis is
dedicated to Sophia

When God created time, he made plenty of it.
Irish saying

Contents

Introduction

This chapter provides a general introduction to the topics covered in this work. Basic concepts of nonlinear optics are discussed, followed by an introduction to the topic of terahertz radiation. The goal and motivation of the entire project are then presented, as all the experimental work was done to achieve this goal. At the end of the chapter, an overview and structure of the work are provided.

1. A little bit of history and electrodynamics

The study of interactions between light and matter has been a subject of interest for many generations of physicists. Starting from the works of Euclid and Ptolemy, we have been studying the nature of light and its interactions with the world around us for more than 2000 years. A major breakthrough in our understanding occurred in the 19th century with the works of Maxwell and Hertz. Maxwell's work formulated modern electrodynamics in the form of the Maxwell equations, and Hertz's work demonstrated that light is an electromagnetic wave.

The Maxwell equations in SI units for the general case are:

$$\begin{aligned} \nabla \cdot \vec{D} &= \rho, \\ \nabla \cdot \vec{B} &= 0, \\ \nabla \times \vec{E} &= -\frac{\partial \vec{B}}{\partial t}, \\ \nabla \times \vec{H} &= \vec{j} + \frac{\partial \vec{D}}{\partial t}, \end{aligned} \tag{1}$$

where $\vec{E}$ and $\vec{D}$ are the electric field and electric displacement, $\vec{H}$ and $\vec{B}$ are the magnetic field and magnetic induction, and ρ and $\vec{j}$ are the charge density and current density, respectively. All these quantities are functions of time t and position $\vec{r}$.

To include the effect of the material on the electromagnetic wave, the material equations must be introduced:

$$\begin{aligned} \vec{B} &= \mu_0\left(\vec{H} + \overrightarrow{M}\right), \\ \vec{D} &= \varepsilon_0\vec{E} + \vec{P}, \\ \overrightarrow{M} &= \chi_m\vec{H}, \\ \vec{P} &= \varepsilon_0\chi\vec{E}, \end{aligned} \tag{2}$$

where ε_0 and μ_0 are the permittivity and permeability of free space, $\vec{P}$ is the electric polarization, $\overrightarrow{M}$ is the magnetization, and χ and χ_m are the electric and magnetic susceptibilities, respectively, which are generally tensors. For nonmagnetic materials, magnetization is usually extremely small and can be ignored. The connection between $\vec{D}$ and $\vec{E}$ can also be written as: $\vec{D} = \varepsilon_0\varepsilon\vec{E} = \varepsilon_0(1+\chi)\vec{E}$ by introducing the relative permittivity ε.

Polarization describes the response of matter under the influence of an electromagnetic field. This response depends not only on the value of $\vec{E}$ at the current moment but also on all previous values of $\vec{E}$. Mathematically, this is expressed as (for simplicity ε_0 assumed to be 1 here and later):

$$\vec{P}(t) = \int_{-\infty}^{\infty} \chi(\tau)\vec{E}(t-\tau)\,\mathrm{d}\tau\,. \tag{3}$$

This means that the susceptibility depends on frequency, which defines the material's dispersion $\varepsilon(\omega)$, where ω is the frequency of the electromagnetic field.

It should now be clear that all the equations so far are *linear* in the fields. Any material response described by these equations will depend linearly on the external field. For many years, this was the extent of our understanding.

However, this changed with the development of the first laser in 1960 by Thomas Maiman [1]. One of the most important developments of the 20th century, it opened the door to many groundbreaking discoveries, including effects described by *nonlinear* optics.

2. Nonlinear optics

As long as the amplitude of an optical electric field is *small*, (1), in combination with (2), perfectly describes the optical response of a material. However, soon after the creation of the laser, Franken and coauthors demonstrated that for *high* amplitudes, this is no longer true [2]. They showed that a ruby laser with an electric field amplitude on the

order of 10^5 V/cm causes the generation of second harmonic in crystalline quartz. This pioneering work initiated a whole new field of nonlinear optics.

A key concept in nonlinear optics is *nonlinear polarization*. While Maxwell's equations (1) remain valid, the material equations (2) must be modified to include the nonlinear response of matter. One can assert that the material's susceptibility χ now depends not only on time t and position $\vec{r}$ but also on the electric field $\vec{E}$ itself. This means that polarization $\vec{P}$ is now a nonlinear function of $\vec{E}$, and can be written as a power series in $\vec{E}$:

$$\begin{aligned}\vec{P}(t) &= \int_{-\infty}^{\infty} \chi\left(\tau; \vec{E}\right)\vec{E}(t-\tau)\,\mathrm{d}\tau = \\ &= \int_{-\infty}^{\infty} \chi^{(1)}(\tau)\vec{E}(t-\tau)\,\mathrm{d}\tau + \\ &+ \int_{-\infty}^{\infty} \chi^{(2)}(\tau_1,\tau_2)\vec{E}(t-\tau_1)\vec{E}(t-\tau_2)\,\mathrm{d}\tau_1\,\mathrm{d}\tau_2 + \\ &+ \int_{-\infty}^{\infty} \chi^{(3)}(\tau_1,\tau_2,\tau_3)\vec{E}(t-\tau_1)\vec{E}(t-\tau_2)\vec{E}(t-\tau_3)\,\mathrm{d}\tau_1\,\mathrm{d}\tau_2\,\mathrm{d}\tau_3 + \ldots\end{aligned} \tag{4}$$

where $\chi^{(n)}$ is the n-th order nonlinear susceptibility.

To be able to write such a series, a small parameter must be introduced. For dielectric media without resonances, this parameter is typically E/E_{at}, where $E_{\text{at}} \approx 3 \cdot 10^8$ V/cm is the atomic field. However, for different systems, the value of the "atomic" field can vary. If the ratio $E/E_{\text{at}} \ll 1$, then (4) is valid, and this is the *perturbative* regime. In the opposite case, when $E/E_{\text{at}} \sim 1$ or greater, the approximation of polarization as a series is no longer valid, and this is the *nonperturbative* regime. In the perturbative regime, the ratio $\chi^{(n+1)}/\chi^{(n)} \sim 1/E_{\text{at}}$ provides an estimate for the scaling of the amplitudes of nonlinear effects.

To understand how (4) leads to harmonic generation (and other nonlinear effects), it is convenient to perform a Fourier transform of (4). For flat monochromatic waves,

$$\vec{E}(t) = \sum_i \vec{E}(\omega_i) = \sum_i \vec{\mathcal{E}} e^{-i\omega_i t} + c.c. \tag{5}$$

the Fourier components of $\vec{P}(t)$ will be:

$$\begin{aligned}\vec{P}(\omega) &= \vec{P}^{(1)}(\omega) + \vec{P}^{(2)}(\omega) + \vec{P}^{(3)}(\omega) + ... = \\ &= \chi^{(1)}(\omega)\vec{E}(\omega) + \\ &+\chi^{(2)}\big(\omega = \omega_i + \omega_j; \omega_i, \omega_j\big)\vec{E}(\omega_i)\vec{E}\big(\omega_j\big) + \\ &+\chi^{(3)}\big(\omega = \omega_i + \omega_j + \omega_k; \omega_i, \omega_j, \omega_k\big)\vec{E}(\omega_i)\vec{E}\big(\omega_j\big)\vec{E}(\omega_k) + ...\end{aligned} \tag{6}$$

This defines the nonlinear response of matter at frequency ω. As an electric field is written in a complex form, both positive and negative frequencies are included in the equation (6). The equality $\omega = \sum_i \omega_i$ can be seen as a conservation of energy law. If the electric field is monochromatic, $E(t) = \mathcal{E}\cos(\omega t)$, and the nonlinear susceptibilities do not depend on frequency, then the nonlinear responses $\vec{P}^{(2)}$ and $\vec{P}^{(3)}$ are:

$$P^{(2)} = \chi^{(2)}\mathcal{E}^2\cos^2(\omega t) = \frac{\chi^{(2)}}{2}\mathcal{E}^2(\cos(2\omega t) + 1), \tag{7}$$

$$P^{(3)} = \chi^{(3)}\mathcal{E}^3\cos^3(\omega t) = \frac{\chi^{(3)}}{4}\mathcal{E}^3(\cos(3\omega t) + 3\cos(\omega t)). \tag{8}$$

It is immediately clear that $P^{(2)}$ and $P^{(3)}$ contain terms at 2ω and 3ω, and the terms scale as $\mathcal{E}^2$ and $\mathcal{E}^3$. This is the phenomenon of harmonic generation, with the predicted power law of the n-th harmonic $P^{(n)} \sim \mathcal{E}^n$. Deviations from this power law behavior can indicate a nonperturbative regime.

While harmonic generation is the main focus of this work, other terms in $P^{(2)}$ and $P^{(3)}$ also play an important role. The term in $P^{(2)} \sim \cos(0\omega t)$ is called "optical rectification," an effect that builds up a DC or quasi-DC electric field in the material under external illumination. The term in $P^{(3)}$ proportional to $\cos(\omega t)$ corresponds to self-modulation, which is the dependence of the refractive index of the material on the intensity of the light itself.

One of the most important properties of nonlinear susceptibilities is their sensitivity to a material's symmetries. It is well known that dielectric permittivity ε is a tensor in the general case, and consequently, χ must also be a tensor. This means that the nonlinear susceptibility $\chi^{(n)}$ is a tensor of rank $n+1$. The component of the nonlinear polarization $P_i^{(n)}$ is then:

$$P_i^{(n)} = \sum_{jkl...} \chi^{(n)}_{ijkl...} E_j E_k E_l ... \tag{9}$$

where $i, j, k, l, ... = \{x, y, z\}$ are coordinate indices. $P_i^{(n)}$ do not depend on the particular order of indices in the sum.

Of particular interest in the context of material symmetries is the case of centrosymmetric materials. It can be shown that *all* even-order nonlinearities vanish in centrosymmetric materials, meaning $\chi^{(2n)} = 0$ for $n = 1, 2, 3....$ This implies that no even-order harmonics are allowed in such materials. This fact is extremely useful for observing symmetry breaking in materials. For a deeper dive into nonlinear optics, classic books by R. Boyd [3] and Y. Shen [4] are excellent sources of information.

3. Terahertz radiation

A second pillar of this work is terahertz (THz) radiation. Terahertz radiation is defined as electromagnetic radiation with frequencies around 10^{12} Hz, typically ranging from 0.1 THz to 10 THz (wavelengths from 3 mm to 30 μm). Sometimes, a slightly shorter range of 0.3–3 THz is used in technical literature. In terms of energy, this electromagnetic region covers photon energies from approximately 0.4 meV to 41 meV. This region is often called the "THz gap" because it lies between the radio and far-infrared regions, as shown in Figure 1.

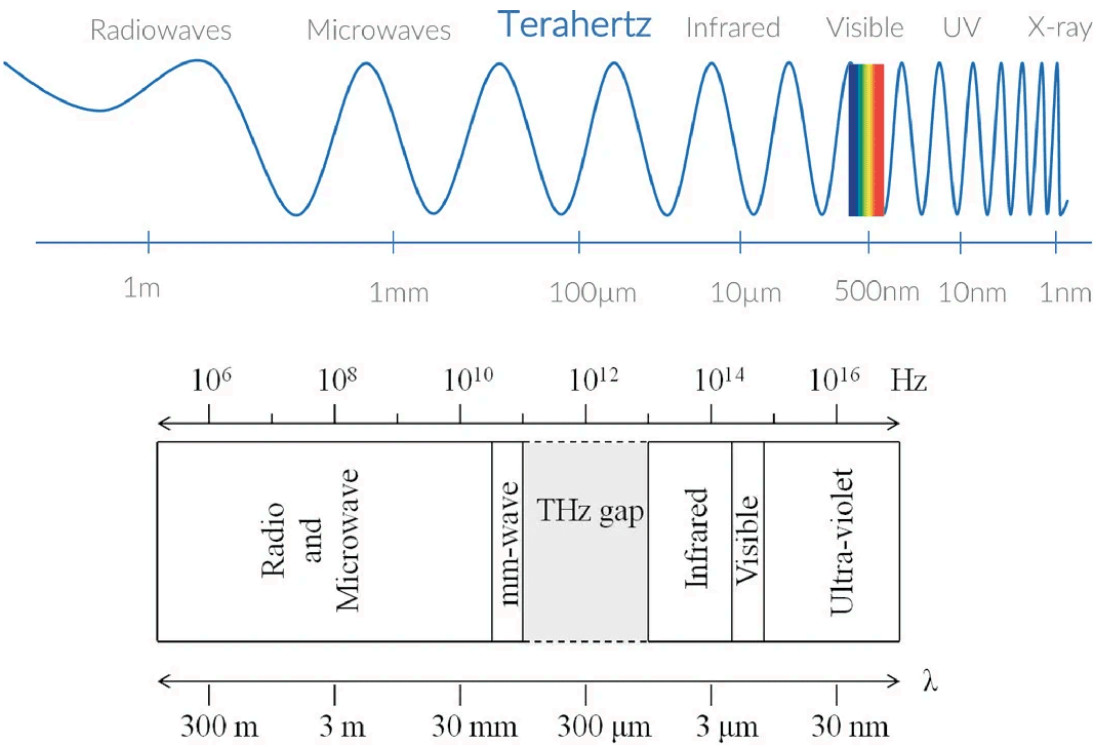

Figure 1: Diagram showing the location of the THz band in the electromagnetic spectrum. *Reproduced from [5] with permission from Springer Nature.*

While closing this gap was a difficult task, the first attempts were made at the beginning of the 20th century. This began with the work of H. Rubens and O. von Baeyer. in 1911,

where radiation with a wavelength of 314 μm (0.95 THz) was detected [6], and continued with the work of E. F. Nichols and J. D. Tear. in 1923, who registered a wavelength of 1.8 mm (0.17 THz) [7]. Further progress was made by A. Glagolewa-Arkadiewa. in 1924, where multiple wavelengths were detected in the range from 50 mm (0.006 THz) to 82 μm (3.66 THz), fully covering the technical THz region [8]. While THz frequencies were observed as early as the beginning of the 20th century, their wide use started only in the late 1980s, with the development of mode-locked lasers and dipole antennas [9,10].

Today, THz radiation is widely used for spectroscopy and imaging in various fields, such as gas spectroscopy [11], liquids [12], solid-state systems [13], and biosystems [14]. It is also used in thickness control [15,16] and is even finding its way into security applications.

In the context of this work, terahertz radiation offers unique advantages compared to other optical frequencies. Due to the low energy of its photons, it allows for the driving of intraband electron transitions, enabling the study of electron dynamics without significantly heating the system, as happens during thermalization after interband transitions under an optical pump. The low frequency, compared to optical frequencies, allows THz fields to be treated as quasi-DC, greatly simplifying the theoretical analysis of physical processes. Finally, the unique ability to access the phase of the THz electric field via time-resolved experiments simplifies experiments in comparison with ellipsometry in optical range, which provides same information about material's properties.

4. Motivation and the goal

Cd_3As_2 is an unique material with an unusual electronic structure and, similar to graphene, it has a linear dispersion of electrons near the Fermi surface. However, while graphene is a 2D material, Cd_3As_2 is a "normal" 3D crystal, meaning it has a higher density of electronic states and, therefore, a stronger potential response from the electrons with linear dispersion. There are theoretical works predicting the creation of novel transient states using external laser fields[17] or magnetic fields[18], as will be discussed in Chapter II.

The goal of the present work is to study the dynamics of the electrons in Cd_3As_2 and to observe induced transient electronic states under the influence of THz or DC magnetic fields.

5. Scope of the Thesis

The thesis consists of six chapters, plus an introduction and conclusion. It is divided into two logical parts. The first two chapters are introductory, while the remaining chapters present the research results.

Chapter I introduces the experimental techniques used in this work. It focuses on THz time-domain spectroscopy and the experimental setup for THz nonlinear spectroscopy. A description of the methods used for THz generation and detection is provided. The chapter concludes with an explanation of how to characterize the polarization state of light, with its application shown in the characterization of a THz waveplate.

Chapter II introduces Cd_3As_2, the material of study, and provides a brief history of its research. The concept of a Dirac point and its topology are discussed, along with how Dirac nodes interact with THz radiation.

Chapter III is the first experimental chapter, presenting the experimental observation of THz high harmonic generation in bulk Cd_3As_2 and the study of its properties. A kinetic model of electrons is used to describe the observed phenomena.

Chapter IV extends the work from Chapter 3, focusing on the control of harmonic generation by varying the ellipticity of the pump beam.

Chapter V explores the observation of induced symmetry breaking in Cd_3As_2. The observed THz second harmonic generation (SHG) is studied as a function of the pump's ellipticity, fluence, and sample orientation. Additional measurements with a magnetic field are conducted. A phenomenological model of the process leading to SHG is developed.

Chapter VI, the final chapter of the thesis, suggests the use of induced changes in the polarization of an optical probe beam as a sensitive probe of the material's symmetries. The theory of the optical Kerr effect is presented to account for the properties of Cd_3As_2, and the theory is used to fit the experimental data of the Kerr effect. Experiments with increased probe beam fluence are then conducted, showing significant changes in the material's response.

The conclusion summarizes all the work that has been done and provides an outlook for the future, discussing how the goal of the work can be further achieved and what remains to be explored.

6. References

[1] T. H. Maiman, *Stimulated Optical Radiation in Ruby*, Nature **187**, 493 (1960).

[2] P. A. Franken, A. E. Hill, C. W. Peters, and G. Weinreich, *Generation of Optical Harmonics*, Physical Review Letters **7**, 118 (1961).

[3] R. W. Boyd, *Nonlinear Optics*, 3rd ed (Academic Press, Burlington, MA, 2008).

[4] Y. R. Shen, *The Principles of Nonlinear Optics*, Wiley classics library edition (Wiley-Interscience, Hoboken, N.J, 2003).

[5] M. E. Jbari, M. Moussaoui, and N. Chahboun, *Coding and Modulation for Terahertz*, in *Terahertz Wireless Communication Components and System Technologies*, edited by M. El Ghzaoui, S. Das, T. R. Lenka, and A. Biswas (Springer, Singapore, 2022), pp. 59–79.

[6] H. Rubens and O. von Baeyer, *LXXX. On Extremely Long Waves, Emitted by the Quartz Mercury Lamp*, The London, Edinburgh, And Dublin Philosophical Magazine and Journal of Science **21**, 689 (1911).

[7] E. F. Nichols and J. D. Tear, *Short Electric Waves*, Physical Review **21**, 587 (1923).

[8] A. Glagolewa-Arkadiewa, *Short Electromagnetic Waves of Wave-length up to 82 Microns*, Nature **113**, 640 (1924).

[9] D. H. Auston, K. P. Cheung, and P. R. Smith, *Picosecond Photoconducting Hertzian Dipoles*, Applied Physics Letters **45**, 284 (1984).

[10] C. Fattinger and D. Grischkowsky, *Point Source Terahertz Optics*, Applied Physics Letters **53**, 1480 (1988).

[11] M. van Exter, C. Fattinger, and D. Grischkowsky, *Terahertz Time-Domain Spectroscopy of Water Vapor*, Optics Letters **14**, 1128 (1989).

[12] D. K. George and A. G. Markelz, *Terahertz Spectroscopy of Liquids and Biomolecules*, in *Terahertz Spectroscopy and Imaging*, edited by K.-E. Peiponen, A. Zeitler, and M. Kuwata-Gonokami (Springer, Berlin, Heidelberg, 2013), pp. 229–250.

[13] G. Gallot, J. Zhang, R. W. McGowan, T.-I. Jeon, and D. Grischkowsky, *Measurements of the THz Absorption and Dispersion of ZnTe and Their Relevance to the Electro-Optic Detection of THz Radiation*, Applied Physics Letters **74**, 3450 (1999).

[14] P. Siegel, *Terahertz Technology in Biology and Medicine*, IEEE Transactions on Microwave Theory and Techniques **52**, 2438 (2004).

[15] A. J. Fitzgerald, B. E. Cole, and P. F. Taday, *Nondestructive Analysis of Tablet Coating Thicknesses Usign Terahertz Pulsed Imaging*, Journal of Pharmaceutical Sciences **94**, 177 (2005).

[16] T. Yasui, T. Yasuda, K. Sawanaka, and T. Araki, *Terahertz Paintmeter for Noncontact Monitoring of Thickness and Drying Progress in Paint Film*, Applied Optics **44**, 6849 (2005).

[17] H. Hübener, M. A. Sentef, U. D. Giovannini, A. F. Kemper, and A. Rubio, *Creating Stable Floquet–Weyl Semimetals by Laser-Driving of 3D Dirac Materials*, Nature Communications **8**, (2017).

[18] E. V. Gorbar, V. A. Miransky, and I. A. Shovkovy, *Engineering Weyl Nodes in Dirac Semimetals by a Magnetic Field*, Physical Review B **88**, 165105 (2013).

Chapter I
Experimental methods

1. Time-domain THz spectroscopy

Experiments with terahertz fields are nowadays typically conducting using one of two different methods. The first is to measure the terahertz spectrum directly in the frequency domain using a Michelson interferometer. This method, known as Fourier-transform infrared spectroscopy (FTIR), has existed since the 1960s [1]. It is a well-developed technique, with commercially available spectrometers making transmission measurements of materials in the THz region a routine task.

For many years, this was the most common way to access material properties in the THz region. However, with the development of femtosecond lasers, photoconductive antennas, and the electro-optical sampling technique (EOS), a method for performing THz spectroscopy in the time domain became possible. A major novelty of this method is the ability to measure both the phase and amplitude of the electric field of a THz pulse, rather than just the intensity spectrum. This capability leads to a better signal-to-noise ratio (SNR) in measurements and allows for the direct measurement of the complex dielectric function of materials.

The improved SNR arises from measuring the electric field rather than its intensity. Indeed, the measured electric field can be represented as:

$$E = E_{\text{signal}} + E_{\text{noise}}, \tag{1}$$

where E_{noise} is a random noise contribution with zero mean value $\langle E_{\text{noise}} \rangle = 0$. The measured intensity I then becomes:

$$I = \left(E_{\text{signal}} + E_{\text{noise}}\right)^2 = E_{\text{signal}}^2 + 2E_{\text{signal}}E_{\text{noise}} + E_{\text{noise}}^2. \tag{2}$$

By averaging multiple measurements, one can see that the averaged intensity has an additional noise term, $\langle I \rangle = \langle I \rangle_{\text{signal}} + \langle I \rangle_{\text{noise}}$, compared to the averaged electric field $\langle E \rangle = \langle E \rangle_{\text{signal}}$. As result, noise contributions will be canceled out. In an extreme case of $I_{\text{noise}} \gg I_{\text{signal}}$, for the field detection SNR $\to \infty$, while intensity detection will demonstrate SNR $\ll 1$. Of course, in reality it can be other sources of noise, like electronic noise of measurement equipment, which will set upper achievable limit of SNR for the field detection.

Access to phase information is crucial not only for extracting the complex dielectric function of materials but also for monitoring material responses to THz fields in various pump-probe experiments, like antiferromagnetic resonances[2] or phonon excitations[3].

In this thesis, there are two major types of experiments: nonlinear THz spectroscopy and THz pump - optical probe measurements. Since the detection of the THz field can also be seen as a pump-probe experiment, both types share optical elements and require synchronization between the THz and optical probe pulses to extract phase information.

1.1. Linear and nonlinear THz spectroscopy

Both linear and nonlinear THz spectroscopies share a similar experimental layout: a sample is irradiated with an incoming THz pulse, and the response is collected. However, the details are significantly different. Since linear spectroscopy focuses only on the linear response, high THz fields are not required. This allows for the use of laser systems with higher repetition rates than those used in nonlinear spectroscopy, which significantly improves the dynamic range of the system. The signal-to-noise ratio can reach approximately 10^4.

Nonlinear THz spectroscopy, on the other hand, focuses on various nonlinear responses of a material, such as harmonic generation, making a high THz field amplitude crucial. Additionally, using narrowband THz fields is necessary to distinguish between different nonlinear effects. For example, a simple case of second-order nonlinearity in a material leads to effects like sum frequency generation (SFG), second harmonic generation (SHG), and difference frequency generation (DFG), sometimes called optical rectification. With a broadband pump, analyzing the experimental data becomes complicated, as all these effects can contribute simultaneously to a response at the same frequencies.

A narrowband THz field can be produced in two ways: either the THz source itself produces a narrowband field, or broadband radiation is filtered by a THz bandpass filter. In this work, both approaches are used. A bandpass filter acts as an *LC* resonator, made of a metal mesh structure where the geometry of the cutouts defines the equivalent capacitance and inductance of the *LC* circuit [4]. For harmonic generation, the quality of the filter is crucial, as parasitic leakage can overshadow the signal of interest. It is also important to filter out the THz field at the pump frequency, as the high field of the residual pump can saturate or otherwise affect the detection of the harmonic signal.

In this work, nonlinear THz spectroscopy was performed via high harmonic generation (HHG). The experimental setup for this is shown in Figure 1. The sources of the THz pump and THz detection will be discussed in detail in the next sections. For any type

of source, a bandpass filter (BPF) at the fundamental frequency *1f* is used to ensure the absence of leakage fields at harmonic frequencies. After the sample, a bandpass filter at *nf* is placed to filter out the nth harmonic and suppress the fundamental frequency.

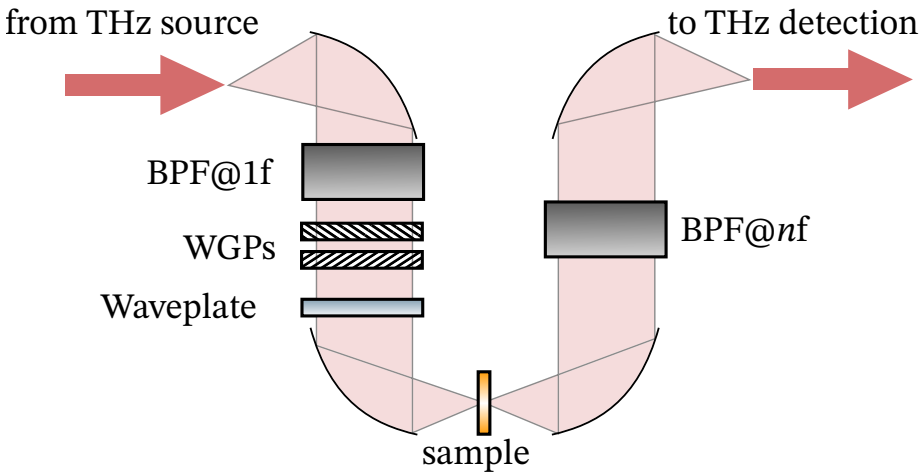

Figure 1: Schematic drawing of the HHG setup. BPF - bandpass filter, WGP - wire grid polarizer

Figure 2 demonstrates how different bandpass filters used in this work affect broadband THz pulses. From the spectra, it is immediately clear what bandwidth and central frequency each filter has. Due to finite rejection outside of the transmission band, some residual pump or other harmonics may still be present in the detected signal after filtering. An example of a detected signal and its spectrum for 3rd harmonic generation in Cd_3As_2 is shown in Figure 3.

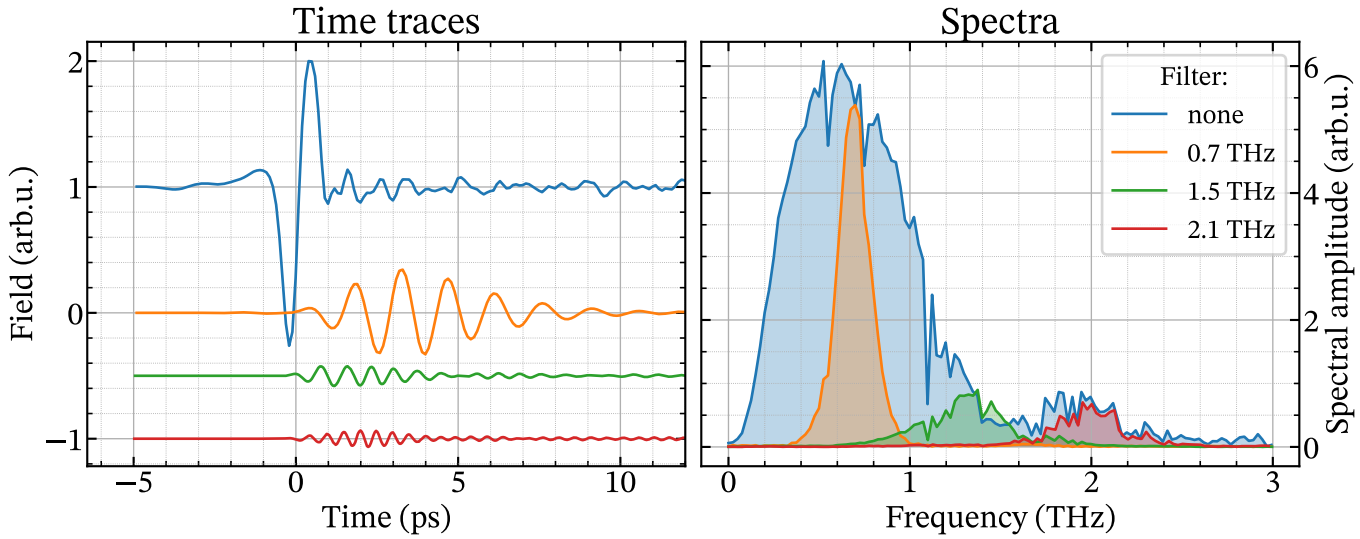

Figure 2: Time traces and corresponding spectra of narrowband THz pulses after various bandpass filters and an unfiltered broadband pulse.

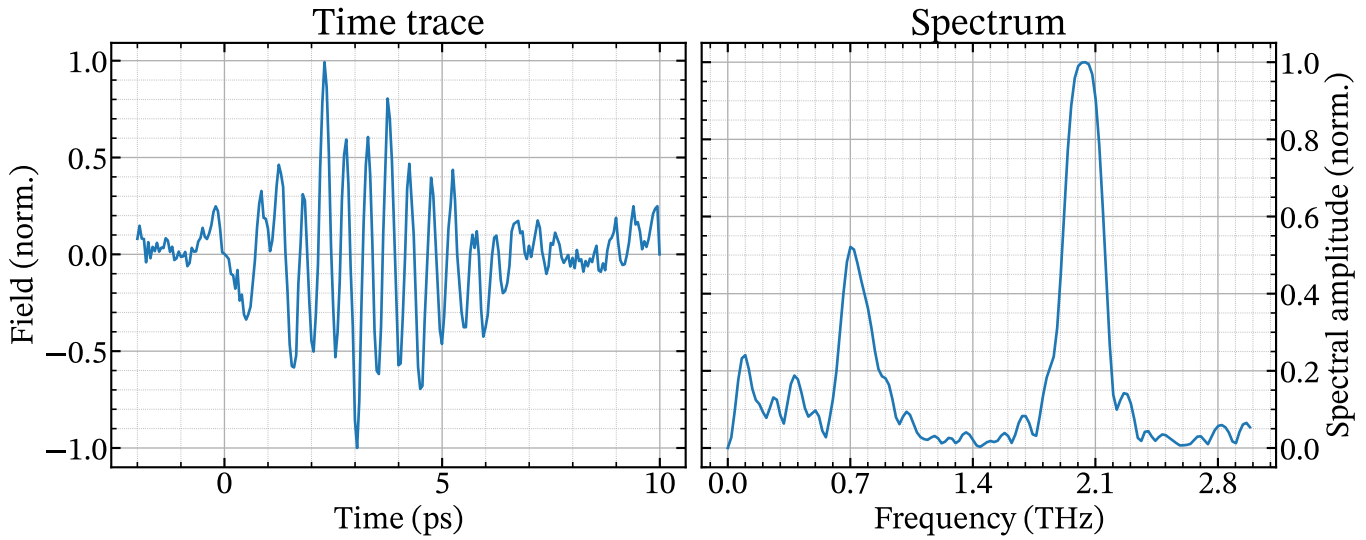

Figure 3: Detected signal of the 3rd harmonic in Cd_3As_2 in time and frequency domains.

THz fluence is controlled using a pair of free-space wire grid polarizers (WGPs) with a variable angle θ between them. The second WGP is kept fixed to the desired polarization orientation. The field strength depends on the angle as $E = E_0 \cos^2 \theta$. However, if the polarizers are not well aligned, the resulting amplitude will depend on the offset angles, described by the equation $E = E_0 \cos(\theta - \theta_1) \cos(\theta - \theta_1 - \theta_2)$, where θ_1 and θ_2 are the offset angles for both polarizers, which are usually unknown. This means θ will incorrectly define the fluence, and either direct measurement of $E(\theta)$ or using the leakage at the fundamental frequency as a reference signal is required to correctly estimate fluence dependence. The second approach has the advantage of saving experimental time, which is important when experiments are performed within a strict time window, such as during beamtime at a facility.

The next element in the setup is the THz waveplate. Typically, it is a piece of crystalline quartz, cut to a specific thickness that defines its retardance at a specific frequency. Since the THz waveplate is often custom-made, its calibration is a necessary procedure, as described in Section 4.

Guiding and focusing of the THz beam are done using either silver- or gold-coated off-axis parabolic mirrors. Both metal coatings have the same reflectance across the entire THz range[5], so the choice of coating depends on other requirements. The parabolic mirror has the advantage of focusing or collimating beams without introducing spherical aberrations. Spherical mirrors cannot be used at large off-axis angles due to astigmatism, which leads to poor focusing of THz beams and to wavefront distortions.

Scanning in the time domain is usually performed using a mechanical translation stage with a retroreflector. Proper alignment of the reflector is crucial to prevent lateral

movement of the reflected beam, which can lead to unwanted effects such as phase or amplitude variations in THz detection or generation. Both the step size of the delay and the length of the translation stage are important, as they define the time and frequency resolution of the setup. The time delay Δt can be calculated as $\Delta t = 2\frac{\Delta x}{c}$, where Δx is the mechanical shift and c is the speed of light. Since the light travels to and from the reflector, the light path is effectively doubled. For THz spectroscopy, it is useful to remember the simple correspondence $1\ \mathrm{mm} \triangleq 6.67\ \mathrm{ps}$, as this helps in quickly estimating time delays.

1.2. THz pump – optical probe spectroscopy

In this type of spectroscopy, instead of detecting the transmitted or emitted THz radiation from a sample, changes in an optical probe beam reflect the material's properties. The experimental layout is shown in Figure 4. The optical probe can reveal various effects in the material under the influence of the THz pump, such as THz-induced transmission or absorption, and THz-induced magneto-optical Kerr or Faraday effects in magnetic materials. In this work, only transmission geometry is considered.

An important effect to account for in such experiments is the propagation effect. The propagation effect arises from the difference in refractive indices at optical and terahertz frequencies, which leads to different propagation speeds for the pump and probe pulses in the material. The propagation effect also impacts terahertz detection in electro-optical sampling and will be discussed in detail in Section 3. In this work, the sample thickness (90–100 nm) is much smaller compared to the wavelengths of both the THz pump (0.1–1 mm) and the optical probe (800 nm), so the propagation effect can be ignored.

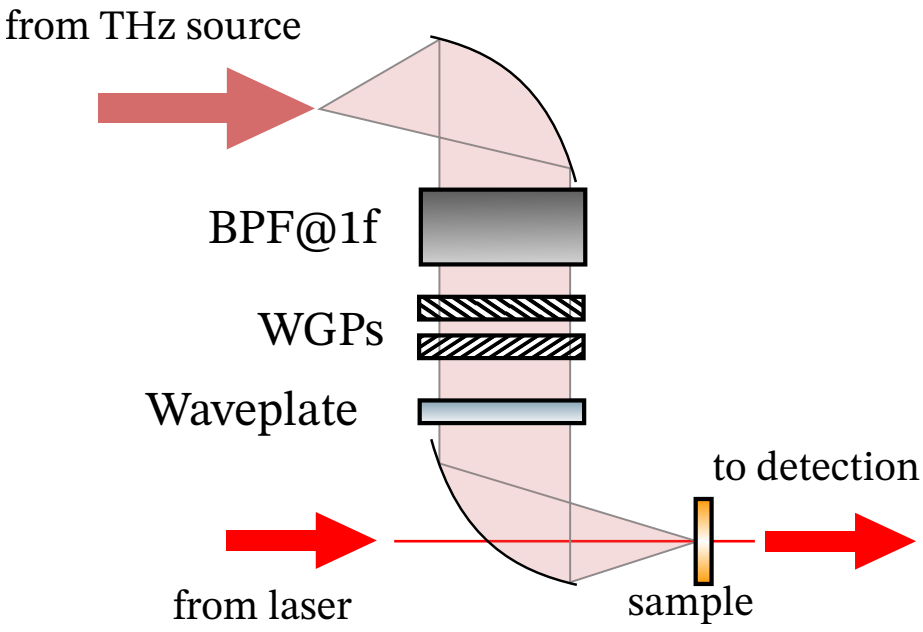

Figure 4: THz pump – optical probe setup.

2. Generation of high field THz radiation

There are many methods to generate THz radiation. Some are less common or even exotic, such as THz lasers, quantum-cascade lasers, or blackbody radiation sources, while others are more widespread today, like free electron lasers and photoconductive antennas. However, only a limited number of methods provide high peak THz fields ($>$ 100kV/cm), and even fewer offer high spectral density for narrowband generation. THz lasers seem to be an obvious choice, and while reported pulse powers up to 1 MW[6] are sufficient to achieve the desired field strength[1] , they lack frequency tunability and typically unique and complicated machines. Nowadays, there are two types of sources mainly used for high-field THz emission: laser-based sources via optical rectification and undulator sources. Both types were used in this work and will be discussed in detail here.

2.1. Undulator

An undulator is a periodic arrangement of magnets with a specific distance between them, as shown in Figure 5. It is installed as part of the beamline of an electron accelerator. The periodic arrangement is characterized by the period λ_U and the strength of the magnetic flux B. A relativistic or ultrarelativistic electron beam deviates under the Lorentz force in the periodic magnetic field and follows a near-sinusoidal trajectory. This causes the electrons to experience additional acceleration, leading to the emission of electromagnetic radiation.

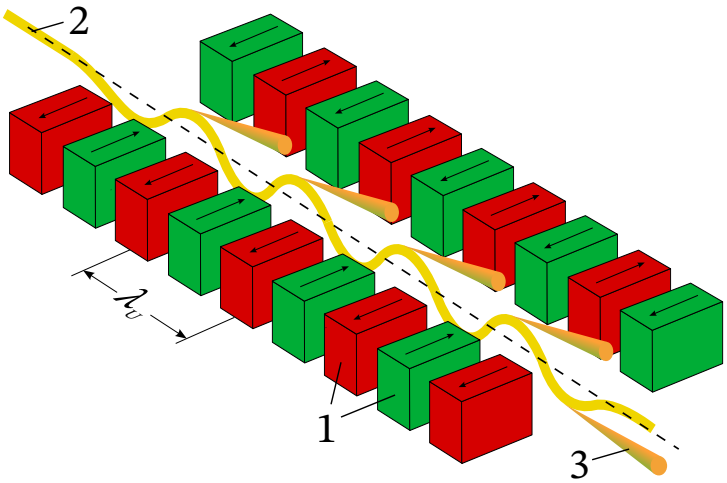

Figure 5: Schematic image of the undulator. 1 – alternating magnets, 2 – electron beam, 3 – emitted radiation, λ_U – period[7].

[1]For 1 THz and diffraction-limited focusing (beam radius $r \approx 0.15$ mm), the corresponding pulse power for $E = 100$kV/cm will be $W = w \cdot c \cdot \pi r^2 \approx 10$ kW, where $w = \frac{1}{2}\varepsilon_0 E^2$ is the energy density, ε_0 is vacuum permittivity, and c is the speed of light.

The concept of radiation emitted by electrons moving in a magnetic field, which underpins the operation of undulators, dates back to the early 20th century. The Lorentz model of the response of an electron to an electromagnetic field and subsequent developments by physicists like Dirac laid the groundwork for understanding electron radiation dynamics. Dirac's work on the classical theory of radiating electrons provides a foundational perspective on the electromagnetic origins of electron radiation [8]. In 1944, D. Ivanenko and A.A. Sokolov discussed the upper energy limit achievable in betatrons [9], and later in 1949, J. Schwinger provided a detailed theory of synchrotron radiation [10]. These works created the foundation for further developments in this field. An undulator and its radiation were first described by H. Motz in 1950 [11], and later, in 1953, the experimental observation of visible light at 440 nm and microwave radiation within the range $0.44 - 2.7$ mm ($\sim 0.1 - 0.7$ THz) was reported [12].

The theoretical works derived that the wavelength of radiation emitted by electrons λ can be written as[13]:

$$\lambda = \frac{\lambda_U}{2\gamma^2}\left(1 + \frac{K^2}{2} + \gamma^2\theta^2\right) \tag{3}$$

where $\gamma = \sqrt{1 - \left(\frac{v}{c}\right)^2}$ is the Lorentz factor, v is the speed of the electrons, λ_U is the spatial period between the magnets, and θ is the angle between the electron beam and the axis of emission detection. The parameter $K = \frac{eB\lambda_U}{2\pi mc^2}$ is the undulator strength parameter, where e and m are the charge and mass of the electron. The value of the strength parameter defines two different regimes for the undulator. At $K < 1$, the undulator operates in the low-field regime, where only a single frequency is observed. At $K > 1$, it enters the high-field regime, where harmonics appear in the emission spectrum [13].

The experiments presented in this work were conducted at the TELBE facility in Helmholtz-Zentrum Dresden-Rossendorf. It is an undulator-based superradiant THz source with a field strength of around 100 kV/cm in the frequency range from 0.1 to 1 THz and a repetition rate of up to 100 kHz [14]. Figure 6 shows a typical measured terahertz time trace at the TELBE facility. The machine was set up to generate pulses with a central frequency of 0.7 THz. From the spectrum, it is clearly seen that most of the pulse energy is concentrated around 0.7 THz. However, there is a clear presence of the second harmonic around 1.4 THz and a weak signal at the third harmonic frequency of 2.1 THz. As predicted by theory, the presence of harmonics occurs when the undulator strength parameter $K > 1$, which is the case here. Consequently, additional filtering of the pump pulses is required for nonlinear THz spectroscopy experiments.

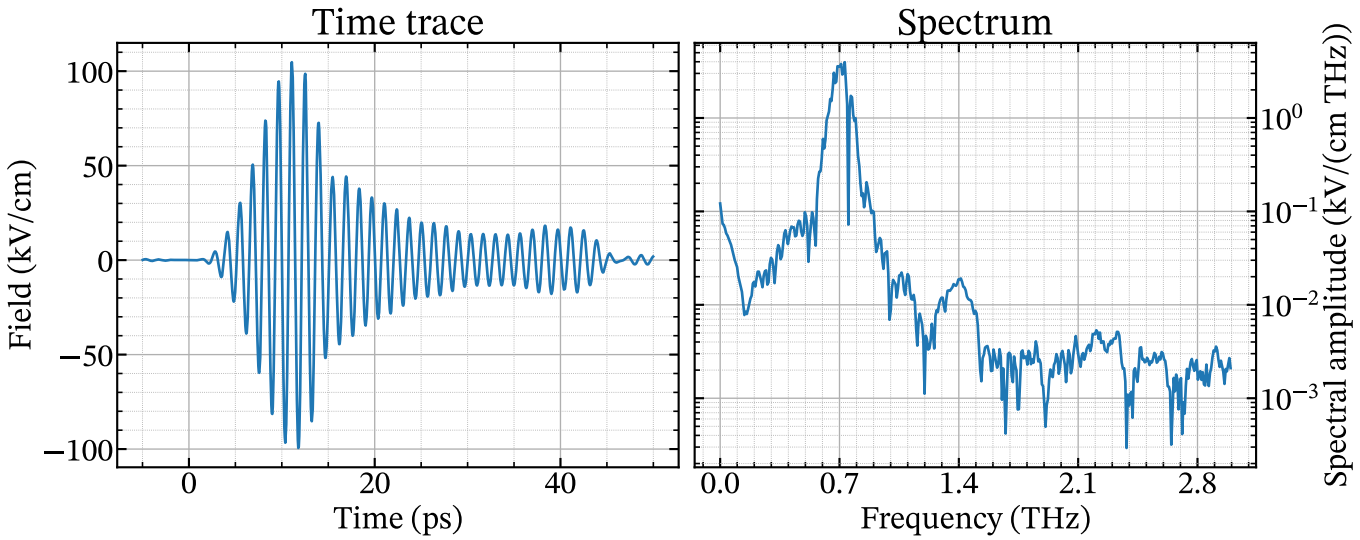

Figure 6: Time trace and spectrum of the THz pump at the TELBE facility.

2.2. Optical rectification

Optical rectification (OR), a second method for generating high-field THz radiation, is a second-order nonlinear process that occurs in noncentrosymmetric media [15]. Due to the nature of the process, optical rectification can provide a high bandwidth of generated THz emission and is considered one of the most efficient methods for THz generation [16,17]. One of the first attempts at generating far-infrared emission using OR was made by Yang, Richards, and Shen in 1971. They used 5 picosecond pulses from a Nd:glass laser ($\lambda \approx 1\mu m$) to pump $LiNbO_3$ and detected far-infrared radiation in the range of 2 to 16 cm^{-1} (0.06 – 0.48 THz) using a Michelson interferometer [18]. The first time-resolved experiments were reported by Auston [19], where the authors observed THz generation via a Cherenkov radiation analog in a $LiTaO_3$ crystal and used the same crystal for detection. Later, Xu, Zhang, and Auston reported the detection of free-space THz radiation from both $LiNbO_3$ and $LiTaO_3$ crystals [20]. These foundational studies shaped the modern design of THz sources based on nonlinear crystals.

As a second-order nonlinear process, OR can be described in terms of nonlinear polarization and the susceptibility tensor, similarly to difference frequency generation. The term “optical rectification” refers to the generation of a DC or quasi-DC (GHz or THz) field through difference frequency generation. The generation of a plane wave $E_{\mathrm{THz}}\left(\vec{k}_{THz}, \Omega\right)$ at difference frequency Ω from two plane waves $E_1\left(\vec{k}_1, \omega_1\right)$ and $E_2\left(\vec{k}_2, \omega_2\right)$ in a nonlinear material with nonresonant real second-order susceptibility $\chi^{(2)}$ is described by the second-order nonlinear polarization $P^{(2)}(\Omega)$:

$$P_i^{(2)}(\Omega) = \chi^{(2)}(\Omega = \omega_1 - \omega_2; \omega_1, \omega_2) E_1(\omega_1) E_2(\omega_2). \tag{4}$$

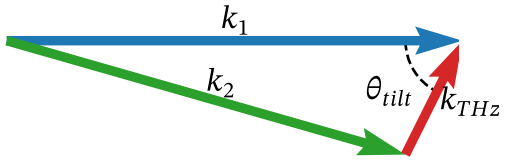

Figure 7: Phase matching as a triangle of wavevectors.

It has been shown that for effective generation, phase matching conditions must be satisfied [21]. The phase matching condition is $\left|\Delta\vec{k}\right|L < \pi$, where $\Delta\vec{k} = \vec{k}_1 - \vec{k}_2 - \vec{k}_{THz}$ is the phase mismatch for the OR process and L is the interaction length. Zero phase mismatch is highly desirable, as the efficiency of nonlinear processes scales with the thickness L.

Crystals like ZnTe and GaP meet the conditions for effective THz generation with femtosecond pulses around 800 and 1500 nm, respectively. For high-field THz generation, crystals such as $LiNbO_3$ or organic DAST are better choices, though they bring additional challenges. The DAST crystal effectively generates from 2 THz and higher but has a low damage threshold, while $LiNbO_3$ requires a noncollinear geometry to achieve high conversion efficiency. This generation geometry, known as "tilted pulse front generation," was proposed by János Hebling in 2002 [22] and is necessary due to poor phase matching in collinear geometry in $LiNbO_3$.

The basic idea behind this method is to produce pairs of $\vec{k}_1$ and $\vec{k}_2$ with some angle θ_{tilt} between them, forming a triangle of vectors with $\Delta\vec{k} = 0$. This satisfies the phase matching conditions for effective THz generation over a relatively broad frequency range. Such pairs can be produced by using a diffraction grating in combination with a telescope. The telescope is needed to image the laser spot on the grating inside the $LiNbO_3$ crystal[23]. The tilt angle θ_{tilt} is defined by the material's dispersion at the corresponding frequencies as $\theta_{\text{tilt}} = \arccos\left(n_{\text{gr}}(\omega)/n(\Omega)\right)$, where $n_{\text{gr}}(\omega)$ is the group index at the central pump frequency, and $n(\Omega)$ is the refractive index at the THz frequency[22]. For a pump wavelength of 800 nm and a central frequency of the generated beam at 1 THz, the corresponding tilt angle is $\theta_{\text{tilt}} = 62.7°$. These parameters define the angles of incidence and diffraction for the diffraction grating together with magnification of the telescope, creating the required wavefront tilt [23]. Figure 8 shows the design of the implemented THz generator for nonlinear THz spectroscopy according to the specified parameters. The calculated angle of incidence is $37.4°$, and the diffraction angle is $56.3°$. The efficiency of THz generation is highly sensitive to both angles, so accurate alignment of the generator with THz power output monitoring is essential. To achieve high diffraction efficiency, the laser polarization is kept *p*-polarized before the grating [24]. A half-wave plate after the grating rotates the polarization to enable the

OR process in the $LiNbO_3$ crystal. To block scattered 800 nm radiation from the THz path, a piece of Si wafer is inserted. Since Si wafers are relatively thin (typically several hundred micrometers), reflections inside the wafer will be close to the main THz pulse, potentially spoiling measurements. Additional reflections can be avoided if the wafer is placed at the Brewster angle of 73.6°.

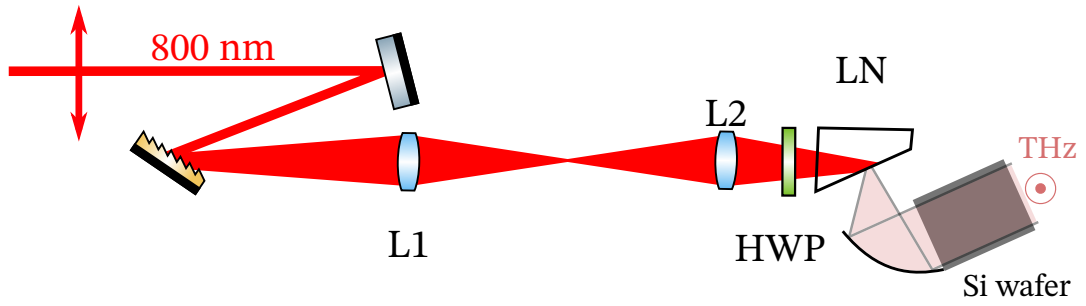

Figure 8: Sketch of the laser-based THz generator. LN is a $LiNbO_3$ crystal, L1 and L2 are telescope lenses with focal lengths of 160 and 100 cm, respectively. HWP is a half-wave plate.

A typical time trace of the generated THz pulse and its corresponding spectrum are shown in Figure 9. The peak field reaches nearly 900 kV/cm, with a long tail of oscillations caused by water vapor absorption in the air. The spectrum of the pulse has a maximum around 0.6 THz and shows a second peak at 1.9 THz. From the inset, it is clear that even at 3 THz, generation still occurs, with about 1% of the maximum amplitude. For THz harmonic generation, such broadband generation is a downside and necessitates the use of bandpass filters.

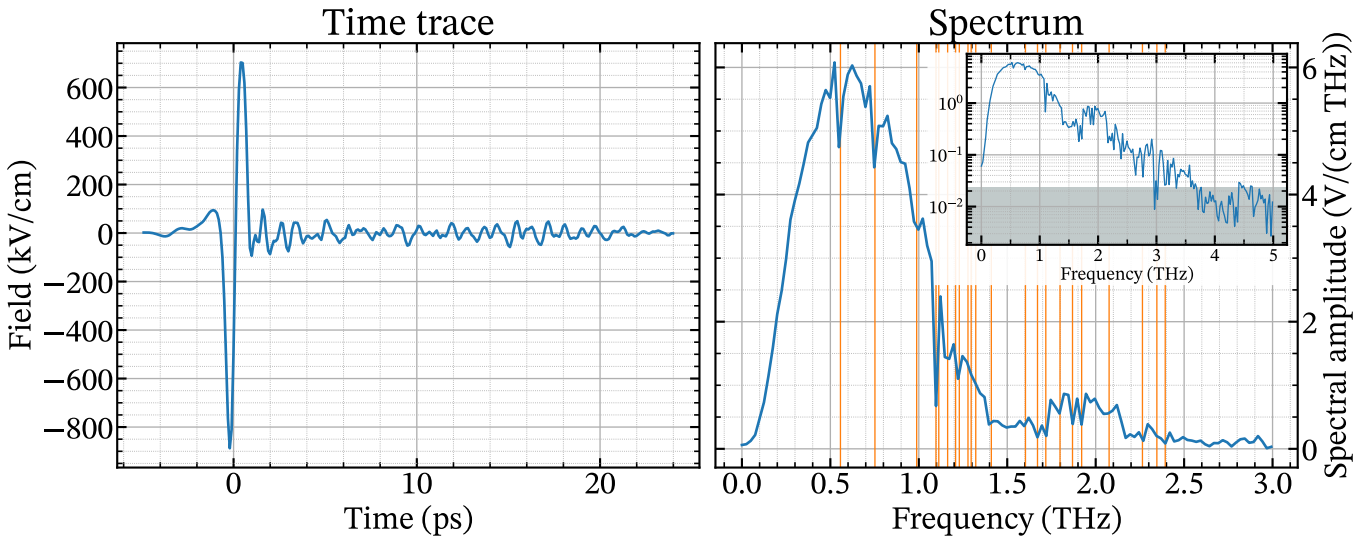

Figure 9: Time trace of the THz pump (left), corresponding spectrum on a linear (right) and logarithmic (inset) scale. Orange lines indicate water vapor absorption lines from [25–27]. The grey zone in the inset marks the noise floor.

3. Detection of THz fields

Terahertz field detection technologies are broadly categorized into two main groups: incoherent and coherent detection. Incoherent detectors measure the power of THz radiation, rather than the electric field. Due to this, these detectors lack the capability to detect phase information, which is crucial for certain applications. The most commonly used incoherent detectors are:

- **Golay cells**: Incoming THz radiation is absorbed by a membrane in a small gas chamber, causing deformation of the chamber walls. This deformation is tracked by an internal optical system and calibrated to show incident THz power [28,29].
- **Pyroelectric sensors**: When radiated by THz waves, these sensors convert absorbed energy into voltage [30,31].
- **Bolometers** and **superconductive bolometers**: A temperature rise caused by THz radiation absorption leads to a change in resistivity [32,33]. This effect is enhanced near the superconductive transition temperature [34,35].

In contrast, coherent detection methods produce a signal directly proportional to the THz field, enabling both amplitude and phase measurements of the electric field. This capability is facilitated by various techniques, including:

- **Photoconductive antennas**: An optical pulse creates short-lived transient charges in a semiconductor material, which are then accelerated by the synchronized THz field. The resulting current is detected [36,37].
- **Air-based coherent detection**: The nonlinear interaction of the THz field with an optical probe pulse in air produces a modulated second harmonic, proportional to the THz field strength [38].
- **Electro-optic sampling** (EOS): The modulation of the polarization state of an optical beam by the THz field through an electro-optic crystal is observed.

For all experiments conducted in this work, EOS was chosen as the detection method. The electro-optic sampling (EOS) technique utilizes the linear Pockels effect in an electro-optical crystal (ZnTe) to probe the electric field of the THz pulse. The electric field of the THz pulse induces birefringence in the crystal through the Pockels effect, which is directly proportional to the applied THz electric field[4]. By measuring the induced birefringence via the change in the polarization state of the optical probe beam, the THz electric field is extracted. Figure 10 shows a typical layout for EOS. The linearly polarized optical probe overlaps with the THz pulse in the nonlinear crystal, and then its polarization is changed from linear to circular by a $\frac{\lambda}{4}$ waveplate. A Wollaston prism splits the beam into x and y polarization components, which are detected by photodiodes. By

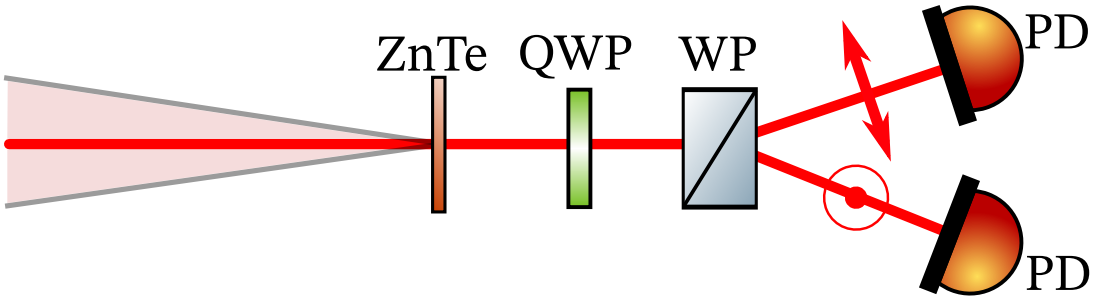

Figure 10: A sketch of EOS detection. QWP - quarter-wave plate, WP - Wollaston prism, PD - photodiodes.

subtracting the signals from the diodes, changes in the ellipticity of the optical beam can be revealed. It has been shown[4] that terahertz radiation at frequency Ω creates phase retardation $\Delta\varphi = \frac{\omega L}{c} n^3 d_{14} E_{\mathrm{THz}}(\Omega)$ [21], where ω is the optical circular frequency, n is the optical refractive index of ZnTe, and d_{14} represents the electro-optical coefficient. Phase retardation changes the detected intensities as:

$$\begin{aligned} I_x &= \frac{I}{2}(1 + \sin(\Delta\varphi)) \approx \frac{I}{2}(1 + \Delta\varphi) \\ I_y &= \frac{I}{2}(1 - \sin(\Delta\varphi)) \approx \frac{I}{2}(1 - \Delta\varphi), \end{aligned} \tag{5}$$

where I is the probe intensity. By normalizing the difference of intensities to their sum, one obtains:

$$S(\Omega) = \frac{I_x - I_y}{I_x + I_y} = \Delta\varphi = \frac{\omega L}{c} n^3 d_{14} E_{\mathrm{THz}}(\Omega) \propto E_{\mathrm{THz}}(\Omega) \tag{6}$$

This simplified equation is valid only when $\Delta\varphi \ll 1$, otherwise the THz waveform will be distorted and "virtual" harmonics will appear in the signal spectrum. This effect is shown in Figure 11. While the time traces are almost identical, in the frequency domain there are peaks at the second and third harmonic frequencies, whereas at reduced fluence the harmonics are gone. If such harmonics were real, the efficiency of second harmonic generation would be nearly 1%, and third harmonic nearly 0.5%, comparable to the efficiency of third harmonic generation in graphene [39] and Cd_3As_2 [40], which are among the most nonlinear materials in the THz range.

So far, the description of the EOS process has not involved phase matching conditions. However, for reliable detection of THz fields, especially at higher frequencies, it is necessary to take this into account. Phase matching can be viewed as a propagation effect. Due to the difference between the group velocity of the femtosecond pulse and

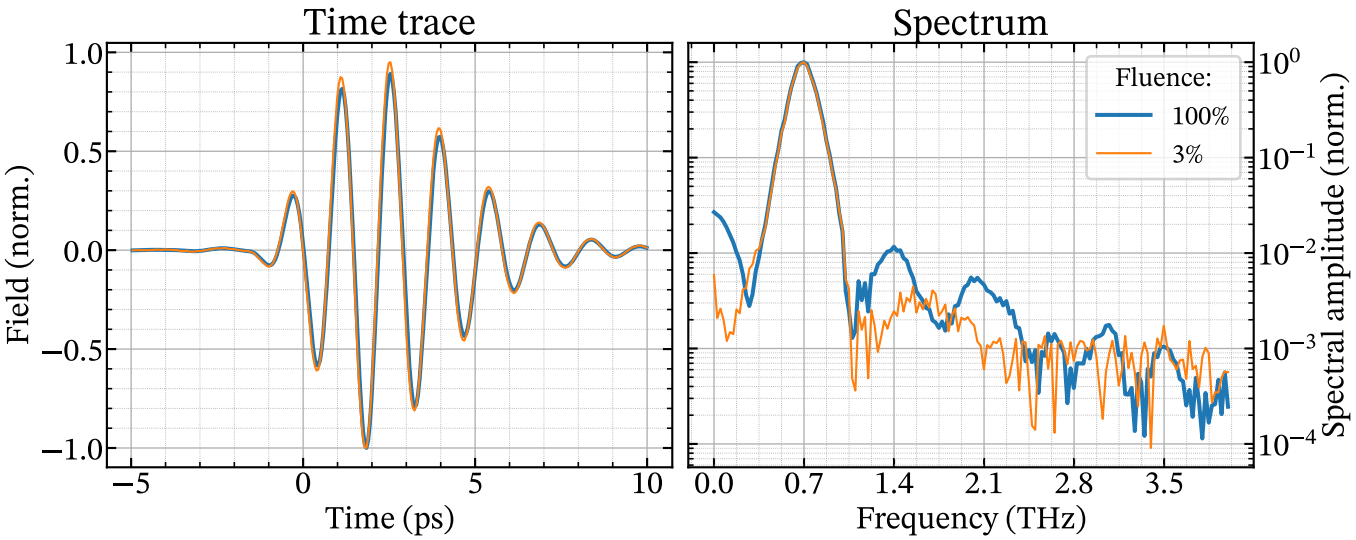

Figure 11: Example of two narrowband THz signals, measured at two different fluences. Other experimental conditions are equivalent.

the phase velocity of the terahertz wave, there is only a limited distance for efficient interaction. Beyond this distance, the accumulated phase difference leads to destructive interference, decreasing the resulting signal. This means that despite the balanced signal $S(\Omega)$ from (6) increasing with the length of the crystal, sensitivity at higher THz frequencies may be limited.

To account for this effect, as well as the importance of laser pulse duration, the angle between the polarizations of the optical and THz beams, and the detector crystal axes, a refined version of the equation (6) can be written as [41]:

$$S(\Omega) \propto \omega L T(\Omega) C(\Omega) f(\theta, \theta'). \tag{7}$$

Here, the three terms correspond to the issues mentioned above. For crystals with a zinc-blende structure and $\langle 110 \rangle$ cut, the term $f(\theta, \theta') = \sin(2\theta + \theta') + \cos 2\theta \sin \theta'$ describes the angular dependence of the detected signal based on the angle θ between the z axis of the crystal and the optical polarization, and the angle θ' between the z axis of the crystal and the THz polarization. The term $C(\Omega) = \int \mathrm{d}\Omega\, A(\omega) A^*(\omega - \Omega)$ is a spectral autocorrelation function, where $A(\omega)$ represents the optical spectral component. Finally, $T(\Omega) = \chi^{(2)} \operatorname{sinc}\left(\frac{\Delta k(\Omega) L}{2}\right)$ describes the phase matching. For a ZnTe crystal, the calculated $T(\Omega)$ for various crystal thicknesses is shown in the left pane of Figure 12. The right pane demonstrates the effect of probe pulse duration on detection.

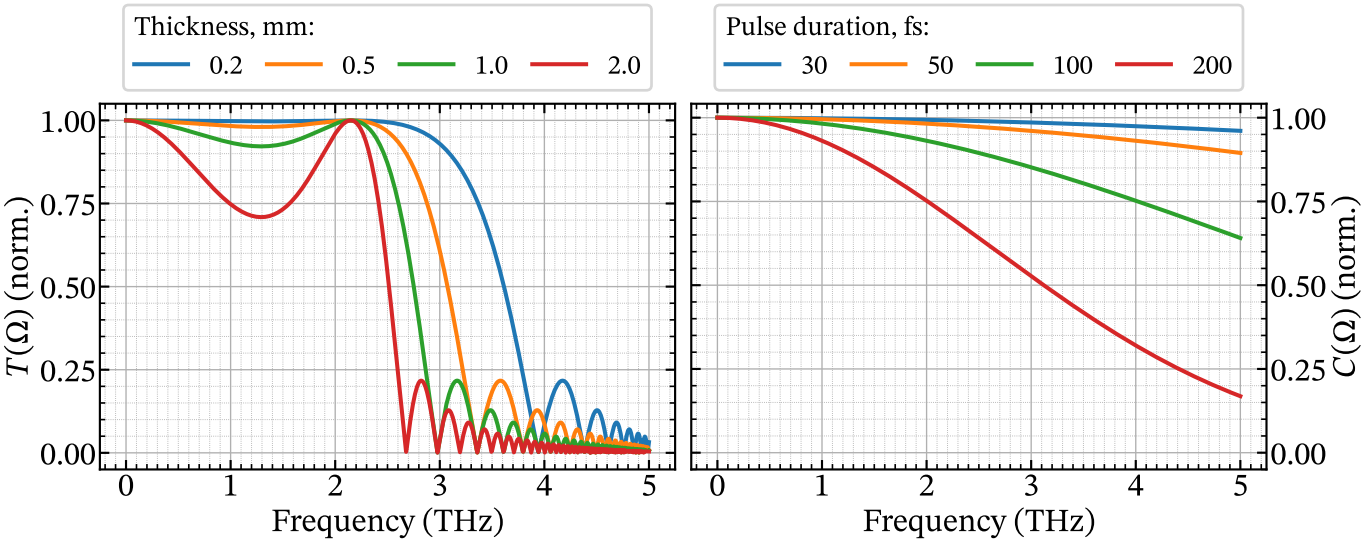

Figure 12: Calculated $T(\Omega)$ (left) and $C(\Omega)$ (right) functions.

4. Polarization state characterization. Application for characterization of THz waveplates

The polarization state of electromagnetic radiation is a crucial property of light in spectroscopic studies. In linear spectroscopy, various polarization orientations provide access to different conductivity tensor components in semiconductors and metals, or allow measurement of the refractive index along different crystallographic axes. Additionally, circularly polarized light can sense or drive magnetic excitations in a material. In nonlinear spectroscopy, the response to different polarization states can reveal material symmetry, as nonlinear tensors follow the symmetries of materials. In pump-probe experiments, changes in polarization are often used to track magnetization dynamics via Faraday or magneto-optical Kerr effects, or to observe the presence of phonon excitations or electron dynamics via the optical Kerr effect.

To characterize the polarization state of an electromagnetic wave, Jones method and Stokes parameters can be used[42]. Since a free-space electromagnetic wave is transverse, only two vector components are needed to describe polarization in a frame where $\vec{e}_z \parallel \vec{k}$ and thus $E_z \equiv 0$:

$$\vec{E}(t) = \begin{pmatrix} \hat{E}_x(t) \\ \hat{E}_y(t) \end{pmatrix}, \tag{8}$$

where $\hat{E}_i(t), i = \{x, y\}$ is the analytical complex signal of the polarization component. For a monochromatic plane wave:

$$\vec{E}(t) = e^{ikz-i\omega t}\begin{pmatrix} E_{0x} \\ E_{0y}e^{i\varphi} \end{pmatrix}, \tag{9}$$

where φ represents the phase difference between polarization components.

Stokes parameters are used to describe the polarization state of an electromagnetic wave. In a fixed frame where horizontal polarization H matches the *x* direction, and vertical polarization V is parallel to *y*, the Stokes parameters can be written as [42]:

$$\begin{aligned} S_0 &= |E_x|^2 + \left|E_y\right|^2, \\ S_1 &= |E_x|^2 - \left|E_y\right|^2, \\ S_2 &= 2\,\mathrm{Re}\big(E_x^* E_y\big), \\ S_3 &= 2\,\mathrm{Im}\big(E_x^* E_y\big). \end{aligned} \tag{10}$$

All Stokes parameters have units of intensity, and $S_0 \equiv I$ by definition. For polarized light, only three parameters are independent, with the binding:

$$S_0^2 = S_1^2 + S_2^2 + S_3^2. \tag{11}$$

The polarization state can be visualized as a point on a sphere with coordinates (S_1, S_2, S_3). This sphere is called a Poincaré sphere. It is an illustrative way to represent the polarization state (see Figure 13) and track changes in polarization.

It is useful to introduce normalized Stokes parameters $s_i = S_i/S_0, i = 1...3$, as these values are easier to interpret. For normalized parameters, the radius of the Poincaré sphere is one, and there are six "poles":

- $\vec{s} = (\pm 1, 0, 0)$ — linear polarization, H — horizontal $(+1)$ or V — vertical (-1),
- $\vec{s} = (0, \pm 1, 0)$ — linear polarization, D — diagonal $(+1)$ or A — antidiagonal (-1),
- $\vec{s} = (0, 0, \pm 1)$ — circular polarization, R — right $(+1)$ or L — left (-1).

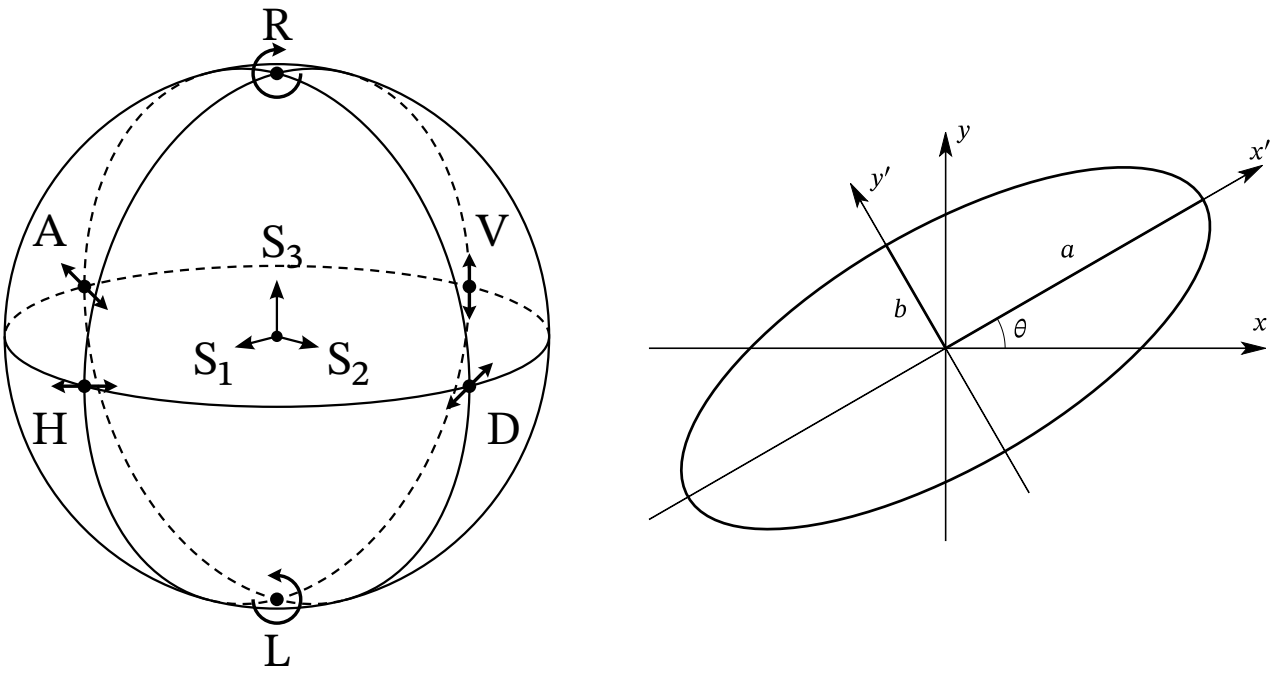

Figure 13: Poincaré sphere (left) and polarization ellipse (right).

The polarization state can also be represented as a polarization ellipse. The ellipse is the trajectory traced by $\vec{E}$ in the polarization plane over one oscillation of the field. In terms of the polarization ellipse, the polarization state can be characterized by two parameters: tilt angle $0 \leq \theta < \pi$ and ellipticity $\xi = \pm b/a \leq 1$ ("+" for right polarized, "−" for left polarized). This representation provides an easier understanding of how light is polarized and its orientation in the lab frame.

Both the tilt angle and ellipticity can be calculated from the Stokes parameters:

$$\begin{aligned} \theta &= \frac{1}{2}\arctan\left(\frac{S_2}{S_1}\right), \\ \xi &= \tan\left(\frac{1}{2}\arcsin\left(\frac{S_3}{S_0}\right)\right). \end{aligned} \tag{12}$$

This means that by measuring the Stokes parameters of the light, the polarization state is fully described.

This method can be utilized to characterize a THz waveplate. Since the waveplate in the THz region is typically a piece of quartz cut to a specified thickness, it is important to characterize it before use and to properly interpret experiments involving such a waveplate. Due to the time-resolved nature of the experiments, the THz electric field is measured directly. By using an additional polarizer, two orthogonal components of the

electric field, $E_x(t)$ and $E_y(t)$, can be measured. The analytical complex signal can be acquired with the Hilbert transform $\mathcal{H}$ as [43]:

$$\hat{E}_i = E_i + j \cdot \mathcal{H}(E_i), i = \{x, y\}. \tag{13}$$

By measuring the transmitted THz radiation through the tested waveplate at different angles α of waveplate rotation, one can calculate $S_i(t, \alpha)$ or $S_i(\omega, \alpha)$ and use it to create mappings $\theta(t, \alpha), \xi(t, \alpha)$ or $\theta(\omega, \alpha), \xi(\omega, \alpha)$.

Such a procedure was performed for the THz quarter waveplate used in this work. Broadband THz pulses allow for a wide range of frequencies to be covered. The measured maps, presented in Figure 14, show how the waveplate changes the polarization state of the beam at various frequencies. It is clearly seen that despite being designed to function as a $\frac{\lambda}{4}$ waveplate at 0.7 THz, the maximum ellipticity achieved at this frequency is only ≈ 0.8. These mappings indicate the potential for using the waveplate to control polarization states at other frequencies as well.

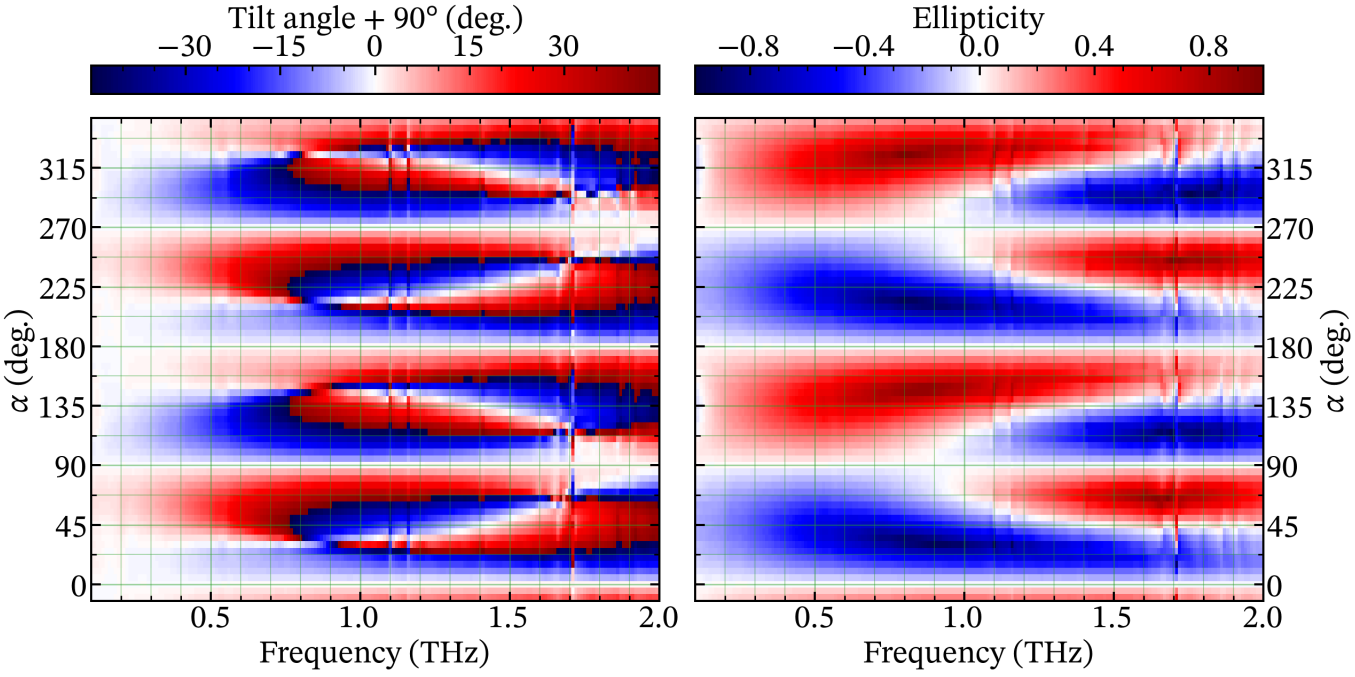

Figure 14: Measured maps of tilt angle θ and ellipticity ξ for the THz waveplate.

5. References

[1] J. Connes and P. Connes, *Near-Infrared Planetary Spectra by Fourier Spectroscopy. I. Instruments and Results*, Journal of the Optical Society of America **56**, 896 (1966).

[2] Z. Wang, S. Kovalev, N. Awari, M. Chen, S. Germanskiy, B. Green, J.-C. Deinert, T. Kampfrath, J. Milano, and M. Gensch, *Magnetic Field Dependence of Antiferromagnetic Resonance in NiO*, Applied Physics Letters **112**, 252404 (2018).

[3] J.-M. Manceau, P. A. Loukakos, and S. Tzortzakis, *Direct Acoustic Phonon Excitation by Intense and Ultrashort Terahertz Pulses*, Applied Physics Letters **97**, 251904 (2010).

[4] Y.-S. Lee, *Principles of Terahertz Science and Technology* (Springer, New York, NY, 2009).

[5] M. Naftaly and R. Dudley, *Terahertz Reflectivities of Metal-Coated Mirrors*, Applied Optics **50**, 3201 (2011).

[6] D. T. Hodges, *A Review of Advances in Optically Pumped Far-Infrared Lasers*, Infrared Physics **18**, 375 (1978).

[7] B. Holst, *Working of the Undulator. An Undulator Is a Device from High-Energy Physics and Usually Part of a Larger Installation, a Synchrotron.*, https://commons.wikimedia.org/wiki/File:Undulator_(numbers).svg, (2005).

[8] P. Dirac, *Classical Theory of Radiating Electrons*, Proceedings of the Royal Society A: Mathematical, Physical and Engineering Sciences **167**, 148 (1938).

[9] D. Iwanenko and I. Pomeranchuk, *On the Maximal Energy Attainable in a Betatron*, Physical Review **65**, 343 (1944).

[10] J. Schwinger, *On the Classical Radiation of Accelerated Electrons*, Physical Review **75**, 1912 (1949).

[11] H. Motz, *Applications of the Radiation from Fast Electron Beams*, Journal of Applied Physics **22**, 527 (1951).

[12] H. Motz, W. Thon, and R. N. Whitehurst, *Experiments on Radiation by Fast Electron Beams*, Journal of Applied Physics **24**, 826 (1953).

[13] Y. Farge, *Emission of Photons by Undulators*, Applied Optics **19**, 4021 (1980).

[14] B. Green, S. Kovalev, V. Asgekar, G. Geloni, U. Lehnert, T. Golz, M. Kuntzsch, C. Bauer, J. Hauser, J. Voigtlaender, et al., *High-Field High-Repetition-Rate Sources for the Coherent THz Control of Matter*, Scientific Reports **6**, 22256 (2016).

[15] M. Bass, P. A. Franken, J. F. Ward, and G. Weinreich, *Optical Rectification*, Physical Review Letters **9**, 446 (1962).

[16] S. B. Bodrov, I. E. Ilyakov, B. V. Shishkin, and M. I. Bakunov, *Highly Efficient Cherenkov-type Terahertz Generation by 2-μm Wavelength Ultrashort Laser Pulses in a Prism-Coupled $LiNbO_3$ Layer*, Optics Express **27**, 36059 (2019).

[17] S.-W. Huang, E. Granados, W. R. Huang, K.-H. Hong, L. E. Zapata, and F. X. Kärtner, *High Conversion Efficiency, High Energy Terahertz Pulses by Optical Rectification in Cryogenically Cooled Lithium Niobate*, Optics Letters **38**, 796 (2013).

[18] K. H. Yang, P. L. Richards, and Y. R. Shen, *Generation of Far-Infrared Radiation by Picosecond Light Pulses in $LiNbO_3$*, Applied Physics Letters **19**, 320 (1971).

[19] D. H. Auston, K. P. Cheung, J. A. Valdmanis, and D. A. Kleinman, *Cherenkov Radiation from Femtosecond Optical Pulses in Electro-Optic Media*, Physical Review Letters **53**, 1555 (1984).

[20] L. Xu, X.-C. Zhang, and D. H. Auston, *Terahertz Beam Generation by Femtosecond Optical Pulses in Electro-Optic Materials*, Applied Physics Letters **61**, 1784 (1992).

[21] R. W. Boyd, *Nonlinear Optics*, 3rd ed (Academic Press, Burlington, MA, 2008).

[22] J. Hebling, G. Almasi, I. Kozma, and J. Kuhl, *Velocity Matching by Pulse Front Tilting for Large Area THz-pulse Generation*, Optics Express **10**, 1161 (2002).

[23] J. A. Fülöp, L. Pálfalvi, G. Almási, and J. Hebling, *Design of High-Energy Terahertz Sources Based on Optical Rectification*, Optics Express **18**, 12311 (2010).

[24] C. Palmer, *Diffraction Grating Handbook*, Seventh edition (Newport Corporation, Rochester, NY, 2014).

[25] M. van Exter, C. Fattinger, and D. Grischkowsky, *Terahertz Time-Domain Spectroscopy of Water Vapor*, Optics Letters **14**, 1128 (1989).

[26] X. Xin, H. Altan, A. Saint, D. Matten, and R. R. Alfano, *Terahertz Absorption Spectrum of Para and Ortho Water Vapors at Different Humidities at Room Temperature*, Journal of Applied Physics **100**, 94905 (2006).

[27] D. M. Slocum, E. J. Slingerland, R. H. Giles, and T. M. Goyette, *Atmospheric Absorption of Terahertz Radiation and Water Vapor Continuum Effects*, Journal of Quantitative Spectroscopy and Radiative Transfer **127**, 49 (2013).

[28] L. O. T. Fernandes, P. Kaufmann, R. Marcon, A. S. Kudaka, A. Marun, R. Godoy, E. C. Bortolucci, M. B. Zakia, and J. A. Diniz, *Photometry of THz Radiation Using*

Golay Cell Detector, in *2011 XXXth URSI General Assembly and Scientific Symposium* (2011), pp. 1–4.

[29] Y. Wang, Z. Zhao, Z. Chen, and L. Wang, *Characterization of Golay Detector for the Absolute Power Measurement of Terahertz Radiation*, in *2012 37th International Conference on Infrared, Millimeter, And Terahertz Waves* (2012), pp. 1–2.

[30] C. W. Berry, N. T. Yardimci, and M. Jarrahi, *Responsivity Calibration of Pyroelectric Terahertz Detectors*, (2014).

[31] R. Müller, B. Gutschwager, J. Hollandt, M. Kehrt, C. Monte, R. Müller, and A. Steiger, *Characterization of a Large-Area Pyroelectric Detector from 300 GHz to 30 THz*, Journal of Infrared, Millimeter, And Terahertz Waves **36**, 654 (2015).

[32] S. Cherednichenko, A. Hammar, S. Bevilacqua, V. Drakinskiy, J. Stake, and A. Kalabukhov, *A Room Temperature Bolometer for Terahertz Coherent and Incoherent Detection*, IEEE Transactions on Terahertz Science and Technology **1**, 395 (2011).

[33] A. Kosarev, S. Rumyantsev, M. Moreno, A. Torres, S. Boubanga, and W. Knap, *Si_xGe_y:H-based Micro-Bolometers Studied in the Terahertz Frequency Range*, Solid-State Electronics **54**, 417 (2010).

[34] A. J. Kreisler and A. Gaugue, *Recent Progress in High-Temperature Superconductor Bolometric Detectors: From the Mid-Infrared to the Far-Infrared (THz) Range*, Superconductor Science and Technology **13**, 1235 (2000).

[35] A. L. Woodcraft, P. A. R. Ade, J. Cox, C. Dunscombe, T. Jones, R. V. Sudiwala, and K. P. Wood, *A Turn-Key Cryogenic Superconducting Bolometer Detector System*, in *2015 40th International Conference on Infrared, Millimeter, And Terahertz Waves (IRMMW-THz)* (IEEE, Hong Kong, China, 2015), pp. 1–2.

[36] P. U. Jepsen, R. H. Jacobsen, and S. R. Keiding, *Generation and Detection of Terahertz Pulses from Biased Semiconductor Antennas*, Journal of the Optical Society of America B **13**, 2424 (1996).

[37] M. T. M. Tani, K. S. K. Sakai, and H. M. H. Mimura, *Ultrafast Photoconductive Detectors Based on Semi-Insulating GaAs and InP*, Japanese Journal of Applied Physics **36**, L1175 (1997).

[38] J. Dai, X. Xie, and X.-C. Zhang, *Detection of Broadband Terahertz Waves with a Laser-Induced Plasma in Gases*, Physical Review Letters **97**, 103903 (2006).

[39] H. A. Hafez, S. Kovalev, J.-C. Deinert, Z. Mics, B. Green, N. Awari, M. Chen, S. Germanskiy, U. Lehnert, J. Teichert, et al., *Extremely Efficient Terahertz High-Harmonic Generation in Graphene by Hot Dirac Fermions*, Nature **561**, 507 (2018).

[40] S. Kovalev, R. M. A. Dantas, S. Germanskiy, J.-C. Deinert, B. Green, I. Ilyakov, N. Awari, M. Chen, M. Bawatna, J. Ling, et al., *Non-Perturbative Terahertz High-Harmonic Generation in the Three-Dimensional Dirac Semimetal Cd_3As_2*, Nature Communications **11**, (2020).

[41] S. P. Kovalev and G. K. Kitaeva, *Terahertz Electro-Optical Detection: Optical Phase or Energy Measurements*, Journal of the Optical Society of America B **30**, 2650 (2013).

[42] M. Born and E. Wolf, *Principles of Optics: 60th Anniversary Edition*, 7th ed. (Cambridge University Press, Cambridge, 2019).

[43] D. Gabor, *Theory of Communication. Part 1: The Analysis of Information*, Journal of the Institution of Electrical Engineers - Part III: Radio and Communication Engineering **93**, 429 (1946).

Chapter II
The Dirac material Cd_3As_2

This chapter provides an overview of the history of semimetallic cadmium arsenide (Cd_3As_2), covering its early experimental studies and the discovery of the Dirac cone in the material. Next, the chapter discusses the basic theory behind the concept of Dirac/Weyl points and offers an overview of experimental works focused on studying Dirac or Weyl materials using terahertz radiation.

1. Early experiments with Cd_3As_2

The material Cd_3As_2 has been known for almost a hundred years, since its first investigations in the 1930s by von Stackelberg and Paulu[1]. Their research involved the preparation of single crystals of Cd_3As_2 through sublimation, allowing them to study its crystallographic properties in detail. They determined that Cd_3As_2 crystallizes in a tetragonal structure with eight atoms units per unit cell. With growing interest in semiconductor materials in the 1960s–1970s, Cd_3As_2 again attracted the attention of the scientific community due to its high electron mobility $> 10^4$ cm^2/(V·s)[2].

Studies by Rosenman[3] and Armitage and Goldsmid[4] focused on the material's electronic band structure using experimental techniques such as Shubnikov-de Haas oscillations and the observation of the saturation magneto-Seebeck and Hall coefficients. These measurements suggested the presence of a non-parabolic conduction band in the material to explain the observed results.

Theoretical models during this period treated Cd_3As_2 as a Kane-type semiconductor, similar to zinc-blende semiconductors. However, discrepancies in band structure parameters, such as the ordering of electronic bands and the presence of additional conduction bands, highlighted the complexity of Cd_3As_2's electronic properties and led to ongoing debates among researchers.

2. Discovery of the Dirac point in Cd_3As_2 and experimental confirmation

The next wave of interest in Cd_3As_2 began in 2013 with the prediction of a 3D Dirac point in the material by Zhijun Wang and coauthors[5]. Their first-principles calculations revealed that Cd_3As_2 is a symmetry-protected topological semimetal, with a single pair of 3D Dirac points in the bulk and nontrivial Fermi arcs on the surfaces. Wang

highlighted the distinct electronic structure of Cd_3As_2, characterized by a single pair of Dirac points along the k_z axis in the Brillouin zone. This differs from conventional semimetals, where band crossings typically occur at multiple points or along entire lines. The crystal symmetry, specifically the C_4 rotational symmetry along the k_z axis, protects these 3D Dirac points, ensuring their robustness. They also proposed that Cd_3As_2 could exhibit unique transport properties due to its 3D Dirac fermions, predicting a large linear quantum magnetoresistance up to room temperature[5].

The theoretical predictions caused a wave of experimental efforts aimed at verifying the existence of 3D Dirac points in Cd_3As_2. In 2014, two independent research groups, led by Neupane and Borisenko, published their findings on the experimental realization of the 3D Dirac semimetal phase in Cd_3As_2[6,7].

Neupane et al.[6] in their experiments grew high-quality single crystals of Cd_3As_2 and performed ARPES measurements at various photon energies. Their data revealed the presence of linearly dispersing electronic states forming narrow conical structures, consistent with the theoretical predictions of 3D Dirac points. The ARPES spectra showed two distinct regions in momentum space where these Dirac cones were located, providing direct evidence for the existence of 3D Dirac points in Cd_3As_2. The researchers also compared their experimental results with theoretical band structure calculations. The close agreement between the ARPES data and the theoretical predictions further confirmed the 3D Dirac semimetal nature of Cd_3As_2. The observation of these Dirac points was a significant breakthrough, as it validated the theoretical framework proposed by Wang et al.[5] and established Cd_3As_2 as a model system for studying 3D Dirac semimetals.

Concurrently, Borisenko and his colleagues [7] conducted similar experiments using ARPES with ultrahigh resolution to confirm the presence of 3D Dirac points in Cd_3As_2. Their measurements revealed narrow, conical features in the electronic dispersion indicative of Dirac cones, and their theoretical calculations aligned with the experimental data, showing a single pair of 3D Dirac points along the Γ–Z direction in the Brillouin zone. They also investigated the material's transport properties, reporting electronic mobility 280000 $cm^2/(V{\cdot}s)$, which is comparable to that of graphene.This high mobility was attributed to the presence of 3D Dirac points, which result in a high Fermi velocity, a low effective mass, and reduced scattering rates for charge carriers, highlighting the potential of Cd_3As_2 for high-performance electronic devices.

3. Dirac point and topology

The concept of the Dirac point is crucial to understanding the properties of Cd_3As_2 and its interaction with light. The Dirac point is a critical feature in the band structure of certain materials where the conduction and valence bands meet at discrete points, and the linear dispersion relation around these points results in unique electronic properties. This linear dispersion means that the energy E of the electrons depends linearly on their momentum $\boldsymbol{k}$, akin to the relativistic Dirac equation for massless fermions. The significance of Dirac points is most prominently observed in materials like graphene and in 3D Dirac semimetals such as Na_3Bi and Cd_3As_2 [8].

The theoretical foundation of Dirac fermions lies in the solution to the Dirac equation in momentum space[9]:

$$\begin{aligned}(E-\boldsymbol{\sigma}\cdot\boldsymbol{p})\chi_+(\boldsymbol{p}) &= m\chi_-(\boldsymbol{p}),\\ (E+\boldsymbol{\sigma}\cdot\boldsymbol{p})\chi_-(\boldsymbol{p}) &= m\chi_+(\boldsymbol{p}),\end{aligned} \tag{1}$$

where E and $\boldsymbol{p}$ are energy and momentum, respectively, $\boldsymbol{\sigma}=\left(\sigma_x,\sigma_y,\sigma_z\right)$ are the Pauli matrices, m is the mass of the particle, and $\chi_\pm(\boldsymbol{p})$ are two-component Weyl spinors. In relativistic quantum mechanics, these equations describe both particles and antiparticles with mass. In the case of massless particles, the equations simplify, and $\chi_\pm$ become independent:

$$(E\mp\boldsymbol{\sigma}\cdot\boldsymbol{p})\chi_\pm(\boldsymbol{p})=0. \tag{2}$$

This equation describes charged massless particles with spin $\frac{1}{2}$ and dispersion relations $E(\boldsymbol{p})=\pm v\ |\boldsymbol{p}|$, where v is the speed of the particle. Another important property is *helicity*, which is defined by the operator $\frac{1}{2}(\boldsymbol{\sigma}\cdot\hat{\boldsymbol{p}})$, where $\hat{\boldsymbol{p}}=\boldsymbol{p}/|\boldsymbol{p}|$. For massless particles described by $\chi_\pm$, the eigenvalues of the helicity operator are $\pm\frac{1}{2}$.

In condensed matter physics, the Hamiltonian describing quasi-massless electrons in a 3D material with linear dispersion can be written in a simplified form as:

$$H(\boldsymbol{k})=\pm\hbar v_F\left(\sigma_x k_x+\sigma_y k_y+\sigma_z k_z\right). \tag{3}$$

The energy of electrons will consequently be $E(\boldsymbol{k})=\pm\hbar v_F\ |\boldsymbol{k}|$, where v_F is the Fermi velocity. This leads to an important consequence: massless electrons have degeneracy in helicity. The degeneracy can be lifted if an additional masslike term is added to the Hamiltonian. Thus, the Dirac cone, described by (1), will split into a pair of Weyl nodes with opposite helicity. The exact nature of the splitting depends on the masslike term

and its form [10]. Each Weyl node acts as a monopole of Berry curvature in momentum space, highlighting the topological nature of Dirac and Weyl nodes in materials.

The Berry curvature $\boldsymbol{\Omega}(\boldsymbol{k})$ is defined as:

$$\boldsymbol{\Omega}(\boldsymbol{k}) = \nabla_{\boldsymbol{k}} \times \boldsymbol{A}(\boldsymbol{k}), \tag{4}$$

where $\boldsymbol{A}(\boldsymbol{k}) = -i\langle u(\boldsymbol{k}) \mid \nabla_{\boldsymbol{k}} \mid u(\boldsymbol{k})\rangle$ is the Berry connection, and $|u(\boldsymbol{k})\rangle$ are the Bloch states. The topological nature of these materials is characterized by the Chern number, an integer that quantifies the total Berry curvature flux through a closed surface in momentum space. The Chern number C is given by:

$$C = \frac{1}{2\pi} \int_{\mathrm{BZ}} \boldsymbol{\Omega}(\boldsymbol{k}) \cdot d\boldsymbol{S}, \tag{5}$$

where the integration is over the Brillouin zone (BZ).

The Berry phase is another important concept related to the Berry curvature and plays a crucial role in the physics of Dirac points. The Berry phase is a geometric phase acquired by the wave function of a quantum particle when it undergoes adiabatic evolution around a closed loop in parameter space, such as the Brillouin zone. Mathematically, the Berry phase γ is given by:

$$\gamma = \oint_C \boldsymbol{A}(\boldsymbol{k}) \cdot d\boldsymbol{k}, \tag{6}$$

where C is the closed loop in momentum space. This phase is a manifestation of the underlying geometric structure of the parameter space and can have profound physical consequences.

In materials with Dirac points, the Berry phase is directly related to the topology of the band structure. For example, in graphene, the Berry phase around a Dirac point is π, which is added to the electron's wavefunction. This phase leads to the suppression of backscattering and contributes to the high electron mobility observed in the material. The nontrivial Berry phase also plays a crucial role in the quantum Hall effect and other topological phenomena.

4. Dirac/Weyl node and THz radiation

Due to the low energy of its photons, THz radiation is a promising tool for studying electron dynamics at Dirac/Weyl cones. Unlike mid-infrared or optical excitations, THz radiation accelerates electrons rather than driving dipole electronic transitions. This

means that the THz field primarily interacts with electrons exhibiting linear dispersion, allowing for direct investigation of their properties. This section provides a brief overview of THz-based experimental approaches to study dynamics of electrons in Dirac and Weyl materials.

Currently, THz spectroscopy of Dirac/Weyl semimetals is not widely adopted. Most experimental studies involve linear THz spectroscopy to examine conductivity features, which are then attributed to the presence of Dirac or Weyl cones. In [10], the authors discuss theoretical predictions for the real part of the conductivity in impurity-free materials (where the Dirac/Weyl point sits at the Fermi level) and in materials with impurities. According to these predictions, optical conductivity should linearly scale with frequency[11–13]. These predictions were experimentally confirmed in various works [14–18] by optical reflectivity measurements in the far-infrared region. However, when comparing these predictions with THz experiments in Cd_3As_2[19] and the Weyl semimetal Mn_3Sn[20], no distinct features could be directly attributed to the Dirac/Weyl cone. This is also true for graphene, the most well-known Dirac material[21]. The simple Drude model, or its modified version, the Drude-Smith model[22], is sufficient to fit the conductivity data without a linear term. This confirms that linear THz spectroscopy is insufficient to probe the specific properties of electrons with linear dispersion in these materials.

The magnetic properties of Weyl semimetals can be studied through Faraday rotation. This approach was employed in [23], where an enormous magneto-optical response of $Co_3Sn_2S_2$ in the THz range was observed. The authors claimed that the observed Faraday rotation of 3.8 mrad/nm originates from the Berry curvature of topological electronic structures, marking a record value in the THz and infrared range.

Consequently, more advanced techniques are used to study the dynamics of Dirac fermions and their interaction with light in Dirac/Weyl systems. For example, in [24], the ability to switch a Weyl material, WTe_2, from noncentrosymmetric to centrosymmetric by driving a shear phonon with terahertz radiation was demonstrated. The authors explained that accelerated electrons cause a lateral shift of atoms, forming a quasi-equilibrium state with changed symmetry. Theoretical calculations showed a phase transition to a topologically trivial state, and the symmetry change was confirmed by a time-resolved second harmonic generation experiment, where the harmonic disappears after the symmetry switch.

A particularly interesting method to study the scattering time of Dirac fermions is through harmonic generation. A pioneering work in this area is the measurement of high harmonic generation (HHG) in graphene [25], which clearly linked high THz

nonlinearities in the material with the presence of Dirac cones. The authors explained harmonic generation using a thermodynamic model, in which THz-induced heating of electrons modulates graphene's conductivity through the energy-dependent scattering time of electrons. In a later study, the same authors investigated the effect of gating on harmonic generation [26], showing that the efficiency of harmonic generation increases with the number of conductive electrons, with the same thermodynamic model explaining the results. However, this thermodynamic model was challenged by Cheng et al. in [27], where third harmonic generation (THG) in Cd_3As_2 was observed. Alongside THG, the authors conducted a THz pump-THz probe experiment and observed modulation of electronic conductivity at double the pump frequency. However, this modulation of conductivity was strongly anisotropic, while the thermodynamic model predicts an isotropic change. A more sophisticated theoretical approach to odd harmonic generation in Dirac materials will be discussed in the next chapter.

In conclusion, THz radiation is a valuable tool for studying, and in some cases controlling, Dirac or Weyl states in semimetals. However, linear THz spectroscopy is insufficient to reveal features specific to Dirac/Weyl materials. More complex experiments, such as harmonic generation, are required to uncover the unique properties of Dirac fermions.

5. References

[1] M. v. Stackelberg and R. Paulu, *Untersuchungen an den Phosphiden und Arseniden des Zinks und Cadmiums. Das Zn_3P_2-Gitter*, Zeitschrift Für Physikalische Chemie 427 (1935).

[2] A. J. Rosenberg and T. C. Harman, *Cd_3As_2—A Noncubic Semiconductor with Unusually High Electron Mobility*, Journal of Applied Physics **30**, 1621 (1959).

[3] I. Rosenman, *Effet Shubnikov de Haas Dans Cd_3As_2: Forme de La Surface de Fermi et Modele Non Parabolique de La Bande de Conduction*, Journal of Physics and Chemistry of Solids **30**, 1385 (1969).

[4] D. Armitage and H. J. Goldsmid, *Non-Parabolic Conduction Band in Cd_3As_2*, Physics Letters. A **28**, 149 (1968).

[5] Z. Wang, H. Weng, Q. Wu, X. Dai, and Z. Fang, *Three-Dimensional Dirac Semimetal and Quantum Transport in Cd_3As_2*, Physical Review B **88**, (2013).

[6] M. Neupane, S.-Y. Xu, R. Sankar, N. Alidoust, G. Bian, C. Liu, I. Belopolski, T.-R. Chang, H.-T. Jeng, H. Lin, et al., *Observation of a Three-Dimensional Topological*

Dirac Semimetal Phase in High-Mobility Cd_3As_2, Nature Communications **5**, 3786 (2014).

[7] S. Borisenko, Q. Gibson, D. Evtushinsky, V. Zabolotnyy, B. Büchner, and R. J. Cava, *Experimental Realization of a Three-Dimensional Dirac Semimetal, Cd_3As_2*, Physical Review Letters **113**, (2014).

[8] P. A. M. Dirac and R. H. Fowler, *The Quantum Theory of the Electron*, Proceedings of the Royal Society of London, Series a **117**, 610 (1928).

[9] K. Gottfried and T.-M. Yan, *Relativistic Quantum Mechanics*, in *Quantum Mechanics: Fundamentals* (Springer, New York, NY, 2003), pp. 577–606.

[10] N. P. Armitage, E. J. Mele, and A. Vishwanath, *Weyl and Dirac Semimetals in Three-Dimensional Solids*, Reviews of Modern Physics **90**, 15001 (2018).

[11] A. A. Burkov and L. Balents, *Weyl Semimetal in a Topological Insulator Multilayer*, Physical Review Letters **107**, 127205 (2011).

[12] P. Hosur, S. A. Parameswaran, and A. Vishwanath, *Charge Transport in Weyl Semimetals*, Physical Review Letters **108**, 46602 (2012).

[13] C. J. Tabert, J. P. Carbotte, and E. J. Nicol, *Optical and Transport Properties in Three-Dimensional Dirac and Weyl Semimetals*, Physical Review B **93**, 85426 (2016).

[14] A. Akrap, M. Hakl, S. Tchoumakov, I. Crassee, J. Kuba, M. O. Goerbig, C. C. Homes, O. Caha, J. Novák, F. Teppe, et al., *Magneto-Optical Signature of Massless Kane Electrons in Cd_3As_2*, Physical Review Letters **117**, 136401 (2016).

[15] R. Y. Chen, S. J. Zhang, J. A. Schneeloch, C. Zhang, Q. Li, G. D. Gu, and N. L. Wang, *Optical Spectroscopy Study of the Three-Dimensional Dirac Semimetal $ZrTe_5$*, Physical Review B **92**, 75107 (2015).

[16] D. Neubauer, J. P. Carbotte, A. A. Nateprov, A. Löhle, M. Dressel, and A. V. Pronin, *Interband Optical Conductivity of the [001]-Oriented Dirac Semimetal Cd_3As_2*, Physical Review B **93**, 121202 (2016).

[17] A. B. Sushkov, J. B. Hofmann, G. S. Jenkins, J. Ishikawa, S. Nakatsuji, S. Das Sarma, and H. D. Drew, *Optical Evidence for a Weyl Semimetal State in Pyrochlore $Eu_2Ir_2O_7$*, Physical Review B **92**, 241108 (2015).

[18] T. Timusk, J. P. Carbotte, C. C. Homes, D. N. Basov, and S. G. Sharapov, *Three-Dimensional Dirac Fermions in Quasicrystals as Seen via Optical Conductivity*, Physical Review B **87**, 235121 (2013).

[19] L. Hou, Y. Yang, A. Li, Q. Wang, Q. Li, M. Wu, P. Ji, Y. Zhang, Y. Xiao, W. Xu, et al., *Temperature-Dependent Terahertz Properties of Carriers and Phonons in the Topological Dirac Semimetal Cd_3As_2*, Physical Review B **108**, 115416 (2023).

[20] B. Cheng, Y. Wang, D. Barbalas, T. Higo, S. Nakatsuji, and N. P. Armitage, *Terahertz Conductivity of the Magnetic Weyl Semimetal Mn_3Sn Films*, Applied Physics Letters **115**, 12405 (2019).

[21] P. R. Whelan, B. Zhou, O. Bezencenet, A. Shivayogimath, N. Mishra, Q. Shen, B. S. Jessen, I. Pasternak, D. M. A. Mackenzie, J. Ji, et al., *Case Studies of Electrical Characterisation of Graphene by Terahertz Time-Domain Spectroscopy*, 2D Materials **8**, 22003 (2021).

[22] T. L. Cocker, D. Baillie, M. Buruma, L. V. Titova, R. D. Sydora, F. Marsiglio, and F. A. Hegmann, *Microscopic Origin of the Drude-Smith Model*, Physical Review B **96**, 205439 (2017).

[23] Y. Okamura, S. Minami, Y. Kato, Y. Fujishiro, Y. Kaneko, J. Ikeda, J. Muramoto, R. Kaneko, K. Ueda, V. Kocsis, et al., *Giant Magneto-Optical Responses in Magnetic Weyl Semimetal $Co_3Sn_2S_2$*, Nature Communications **11**, 4619 (2020).

[24] E. J. Sie, C. M. Nyby, C. D. Pemmaraju, S. J. Park, X. Shen, J. Yang, M. C. Hoffmann, B. K. Ofori-Okai, R. Li, A. H. Reid, et al., *An Ultrafast Symmetry Switch in a Weyl Semimetal*, Nature **565**, 61 (2019).

[25] H. A. Hafez, S. Kovalev, J.-C. Deinert, Z. Mics, B. Green, N. Awari, M. Chen, S. Germanskiy, U. Lehnert, J. Teichert, et al., *Extremely Efficient Terahertz High-Harmonic Generation in Graphene by Hot Dirac Fermions*, Nature **561**, 507 (2018).

[26] S. Kovalev, H. A. Hafez, K.-J. Tielrooij, J.-C. Deinert, I. Ilyakov, N. Awari, D. Alcaraz, K. Soundarapandian, D. Saleta, S. Germanskiy, et al., *Electrical Tunability of Terahertz Nonlinearity in Graphene*, Science Advances **7**, eabf9809 (2021).

[27] B. Cheng, N. Kanda, T. N. Ikeda, T. Matsuda, P. Xia, T. Schumann, S. Stemmer, J. Itatani, N. P. Armitage, and R. Matsunaga, *Efficient Terahertz Harmonic Generation with Coherent Acceleration of Electrons in the Dirac Semimetal Cd_3As_2*, Physical Review Letters **124**, 117402 (2020).

Chapter III
Non-perturbative terahertz high-harmonic generation in the three-dimensional Dirac semimetal Cd_3As_2

1. Introduction

In atomic gases[1], high-harmonic radiation is produced via a three-step process of ionization, acceleration, and recollision by strong-field infrared laser. This mechanism has been intensively investigated in the extreme ultraviolet and soft X-ray regions[2,3], forming the basis of attosecond research. In solid-state materials, which are characterized by crystalline symmetry and strong interactions, yielding of harmonics has just recently been reported[4–20].

The observed high-harmonic generation was interpreted with fundamentally different mechanisms, such as interband tunneling combined with dynamical Bloch oscillations[4,5,7–12,21,22], intraband thermodynamics[22], and nonlinear dynamics[23], and many-body electronic interactions[6,15,17–19,24]. Here, in a distinctly different context of three-dimensional Dirac semimetal, we report on experimental observation of high-harmonic generation up to the seventh order driven by strong-field terahertz pulses. The observed non-perturbative high-harmonic generation is interpreted as a generic feature of terahertz-field driven nonlinear intraband kinetics of Dirac fermions. We anticipate that our results will trigger great interest in detection, manipulation, and coherent control of the nonlinear response in the vast family of three-dimensional Dirac and Weyl materials.

High-harmonic generation (HHG) in two-dimensional Dirac semimetals (single-layer graphene[14,16,17] and 45-layer graphene[7]) has been reported very recently for pump pulses both in the terahertz (10^{12} Hz, 1 THz$\sim$4 meV)[7,16] and mid- or near-infrared (0.2 – 0.8 eV) ranges[14,17]. Although previous theoretical investigations pointed out that the peculiar linear energy-momentum dispersion relation (Dirac cone) should be essential for HHG in graphene (see e.g. [25–27]), the strong dependence on pump laser frequencies observed in the experiments favors different mechanisms. For the mid- or near-infrared HHG, the interband transitions (combined with Bloch oscillations) play the crucial role, while the linear dispersion relation is not a prerequisite[14]. A similar mechanism involving interband transitions can also be applied to THz HHG

in lightly-doped multi-layer graphene, whereas the exact shape of the carrier distribution was found to only play a minor role[7]. In contrast, for heavily electron-doped graphene, intraband processes become important, and HHG was ascribed to THz-field heated hot-electrons while assuming the electron subsystem thermalized quasi-instantaneously[16].

One may expect to observe THz HHG universally in the Dirac materials also of higher dimension, e.g. three-dimensional (3D) Dirac or Weyl semimetals. However, THz HHG so far has not been reported for this class of materials, and the mechanism for observing THz HHG in a 3D Dirac material remains elusive. Here we report on time-resolved detection of non-perturbative THz HHG in the 3D Dirac semimetal Cd_3As_2, and a real-time theoretical analysis of the THz-field driven kinetics of the Dirac fermions that is directly linked to the linear dispersion relation. Our results show that the THz-field driven nonlinear kinetics of the Dirac electrons is the mechanism responsible for the efficient generation of high-harmonic radiation, as well as for its non-perturbative fluence dependence in Cd_3As_2.

2. Results

3. Third harmonic generation

As being both theoretically predicted and experimentally confirmed[28–33], Cd_3As_2 is a well-established room-temperature 3D Dirac semimetal with Fermi velocity about 10^5-10^6 m/s. Very compelling topological properties such as topological surface states and 3D quantum Hall effects have been realized in this system[34–38]. In high-quality Cd_3As_2 thin films prepared by molecular beam epitaxy[39], we observe HHG unprecedentedly up to the seventh order in the non-perturbative regime. THz harmonic radiations were recorded with femtosecond resolution at room temperature. Figure 1(a) displays the detected electric field as a function of time delay for the third harmonic radiation, induced by a multi-cycle pump pulse (Figure 2(a)) with a peak field of 144 kV/cm characterized by its central frequency of $f = 0.67$ THz (Figure 1(b)). The power spectrum of the harmonic radiation is obtained by Fourier transformation of the time-domain signals, which exhibits a sharp peak at $3f = 2.01$ THz (Figure 1(b)). The intensity of the harmonic radiation is nearly independent on the polarization of the pump pulse within the sample surface (see Supplementary information Figure 2). To further characterize the third harmonic generation, we measured the time-resolved signals for different pump-pulse intensities. As summarized in Figure 1(c), the fluence dependence of the third harmonic radiations remarkably does not follow the cubic law, but exhibits a power-law dependence as $I_{3f} \propto I_f^{2.5}$ on the pump-pulse intensity I_f, which reveals a non-perturbative nonlinear response.

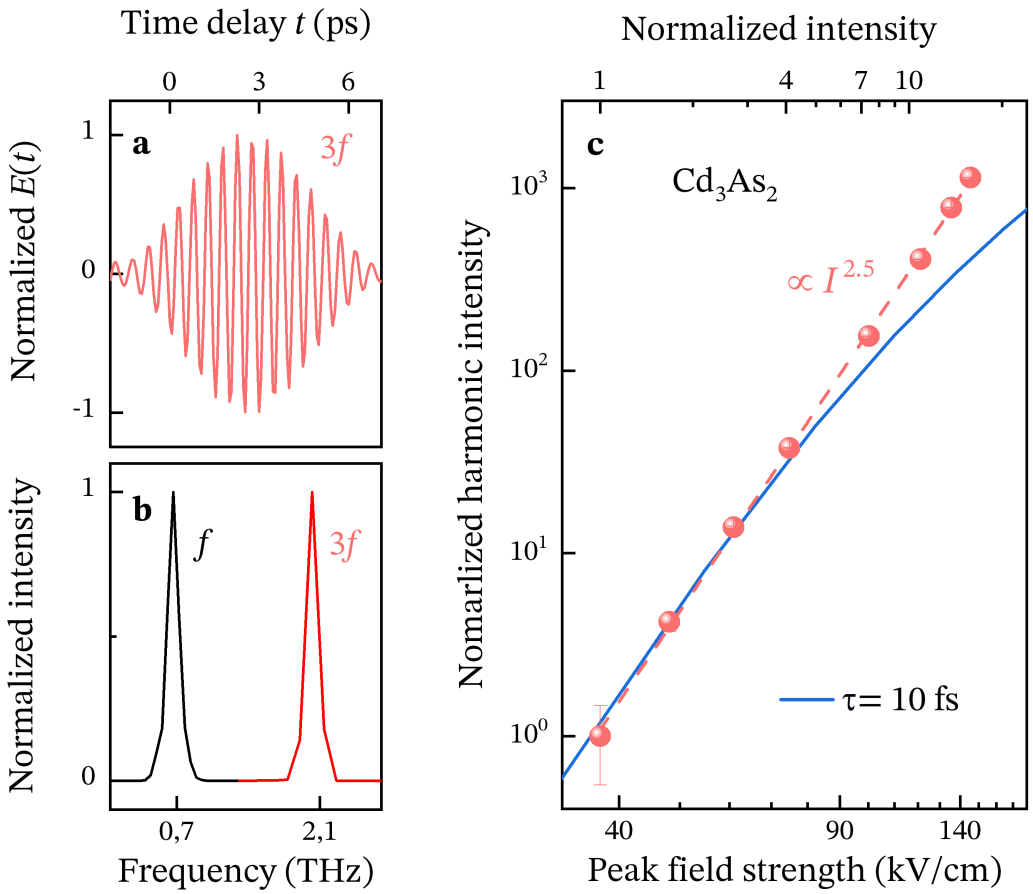

Figure 1: **Third harmonic generation in Cd_3As_2.** **a**, Time-resolved third-harmonic radiation characterized by its time-dependent electric field $E(t)$ recorded at room temperature. **b**, Normalized power spectra of the harmonic radiation $3f = 2.01$ THz, and the excitation pulse $f = 0.67$ THz. **c**, Dependence of the third-harmonic radiation intensity on the pump intensity (symbols) follows $I_{3f} \propto I_f^{2.5}$ (dashed line). Fit of the theoretical results is shown for the relaxation time $\tau = 10$ fs (solid line). The error bars indicate the noise level at the corresponding data point.

4. THz driven nonlinear kinetics

To understand the non-perturbative harmonic generation, we performed real-time theoretical analysis of the THz driven kinetics of the 3D Dirac electrons. For the electron-doped system, interband electronic excitations are Pauli-blocked for one-photon transitions in the THz frequency range, thus we focus on the intraband kinetics of the nonequilibrium state by adopting a statistical approach of the Boltzmann transport theory. The initial state of thermodynamic equilibrium is defined by the room-temperature Fermi-Dirac distribution

$$f_0[\epsilon(\mathbf{p})] = \left[1 + e^{\frac{\epsilon(\mathbf{p})-\epsilon_F}{k_B T}}\right]^{-1} \tag{1}$$

for the 3D Dirac electrons obeying the linear dispersion relation $\epsilon(\mathbf{p}) = v_F|\mathbf{p}|$, with $\mathbf{p}$ and v_F denoting momentum and Fermi velocity, respectively, ϵ_F for Fermi energy, k_B the Boltzmann constant, and T for temperature. In the presence of the THz pulse, the driven transient state is characterized by a distribution function $f(t, \mathbf{p})$, the time-dependent evolution of which is governed by the Boltzmann equation[40,41]:

$$\left(\frac{\partial}{\partial t} + \frac{1}{\tau}\right) f(t, \mathbf{p}) - e\mathbf{E}(t) \cdot \nabla_{\mathbf{p}} f(t, \mathbf{p}) = \frac{f_0(\mathbf{p})}{\tau} \tag{2}$$

where the linear dispersion relation has been implemented, e and $\mathbf{E}(t)$ denote the electron charge and the THz electric field, respectively, and τ is the characteristic relaxation time for intraband processes, which is a phenomenological parameter (see Methods). In particular, we do not presume that the electron subsystem thermalizes quasi-instantaneously or a Fermi-Dirac distribution should be obeyed by the transient states. In contrast, by solving the Boltzmann equation, we obtain the real-time distribution of the transient state. By comparing it with equilibrium-state Fermi-Dirac distribution, we can claim whether the corresponding transient state is nearly thermalized or far from thermodynamic equilibrium. Furthermore, we can derive the time-dependent current density, hence the THz field-induced harmonic radiations, the fluence dependence of which can be compared to the experimental observations.

By solving the Boltzmann equation, we obtain the real-time distribution of the transient state. By comparing it with the equilibrium-state Fermi-Dirac distribution, we can claim whether the corresponding transient state is nearly thermalized or far from thermodynamic equilibrium. Furthermore, we can derive the time-dependent current density, hence the THz field-induced harmonic radiations, the fluence dependence of which can be compared to the experimental observations.

For the experimentally implemented THz pump pulses (see Figure 2(a) for the waveform) with a typical electric-field peak strength of 110 kV/cm, the obtained current density (Figure 2(b)) and transient-state distribution functions are illustrated in Figures Figure 2(c-f), corresponding to the representative time delays (red symbols) marked in Figure 2(a) and Figure 2(b), for the experimental values of Fermi energy $\epsilon_F = 118$ meV and Fermi velocity $v_F = 7.8 \times 10^5$ m/s as estimated from Shubnikov-de Haas oscillations [39], and the relaxation time $\tau = 10$ fs. The electric field of the linearly-polarized pump pulse is set along the p_z direction.

The microscopic origin of HHG resides in the nonlinear kinetics of the electron distribution (see Figure 2(d-f) and Supplementary Figure 5) combined with the linear

energy-momentum dispersion relation. Before the pump pulse arrives, the electrons in the upper band are in thermodynamic equilibrium, and fills the Dirac-cone up to around the Fermi energy according to the Fermi-Dirac distribution (Figure 2(c)). When the pump pulse is present, the electrons are not only accelerated by the THz electric fields, but at the same time also scattered. Although the latter process is dissipative, the former one can very efficiently accumulate energy into the electron subsystem, leading to a stretched and shifted distribution along the field. In particular, at the peak field (symbol point 2 marked in Figure 2(a)), the distribution is most strongly stretched and shifted in the field direction (Figure 2(d)) resulting in the maximum current density and a peculiar flat-peak-like feature (Figure 2(b)), thereby leading to very efficient HHG. In clear contrast to the Fermi-Dirac distribution of a thermodynamic equilibrium state that is spherically symmetric for the 3D Dirac electrons (manifested as circularly symmetric in the 2D plots), the obtained strongly stretched and highly asymmetric distribution due to the presence of the strong THz field evidently shows that the electron subsystem is far from thermodynamic equilibrium. As shown in Figure 2(f), the electron distribution becomes nearly symmetric in low THz fields, indicating that a quasi-thermalized situation is reconciled in the low-field limit.

For various pump-pulse peak field strength, the intensity of the third-harmonic radiation is shown in Figure 1(c) for relaxation time $\tau = 10$ fs. The peak field strength in the sample is estimated as the average value over the film thickness. The theoretical results reproduce excellently the observed non-perturbative fluence dependence of the third-harmonic generation up to about 80 kV/cm of the peak field strength, though a deviation from the experimental data occurs at higher fluences. This deviation could be due to enhanced probability of interband multiphoton tunneling in the high electric-field limit, which is not included in our semi-classical analysis. Nevertheless, we found that the non-perturbative dependence on pump-pulse fluence is a generic feature of the THz driven nonequilibrium states in the Dirac semimetals. Furthermore, we found that efficiency and fluence-dependence of the THz HHG is very sensitive to the scattering rate $1/\tau$. By decreasing the scattering rate (or suppressing the dissipative processes), the transient distribution function is further stretched for the same electric-field strength, resulting in greater current density (see $\tau = 30$ fs in Figure 2(b)) and enhanced THz HHG (see Supplementary Figure 4, Supplementary Figure 5, and Supplementary Movie 1 Supplementary Movie 2[42] for the real-time evolution of the distribution driven by the THz pulse in Figure 2(a)). Our theoretical calculations further reveal that for a fixed scattering rate the harmonic generation is enhanced at a higher Fermi energy (see Supplementary Figure 6), which is compelling for further experimental studies.

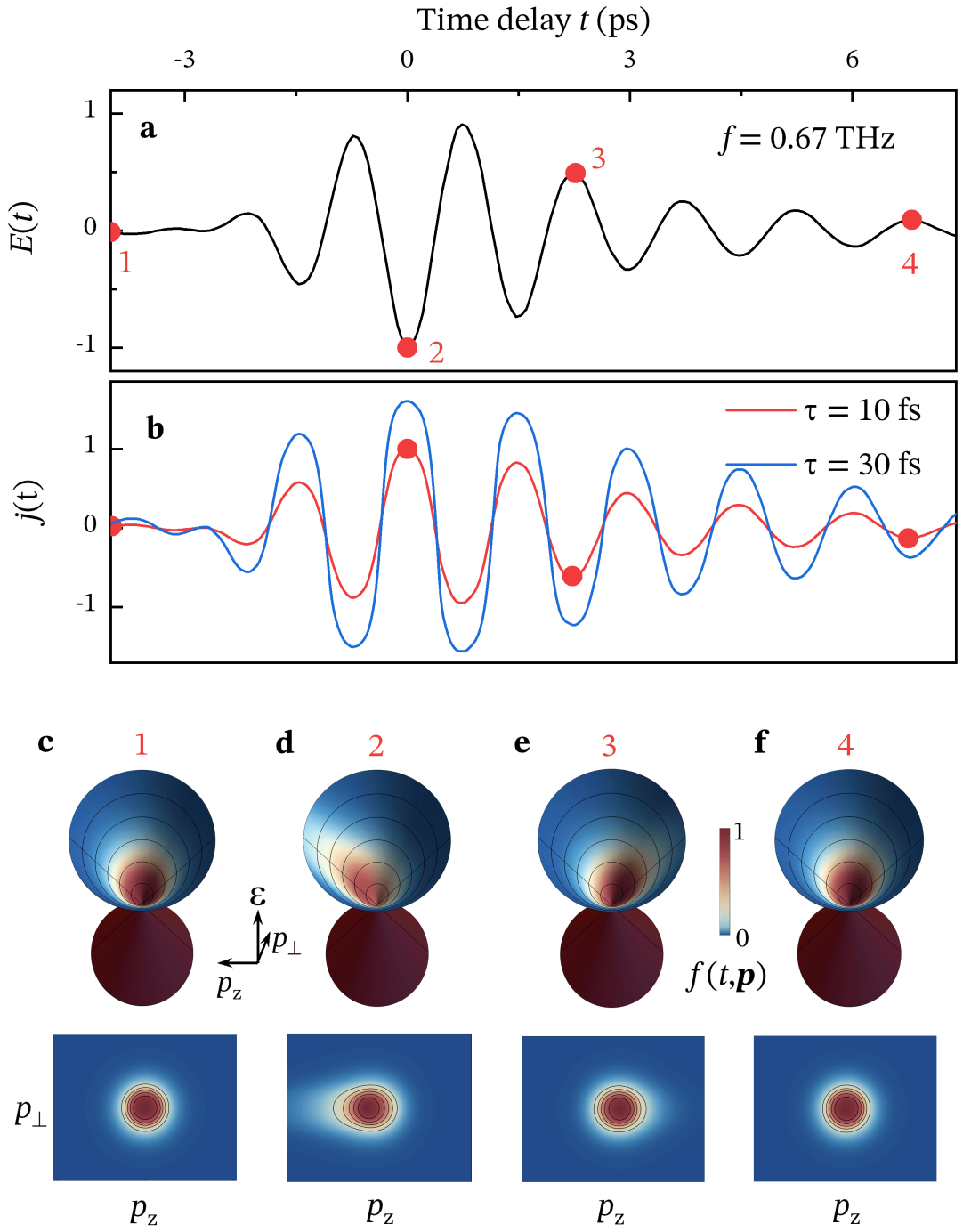

Figure 2: **THz-driven nonlinear kinetics and time-resolved distribution function**. **a**, Multicycle pump pulse of $f = 0.67$ THz characterized in air by its time-dependent electric field $E(t)$. **b**, The derived current density $j(t)$ by solving the Boltzmann equation for $\tau = 10$ and 30 fs, respectively, for the pump pulse with peak field strength of 110 kV/cm. **c-f**, 3D and 2D illustration of the distribution function $f(t, p)$ in the upper band of the Dirac cone, corresponding to $\tau = 10$ fs for various time-delays as marked by the points 1 - 4 in (a,b), respectively. ϵ denotes energy. p_z denotes momentum component along the linearly-polarized pump-pulse electric field. $p_\perp$ denotes momentum in the perpendicular direction. See Supplementary Figure 5 and supplemented movies[42] for more comparisons between $\tau = 10$ and 30 fs.

5. Higher-order harmonic generation

In order to detect higher-order harmonic radiations, we utilized lower-frequency and strong-field THz pump pulses (see Methods)[43]. Figure 3(a) shows the observed harmonic radiations up to the seventh order for the pump-pulse frequency of 0.3 THz (see Figure 3(b) for the waveform). Only the odd-order harmonics are observed, providing the spectroscopic evidence for the existence of inversion symmetry in the crystalline structure of Cd_3As_2 (see [33]). Our experimental results not only set the record for THz HHG in the 3D Dirac materials but also present the striking observation of the non-perturbative fluence dependence for all the observed harmonic radiations, as presented in Figure 3(c-e).

For the third harmonic radiations, the fluence dependence is also slightly below the cubic power-law dependence, similar to the behavior for the 0.7 THz pump pulse. Moreover, for the higher-order harmonics, the deviation from the corresponding perturbative power-law dependence is further increased. These features are perfectly captured by our quantitative theoretical analysis. By implementing the experimental pump pulse (see Figure 3(b)) in our calculations, the time-resolved harmonic signals are derived as a function of pump-pulse fluence. The best fitting for all the experimentally observed HHG is achieved at $\tau = 10$ fs (see Figure 3(c-e)). The obtained value of $\tau = 10$ fs is comparable to that in graphene as directly obtained via time- and angle-resolved photoemission spectroscopic measurements[44]. While such measurements have not been reported in Cd_3As_2, an estimate based on the Shubnikov-de Haas measurements provides a τ value of the same order[39]. These results strongly indicate that the THz field-driven nonlinear kinetics of the Dirac electrons is the mechanism responsible for the observed non-perturbative nonlinear response in Cd_3As_2. Although for the seventh harmonic the experimental uncertainty is enhanced at the lowest fluence, the fluence dependence far away from the perturbative one is a clear and consistent experimental and theoretical observation. The non-perturbative response could be qualitatively understood in a way that the effective nonlinear susceptibilities are also a function of the THz field due to the higher-order nonlinear response. We note that the observed non-perturbative response suggests that the experimental setting is close to but still below the so-called high-harmonic plateau regime, in which the HHG intensity remains almost constant for the high orders and drops abruptly at a cutoff frequency as found in gases as well as in solids[1,20].

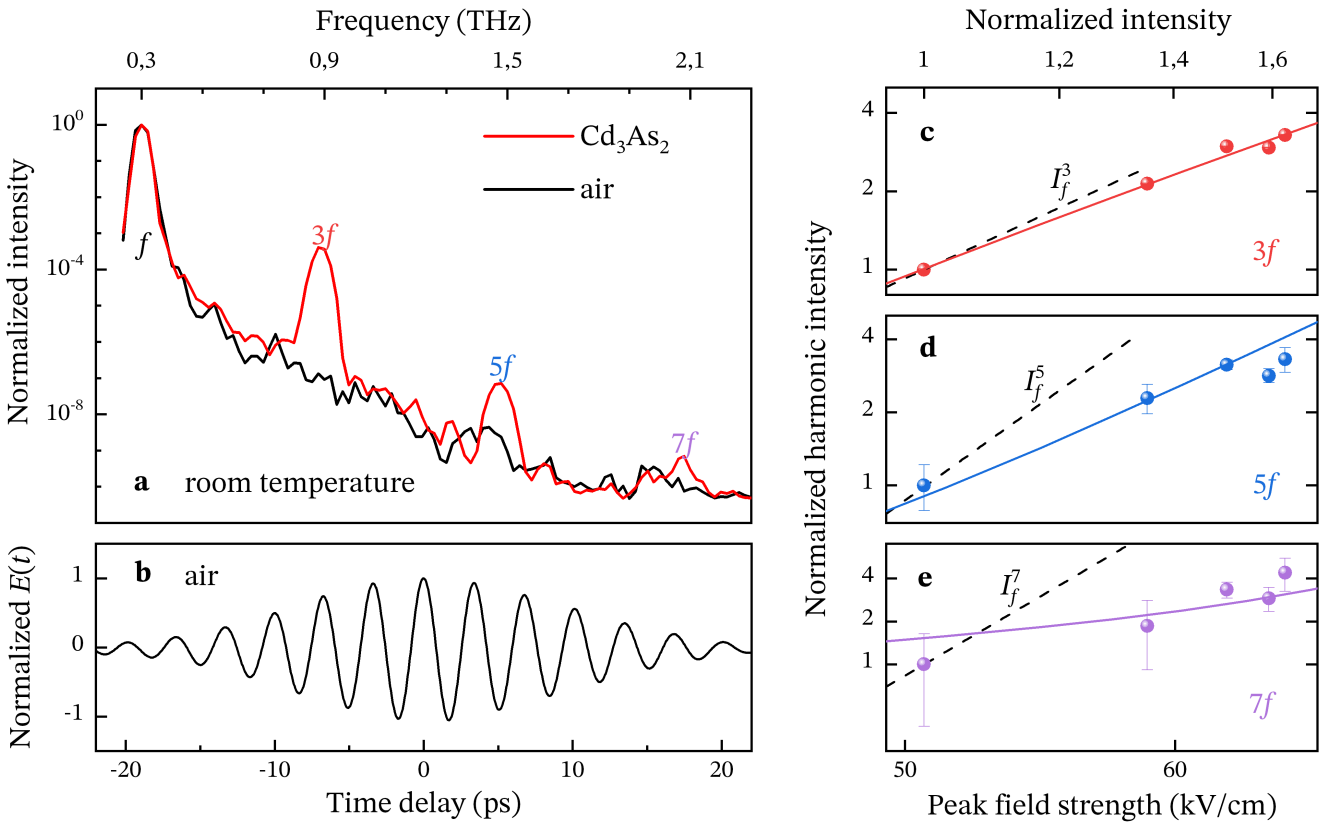

Figure 3: **High-harmonic generations in Cd_3As_2. a**, Room-temperature spectrum of high-harmonic generations in Cd_3As_2 for **b**, multicycle pump pulse of $f = 0.3$ THz, compared with air as a reference. Pump-intensity dependence of the **c**, third-, **d**, fifth-, and **e**, seventh-harmonic generation (symbols) follows the power laws of $I_f^{2.6\pm0.1}$, $I_f^{2.8\pm0.1}$, and $I_f^{2.8\pm0.7}$, respectively. The dashed lines indicate the corresponding perturbative power laws, i.e. $\propto I_f^3, I_f^5$, and I_f^7. In **c,d,e**, the solid lines show the fitted theoretical results corresponding to the relaxation time $\tau = 10$ fs. The error bars indicate the noise level at the corresponding data point.

6. Discussion

The established mechanism of THz HHG here, based on the driven nonlinear kinetics of Dirac electrons, is different from those mechanisms proposed for HHG in graphene[7,14,16,17], in which either the interband transitions were found playing the dominant role or the intraband electron subsystem is assumed to thermalize quasi-instantaneously. In contrast, in the context of the 3D Dirac system, we found that, firstly, in the presence of strong THz fields, the entire intraband distribution is strongly stretched and highly asymmetric, denying a description using the Fermi-Dirac distribution of thermodynamic equilibrium states that is symmetric along the Dirac cone. Secondly, for the intraband kinetics, the linear energy-momentum dispersion is crucial for the THz HHG, whereas for a parabolic dispersion in the single-particle picture, the induced radiation field $E_{out} \propto \frac{dj}{dt} \propto \frac{dv}{dt} \propto E_{in}$ should follow the pump field E_{in}, hardly

yielding harmonics. Thirdly, the exact shape of the electron distribution and its real-time evolution, as obtained from the Boltzmann transport theory, is directly responsible for the THz HHG. A higher efficiency is revealed for the cases of a more strongly stretched and highly asymmetric distribution, due to stronger THz electric field and/or reduced scattering rate.

In conclusion, we have observed THz-driven high-harmonic generation up to the seventh order unprecedentedly in the 3D Dirac semimetal Cd_3As_2. The fluence dependence of all the observed HHG was found well beyond the perturbative regime. By performing real-time quantitative analysis of the THz field-driven intraband kinetics of the Dirac electrons using the Boltzmann transport theory, we have established the nonlinear intraband kinetics as the mechanism for the observed THz HHG in Cd_3As_2. The mechanism found here for THz HHG is expected to be universal in the vast family of 3D Dirac and Weyl materials[45], which provides strategies for pursuing high efficiency of THz HHG, and establishes HHG as a sensitive tool for exploring the interplay of various degrees of freedom. Towards the high electric-field regime, an experimental realization of THz HHG plateau in the Dirac materials and a full quantum-mechanical dynamic analysis are still outstanding from both the fundamental and the application points of view. Recently, non-perturbative THz third-harmonic generation in Cd_3As_2 was also reported in [46]

7. Methods

7.1. Terahertz spectroscopy

We performed terahertz (THz) high-harmonic generation (HHG) experiments with THz sources based on a femtosecond laser system and on a linear electron accelerator. For the former, broadband THz radiation was generated through a tilted pulse front scheme utilizing a lithium niobate crystal[47–49]. With an initial laser pulse energy around 1.5 mJ at 800 nm central wavelength and 100 fs pulse duration, broadband THz radiation with up to 3 μJ pulse energy was generated. At the linear accelerator in Helmholtz Zentrum Dresden-Rossendorf, multi-cycle superradiant THz pulses were generated in an undulator from ultra-short relativistic electron bunches[43]. The generated THz radiation is carrier envelope phase stable, linearly polarized with tunable emitted radiation frequency. The accelerator was operated at 100 kHz and synchronized with an external femtosecond laser system. The latter served as a probe in electro-optical sampling. To achieve a high level of synchronization, a pulse-resolved detection scheme was employed[50]. To produce narrow-band THz radiation, the corresponding bandpass filters were adopted (see Supplementary information Figure 1 for more information).

7.2. Sample preparation and characterization

High-quality thin films of Cd_3As_2 were grown by a PerkinElmer (Waltham, MA) 425B molecular beam epitaxy system[39]. The substrate of freshly cleaved 2-inch mica ($\sim$ 70 μm in thickness) was annealed at 300°C for 30 min to remove absorbed molecules. Then, a 10 nm-thick CdTe was deposited as a buffer layer before the Cd_3As_2 growth. Cd_3As_2 bulk material (99.9999% , American Elements Inc., Los Angeles, CA) was evaporated onto CdTe at 170°C. The growth was *in situ* monitored by reflection high-energy electron diffraction (RHEED) system. The sample surface is parallel to the crystallographic (112) plane. Part of the sample was patterned in Hall bar geometry and underwent magnetic resistance measurement on a physical properties measurement system (PPMS) (Quantum Design Inc.). Fermi energy and Fermi velocity of the 120 nm-thick Cd_3As_2 samples were estimated as $E_F = 118$ meV and $v_F = 7.8 \times 10^5$ m/s from the Shubnikov-de Haas oscillations. THz transmission was characterized in the linear response regime by a standard electro-optical sampling scheme.

7.3. Kinetic theory

Our theoretical analysis employed a statistical approach using the semiclassical Boltzmann transport theory with an effective relaxation time[40,41,51–54]. The semiclassical description of particles is captured by a single-particle distribution function $f(t, \mathbf{r}, \mathbf{p})$ in phase space. Observables can be calculated as integrals over momentum space. To calculate $f(t, \mathbf{r}, \mathbf{p})$, one needs to solve the Boltzmann equation:

$$df \equiv \partial_t f + \nabla_{\mathbf{r}} f \cdot \dot{\mathbf{r}} + \nabla_{\mathbf{p}} f \cdot \dot{\mathbf{p}} = \mathcal{C}[f] \tag{3}$$

The left-hand side of this equation corresponds to the collisionless evolution in phase space. The collision integral $\mathcal{C}$ can either be calculated perturbatively from scattering amplitudes or chosen phenomenologically. In this work, we use the phenomenological relaxation time approximation and choose the Bhatnagar-Gross-Krook (BGK) collision operator[40]. The explicit form of the Boltzmann equation follows from the (inverted) equations of motion for the electron's wavepacket[51–53]

$$\begin{aligned} \dot{\mathbf{r}} &= \frac{1}{\hbar D}\Big[\nabla_{\mathbf{k}}\epsilon_{\mathbf{k}} + e\mathbf{E}\times\boldsymbol{\Omega} + \frac{\mathbf{e}}{\hbar}(\nabla_{\mathbf{k}}\epsilon_k\cdot\boldsymbol{\Omega})\mathbf{B}\Big], \\ \hbar\dot{\mathbf{k}} &= \frac{1}{D}\left[-e\mathbf{E} - \frac{\mathbf{e}}{\hbar}\nabla_{\mathbf{k}}\epsilon_{\mathbf{k}}\times\mathbf{B} - \frac{\mathbf{e^2}}{\hbar}(\mathbf{E}\cdot\mathbf{B})\boldsymbol{\Omega}\right] \end{aligned} \tag{4}$$

with the electromagnetic fields $\mathbf{E}$ and $\mathbf{B}$, the Berry curvature $\boldsymbol{\Omega}$, the Planck constant $\hbar$, and the elementary charge $\mathbf{e}$. $\epsilon_{\mathbf{k}}$ denotes the dispersion relation and $D = 1 + \frac{\mathbf{e}}{\hbar}\,\mathbf{B}\cdot\boldsymbol{\Omega}$ is the modified phase space volume element. For the linearly polarized THz pulses,

we consider the dominant effects of the electric field while neglecting the magnetic field in our further analysis. Consequently, the (inverted) equations of motion take the following simple form

$$\dot{\mathbf{r}} = \nabla_{\mathbf{p}}\epsilon_{\mathbf{p}} + \frac{e}{\hbar}\mathbf{E}\times\mathbf{\Omega},\ \ \dot{\mathbf{p}} = \hbar\dot{\mathbf{k}} = -e\mathbf{E}. \tag{5}$$

Since we are interested in a homogenous solution, only the equation for $\dot{\mathbf{p}}$ is incorporated in the Boltzmann equation. The equation for $\dot{\mathbf{r}}$ is used to define the current density as follows

$$\mathbf{j}(t) = -e\int \frac{d^3p}{(2\pi\hbar)^3}\dot{\mathbf{r}}\ f(t,\mathbf{p}). \tag{6}$$

Nevertheless, it can be shown that the second term in this equation (proportional to $\mathbf{E}\times\mathbf{\Omega}$) does not contribute to $\mathbf{j}(t)$ in the case of linearly polarized THz pulse, corresponding to the present experimental setting. Therefore, for the particular experiment being reported now, we can write

$$\dot{\mathbf{r}} = \nabla_{\mathbf{p}}\epsilon_{\mathbf{p}},\ \ \dot{\mathbf{p}} = -e\mathbf{E}. \tag{7}$$

For the THz frequencies in our experiments, interband electronic transitions are Pauli-blocked for the electron-doped Cd_3As_2 samples. Thus, to study the intraband electron dynamics, it is justified to adopt one relaxation scale. In addition to that the underlying impurities in the system can lead to non-conservation of charge and momentum. As a result, we expect that the collision integral of the following form

$$\mathcal{C}[f] = \frac{f_0 - f}{\tau} \tag{8}$$

will correctly reproduce the experimental data. In equilibrium, the distribution function depends on collisional invariants

$$f_0(\beta,\mathbf{p},\epsilon_F) = \left[1 + e^{\beta(v_F|\mathbf{p}|-\epsilon_F)}\right]^{-1}, \tag{9}$$

where $\beta \equiv 1/k_BT$ with the Boltzmann constant k_B, ϵ_F denotes the Fermi energy, and the linear dispersion relation $\epsilon_{\mathbf{p}} = v_F|\mathbf{p}|$ of the Dirac material has been implemented. Finally, considering only homogeneous response, we arrived at the following Boltzmann equation

$$\left(\partial_t + \frac{1}{\tau}\right) f - e\mathbf{E} \cdot \nabla_{\mathbf{p}} f = \frac{f_0}{\tau}, \tag{10}$$

where the external driving force $\mathbf{F} = -e\mathbf{E}$ is implemented for electrons moving in the THz electric field $\mathbf{E}$. In order to solve this equation, we Fourier transform the distribution function $f(t, \mathbf{p}) = \frac{1}{2\pi} \int dz \tilde{f}(t, p_x, p_y, z) \exp(izp_z)$, which gives an ordinary differential equation

$$\left(\partial_t + \frac{1}{\tau}\right) \tilde{f} - izeE\tilde{f} = \frac{\tilde{f}_0}{\tau}, \tag{11}$$

where the electric field $\mathbf{E}$ has been set along the z direction.

The ordinary differential equation is solved numerically with the experimental THz fields as an input. Having the distribution function, we calculate its moments to get current density. The expression for current density has the following form

$$\mathbf{j}(t) = -e \int \frac{d^3p}{(2\pi\hbar)^3} v_F \hat{\mathbf{p}} f(t, \mathbf{p}), \tag{12}$$

where $\hat{\mathbf{p}}$ denotes the unit vector along the momentum direction. The relation between the induced current and the external oscillating field serves as the basis for analysis of higher-harmonic generation.

8. Supplementary information

8.1. Experimental setup

We performed terahertz (THz) high-harmonic generation (HHG) experiments with THz sources based on a femtosecond laser system and on a linear electron accelerator. For the former, broadband THz radiation was generated through tilted pulse front scheme utilizing lithium niobate crystal. With initial laser pulse energy around 1.5 mJ at 800 nm central wavelength and 100 fs pulse duration broadband THz radiation with up to 3 μJ pulse energy was generated. The spectral distribution of the THz pulses had maximum around 700 GHz. To produce narrow band radiation two bandpass filters (BP1) with central frequency of 670 GHz and 20% bandwidth were applied in the THz beam path (see Supplementary Figure 1). With parabolic mirrors (OAP) THz radiation was focused onto the sample with spot size of around 500 μm in diameter (FWHM) and 200 nJ pulse energy. To perform electro-optical sampling, 5% of initial laser pulse was split for probe. Wire grid polarizer (WG3) was inserted into the THz beam after the Cd_3As_2 (Cd_3As_2) sample for polarization-dependent detection of HHG. At the linear accelerator

in Helmholtz Zentrum Dresden-Rossendorf, multi-cycle superradiant THz pulses were generated in an undulator from ultra-short relativistic electron bunches. The generated THz radiation is carrier envelope phase stable, linear polarized with tunable emitted radiation frequency. Two bandpass filters (BP1) with 300 GHz central frequency and 20% bandwidth were used to substantially suppress radiations other than of 300 GHz. The accelerator was operated at 100 kHz and was synchronized with an external femtosecond laser system. The latter served as probe in electro-optical sampling. To achieve high level of synchronization, pulse-resolved detection scheme was employed. The laser repetition rate was 200 kHz to enable active background subtraction. THz radiation was focused on the Cd_3As_2 sample with the typical spot size of 0.6 mm (FWHM) with 300 nJ pulse energy. For both experiments, THz radiations after the sample was bandpass filtered (BP2) and refocused on to ZnTe crystal for standard electro-optical sampling (see Supplementary Figure 1). As thickness of the thin-film samples is smaller than the THz wavelength by more than three orders of magnitude, the electric-field strength within the sample was treated as uniform with the value being the average over the sample thickness.

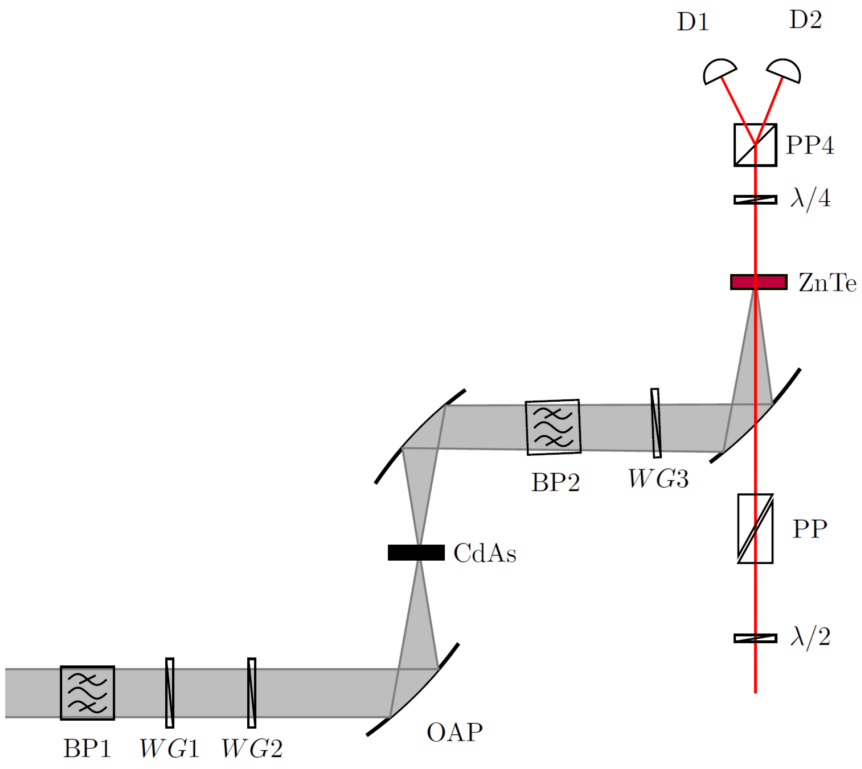

Supplementary Figure 1: Sketch of basic experimental setup for high-harmonic generation measurements. BP – band-pass filter; WG – wire-grid polarizer; OAP – off-axis parabolic mirror; λ/2 – half-wave plate; λ/4 – quarter-wave plate; PP – Glan-Tailor prism; PP4 – Wollaston prism; D1 and D2 – photodiode detectors.

8.2. Polarization dependence of harmonic radiation

Third-harmonic radiation of the parallel polarization (with central frequency of $3f = 2.02$ THz) were recorded as a function of the pump-pulse polarization corresponding to $f = 0.67$ THz, as shown in Supplementary Figure 2. The intensity of the harmonic radiation is nearly independent on the polarization of the pump pulse within the sample surface.

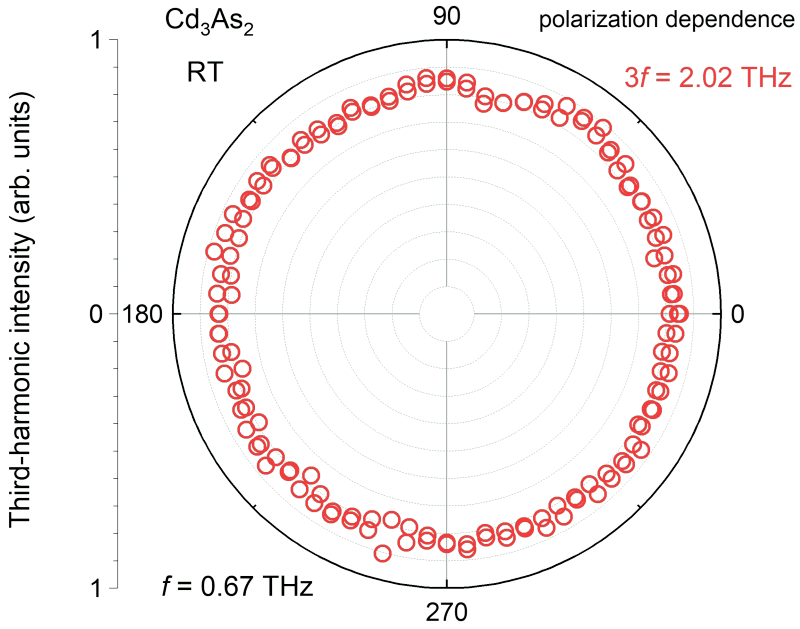

Supplementary Figure 2: Intensity of third harmonic radiation ($3f = 2.02$ THz) as a function of pump-pulse polarization at room temperature (RT). The noise level is smaller than the symbol size.

8.3. Dependence of harmonic on fluence, scattering rate, and Fermi energy

Different relaxation times are studied theoretically for the pump pulse of f = 0.67 THz as a function of the pump-pulse fluence. The obtained third harmonic intensity is compared for $\tau = 10$ and 30 fs in Supplementary Figure 3 with the experimental parameters $v_F = 7.8 \times 10^5$ m/s and E_F=118 meV. The HHG efficiency is very sensitive to the scattering rate. When the scattering rate is reduced by a factor of three, the HHG efficiency can be enhanced up to two orders of magnitude. For the electric-field peak strength of 110 kV/cm, the corresponding current density, time derivative of the current density, as well as HHG spectrum are shown in Figure 2(b), Supplementary Figure 4(a), and Supplementary Figure 4(b), respectively. For $\tau = 10$ fs, not only the third-harmonic, but also the fifth-harmonic radiations should be resolvable. For $\tau = 30$ fs, the efficiency is highly enhanced that harmonic radiations are expected to be detectable at higher orders. The dependence on scattering rate and electric field is further illustrated by comparing

the transient distribution functions. For the electric fields marked in Figure 2, the distribution functions are illustrated in Supplementary Figure 5. At the same field strength, the distribution function for $\tau = 30$ fs is much more stretched compared with that for $\tau = 10$ fs, which leads to the much higher HHG efficiency, as shown in Supplementary Figure 3 and Supplementary Figure 4. Based on the kinetic theory, we perform theoretical analysis of the effects of varying Fermi energy, although we cannot freely modify the Fermi energy in the present experiment. As shown in Supplementary Figure 6, the third harmonic generation increases monotonically with increasing Fermi energy. The waveform of the 0.67 THz pump pulse (see Figure 2) with a peak field of 56 kV/cm has been used for these simulations.

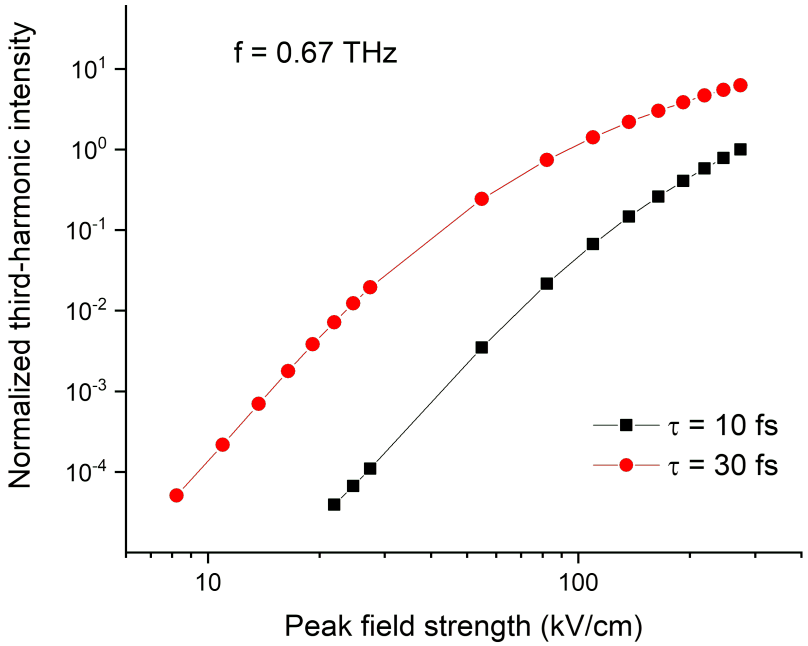

Supplementary Figure 3: Normalized intensity of third harmonic radiation ($3f = 2.01$ THz) as a function of pump-pulse peak field strength for the pump pulse of $f = 0.67$ THz, obtained by solving the Boltzmann equation

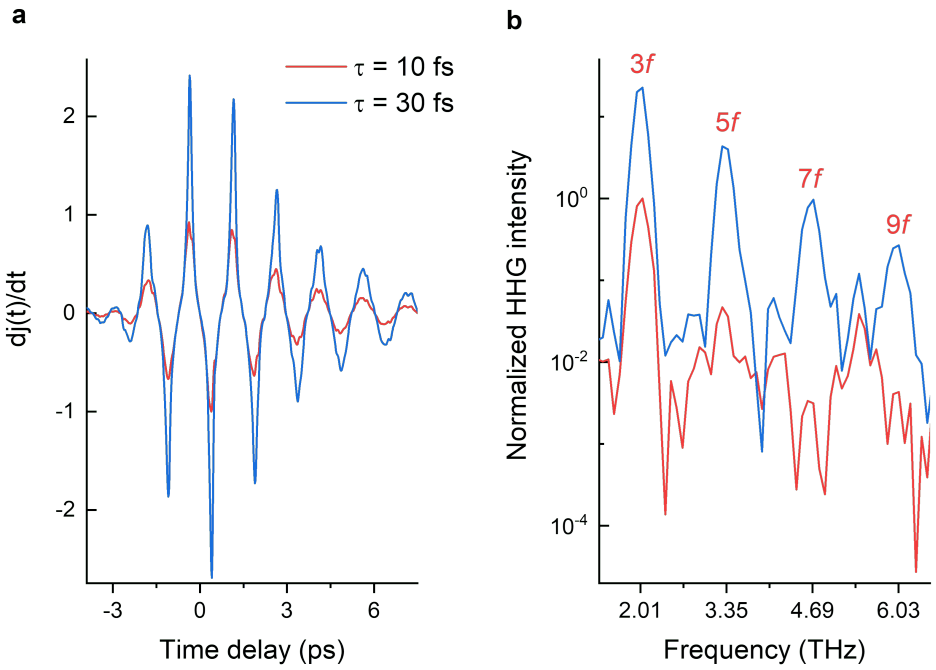

Supplementary Figure 4: **a**, Normalized time-derivative of current density $\partial j(t)/\partial t$, and **b**, HHG intensity induced by the pump pulse of $f = 0.67$ THz for $\tau = 10$ and 30 fs, obtained by solving the Boltzmann equation. See Figure 2 for the corresponding current density.

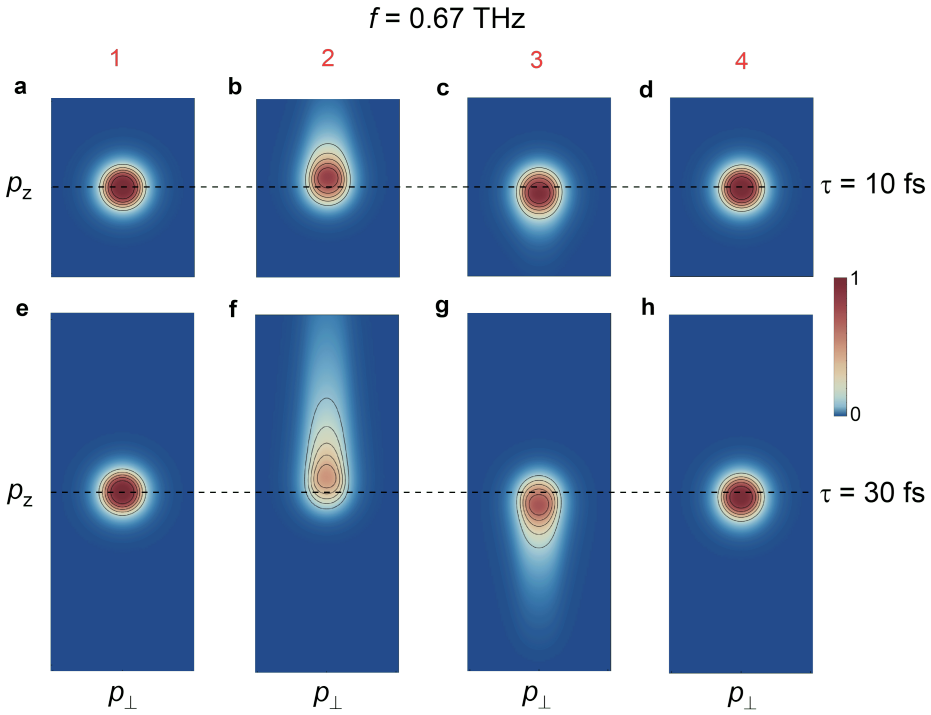

Supplementary Figure 5: 2D plots of the transient distribution functions corresponding to different electric fields (marked in Figure 2) for $\tau = 10$and 30 fs.

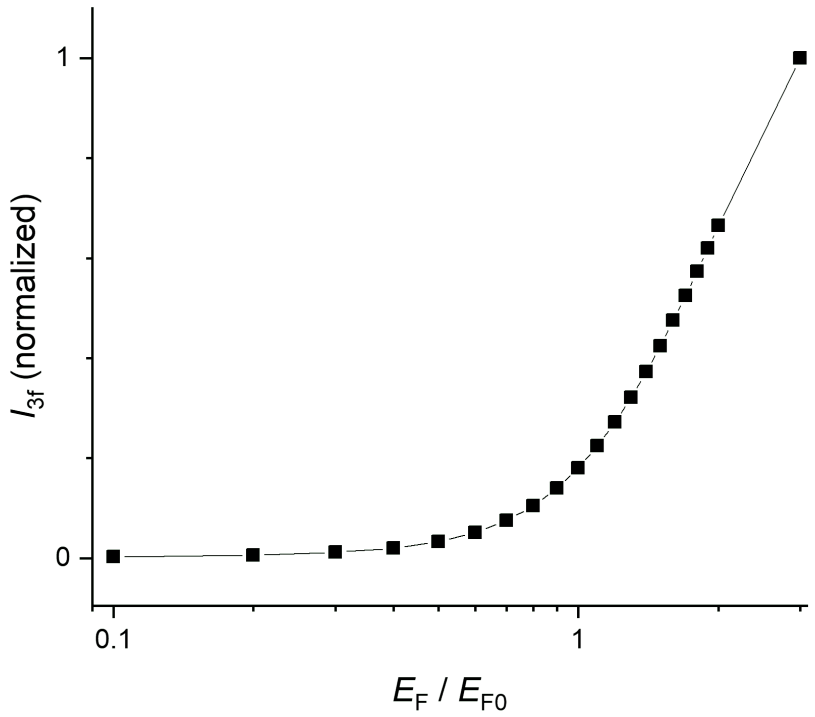

Supplementary Figure 6: Normalized THG intensity I_{3f} increases with increasing Fermi energy E_F. The waveform of the 0.67 THz pump pulse (see Figure 2) with a peak field of 56 kV/cm is used for the simulations. The other parameters are fixed to $E_{F0} = 118\text{meV}$, $v_F = 10^6$ m/s, $\tau = 10\text{fs}$.

9. Contributions

This chapter was published as:

Kovalev, S., Dantas, R.M.A., Germanskiy, S., Deinert, J.-C., Green, B., Ilyakov, I., Awari, N., Chen, M., Bawatna, M., Ling, J., Xiu, F., Loosdrecht, P.H.M. van, Surówka, P., Oka, T., Wang, Z.,
Non-perturbative terahertz high-harmonic generation in the three-dimensional Dirac semimetal Cd_3As_2.
Nature Communications **11**, 2451 (2020)
https://doi.org/10.1038/s41467-020-16133-8

Z.W. and T.O. conceived the project with P.S. S.K., and Z.W. carried out the THz HHG experiments and analyzed the data with **S.G.**, J.-C.D., B.G., I.I., N.A., M.C., M.B. R.M.A.D., P.S., and T.O. performed the theoretical calculations and analyzed the data. J.L. and F.X. fabricated and characterized the high-quality samples. **S.G.**, P.v.L., and Z.W. characterized linear THz response of the samples. Z.W. wrote the manuscript with contributions from S.K., R.M.A.D., **S.G.**, J.L., P.S., and T.O. All authors commented the manuscript.

10. References

[1] P. B. Corkum and F. Krausz, *Attosecond Science*, Nature Physics **3**, (2007).

[2] M. Drescher, M. Hentschel, R. Kienberger, G. Tempea, C. Spielmann, G. A. Reider, P. B. Corkum, and F. Krausz, *X-Ray Pulses Approaching the Attosecond Frontier*, Science **291**, 1923 (2001).

[3] P. M. Paul, E. S. Toma, P. Breger, G. Mullot, F. Augé, P. Balcou, H. G. Muller, and P. Agostini, *Observation of a Train of Attosecond Pulses from High Harmonic Generation*, Science **292**, 1689 (2001).

[4] S. Ghimire, A. D. DiChiara, E. Sistrunk, P. Agostini, L. F. DiMauro, and D. A. Reis, *Observation of High-Order Harmonic Generation in a Bulk Crystal*, Nature Physics **7**, 138 (2011).

[5] O. Schubert, M. Hohenleutner, F. Langer, B. Urbanek, C. Lange, U. Huttner, D. Golde, T. Meier, M. Kira, S. W. Koch, et al., *Sub-Cycle Control of Terahertz High-Harmonic Generation by Dynamical Bloch Oscillations*, Nature Photonics **8**, 119 (2014).

[6] R. Matsunaga, N. Tsuji, H. Fujita, A. Sugioka, K. Makise, Y. Uzawa, H. Terai, Z. Wang, H. Aoki, and R. Shimano, *Light-Induced Collective Pseudospin Precession Resonating with Higgs Mode in a Superconductor*, Science **345**, 1145 (2014).

[7] P. Bowlan, E. Martinez-Moreno, K. Reimann, T. Elsaesser, and M. Woerner, *Ultrafast Terahertz Response of Multilayer Graphene in the Nonperturbative Regime*, Physical Review B **89**, 41408 (2014).

[8] G. Vampa, T. J. Hammond, N. Thiré, B. E. Schmidt, F. Légaré, C. R. McDonald, T. Brabec, and P. B. Corkum, *Linking High Harmonics from Gases and Solids*, Nature **522**, 462 (2015).

[9] T. T. Luu, M. Garg, S. Y. Kruchinin, A. Moulet, M. T. Hassan, and E. Goulielmakis, *Extreme Ultraviolet High-Harmonic Spectroscopy of Solids*, Nature **521**, 498 (2015).

[10] M. Hohenleutner, F. Langer, O. Schubert, M. Knorr, U. Huttner, S. W. Koch, M. Kira, and R. Huber, *Real-Time Observation of Interfering Crystal Electrons in High-Harmonic Generation*, Nature **523**, 572 (2015).

[11] Y. S. You, D. A. Reis, and S. Ghimire, *Anisotropic High-Harmonic Generation in Bulk Crystals*, Nature Physics **13**, 345 (2017).

[12] F. Langer, M. Hohenleutner, C. P. Schmid, C. Poellmann, P. Nagler, T. Korn, C. Schüller, M. S. Sherwin, U. Huttner, J. T. Steiner, et al., *Lightwave-Driven Quasiparticle Collisions on a Subcycle Timescale*, Nature **533**, 225 (2016).

[13] F. Giorgianni, E. Chiadroni, A. Rovere, M. Cestelli-Guidi, A. Perucchi, M. Bellaveglia, M. Castellano, D. Di Giovenale, G. Di Pirro, M. Ferrario, et al., *Strong Nonlinear Terahertz Response Induced by Dirac Surface States in Bi2Se3 Topological Insulator*, Nature Communications **7**, 11421 (2016).

[14] N. Yoshikawa, T. Tamaya, and K. Tanaka, *High-Harmonic Generation in Graphene Enhanced by Elliptically Polarized Light Excitation*, Science **356**, 736 (2017).

[15] S. Rajasekaran, J. Okamoto, L. Mathey, M. Fechner, V. Thampy, G. D. Gu, and A. Cavalleri, *Probing Optically Silent Superfluid Stripes in Cuprates*, Science **359**, 575 (2018).

[16] H. A. Hafez, S. Kovalev, J.-C. Deinert, Z. Mics, B. Green, N. Awari, M. Chen, S. Germanskiy, U. Lehnert, J. Teichert, et al., *Extremely Efficient Terahertz High-Harmonic Generation in Graphene by Hot Dirac Fermions*, Nature **561**, 507 (2018).

[17] G. Soavi, G. Wang, H. Rostami, D. G. Purdie, D. De Fazio, T. Ma, B. Luo, J. Wang, A. K. Ott, D. Yoon, et al., *Broadband, Electrically Tunable Third-Harmonic Generation in Graphene*, Nature Nanotechnology **13**, 583 (2018).

[18] H. Chu, M.-J. Kim, K. Katsumi, S. Kovalev, R. D. Dawson, L. Schwarz, N. Yoshikawa, G. Kim, D. Putzky, Z. Z. Li, et al., *Phase-Resolved Higgs Response in Superconducting Cuprates*, Nature Communications **11**, 1793 (2020).

[19] X. Yang, C. Vaswani, C. Sundahl, M. Mootz, L. Luo, J. H. Kang, I. E. Perakis, C. B. Eom, and J. Wang, *Lightwave-Driven Gapless Superconductivity and Forbidden Quantum Beats by Terahertz Symmetry Breaking*, Nature Photonics **13**, 707 (2019).

[20] S. Ghimire and D. A. Reis, *High-Harmonic Generation from Solids*, Nature Physics **15**, (2019).

[21] G. Vampa, C. R. McDonald, G. Orlando, D. D. Klug, P. B. Corkum, and T. Brabec, *Theoretical Analysis of High-Harmonic Generation in Solids*, Physical Review Letters **113**, 73901 (2014).

[22] U. Huttner, M. Kira, and S. W. Koch, *Ultrahigh Off-Resonant Field Effects in Semiconductors*, Laser & Photonics Reviews **11**, 1700049 (2017).

[23] A. F. Kemper, B. Moritz, J. K. Freericks, and T. P. Devereaux, *Theoretical Description of High-Order Harmonic Generation in Solids*, New Journal of Physics **15**, 23003 (2013).

[24] R. E. F. Silva, I. V. Blinov, A. N. Rubtsov, O. Smirnova, and M. Ivanov, *High-Harmonic Spectroscopy of Ultrafast Many-Body Dynamics in Strongly Correlated Systems*, Nature Photonics **12**, 266 (2018).

[25] S. A. Mikhailov and K. Ziegler, *Nonlinear Electromagnetic Response of Graphene: Frequency Multiplication and the Self-Consistent-Field Effects*, Journal of Physics: Condensed Matter **20**, 384204 (2008).

[26] K. L. Ishikawa, *Nonlinear Optical Response of Graphene in Time Domain*, Physical Review B **82**, 201402 (2010).

[27] I. Al-Naib, M. Poschmann, and M. M. Dignam, *Optimizing Third-Harmonic Generation at Terahertz Frequencies in Graphene*, Physical Review B **91**, 205407 (2015).

[28] Z. Wang, H. Weng, Q. Wu, X. Dai, and Z. Fang, *Three-Dimensional Dirac Semimetal and Quantum Transport in Cd_3As_2*, Physical Review B **88**, (2013).

[29] M. N. Ali, Q. Gibson, S. Jeon, B. B. Zhou, A. Yazdani, and R. J. Cava, *The Crystal and Electronic Structures of Cd\textsubscript{3} As\textsubscript{2} , the Three-Dimensional Electronic Analogue of Graphene*, Inorganic Chemistry **53**, 4062 (2014).

[30] Z. K. Liu, J. Jiang, B. Zhou, Z. J. Wang, Y. Zhang, H. M. Weng, D. Prabhakaran, S.-K. Mo, H. Peng, P. Dudin, et al., *A Stable Three-Dimensional Topological Dirac Semimetal Cd_3As_2*, Nature Materials **13**, 677 (2014).

[31] S. Borisenko, Q. Gibson, D. Evtushinsky, V. Zabolotnyy, B. Büchner, and R. J. Cava, *Experimental Realization of a Three-Dimensional Dirac Semimetal, Cd_3As_2*, Physical Review Letters **113**, (2014).

[32] M. Neupane, S.-Y. Xu, R. Sankar, N. Alidoust, G. Bian, C. Liu, I. Belopolski, T.-R. Chang, H.-T. Jeng, H. Lin, et al., *Observation of a Three-Dimensional Topological Dirac Semimetal Phase in High-Mobility Cd_3As_2*, Nature Communications **5**, 3786 (2014).

[33] I. Crassee, R. Sankar, W.-L. Lee, A. Akrap, and M. Orlita, *3D Dirac Semimetal Cd_3As_2 : A Review of Material Properties*, Physical Review Materials **2**, (2018).

[34] P. J. W. Moll, N. L. Nair, T. Helm, A. C. Potter, I. Kimchi, A. Vishwanath, and J. G. Analytis, *Transport Evidence for Fermi-arc-mediated Chirality Transfer in the Dirac Semimetal Cd_3As_2*, Nature **535**, 266 (2016).

[35] C. Zhang, A. Narayan, S. Lu, J. Zhang, H. Zhang, Z. Ni, X. Yuan, Y. Liu, J.-H. Park, E. Zhang, et al., *Evolution of Weyl Orbit and Quantum Hall Effect in Dirac Semimetal Cd_3As_2*, Nature Communications **8**, 1272 (2017).

[36] C. Zhang, Y. Zhang, X. Yuan, S. Lu, J. Zhang, A. Narayan, Y. Liu, H. Zhang, Z. Ni, R. Liu, et al., *Quantum Hall Effect Based on Weyl Orbits in Cd_3As_2*, Nature **565**, 331 (2018).

[37] M. Uchida, Y. Nakazawa, S. Nishihaya, K. Akiba, M. Kriener, Y. Kozuka, A. Miyake, Y. Taguchi, M. Tokunaga, N. Nagaosa, et al., *Quantum Hall States Observed in Thin Films of Dirac Semimetal Cd_3As_2*, Nature Communications **8**, 2274 (2017).

[38] T. Schumann, L. Galletti, D. A. Kealhofer, H. Kim, M. Goyal, and S. Stemmer, *Observation of the Quantum Hall Effect in Confined Films of the Three-Dimensional Dirac Semimetal Cd 3 As 2*, Physical Review Letters **120**, 16801 (2018).

[39] Y. Liu, C. Zhang, X. Yuan, T. Lei, C. Wang, D. Di Sante, A. Narayan, L. He, S. Picozzi, S. Sanvito, et al., *Gate-Tunable Quantum Oscillations in Ambipolar Cd_3As_2 Thin Films*, NPG Asia Materials **7**, e221 (2015).

[40] P. L. Bhatnagar, E. P. Gross, and M. Krook, *A Model for Collision Processes in Gases. I. Small Amplitude Processes in Charged and Neutral One-Component Systems*, Physical Review **94**, 511 (1954).

[41] D. Xiao, M.-C. Chang, and Q. Niu, *Berry Phase Effects on Electronic Properties*, Reviews of Modern Physics **82**, 1959 (2010).

[42] S. Kovalev, R. M. A. Dantas, S. Germanskiy, J.-C. Deinert, B. Green, I. Ilyakov, N. Awari, M. Chen, M. Bawatna, J. Ling, et al., *Non-Perturbative Terahertz High-Harmonic Generation in the Three-Dimensional Dirac Semimetal Cd_3As_2*, Nature Communications **11**, (2020).

[43] B. Green, S. Kovalev, V. Asgekar, G. Geloni, U. Lehnert, T. Golz, M. Kuntzsch, C. Bauer, J. Hauser, J. Voigtlaender, et al., *High-Field High-Repetition-Rate Sources for the Coherent THz Control of Matter*, Scientific Reports **6**, 22256 (2016).

[44] I. Gierz, J. C. Petersen, M. Mitrano, C. Cacho, I. C. E. Turcu, E. Springate, A. Stöhr, A. Köhler, U. Starke, and A. Cavalleri, *Snapshots of Non-Equilibrium Dirac Carrier Distributions in Graphene*, Nature Materials **12**, 1119 (2013).

[45] N. P. Armitage, E. J. Mele, and A. Vishwanath, *Weyl and Dirac Semimetals in Three-Dimensional Solids*, Reviews of Modern Physics **90**, 15001 (2018).

[46] B. Cheng, N. Kanda, T. N. Ikeda, T. Matsuda, P. Xia, T. Schumann, S. Stemmer, J. Itatani, N. P. Armitage, and R. Matsunaga, *Efficient Terahertz Harmonic Generation with Coherent Acceleration of Electrons in the Dirac Semimetal Cd_3As_2*, Physical Review Letters **124**, 117402 (2020).

[47] H. Hirori, A. Doi, F. Blanchard, and K. Tanaka, *Single-Cycle Terahertz Pulses with Amplitudes Exceeding 1 MV/cm Generated by Optical Rectification in $LiNbO_3$*, Applied Physics Letters **98**, 91106 (2011).

[48] K.-L. Yeh, M. C. Hoffmann, J. Hebling, and K. A. Nelson, *Generation of 10μJ Ultrashort Terahertz Pulses by Optical Rectification*, Applied Physics Letters **90**, 171121 (2007).

[49] T. Kampfrath, K. Tanaka, and K. A. Nelson, *Resonant and Nonresonant Control over Matter and Light by Intense Terahertz Transients*, Nature Photonics **7**, 680 (2013).

[50] S. Kovalev, B. Green, T. Golz, S. Maehrlein, N. Stojanovic, A. S. Fisher, T. Kampfrath, and M. Gensch, *Probing Ultra-Fast Processes with High Dynamic Range at 4th-Generation Light Sources: Arrival Time and Intensity Binning at Unprecedented Repetition Rates*, Structural Dynamics **4**, 24301 (2017).

[51] C. Duval, Z. Horváth, P. A. Horváthy, L. Martina, and P. C. Stichel, *Berry Phase Correction To Electron Density In Solids And "Exotic" Dynamics*, Modern Physics Letters B **20**, 373 (2006).

[52] M. A. Stephanov and Y. Yin, *Chiral Kinetic Theory*, Physical Review Letters **109**, 162001 (2012).

[53] R. Loganayagam and P. Surówka, *Anomaly/Transport in an Ideal Weyl Gas*, Journal of High Energy Physics **2012**, 97 (2012).

[54] R. M. A. Dantas, F. Peña-Benitez, B. Roy, and P. Surówka, *Magnetotransport in Multi-Weyl Semimetals: A Kinetic Theory Approach*, Journal of High Energy Physics **2018**, 69 (2018).

Chapter IV
Ellipticity control of terahertz high-harmonic generation in a Dirac semimetal

1. Introduction

Strong-field driven nonlinear response provides a fruitful path for the discovery and understanding of intriguing dynamical processes of quantum matter [1–3]. The dependence of high-order harmonic generation on the ellipticity of the driving laser exhibits characteristic features of the nonlinear dynamics [4–16]. The polarization state of electromagnetic waves has not only been employed extensively to investigate fundamental physical properties of matter, which for linear response underlies numerous spectroscopic techniques, but also been demonstrated to be very efficient in controlling nonequilibrium states of matter and their nonlinear response via strong light-matter interactions. A plethora of very interesting nonlinear physical phenomena have been found in different states of matter, i.e. gases [1,3], liquids [17], and solids [2,3]. In particular, high-order harmonic generation (HHG) is found to exhibit characteristics of nonlinear response in atomic or molecular gases [18–21] as well as in solid-state materials (see e.g. [5,6,10–13,22–30]).

Decades ago high-harmonic generation was observed when driving noble gases with picosecond laser radiation [19–21]. The coherent radiation emitted in strong-field driven atomic and molecular gases has enabled spectroscopic studies in the extreme ultraviolet and soft X-ray regimes and also for ultrafast dynamics on attosecond time scales [1,3]. The yield of high harmonics in atomic gases is maximized for linearly polarized lasers, but drops rapidly with increasing ellipticity of the driving laser, already by two orders of magnitude at a relatively small ellipticity $\epsilon_f \lesssim 0.5$ (see e.g. [20,21]). The strong ellipticity dependence of HHG provides tremendous opportunities for applications, including production of isolated attosecond pulses [4], probing chiral interactions of molecules through sub-femtosecond electronic dynamics [7], and detection of soft X-ray magnetic circular dichroism in magnetic substances [8,9].

Reprinted paper with permission from S. Germanskiy et al., *Ellipticity Control of Terahertz High-Harmonic Generation in a Dirac Semimetal*, Physical Review B **106**, 81127 (2022).

In contrast to the atomic gases where the HHG is well understood in terms of three-step processes (ionization, acceleration, and recollision) [1,31], solid-state materials exhibit versatile ellipticity dependence of HHG [5,6,10–13]. On the one hand, atomic-like ellipticity dependence was also found in some solids (e.g. rare-gas solids [6], ZnO crystal [5], monolayer MoS_2 [10]). On the other hand, enhanced harmonic yield can be realized at larger ellipticity reaching a maximum for circularly polarization ($\epsilon_f = 1$) such as in MgO [11], or at finite ellipticity, e.g. $\epsilon_f = 0.32$ in graphene [12]. The ellipticity dependence appears to also vary with driving-pulse energy, suggesting frequency-dependent mechanisms. For example, graphene exhibits the unusual ellipticity dependence for a driving-pulse energy of 0.26 eV [12], whereas for slightly higher energies 0.32 and 0.4 eV an atomic-like behavior is restored [13].

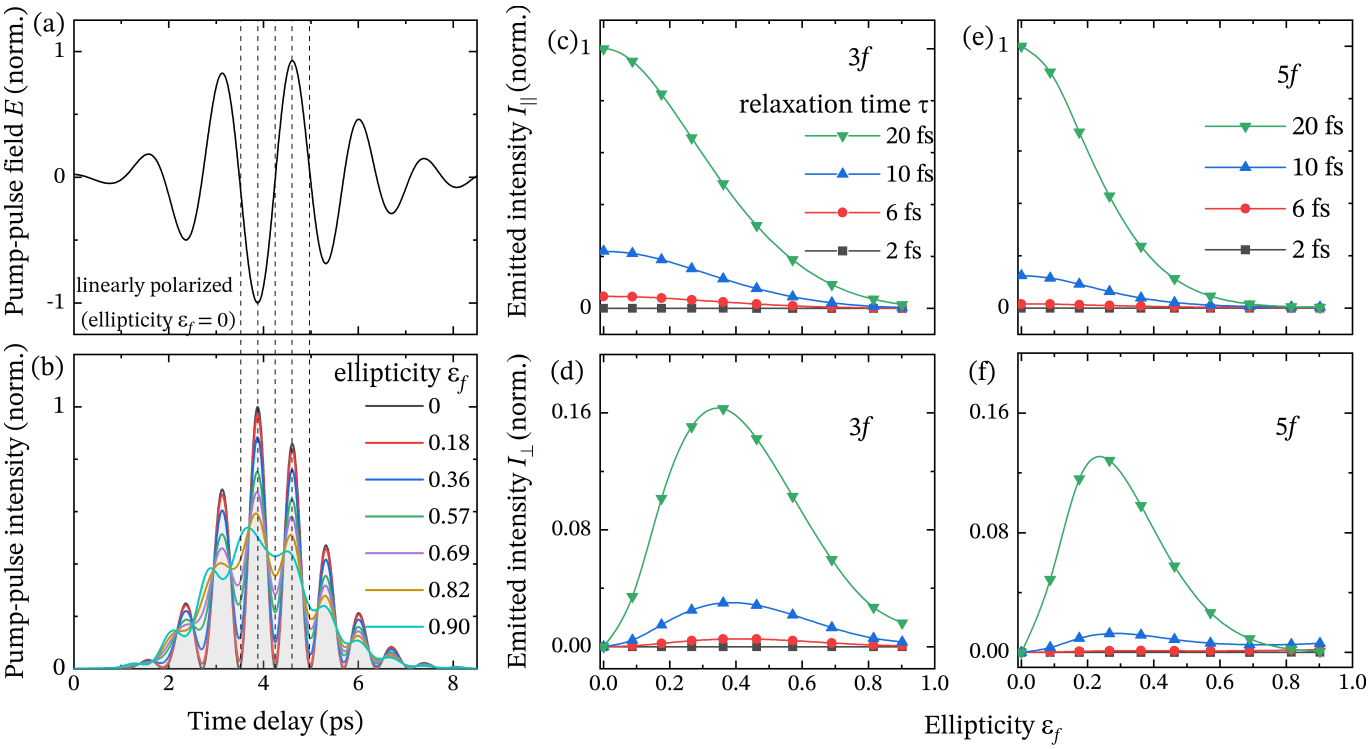

Figure 1: (a) An idealized driving pulse with linear polarization, a central frequency of $f = 0.69$ THz, and full width at half maximum (FWHM) of 0.11 THz. (b) Intensity of driving pulse for various ellipticities ε_f. Intensity of emitted third-order harmonic radiation ($3f$), for (c) parallel $I_\parallel$ and (d) perpendicular $I_\perp$ components, as a function of the ellipticity for various relaxation times $\tau = 2$, 6, 10, and 20 fs. The intensity is normalized to the maximum value of $I_\parallel$. Intensity of emitted fifth-order harmonic radiation ($5f$) versus ellipticity for (e) parallel and (f) perpendicular components.

A crucial role of interband excitations in determining the ellipticity dependence of HHG has been emphasized by previous studies (see e.g. [12,14–16]). The experimentally observed ellipticity dependencies can result from combined effects of interband

excitations with dynamical Bloch oscillations [15], nonlinear coupling to intraband excitations [14,16], or other quantum mechanical effects (e.g. Zener tunneling) [12]. In this work, without the need for the complex interband processes, we investigate ellipticity dependence of HHG in a very different but very representative setting, in which the field-driven intraband kinetics of massless Dirac fermions is primarily responsible for the ellipticity dependence. We study HHG of terahertz (THz) field-driven relativistic quasiparticles in an electron-doped Dirac semimetal, where the interband transitions are essentially Pauli-blocked due to the low energy of THz photons. By measuring THz third-harmonic generation (THG) in the well-established three-dimensional Dirac semimetal Cd_3As_2, we find an evident dependence of the THG ellipticity and intensity on the driving-pulse ellipticity, in good agreement with our results based on kinetic theory. Our work provides a very efficient approach to control the THz HHG and reveals the underlying nonlinear kinetics.

2. Results

2.1. Theoretical analysis

We start with a theoretical analysis of the THz driven kinetics in a single Dirac-electron band by Boltzmann transport theory. While the initial equilibrium state is defined by the Fermi-Dirac distribution $f_0(\mathbf{p})$ at room temperature, we evaluate the time evolution of the distribution function $f(t,\mathbf{p})$ under the drive of an external THz field $\mathbf{E}(t)$ via the Boltzmann equation

$$\left(\frac{\partial}{\partial t}+\frac{1}{\tau}\right)f(t,\mathbf{p})-e\mathbf{E}(t)\cdot\nabla_{\mathbf{p}}f(t,\mathbf{p})=\frac{1}{\tau}f_0(\mathbf{p}), \tag{1}$$

where τ is a characteristic relaxation time for intraband processes and e denotes the elementary charge. Idealized THz pulses with linear or elliptical polarizations (see Figure 1(a,b)) are adopted to simulate the driven intraband processes of the relativistic quasiparticles in the time domain. Ellipticity ε_f of the terahertz pulses was computed via $\varepsilon=\tan\left[\frac{1}{2}\arcsin(S_3/S_0)\right]$ with the Stokes parameters given by $S_0=\left\langle\left|\hat{E}_\perp\hat{E}_\perp^*\right|+\left|\hat{E}_\parallel\hat{E}_\parallel^*\right|\right\rangle$ and $S_3=\left\langle 2\,\mathrm{Im}(\hat{E}_\perp^*\hat{E}_\parallel)\right\rangle$, where $\hat{E}_\parallel(t)$ and $\hat{E}_\perp(t)$ are the THz electric-field components and $\langle\ldots\rangle$ represents time averaging [32,33]. The ellipticity can be roughly interpreted as the ratio between the maximum electric-field components, $E_\perp$ and $E_\parallel$, along the minor- and major-axes of the polarization ellipse, respectively (see Figure 3(b) for an illustration). In the following, perpendicular or parallel components of other quantities are defined in a similar way, as perpendicular or parallel to the linear polarization ($\varepsilon_f=0$), respectively.

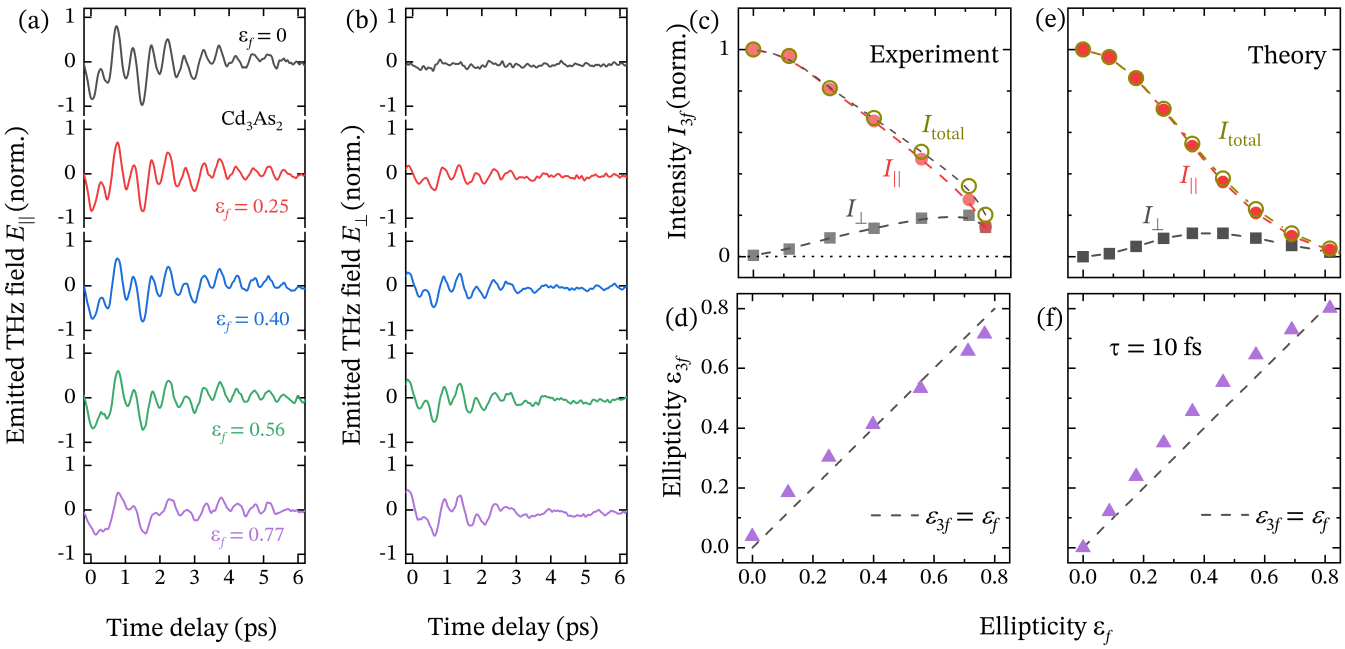

Figure 2: Electric-field components (a) $E_{\parallel}$ and (b) $E_{\perp}$ of emitted terahertz radiation from Cd_3As_2 at room temperature. The data are normalized to the maximum value of $E_{\parallel}$ at $\varepsilon_f = 0$. (c) Intensity I_{3f} of terahertz THG from Cd_3As_2 as a function of ellipticity at room temperature. The dashed lines are guides to the eyes. (d) Ellipticity ε_{3f} of observed THG versus driving-pulse ellipticity ε_f. The dashed line depicts $\varepsilon_{3f} = \varepsilon_f$. (e) Intensity and (f) ellipticity of theoretically obtained THG versus driving-pulse ellipticity ε_f for $\tau = 10$ fs.

The analytical solution for the Boltzmann equation [equation (1)] satisfying the boundary condition $f(0, \mathbf{p}) = f_0(\mathbf{p})$ is given by [34,35]

$$\begin{aligned} f(t, \mathbf{p}) = & \exp(-\frac{t}{\tau}) f_0(\mathbf{p} - e\mathbf{\Delta}(t, 0)) \\ & + \frac{1}{\tau} \int_0^t ds \exp(\frac{s-t}{\tau}) f_0(\mathbf{p} - e\mathbf{\Delta}(t, s)), \end{aligned} \tag{2}$$

where $\mathbf{\Delta}(t, s) = -\int_s^t \mathbf{E}(\tilde{s})\, d\tilde{s}$. The current density is defined as

$$\mathbf{j}(t) = -2\, e \left[\exp\left(-\frac{t}{\tau}\right) \langle \mathbf{v}(t, 0) \rangle + \int_0^t \frac{ds}{\tau} \exp\left(\frac{s-t}{\tau}\right) \langle \mathbf{v}(t, s) \rangle \right], \tag{3}$$

where $\langle \mathbf{v}(t, s) \rangle = \int \frac{d^3p}{(2\pi\hbar)^3} \mathbf{v}_{\mathbf{p}} f_0(\mathbf{p} - e\mathbf{\Delta}(t, s))$ corresponds to the expectation value of the group velocity of the Dirac fermions. The electric field of the emitted THz radiation is proportional to the time derivative of the current density. Through a Fourier transformation of the time-domain data, we compute the HHG intensity. The obtained intensity

of the emitted third-harmonic $3f$ and fifth-harmonic $5f$ radiation versus ellipticity is shown in Figure 1(c-f) for various relaxation times τ, a peak electric field of 212 kV/cm and typical values of Fermi energy $E_F = 118$ meV and Fermi velocity $v_F = 7.8 \times 10^5$ m/s in a Dirac semimetal, Cd_3As_2 [26].

The obtained parallel $I_\parallel$ and perpendicular $I_\perp$ intensity components exhibit clearly different ellipticity dependence for every relaxation time and harmonic. Whereas $I_\parallel$ drops monotonically with increasing ellipticity, an initial increase of $I_\perp$ is followed by a continuous decrease approaching the circular polarization, exhibiting a maximum at a finite ellipticity. For $\tau = 20$ fs, the maximum of the THG occurs at $\varepsilon_f^{\max} = 0.36$, while at $\varepsilon_f^{\max} = 0.24$ for the fifth-harmonic generation (FHG). For both harmonics the position of the maximum shifts towards larger ellipticity with decreasing relaxation time. Moreover, for different harmonics or relaxation times, $I_\perp$ is always considerably smaller than $I_\parallel$, thus the total intensity decreases continuously with increasing ellipticity. This is clearly in contrast to an enhanced THG at finite ellipticity due to interband excitations involved [12].

2.2. Experiment

To experimentally study the nonlinear response due to intraband processes, we measure THz-driven third harmonic generation from electronically doped Cd_3As_2 thin films, a well-established three-dimensional Dirac semimetal [36–39]. High-quality thin films of Cd_3As_2 with a typical thinkness of 120 nm were grown by molecular beam epitaxy, as described in [40] in detail.

Intense THz radiation is generated based on optical rectification of laser pulses (80 fs, 4 mJ, 800 nm) in a $LiNbO_3$ crystal using a conventional tilted-pulse-front scheme (see e.g. [41,42]). Narrow-band multicycle THz driving pulses with a peak field of 130 kV/cm, a central frequency around $f = 0.67$ THz and linewidth of 0.15 THz were obtained through a band-pass filter. An *x*-cut single crystalline quartz with a thickness of 2.18 mm was adopted to tune the polarization state of terahertz driving pulses. The experimentally obtained driving pulses for various ellipticities are displayed in Supplementary Figure 1(a), with a largest achieved ellipticity of $\varepsilon_f = 0.77$. Emitted THz pulses from a Cd_3As_2 thin film in a transmission configuration were detected via electro-optic sampling in a $\langle 110 \rangle$-cut GaP crystal. The electric field of the emitted radiation from a Cd_3As_2 thin film at room temperature was recorded through a $3f$ band-pass filter as a function of time delay. The parallel $E_\parallel(t)$ and perpendicular $E_\perp(t)$ components are measured separately by using THz wire-grid polarizers, which are presented in Figure 2(a) and Figure 2(b), respectively, for various ellipticities from $\varepsilon_f = 0$ to 0.77.

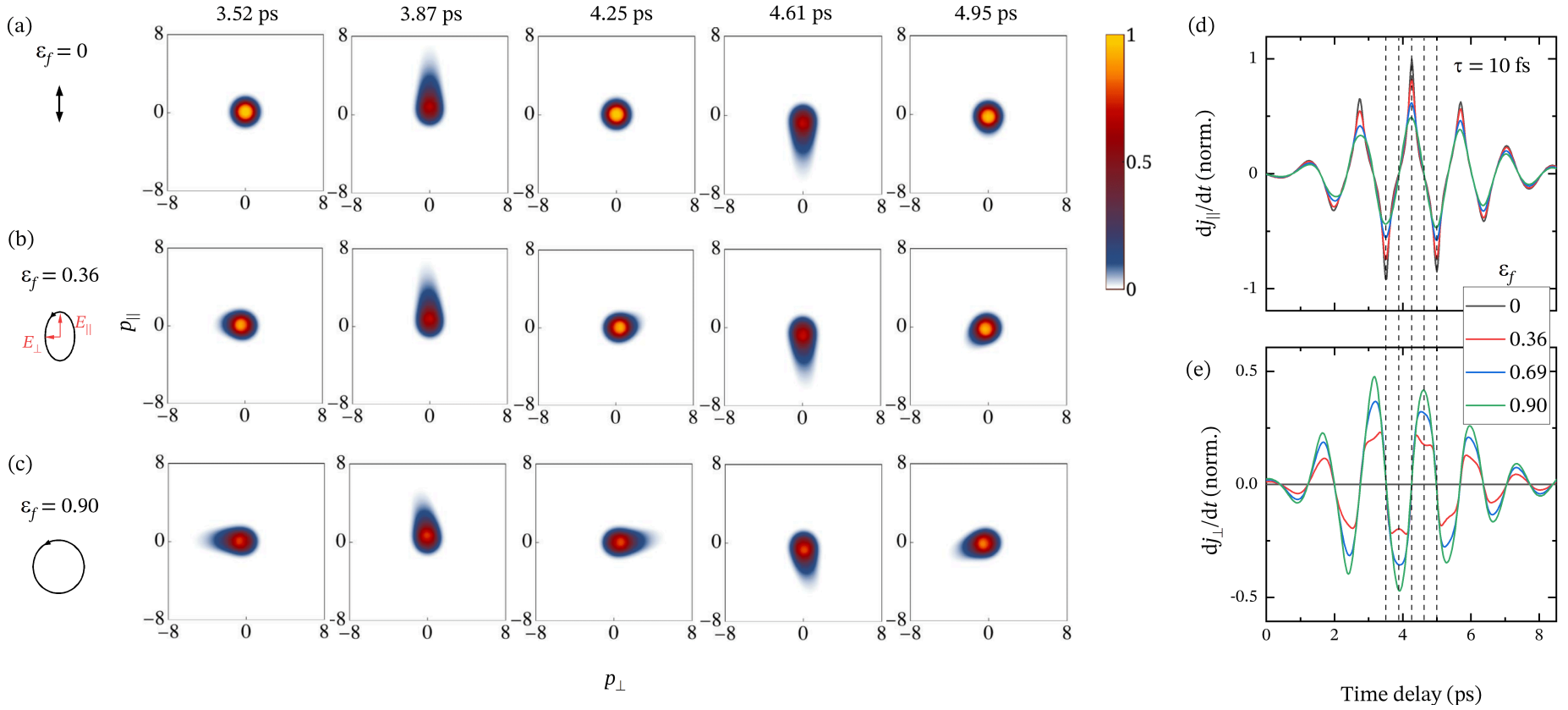

Figure 3: Projection of the electron distribution function on the ($p_\perp$,$p_\parallel$) momentum plane at selected time delays 3.52, 3.87, 4.25, 4.51, and 4.95 ps (corresponding to the dashed lines in (d-e) and in Figure 1(a-b)) for a relaxation time $\tau = 10$ fs and various ellipticities (a) $\varepsilon_f = 0$, (b) 0.36, and (c) 0.90. The momenta are given in units of the Fermi momentum E_F/v_F. The time-derivative of the current density (d) $dj_\parallel/dt$ and (e) $dj_\perp/dt$ as a function of time delay, which is normalized to the maximum value of $dj_\parallel/dt$.

For a linearly polarized driving pulse, $E_{\parallel}(t)$ exhibits strong oscillations corresponding to the frequency of $3f$ (see Supplementary Figure 1(b) for the spectrum in frequency domain), whereas $E_{\perp}(t)$ is almost zero. At finite ellipticity $E_{\perp}(t)$ starts to increase, and exhibits also the $3f$ oscillations. In contrast, the parallel component $E_{\parallel}(t)$ decreases continuously with enhanced ellipticity. The obtained THG intensity and ellipticity is shown in Figure 2(c-d) as a function of ellipticity. For comparison theoretical results for the same peak field and $\tau = 10$ fs are shown in Figure 2(e-f).

Experimentally we observe that $I_{\parallel}$ decreases continuously with increasing ellipticity, whereas $I_{\perp}$ exhibits a broad maximum around $\varepsilon_f^{\max} = 0.6$. These ellipticity dependence qualitatively agrees very well with the theory results (Figure 2(e)), apart from the quantitative difference on $\varepsilon_f^{\max}$. Moreover, the observed $I_{\perp}$ is notably smaller than $I_{\parallel}$, leading to a monotonic drop of the total THG intensity I_{total} with increased ellipticity (Figure 2(c)), which is also in very good agreement with the theory results (Figure 2(e)). Furthermore, both the experimentally and theoretically obtained ellipticity of the emitted $3f$-radiation ε_{3f} tends to follows the driving-pulse ellipticity, as summarized in Figure 2(d-f). These results confirm the sensitive control of the THG through ellipticity tuning, and support the interpretation of the ellipticity dependence by field-driven nonlinear intraband kinetic processes of the Dirac fermions.

To understand these ellipticity-dependent features, we scrutinise the time-dependent evolution of the electron distribution function. For an experimentally relevant relaxation time $\tau = 10$ fs [26], snapshots of the distribution function projected onto the $\left(p_{\perp}, p_{\parallel}\right)$ momentum plane are presented in Figure 3(a-c) for representative ellipticities. The selected delay-times correspond to the THz fields marked by dashed lines in Figure 1(a-b). The obtained time derivative of the current density is shown in Figure 3(d-e), which is proportional to the emitted THz electric field.

For linearly polarized driving pulses (Figure 3(a)) the distribution function is strongly stretched along the field direction especially at the peak fields (see 3.87 and 4.61 ps), however the emitted electric field $\propto dj_{\parallel}/dt$ is nearly zero (Figure 3(d)). In contrast, strong emission occurs when the driving THz field switches sign (e.g. at 3.52, 4.25, and 4.95 ps). Since the time-dependent curve $\frac{dj_{\parallel}(t)}{dt}$ exhibits sharp peaks at these points, its overall profile deviates strongly from a $\sin$- or $\cos$-function. This is what leads to very efficient generation of high-order harmonics. Moreover, the emitted harmonic radiation is also linearly polarized, because the perpendicular component $dj_{\perp}/dt = 0$ (Figure 3(e)).

For an elliptical driving pulse (Figure 3(b,c)), the distribution function $f(\mathbf{p})$ can be stretched along different directions as a function of time, depending on the orientation of the driving electric field. The effects of the elliptical polarization on the harmonic generation are mainly two-fold: (i) With increasing ellipticity the current component $j_{\parallel}$ reduces, because the driving field component $E_{\parallel}$ decreases and, consequently, the distribution function is less stretched along this direction. (ii) At the same time, the sharp peaks in the time-dependent curve $\frac{dj_{\parallel}(t)}{dt}$ become more rounded (Figure 3(d)), resulting in reduced high-harmonic generation. These two effects collaboratively cause the monotonic decrease of the harmonic yields with increasing ellipticity, as presented in Figure 1(c-e) and Figure 2(c-e).

In contrast, the perpendicular HHG component experiences two competing effects. Whereas with increasing ellipticity the current density $j_{\perp}$ increases in favor of harmonic yielding along the same direction, its time derivative $\frac{dj_{\perp}(t)}{dt}$ evolves towards a $\sin$- or $\cos$-like function (Figure 3(e)), suppressing the generation of high harmonics. The maxima exhibited in the ellipticity dependent $I_{\perp}$ curves (Figure 1(d-f) and Figure 2(c-e)) can be understood as a consequence of this competition.

In comparison with the ellipticity-dependent THG curves of the same relaxation time, the FHG intensity $I_{\parallel}^{5f}$ decreases more rapidly with increasing ellipticity (see Figure 1(c) and Figure 1(e)). Moreover, the maximum of $I_{\perp}^{5f}$ appears at a smaller ellipticity than for THG $I_{\perp}^{3f}$ (see Figure 1(d) and Figure 1(f)). These differences show that the higher-order nonlinear effects are more sensitive to the change of the driving pulses.

In the limit case of a circular driving pulse, the distribution function is distorted by the same amount, but only the orientation rotates following the driving electric field. The corresponding current is essentially a $\sin$- or $\cos$-function of time, i.e. without high-harmonic generation.

Qualitatively, the ellipticity dependence of HHG can be obtained also analytically but for a very simplified setting (i.e. monochromatic driving pulse and perturbative regime, see Supplemental Material). Nonetheless, these theoretical results clearly indicate that the THz high-harmonic generation in a Dirac semimetal due to intraband processes is not only very efficient, but also sensitive to the ellipticity of the driving pulses.

3. Conclusions

In conclusion, we obtain a very efficient control of terahertz third-harmonic yield and polarization state in thin films of the three-dimensional Dirac semimetal Cd_3As_2 via tuning ellipticity of the fundamental frequency. The sensitive dependence of the high-harmonic yields on the ellipticity can be understood in terms of terahertz field driven

intraband kinetics of massless Dirac fermions, which are characterized by a linear dispersion relation. Our study paves the way for realizing novel nonlinear photonic devices in few terahertz frequency range based on Dirac or Weyl semimetals, where terahertz high-harmonic generation and its ellipticity tunability could be exploited for signal processing and optical communications.

4. Supplementary information

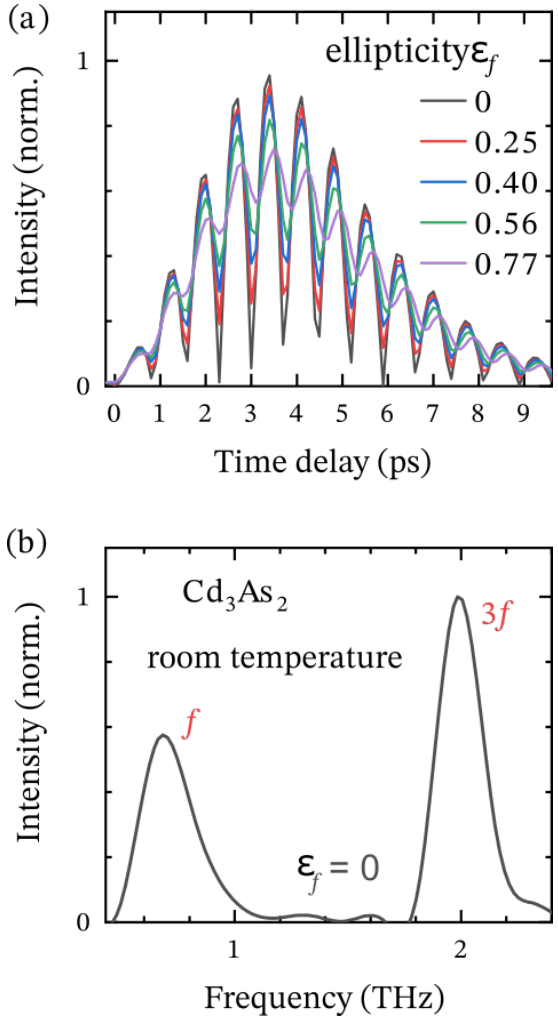

Supplementary Figure 1: (a) Intensity of the experimentally realized driving pulses with various ellipticities. (b) Spectrum of emitted terahertz radiation from Cd_3As_2 for linearly polarized driving pulse ($\varepsilon_f = 0$), measured through a $3f$-bandpass filter.

Analytical perturbative theory. In the perturbative regime [34], one can perform an analytical analysis at zero temperature for a sinusoidal pulse $\mathbf{E}(t) = \frac{E}{\sqrt{\varepsilon_f^2+1}}\left[\varepsilon_f \cos(\omega t)\hat{\mathbf{e}}_\perp + \sin(\omega t)\hat{\mathbf{e}}_\parallel\right]$ with $\omega = 2\pi f$. In the limit of no collisions, i.e. $\tau \to \infty$, the current is simply given by $\mathbf{j}(t) = -2e\langle \mathbf{v}(t,0)\rangle$ and the intensity of the third-harmonic generation is given by

$$\{I^P_{3\omega,\perp}, I^P_{3\omega,\parallel}\} \propto \left[\frac{3\kappa e}{80\pi^2 f^2}\left(\frac{v_F eE}{\mu}\right)^3\right]^2 \frac{(\varepsilon_f^2-1)^2}{(\varepsilon_f^2+1)^3}\{\varepsilon_f^2, 1\}, \tag{4}$$

where $\kappa = \frac{\mu^3}{6\pi^2\hbar^3 v_F^2}$. This means that for a monochromatic driving pulse, the parallel component $I^P_{\parallel,3f}$ of THG drops monotonically with increasing ellipticity, while the perpendicular component $I^P_{3f,\perp}$ reaches a maximum for $\varepsilon_f^{\max} = \frac{1}{\sqrt{5}} \approx 0.45$. If collisions with a finite relaxation time τ (with $\tau \ll 1/f$) are taken into account, the THG intensity becomes

$$\{I^{P,\tau}_{3\omega,\perp}, I^{P,\tau}_{3\omega,\parallel}\} \propto \frac{36}{\left(36 + \frac{49}{\tau^2\omega^2} + \frac{14}{\tau^4\omega^4} + \frac{1}{\tau^6\omega^6}\right)}\{I^P_{3\omega,\perp}, I^P_{3\omega,\parallel}\}. \tag{5}$$

On the one hand, the third-harmonic yield reduces with increasing scattering rate $1/\tau$. On the other hand, for a fixed $1/\tau$, the maximum of $I^P_{3f,\perp}$ occurs at the same ellipticity $\varepsilon_f^{\max} = \frac{1}{\sqrt{5}}$. We should note that these analytical results are valid for an homogenous electric field in the perturbative regime, which for Cd_3As_2 means an THz electric field of $E \lesssim 5$ kV/cm [34,35]. With a typical peak THz electric field of 100 kV/cm, our experiment deals with the non-perturbative regime [34], for which the ellipticity dependence is also a function of the THz electric field, the driving-pulse waveform, and the relaxation time, therefore we have to solve the problem numerically as presented in the main text.

5. Contributions

This chapter was published as:

> Germanskiy, S., Dantas, R.M.A., Kovalev, S., Reinhoffer, C., Mashkovich, E.A., van Loosdrecht, P.H.M., Yang, Y., Xiu, F., Surówka, P., Moessner, R., Oka, T., Wang, Z., Ellipticity control of terahertz high-harmonic generation in a Dirac semimetal. Phys. Rev. B **106**, L081127(2022)
> https://doi.org/10.1103/PhysRevB.106.L081127

Z.W. and T.O. conceived the project with P.S. **S.G.** designed and implemented the experimental setup. **S.G.** with C.R. carried out the THz ellipticity experiments and analyzed the data with E.A.M., P.v.L and Z.W., R.M.A.D., P.S., and T.O. performed the theoretical calculations. J.L. and F.X. fabricated and characterized the high-quality samples. Z.W. and **S.G.** wrote the manuscript with contributions from S.K., R.M.A.D., R.M, P.S., and T.O.

6. References

[1] P. B. Corkum and F. Krausz, *Attosecond Science*, Nature Physics **3**, 381 (2007).

[2] S. Ghimire and D. A. Reis, *High-Harmonic Generation from Solids*, Nature Physics **15**, 10 (2019).

[3] J. Li, J. Lu, A. Chew, S. Han, J. Li, Y. Wu, H. Wang, S. Ghimire, and Z. Chang, *Attosecond Science Based on High Harmonic Generation from Gases and Solids*, Nature Communications **11**, 2748 (2020).

[4] G. Sansone, E. Benedetti, F. Calegari, C. Vozzi, L. Avaldi, R. Flammini, L. Poletto, P. Villoresi, C. Altucci, R. Velotta, et al., *Isolated Single-Cycle Attosecond Pulses*, Science **314**, 443 (2006).

[5] S. Ghimire, A. D. DiChiara, E. Sistrunk, P. Agostini, L. F. DiMauro, and D. A. Reis, *Observation of High-Order Harmonic Generation in a Bulk Crystal*, Nature Physics **7**, 138 (2011).

[6] G. Vampa, T. J. Hammond, N. Thiré, B. E. Schmidt, F. Légaré, C. R. McDonald, T. Brabec, and P. B. Corkum, *Linking High Harmonics from Gases and Solids*, Nature **522**, 462 (2015).

[7] R. Cireasa, A. E. Boguslavskiy, B. Pons, M. C. H. Wong, D. Descamps, S. Petit, H. Ruf, N. Thiré, A. Ferré, J. Suarez, et al., *Probing Molecular Chirality on a Sub-Femtosecond Timescale*, Nature Physics **11**, 654 (2015).

[8] O. Kfir, P. Grychtol, E. Turgut, R. Knut, D. Zusin, D. Popmintchev, T. Popmintchev, H. Nembach, J. M. Shaw, A. Fleischer, et al., *Generation of Bright Phase-Matched Circularly-Polarized Extreme Ultraviolet High Harmonics*, Nature Photonics **9**, 99 (2015).

[9] T. Fan, P. Grychtol, R. Knut, C. Hernández-García, D. D. Hickstein, D. Zusin, C. Gentry, F. J. Dollar, C. A. Mancuso, C. W. Hogle, et al., *Bright Circularly Polarized Soft X-ray High Harmonics for X-ray Magnetic Circular Dichroism*, PNAS **112**, 14206 (2015).

[10] H. Liu, Y. Li, Y. S. You, S. Ghimire, T. F. Heinz, and D. A. Reis, *High-Harmonic Generation from an Atomically Thin Semiconductor*, Nature Physics **13**, 262 (2017).

[11] Y. S. You, D. A. Reis, and S. Ghimire, *Anisotropic High-Harmonic Generation in Bulk Crystals*, Nature Physics **13**, 345 (2017).

[12] N. Yoshikawa, T. Tamaya, and K. Tanaka, *High-Harmonic Generation in Graphene Enhanced by Elliptically Polarized Light Excitations*, Science **356**, 736 (2017).

[13] M. Taucer, T. J. Hammond, P. B. Corkum, G. Vampa, C. Couture, N. Thiré, B. E. Schmidt, F. Légaré, H. Selvi, N. Unsuree, et al., *Nonperturbative Harmonic Generation in Graphene from Intense Midinfrared Pulsed Light*, Physical Review B **96**, 195420 (2017).

[14] N. Tancogne-Dejean, O. D. Mücke, F. X. Kärtner, and A. Rubio, *Ellipticity Dependence of High-Harmonic Generation in Solids Originating from Coupled Intraband and Interband Dynamics*, Nature Communications **8**, (2017).

[15] X. Zhang, J. Li, Z. Zhou, S. Yue, H. Du, L. Fu, and H.-G. Luo, *Ellipticity Dependence Transition Induced by Dynamical Bloch Oscillations*, Physical Review. B **99**, 14304 (2019).

[16] S. A. Sato, H. Hirori, Y. Sanari, Y. Kanemitsu, and A. Rubio, *High-Order Harmonic Generation in Graphene: Nonlinear Coupling of Intraband and Interband Transitions*, Physical Review. B **103**, L41408 (2021).

[17] E. A. Ponomareva, A. O. Ismagilov, S. E. Putilin, A. N. Tsypkin, S. A. Kozlov, and X.-C. Zhang, *Varying Pre-Plasma Properties to Boost Terahertz Wave Generation in Liquids*, Communications on Physics **4**, 4 (2021).

[18] M. Ferray, A. L'Huillier, X. F. Li, L. A. Lompre, G. Mainfray, and C. Manus, *Multiple-Harmonic Conversion of 1064 nm Radiation in Rare Gases*, Journal of Physics B: Atomic, Molecular and Optical Physics **21**, L31 (1988).

[19] R. Rosman, G. Gibson, K. Boyer, H. Jara, T. S. Luk, I. A. McIntyre, A. McPherson, J. C. Solem, and C. K. Rhodes, *Fifth-Harmonic Production in Neon and Argon with Picosecond 248-nm Radiation*, Journal of the Optical Society of America **5**, 1237 (1988).

[20] K. S. Budil, P. Salières, A. L'Huillier, T. Ditmire, and M. D. Perry, *Influence of Ellipticity on Harmonic Generation*, Physical Review. A **48**, R3437 (1993).

[21] P. Dietrich, N. H. Burnett, M. Ivanov, and P. B. Corkum, *High-Harmonic Generation and Correlated Two-Electron Multiphoton Ionization with Elliptically Polarized Light*, Physical Review A **50**, R3585 (1994).

[22] O. Schubert, M. Hohenleutner, F. Langer, B. Urbanek, C. Lange, U. Huttner, D. Golde, T. Meier, M. Kira, S. W. Koch, et al., *Sub-Cycle Control of Terahertz High-*

Harmonic Generation by Dynamical Bloch Oscillations, Nature Photonics **8**, 119 (2014).

[23] H. A. Hafez, S. Kovalev, J.-C. Deinert, Z. Mics, B. Green, N. Awari, M. Chen, S. Germanskiy, U. Lehnert, J. Teichert, et al., *Extremely Efficient Terahertz High-Harmonic Generation in Graphene by Hot Dirac Fermions*, Nature **561**, 507 (2018).

[24] G. Soavi, G. Wang, H. Rostami, D. G. Purdie, D. De Fazio, T. Ma, B. Luo, J. Wang, A. K. Ott, D. Yoon, et al., *Broadband, Electrically Tunable Third-Harmonic Generation in Graphene*, Nature Nanotechnology **13**, 583 (2018).

[25] B. Cheng, N. Kanda, T. N. Ikeda, T. Matsuda, P. Xia, T. Schumann, S. Stemmer, J. Itatani, N. P. Armitage, and R. Matsunaga, *Efficient Terahertz Harmonic Generation with Coherent Acceleration of Electrons in the Dirac Semimetal Cd_3As_2*, Physical Review Letters **124**, 117402 (2020).

[26] S. Kovalev, R. M. A. Dantas, S. Germanskiy, J.-C. Deinert, B. Green, I. Ilyakov, N. Awari, M. Chen, M. Bawatna, J. Ling, et al., *Non-Perturbative Terahertz High-Harmonic Generation in the Three-Dimensional Dirac Semimetal Cd_3As_2*, Nature Communications **11**, (2020).

[27] H. Chu, M.-J. Kim, K. Katsumi, S. Kovalev, R. D. Dawson, L. Schwarz, N. Yoshikawa, G. Kim, D. Putzky, Z. Z. Li, et al., *Phase-Resolved Higgs Response in Superconducting Cuprates*, Nature Communications **11**, 1793 (2020).

[28] S. Kovalev, T. Dong, L.-Y. Shi, C. Reinhoffer, T.-Q. Xu, H.-Z. Wang, Y. Wang, Z.-Z. Gan, S. Germanskiy, J.-C. Deinert, et al., *Band-Selective Third-Harmonic Generation in Superconducting MgB_2: Possible Evidence for the Higgs Amplitude Mode in the Dirty Limit*, Physical Review. B **104**, l140505 (2021).

[29] J. Lim, Y. S. Ang, L. K. Ang, and L. J. Wong, *Maximal Terahertz Emission in High Harmonic Generation from 3D Dirac Semimetals*, Communications Physics **4**, 235 (2021).

[30] W. Mao, A. Rubio, and S. A. Sato, *Terahertz-Induced High-Order Harmonic Generation and Nonlinear Charge Transport in Graphene*, Physical Review B **106**, 24313 (2022).

[31] M. Lewenstein, P. Balcou, M. Y. Ivanov, A. L'Huillier, and P. B. Corkum, *Theory of High-Harmonic Generation by Low-Frequency Laser Fields*, Physical Review A **49**, 2117 (1994).

[32] D. Gabor, *Theory of Communication. Part 1: The Analysis of Information*, Journal of the Institution of Electrical Engineers - Part III: Radio and Communication Engineering **93**, 429 (1946).

[33] T. Max Born Emil Wolf, *Principles of Optics* (Cambridge University Press, 2019).

[34] R. M. A. Dantas, Z. Wang, P. Surówka, and T. Oka, *Nonperturbative Topological Current in Weyl and Dirac Semimetals in Laser Fields*, Physical Review. B **103**, L201105 (2021).

[35] P. Matus, R. M. A. Dantas, R. Moessner, and P. Surówka, *Skin Effect as a Probe of Transport Regimes in Weyl Semimetals*, PNAS **119**, (2022).

[36] Z. Wang, H. Weng, Q. Wu, X. Dai, and Z. Fang, *Three-Dimensional Dirac Semimetal and Quantum Transport in Cd_3As_2*, Physical Review B **88**, 125427 (2013).

[37] S. Borisenko, Q. Gibson, D. Evtushinsky, V. Zabolotnyy, B. Büchner, and R. J. Cava, *Experimental Realization of a Three-Dimensional Dirac Semimetal*, Physical Review Letters **113**, 27603 (2014).

[38] M. Neupane, S.-Y. Xu, R. Sankar, N. Alidoust, G. Bian, C. Liu, I. Belopolski, T.-R. Chang, H.-T. Jeng, H. Lin, et al., *Observation of a Three-Dimensional Topological Dirac Semimetal Phase in High-Mobility Cd_3As_2*, Nature Communications **5**, (2014).

[39] Z. K. Liu, J. Jiang, B. Zhou, Z. J. Wang, Y. Zhang, H. M. Weng, D. Prabhakaran, S.-K. Mo, H. Peng, P. Dudin, et al., *A Stable Three-Dimensional Topological Dirac Semimetal Cd_3As_2*, Nature Materials **13**, 677 (2014).

[40] Y. Liu, C. Zhang, X. Yuan, T. Lei, C. Wang, D. Di Sante, A. Narayan, L. He, S. Picozzi, S. Sanvito, et al., *Gate-Tunable Quantum Oscillations in Ambipolar Cd_3As_2 Thin Films*, NPG Asia Materials **7**, e221 (2015).

[41] J. Hebling, G. Almasi, I. Kozma, and J. Kuhl, *Velocity Matching by Pulse Front Tilting for Large Area THz-pulse Generation*, Optics Express **10**, 1161 (2002).

[42] H. Hirori, A. Doi, F. Blanchard, and K. Tanaka, *Single-Cycle Terahertz Pulses with Amplitudes Exceeding 1 MV/cm Generated by Optical Rectification in $LiNbO_3$*, Applied Physics Letters **98**, 91106 (2011).

Chapter V
Terahertz second harmonic generation by transient thermoelectric currents in centrosymmetric Cd_3As_2

1. Introduction

Over 60 years ago, the phenomenon of nonlinear frequency conversion was first observed through second harmonic generation (SHG) of visible light in crystalline quartz [1]. Since then, nonlinear frequency conversion experiments have become versatile tools to study a variety of physical phenomena, including phase transitions [2–5], molecular aggregation structures [6,7], particle adsorption on interfaces and surfaces [8–10], and much more. These techniques rely on the symmetry properties of the material, which impose selection rules on the generated harmonics. For instance, even-order harmonic generation is only allowed in materials lacking inversion symmetry [11]. Moreover, the efficiency of nonlinear processes is strongly dependent on the intensity of the laser source. Whereas in the optical and mid-infrared range modern laser sources have provided access to non-linear spectroscopies for decades, allowing detection of harmonics as high as the tenth order [12], terahertz (THz) range harmonic generation in the time domain arose more recently [13–17].

The THz range can loosely be defined as the low photon energy spectrum between 1 and 100 meV (0.24-24 THz), covering a plethora of, often collective, eigenmode excitations in materials. These include magnons in magnetic systems [18], amplitude or phase modes in charge density wave materials [19], Goldstone and Higgs modes in superconductors [20], and phonon modes. In non-centrosymmetric systems, in which the bulk crystal symmetry allows for SHG, examples of THz-second harmonic generation (THz-SHG) are readily found, e.g. [13,21,22]. Not surprisingly, THz-SHG in centrosymmetric materials is relatively rare since this requires an additional symmetry breaking such as for instance an interface between two media which lead to surface second harmonic generation [23] or special symmetry breaking realized in the metamaterial structures [24]. Two examples of THz-SHG making use of centrosymmetric media are the observation of SHG from the topological insulator Bi_2Se_3 attributed to the presence of Dirac surface states [25], and non-stationary THz-SHG generation originating from a strongly perturbed superconducting state in Nb_3Sn [26].

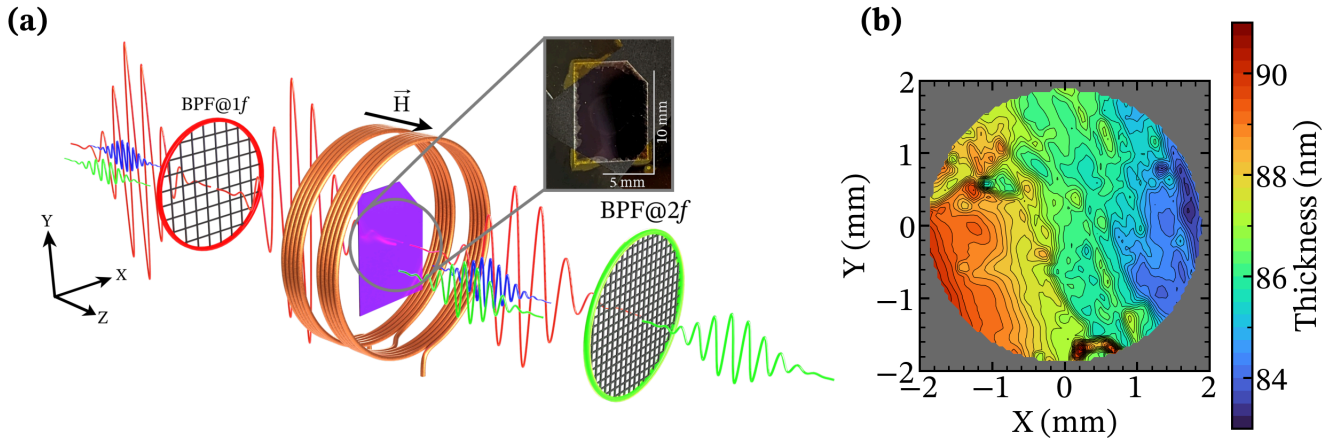

Figure 1: **(a)** Sketch of the experimental setup for THz-SHG. A quarter wave plate (not shown) is used to control the incoming THz polarization. Inset: a photo of the Cd_3As_2 thin film in an optical holder. **(b)** Optical absorption derived thickness map of the thin film used in the THz-SHG experiments.

Optical rectification is complementary to SHG, obeying the same symmetry rules. A variety of effects have been reported to contribute to rectification processes, including photogalvanic [25], spin-galvanic [27], photo-Dember [28], photon-drag [29], and Seebeck effects [21,30,31]. Their contribution are strongly affected by the experimental configuration and specific transport properties. The photon-drag effect is most pronounced for an oblique incidence geometry. The spin-galvanic effect requires an unequal spin distribution in a material, while the photogalvanic and photo-Dember effects rely on a significant differences in population and mobility of the different types of charge carriers, respectively.

The Dirac semimetal Cd_3As_2 has attracted a lot of an attention over the past years owing to the presence of a bulk Dirac cone making it a 3D analog of graphene [32]. The material demonstrates efficient odd high harmonic generation at terahertz frequencies, which origin lies in the linear dispersion of the Dirac cone [15]. Since the material is centrosymmetric one does not expect rectification or even-order harmonic generation in the bulk. Nevertheless, non-linear rectification in a thin Cd_3As_2 film has been observed in a recent experiment where near-infrared excitation led to THz emission through nonlinear current generation [31]. Since the material has relatively large Seebeck and Nernst coefficients [33], this observation has been interpreted to result from strong thermoelectric effects combined with thickness variations of the thin film.

The presence of optical rectification strongly suggests that other second order nonlinear effects, like terahertz even-harmonic generation, can in principle be expected under similar experimental conditions.

This paper reports on the experimental observation of terahertz second harmonic generation (THz-SHG) in a thin film of centrosymmetric Cd_3As_2. The role of thermoelectric and thermomagnetic contributions to the THz-SHG are investigated using THz pump fluence, polarization, and external magnetic field dependent experiments. The second harmonic generation in the absence of an external magnetic field is attributed to the thermoelectric Seebeck effect. The presence of a magnetic field gives rise to a thermomagnetic contribution known as the Nernst effect. Moreover, by utilizing electro-optical sampling to resolve the THz pulse waveform, the phase information of the THz-SHG response is extracted, shedding light on the distinct contributions to the THz-SHG response. The extracted SHG amplitude is found to be in a good agreement with a phenomenological model which accounts for contributions from the Seebeck, Nernst, and Hall effects. The findings are pivotal for the further development of thermoelectric and thermomagnetic THz harmonic generation as well as for the potential to use THz-SHG as a symmetry probe.

2. Second harmonic generation in centrosymmetric Cd_3As_2

THz-SHG experiments on Cd_3As_2 have been conducted at the TELBE facility (Helmholtz-Zentrum Dresden-Rossendorf), using an undulator radiation with a fundamental frequency of 0.7 THz, a repetition rate of 50 kHz, and a pulse energy of about 1.1 μJ, as THz pump [34]. A sketch of the experimental setup is shown in Figure 1(a). The well-established electro-optical sampling technique using a ZnTe crystal [35] was used for detection of the terahertz radiation. Since the undulator source radiates THz waves not only at the fundamental frequency but also at higher harmonic frequencies, the THz spectrum was cleaned from parasitic high-frequency components using a pair of bandpass filters (BPF@1f) with a central frequency of 0.7 THz placed before the sample. A second pair of 1.4 THz bandpass filters was placed after the sample (BPF@2f) to reduce contributions from the fundamental frequency and the third harmonic (THG) at 2.1 THz, which is efficiently produced by the sample [15].

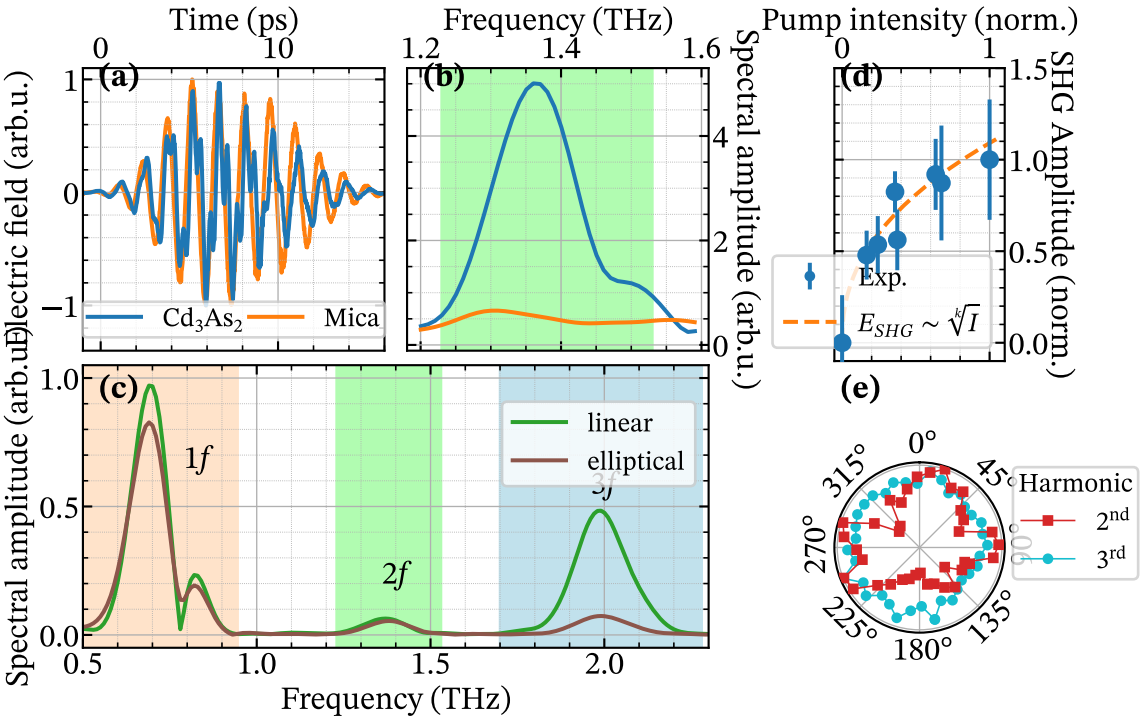

Figure 2: **(a)** Terahertz waveform measured from Cd_3As_2 thin film and its substrate mica. **(b)** Corresponding Fourier spectra in a vicinity of the second harmonic frequency of the pump pulse. **(c)** The Fourier spectra for two different pump polarization states. The THG peak is red shifted due to the transfer function of the BPF@2f. **(d)** The experimental fluence dependence of the SHG (dots) and sublinear fit corresponding to nonpertubative SHG with $k = 2.3 \pm 0.6$. **(e)** The measured angular dependence of the y component of the SHG and THG amplitudes. The angles correspond to the rotation of the sample around the z direction and relative to the y axis.

The sample used in this work is a molecular beam epitaxy grown 90 nm thick thin film of Cd_3As_2 on a mica substrate, with the growth direction along $\langle 112 \rangle$. Since the sample has thickness variations, which turn out to be crucial for the THz-SHG experiments, the thin film has been characterized using optical absorption microscopy employing a CW-laser source (473 nm, see Supplementary information for more details), yielding the thickness variation map shown in Figure 1(b). More details on sample properties are provided in [15,36,37].

Figure 2(a) presents a typical THz response from the Cd_3As_2 thin film (blue curve) using a linearly polarized THz pump, together with the response from a mica substrate (orange curve) under the same conditions. A higher frequency component in the THz waveform of the film is clearly discerned, while it is absent for the mica substrate. The Fourier transforms of the waveforms shown in Figure 2(a), show a pronounced second harmonic peak around 1.38 THz for Cd_3As_2 and, as expected, the absence of any signal near this frequency region for the pure mica substrate, see Figure 2(b). Changing the

polarization state from linear to elliptical with an ellipticity of 0.77 affects the nonlinear THz response, as illustrated in Figure 2(c). The peaks labeled 1*f* and 3*f* are due to imperfect suppression of the THz pump at the fundamental frequency by the BPF@1f and the sample generated third harmonic by the BPF@2f filters, respectively. Whereas amplitude of the THG peak decreases by approximately five times upon changing from linear to elliptical polarization, consistent with previous observations [37], the amplitude of the second harmonic does not show change within measurement tolerance. This strongly suggests that the underlying mechanism of the second harmonic generation significantly differs from the Dirac-cone electron-dynamics driven third harmonic generation in Cd_3As_2 [15].

To obtain a further insight into the origin of the SHG generation process, fluence dependence measurements have been conducted, see Figure 2(d). Surprisingly, the fluence dependence is not well described by the usual linear scaling $E_{\mathrm{SHG}} \propto I$ expected for a perturbative mechanism. The fluence dependence is best described by an unusual sublinear power law behaviour $E_{\mathrm{SHG}} \propto \sqrt[k]{I}$, with $k = 2.3 \pm 0.6$, indicating that a non-perturbative mechanism is responsible for the THz-SHG.

Finally Figure 2(e) shows the SHG and THG signals as a function of sample rotation. As observed before, the THG exhibits an isotropic behaviour [15]. In contrast, the SHG demonstrates a clear asymmetry, which is not directly related to the crystal symmetry. As will be discussed later, the observed SHG asymmetry originates from the fact that in the experiment there is an offset between the rotation axis and the THz pump focusing point leading to a probing of different sample areas with varying thickness gradients upon rotation.

3. Theoretical description of SHG in centrosymmetric materials

In order to provide a qualitative description of the observed second harmonic generation process, a theory based on the photo-Seebeck effect is employed. This effect arises from a photoinduced temperature gradient in the sample $\vec{\nabla}T$, which leads to the generation of a current given by $\vec{J} = -\hat{\sigma}\hat{S}\vec{\nabla}T$, where $\hat{\sigma}$ and $\hat{S}$ are corresponding conductivity and Seebeck tensors, respectively. The coordinate system utilized in the analysis is illustrated in the sketch presented in Figure 1(a). Tetragonal crystal lattice of Cd_3As_2 [32] with $\langle 112 \rangle$ crystal plane can be treated as cubic leading to isotropic in-plane behaviour of $\sigma = \sigma_{xx} = \sigma_{yy}$. This is also consistent with the absence of angular dependence in THz pump absorption (see Supplementary information). Next, theory assumes that the part of the absorbed photo energy of the pump beam $\mathcal{E}_{abs}$ changes electronic subsystem energy by $\Delta\mathcal{E}_{el} = \mathcal{E}_{abs}$.

The penetration depth at terahertz frequencies is significantly larger than the sample thickness $d(x,y)$, therefore the absorbed energy at position (x,y) and at a given time t can be calculated through the Beer–Lambert law:

$$\mathcal{E}_{abs}(x,y,t) \propto I(x,y,t)\big(1-e^{-\alpha d(x,y)}\big), \tag{1}$$

where $I(x,y,t)$ represents the intensity of the incoming light and α is the absorption coefficient. For the Cd_3As_2 thin film absorption coefficient at fundamental frequency 0.7 THz is estimated $\alpha \approx 9000\,\mathrm{cm}^{-1}$ [38,39]. The change in the electron energy can be expressed as $\Delta\mathcal{E}_{el} = \int_{T_i}^{T} c(T')dT'$, where $c(T')$ denotes the specific heat of the electrons, T_i and T represent the electron temperature in the steady and perturbed states, respectively. The specific heat can be modeled as $c(T) = \gamma_n T^n$, where $n = 1$ corresponds to a typical metal with a quadratic dispersion and $n = 3$ corresponds to a material with a linear dispersion and the Fermi level close to the Dirac point [40]. From this, the perturbed electronic temperature can be derived as

$$T(x,y,t) = T_i \sqrt[n+1]{1+(n+1)\frac{\mathcal{E}_{abs}(x,y,t)}{\mathcal{E}_{el}(T_i)}}, \tag{2}$$

where $\mathcal{E}_{el}(T_i)$ represents the energy of the electron subsystem in the steady state. A detailed derivation is provided in the Supplementary information.

To simplify calculation of temperature gradients, two limiting regimes in equation (2) are considered: the pertubative regime $\mathcal{E}_{abs} \ll \mathcal{E}_{el}(T_i)$, and the nonperturbative regime $\mathcal{E}_{abs} \gg \mathcal{E}_{el}(T_i)$.

In the pertubative regime, the electron temperature changes only slightly from its steady state:

$$\frac{\partial}{\partial x_i}T \approx \frac{T_i}{\mathcal{E}_{el}(T_i)}\frac{\partial}{\partial x_i}\mathcal{E}_{abs} + O\left(\frac{\mathcal{E}_{abs}}{\mathcal{E}_{el}(T_i)}\right)^2, \tag{3}$$

while in the nonperturbative one, the temperature is primarily determined by the absorbed energy:

$$\frac{\partial}{\partial x_i}T \approx \frac{\sqrt[n+1]{(n+1)\frac{\mathcal{E}_{abs}}{\gamma_n}}}{(n+1)\mathcal{E}_{abs}}\frac{\partial}{\partial x_i}\mathcal{E}_{abs}, \tag{4}$$

where $x_i = \{x,y\}$ and the gradient of the absorbed photoenergy is given by

$$\frac{\partial}{\partial x_i}\mathcal{E}_{abs}(x,y,t) \propto \frac{\partial I(x,y,t)}{\partial x_i}\left(1-e^{-\alpha d(x,y)}\right)$$

$$+I(x,y,t)e^{-\alpha d(x,y)}\frac{\partial d(x,y)}{\partial x_i} \qquad (5)$$

The first term in equation (5) accounts for the inhomogeneous pump profile, while the second term represents the contribution from the film thickness gradient. If no thickness gradient is present, the generation of a nonzero thermoelectric current is anticipated if the pump beam is incident near the edges of the sample, as demonstrated in [30] or when intensity profile does not show polar symmetry. Both terms are strongly dependent on absorption. In the case of weak absorption, the first term will be canceled out, whereas in the opposite case the second term approaches zero.

By considering a monochromatic light source, where $I(x,y,t) = I_0 g(x,y)\cos^2\omega t$ with frequency ω, intensity I_0 and a spatial profile $g(x,y)$, and substituting equation (5) into (3) and (4) one finds for the weak and strong pump cases:

$$\frac{\partial}{\partial x_i}T(t) \propto I_0\cos^2\omega t, \qquad (6)$$

$$\frac{\partial}{\partial x_i}T(t) \propto \sqrt[n+1]{I_0\cos^2\omega t}. \qquad (7)$$

In both limit cases, the current induced by the temperature gradient has two components: a rectified DC component and a periodic component at 2ω. The former is not observable in free space emission experiments, while the latter emits THz radiation $\vec{E} \propto \frac{\partial}{\partial t}\vec{J}(t)$ at double the pump frequency. The dependence of efficiency of this second harmonic generation on the pump intensity depends crucial on the value of n. A fit to the experimental data yields a value of $n = 1.3 \pm 0.6$. This implies that the specific heat is nearly linear in temperature, which originates from the relatively high Fermi level $\sim$ 120 meV of the material [15] (see Supplementary information).

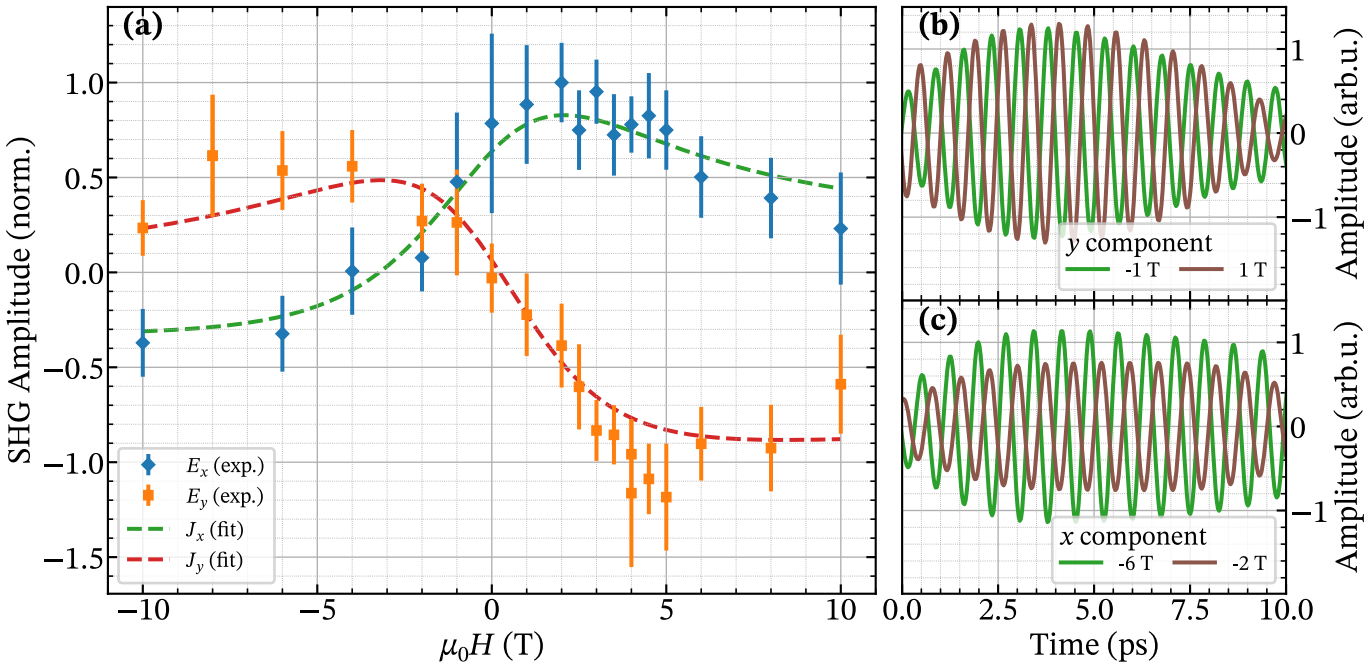

Figure 3: **(a)** The experimentally measured Fourier amplitudes of the *x*- and *y*- components of the SHG after phase unwrapping. Dotted lines present the fits plotted according to equations (9). **(b-c)** The digitally filtered waveform of the *y*- and *x*- components of measured SHG signal close to the phase flip field.

4. Magnetic field dependence

Naturally, it is anticipated that the application of an external magnetic field will alter the direction of the THz induced current through the Hall and Nernst effects, influencing the polarization state of emitted THz electric field. Furthermore, if the magnetic field applied along the *z*-axis $\vec{B} = (0, 0, B_z)$, it affects only the currents in the *xy*-plane. Hence, writing Ohm's law with thermoelectric and thermomagnetic contributions, one obtains [41]

$$\vec{E} = \sigma^{-1}\vec{J} + R_H\left[\vec{B} \times \vec{J}\right] + S\vec{\nabla}T + N\left[\vec{B} \times \vec{\nabla}T\right], \tag{8}$$

where $\vec{E}$ denotes the electric field present within the sample, $\vec{J}$ is the induced current, and $R_H, S,$ and N are the Hall, Seebeck, and Nernst coefficients, respectively. Noting that the THz pump beam is considerably smaller than the lateral dimension of the sample, no built-in electric field can be formed from charge accumulation at boundaries. Since there is no external field at second harmonic frequency, the left side in equation (8) becomes $\vec{E} = 0$. With this condition, the $J_{x,y}$-projections of the current can be derived, with the calculation details provided in the Supplementary information:

$$J_x = -\sigma\left(\frac{S+\mu N B_z^2}{1+(\mu B_z)^2}\nabla_x T + \frac{(S/\mu - N)B_z}{1+(\mu B_z)^2}\nabla_y T + S^a_{xy}(B)\nabla_y T\right) \tag{9.1}$$

$$J_y = -\sigma\left(\frac{S+\mu N B_z^2}{1+(\mu B_z)^2}\nabla_y T - \frac{(S/\mu - N)B_z}{1+(\mu B_z)^2}\nabla_x T + S^a_{xy}(B)\nabla_x T\right) \tag{9.2}$$

where $\mu = \sigma R_H$ represents the charge carrier mobility. In the presence of the magnetic field, the Dirac cone in Cd_3As_2 can split into a pair of the Weyl nodes, thereby creating nonzero Berry curvature in the material [42]. This leads to additional contribution to thermoelectric properties of the Dirac material [43]. In Cd_3As_2, it leads to the anomalous Nernst effect, which was previously observed and described in [44]. The anomalous Nernst effect is phenomenologically added to equations 9.1 and 9.2 as the off-diagonal term $S^a_{xy}(B) = S^a \tanh(B_z/B_0)$, where S^a represents the amplitude of the effect, and B_0 is a critical field.

To test the theoretical model, two polarization components of the emitted current were measured while varying the external magnetic field. The experiment reveals, that in the absence of an applied magnetic field, mainly *x*-polarized SHG observed, as shown in Figure 3(a). Applying the external magnetic field affects the x and y-components of the current differently as follows from equations (9). It leads to the emergence of the *y*-component, which undergoes a sign change in vicinity of zero applied field. This phase flip is demonstrated by the time domain waveforms of the digitally filtered SHG responses at ± 1 T, as shown in Figure 3(b). The *x*-component exhibits a strong asymmetry and is nearly zero when the external magnetic field reaches -3 T. This field also corresponds to a phase flip, as shown in Figure 3(c).

The presence of the phase flip was taken into account for plotting and fitting the *x* and *y* components of SHG response presented in Figure 3(c). By conducting a simultaneous fit for both polarization components, a good agreement with the experimental data is observed, providing compelling evidence that the second harmonic generation in Cd_3As_2 indeed arises from thermoelectric and thermomagnetic effects. It is worth noting that despite the presence of a large number of variables in equations (9), the absolute values of mobility $\mu \approx 2300\,\mathrm{cm^2/(V{\cdot}s)}$ and the critical field $B_0 \approx 2.6\mathrm{T}$; are extracted matching the order of magnitude as the previously reported data in [44,45]. Despite being impossible to extract absolute values of S, N and S^a due to unknown multiplier between generated thermoelectric current J and detected terahertz field E_{SHG}, it is possible to use ratio of these values to compare contributions to generated current of the anomalous and ordinary Nernst effects $S^a_{xy}(B)/S_{xy}(B)\big|_{B\to 0} = 0.76$ (see Supplementary informa-

tion). Significant contribution of the anomalous Nernst effect explains asymmetry of obtained currents and shows importance of the effect for the process of second harmonic generation.

5. Summary and Discussion

In summary, we have experimentally observed the generation of the second harmonic of the THz pump pulse in a film of Cd_3As_2, which has a centrosymmetric crystal structure. The presence of a film thickness gradient is attributed as the primary reason for breaking the inversion symmetry, thereby enabling the up-conversion process. The scaling of the second harmonic generation amplitude with the THz pump power and the angular dependence of the radiation pattern suggest that the SHG generation is induced by thermoelectric currents.

Furthermore, our phenomenological model implies that the generation process is non-perturbative and that the SHG polarization is determined by the direction of the film's thickness gradient. By applying an external magnetic field, the direction of the thermoelectric current is bent via the Nernst and Hall effects, thereby changing the polarization state of the SHG. The model, accounting for Seebeck, Nernst and Hall effects, demonstrates excellent agreement with the experimental data. This research highlights the importance of taking into account the thickness inhomogeneity of the thin film when considering the effects of nonlinear THz conversion.

The measured data that support the findings of this study are available in Zenodo database at https://zenodo.org/doi/10.5281/zenodo.12582038 [46]

6. Supplementary information

6.1. Optical absorption microscopy

To address spatial thickness variations of the Cd_3As_2 thin film, a continuous wave laser with a wavelength of 473 nm was used to measure the absorption. The wavelength was chosen within the visible frequency region to take advantage of Cd_3As_2 high optical absorption, thereby increasing sensitivity to thickness variations. The setup sketch can be found in Figure 4. A lens with a focal length of 50 mm was used to focus the beam onto the sample. The tight focal length facilitated the achievement of a beam spot size of approximately 30 μm, as measured by the knife-edge technique, see Figure 4(b). Based on this measurement, a step size of 50 μm was set for the translational XY-stage during surface scanning.

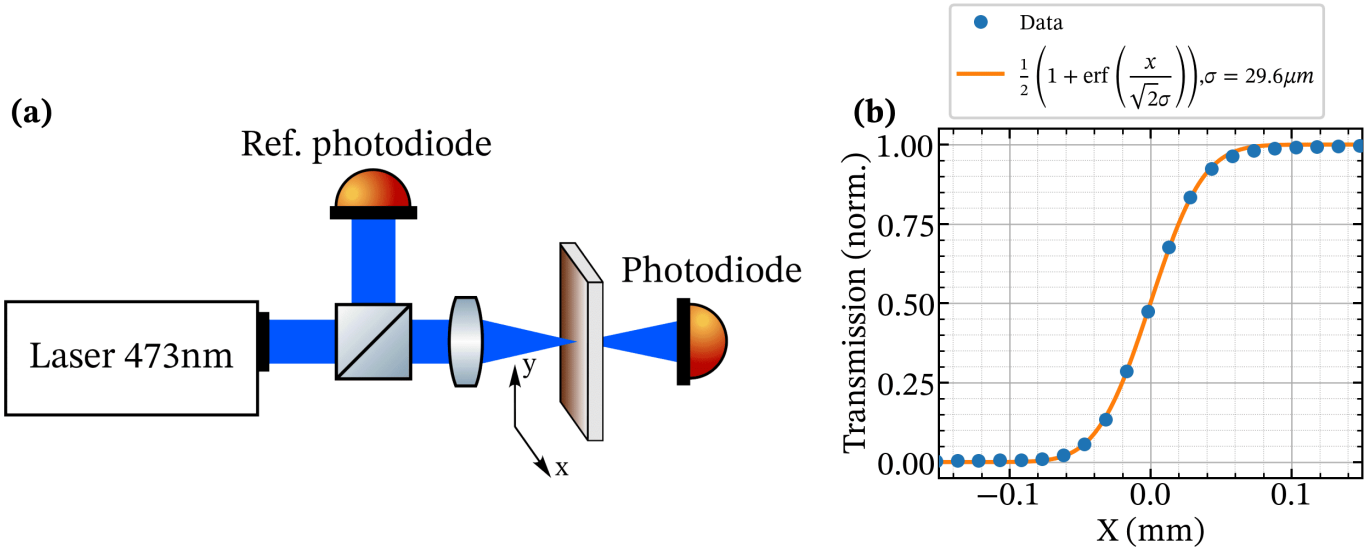

Figure S4: **(a)** A schematic representation of an optical absorption microscopy setup; **(b)** A knife-edge spot size measurement.

6.2. Angular dependence of second harmonic generation

Due to the gradient of absorbed energy in the material ($\vec{J} \sim \vec{\nabla}\mathcal{E}_{abs}$), the thermoelectric current associated with SHG follows this energy gradient. Consequently, the angular dependence of both the current and the emitted second harmonic aligns with the angular dependence of absorbed energy. The spot size of the THz pump on the sample is 1.6 mm, which is smaller than the sample dimensions. Furthermore, when the axis of rotation does not coincide with the pump $\vec{k}$ vector (as is the case in the experiment), different areas of the sample are irradiated at various angles, resulting in an angular dependence of absorbed photoenergy.

The polarization direction of the second harmonic depends on the orientation of the thermoelectric current. To simulate this behavior, the expected sample response has been computed for two thickness profiles, linear $d(x,y) = d_0 - \beta x$ and Gaussian $d(x,y) = d_0 e^{-\frac{x^2}{\sigma}}$, where β and σ are fixed parameters and d_0 is the maximum thickness. The simulation involved calculating the average thickness over the beam size $\langle d \rangle = \frac{\iint d(x,y)I(x,y)dxdy}{\iint I(x,y)dxdy}$ and using this value to estimate the transmission of the fundamental frequency through the sample ($\sim e^{-\alpha\langle d\rangle}$) and the intensity of the third harmonic ($\sim \langle d \rangle$). The simulation results, in comparison with the experimental data, are illustrated in Figure 5. In the case of a linear profile, a dipole-like response is evident, while the Gaussian profile exhibits clear asymmetry. Values dependent on thickness demonstrate nearly isotropic behavior for the fundamental and third harmonic response, consistent with the experimental data. Given that the actual thickness profile of the sample deviates significantly from the models employed, the experimental response at the second harmonic is more intricate and feature-rich.

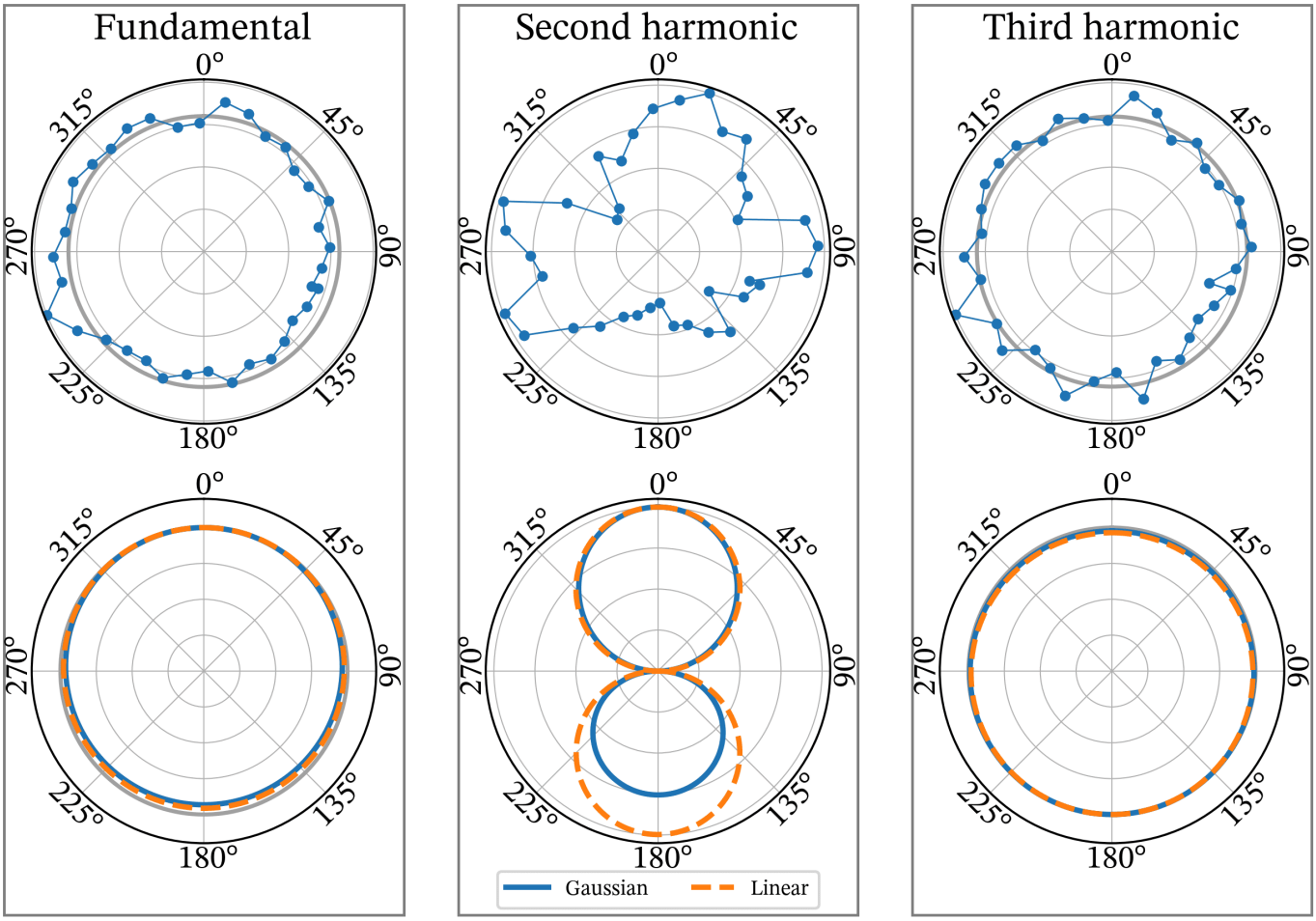

Figure S5: Experimental data (top) and simulation results (bottom) depicting angular dependence.

6.3. Derivation of expression for local temperature T_f

A detailed derivation for $T_f(x, y)$ is provided. The conservation of energy equation is the starting point, from which the electronic energy is expanded:

$$\mathcal{E}_{abs} = \mathcal{E}_{el} = \int_{T_i}^{T_f} c(T')dT' = \int_{T_i}^{T_f} \gamma_n T^{(\prime)^n} dT' = \frac{\gamma_n}{n+1}\left(T_f^{n+1} - T_i^{n+1}\right) \quad \text{S(10)}$$

And an expression for the final temperature is then obtained:

$$T_f = \sqrt[n+1]{T_i^{n+1} + \frac{n+1}{\gamma_n}\mathcal{E}_{abs}} = T_i \sqrt[n+1]{1 + (n+1)\frac{\mathcal{E}_{abs}}{\mathcal{E}_{el}(T_i)}}, \quad \text{S(11)}$$

where $\mathcal{E}_{el}(T_i) = c(T_i)T_i = \gamma_n T_i^{n+1}$ represents the initial energy of the electronic subsystem. In the perturbative regime $(\mathcal{E}_{abs}/\mathcal{E}_{el}(T_i) \ll 1)$,

the expansion $(1+x)^n\big|_{x\to 0} = 1 + nx + \frac{1}{2}n(n-1)x^2 + \ldots$ is used, which yields:

$$T_f = T_i\left(1 + \frac{\mathcal{E}_{abs}}{\mathcal{E}_{el}(T_i)} - \frac{1}{2}n\left(\frac{\mathcal{E}_{abs}}{\mathcal{E}_{el}(T_i)}\right)^2 + \ldots\right) \quad \text{S(12)}$$

Conversely, in the nonperturbative regime ($\mathcal{E}_{abs}/\mathcal{E}_{el}(T_i) \gg 1$), the term 1 under the root is disregarded:

$$T_f = T_i \sqrt[n+1]{(n+1)\frac{\mathcal{E}_{abs}}{\mathcal{E}_{el}(T_i)}} \quad \text{S(13)}$$

6.4. Specific heat of electrons in Cd_3As_2

Energy density $u(T)$ and specific heat $c_V(T)$ of electrons with linear dispersion in 3D solid can be numerically calculated according to formulas [40]:

$$u(T) = 12\frac{(k_B T)^4}{\pi^2\hbar^3 v_F^3} F_3\left(\frac{\mu}{k_B T}\right), \quad \text{S(14)}$$

$$\begin{aligned} c_V(T) &= \frac{\partial}{\partial T}u(T) = \\ &= 48\frac{k_B^4 T^3}{\pi^2\hbar^3 v_F^3} F_3\left(\frac{\mu}{k_B T}\right) - 12\mu\frac{k_B^3 T^2}{\pi^2\hbar^3 v_F^3} F_2\left(\frac{\mu}{k_B T}\right), \end{aligned} \quad \text{S(15)}$$

where k_B is a Boltzmann constant, $v_F = 7.8 \times 10^5$ m/s is a Fermi velocity, $\mu \approx 120$ meV, and $F_j(\eta) = \frac{1}{\Gamma(j+1)}\int_0^\infty dx \frac{x^j}{\exp(x-\eta)+1}$ is a Fermi-Dirac integral. Compared to equation in [40], there is an additional factor 2 added to account for the presence of 2 Dirac cones in the material [47]. Formula S(14) allows theoretically estimate maximal

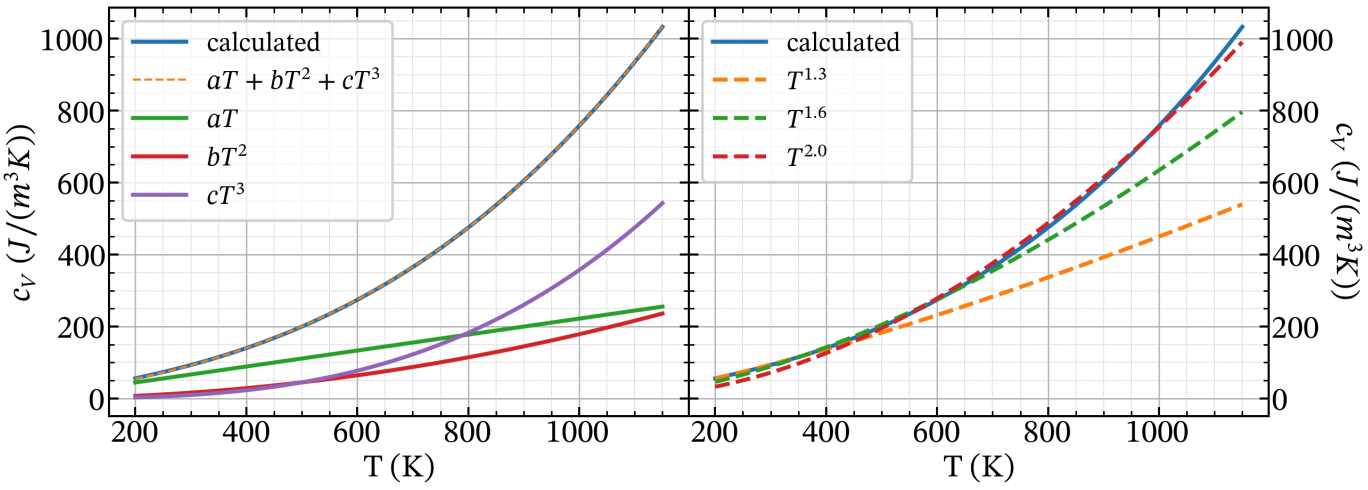

Figure S6: Specific heat $c_V(T)$ according to equation S(15) fitted with 3rd order polynom (left) and with different power dependences (right)

temperature T_f electrons can have after absorbing part of THz energy. For beam diameter ~ 1.6 mm and average thickenss of 85 nm, the estimated $T_f \approx 1100$K.

Figure 6 shows the calculated $c_V(T)$. In the left pane it is clearly seen, that despite being almost linear at room temperature (linear contribution $> 90\%$), the specific heat shows a clear nonlinear behavior at higher temperatures. The right pane demonstrates a fitting with various power laws $c_V(T) = \gamma_n T^n$. It is clear that an estimated value of $n = 1.3$ from fluence dependence in the main text describes specific heat's behavior only at temperatures up to 500K, meanwhile value $n = 2$ works up to maximal estimated temperature of 1100K.

6.5. Current in the presence of a magnetic field

To derive, how the thermoelectric current is affected by an external magnetic field, a modified Ohm's law is used:

$$\vec{E} = \rho\vec{J} + R_H\left[\vec{B}\times\vec{J}\right] + S\vec{\nabla}T + N\left[\vec{B}\times\vec{\nabla}T\right] \tag{S16}$$

with assumptions from the main text, the equation is rewritten to group all $\vec{J}$ terms on the left side:

$$\vec{J} + \sigma R_H\left[\vec{B}\times\vec{J}\right] = -\sigma S\vec{\nabla}T - \sigma N\left[\vec{B}\times\vec{\nabla}T\right]. \tag{S17}$$

In the experiment the magnetic field is aligned along the z axis, $\vec{B} = (0, 0, B_z)$, yielding $\left[\vec{B}\times\vec{J}\right] = (-J_y B_z, J_x B_z, 0)$ and $\left[\vec{B}\times\vec{\nabla}T\right] = \left(-\nabla_y T B_z, \nabla_x T B_z, 0\right)$. In matrx form equation S(17) reads

$$\begin{pmatrix} 1 & -\Sigma_H & 0 \\ \Sigma_H & 1 & 0 \\ 0 & 0 & 1 \end{pmatrix}\begin{pmatrix} J_x \\ J_y \\ J_z \end{pmatrix} = -\sigma\begin{pmatrix} S & -NB_z & 0 \\ NB_z & S & 0 \\ 0 & 0 & S \end{pmatrix}\begin{pmatrix} \nabla_x T \\ \nabla_y T \\ \nabla_z T \end{pmatrix}, \tag{S18}$$

with $\Sigma_H = \sigma R_H B_z$. This equation is easily solved using

$$\begin{pmatrix} 1 & -\Sigma_H & 0 \\ \Sigma_H & 1 & 0 \\ 0 & 0 & 1 \end{pmatrix}^{-1} = \frac{1}{\Sigma_H^2 + 1}\begin{pmatrix} 1 & \Sigma_H & 0 \\ -\Sigma_H & 1 & 0 \\ 0 & 0 & \Sigma_H^2 + 1 \end{pmatrix}, \tag{S19}$$

yielding:

$$\begin{pmatrix} J_x \\ J_y \\ J_z \end{pmatrix} = \begin{pmatrix} 1 & \Sigma_H & 0 \\ -\Sigma_H & 1 & 0 \\ 0 & 0 & \Sigma_H^2 + 1 \end{pmatrix}\begin{pmatrix} S & -NB_z & 0 \\ NB_z & S & 0 \\ 0 & 0 & S \end{pmatrix}\begin{pmatrix} \nabla_x T \\ \nabla_y T \\ \nabla_z T \end{pmatrix} \tag{S20}$$

As one can see, the z component is decoupled from x,y components, so only planar components need to be taken into account:

$$\begin{pmatrix} J_x \\ J_y \end{pmatrix} = -\frac{\sigma}{\Sigma_H^2+1}\begin{pmatrix} 1 & \Sigma_H \\ -\Sigma_H & 1 \end{pmatrix}\begin{pmatrix} S & -NB_z \\ NB_z & S \end{pmatrix}\begin{pmatrix} \nabla_x T \\ \nabla_y T \end{pmatrix} \tag{S(21)}$$

or

$$\begin{pmatrix} J_x \\ J_y \end{pmatrix} = -\frac{\sigma}{\Sigma_H^2+1}\begin{pmatrix} S+\Sigma_H NB_z & S\Sigma_H - NB_z \\ -S\Sigma_H + NB_z & S+\Sigma_H NB_z \end{pmatrix}\begin{pmatrix} \nabla_x T \\ \nabla_y T \end{pmatrix} \tag{S(22)}$$

The final result obtained by substituting back Σ_H and introducing the mobility $\mu = \sigma R_H$:

$$J_x = -\sigma\frac{S+\mu N B_z^2}{1+(\mu B_z)^2}\nabla_x T - \sigma\frac{(S\mu - N)B_z}{1+(\mu B_z)^2}\nabla_y T, \tag{S(23)}$$

$$J_y = -\sigma\frac{S+\mu N B_z^2}{1+(\mu B_z)^2}\nabla_y T + \sigma\frac{(S\mu - N)B_z}{1+(\mu B_z)^2}\nabla_x T. \tag{S(24)}$$

6.6. Anomalous Nernst effect contribution

To estimate the contribution of the anomalous Nernst effect, the equation for the x component of the current should be rewritten as follows:

$$J_x = -\sigma\big(S_{xx}(B)\nabla_x T + S_{xy}(B)\nabla_y T + S^a_{xy}(B)\nabla_y T\big), \tag{S(25)}$$

where $S_{xx}(B) = \frac{S+\mu N B_z^2}{1+(\mu B_z)^2}$, $S_{xy}(B) = (S\mu - N)\frac{B_z}{1+(\mu B_z)^2}$ represent the ordinary contributions, while $S^a_{xy}(B) = S^a \tanh(B_z/B_0)$ represents the anomalous part. To estimate, how a contribution of the anomalous Nernst effect comparable with ordinary one $S_{xy}(B)$, low B field limit ($\mu B \ll 1$, $B/B_0 \ll 1$) is used. This leads to:

$$\begin{aligned} S_{xy}(B)\big|_{B\to 0} &\approx (S\mu - N)B, \\ S^a_{xy}(B)\big|_{B\to 0} &\approx S^a B/B_0. \end{aligned} \tag{S(26)}$$

The contribution of the anomalous Nernst effect, according to the fit of the experimental data, is:

$$S^a_{xy}(B)/S_{xy}(B)\big|_{B\to 0} = \frac{S^a/B_0}{S\mu - N} = 0.76 \tag{S(27)}$$

7. Contributions

This chapter has been prepared for submission as manuscript:

> Germanskiy, S., Reinhoffer, C., Kovalev, S., Deinert, J.-C., Awari, N., Chen, M., Ilyakov, I., de Oliveira, T., Ponomaryov, A., Yang, Y., Xiu, F., Zhu, C., Pilch, P., Reinold, A., Mashkovich, E.A., van Loosdrecht, P.H.M.
> Terahertz second harmonic generation by transient thermoelectric currents in centrosymmetric Cd_3As_2.

P.H.M.L. and **S.G.** conceived project. S.K., J.-C.D., N.A., M.C., I.I., T.d.O., A.P. set up the experiment at TELBE; **S.G.** and C.R. performed experiments with C.Z., P.P. and A.R.; Y.Y. and F.X. fabricated and characterized the samples. **S.G.** developed theoretical model with help of E.A.M., C.R. and P.H.M.L.; **S.G.** and E.A.M. wrote the manuscript with contributions from C.R. and P.H.M.L.. All authors thoroughly discussed and commented on the manuscript.

8. References

[1] P. A. Franken, A. E. Hill, C. W. Peters, and G. Weinreich, *Generation of Optical Harmonics*, Physical Review Letters **7**, 118 (1961).

[2] M. Ayoub, J. Imbrock, and C. Denz, *Ferroelectric Domain Diagnostics near the Phase Transition by. Cerenkov Second-Harmonic Generation*, Optical Materials Express **7**, 3448 (2017).

[3] S. Soria, G. Marowsky, Y. G. Fokin, T. V. Murzina, and O. A. Aktsipetrov, *Second Harmonic Generation Studies of Phase Transitions in Ferroelectric Liquid Crystals*, Molecular Crystals and Liquid Crystals **375**, 755 (2002).

[4] J. E. Taylor, Z. Zhang, G. Cao, L. H. Haber, R. Jin, and E. W. Plummer, *Electronic Phase Transition of $IrTe_2$ Probed by Second Harmonic Generation*, Chinese Physics Letters **35**, 97102 (2018).

[5] J. Wang, K. Jin, H. Yao, J. Gu, X. Xu, C. Ge, C. Wang, M. He, and G. Yang, *Temperature-Dependent Phase Transition in Barium Titanate Crystals Probed by Second Harmonic Generation*, Applied Physics Letters **112**, 102904 (2018).

[6] G. J. Ashwell, P. Leeson, G. S. Bahra, and C. R. Brown, *Aggregation-Induced Second-Harmonic Generation*, Journal of the Optical Society of America B **15**, 484 (1998).

[7] K. Fujiwara, S. Wada, H. Monjushiro, and H. Watarai, *Ion-Association Aggregation of an Anionic Porphyrin at the Liquid/Liquid Interface Studied by Second Harmonic Generation Spectroscopy*, Langmuir **22**, 2482 (2006).

[8] W. Gan, G. Gonella, M. Zhang, and H.-L. Dai, *Communication: Reactions and Adsorption at the Surface of Silver Nanoparticles Probed by Second Harmonic Generation*, The Journal of Chemical Physics **134**, 41104 (2011).

[9] S. A. Mitchell, *Indole Adsorption to a Lipid Monolayer Studied by Optical Second Harmonic Generation*, The Journal of Physical Chemistry B **113**, 10693 (2009).

[10] J. S. Salafsky and K. B. Eisenthal, *Protein Adsorption at Interfaces Detected by Second Harmonic Generation*, The Journal of Physical Chemistry B **104**, 7752 (2000).

[11] Y. R. Shen, *The Principles of Nonlinear Optics*, Wiley classics library edition (Wiley-Interscience, Hoboken, N.J, 2003).

[12] E. Goulielmakis and T. Brabec, *High harmonic generation in condensed matter*, Nature Photonics **16**, 411 (2022).

[13] O. Schubert, M. Hohenleutner, F. Langer, B. Urbanek, C. Lange, U. Huttner, D. Golde, T. Meier, M. Kira, S. W. Koch, et al., *Sub-Cycle Control of Terahertz High-Harmonic Generation by Dynamical Bloch Oscillations*, Nature Photonics **8**, 119 (2014).

[14] H. A. Hafez, S. Kovalev, J.-C. Deinert, Z. Mics, B. Green, N. Awari, M. Chen, S. Germanskiy, U. Lehnert, J. Teichert, et al., *Extremely Efficient Terahertz High-Harmonic Generation in Graphene by Hot Dirac Fermions*, Nature **561**, 507 (2018).

[15] S. Kovalev, R. M. A. Dantas, S. Germanskiy, J.-C. Deinert, B. Green, I. Ilyakov, N. Awari, M. Chen, M. Bawatna, J. Ling, et al., *Non-Perturbative Terahertz High-Harmonic Generation in the Three-Dimensional Dirac Semimetal Cd_3As_2*, Nature Communications **11**, (2020).

[16] K. Lee, J. Park, B. J. Kang, W. T. Kim, H. Kim, S. Baek, K. J. Ahn, B. Min, and F. Rotermund, *Electrically Controllable Terahertz Second-Harmonic Generation in GaAs*, Advanced Optical Materials **8**, (2020).

[17] K.-J. Tielrooij, A. Principi, D. S. Reig, A. Block, S. Varghese, S. Schreyeck, K. Brunner, G. Karczewski, I. Ilyakov, O. Ponomaryov, et al., *Milliwatt Terahertz Harmonic Generation from Topological Insulator Metamaterials*, Light: Science & Applications **11**, 315 (2022).

[18] S. Baierl, J. H. Mentink, M. Hohenleutner, L. Braun, T.-M. Do, C. Lange, A. Sell, M. Fiebig, G. Woltersdorf, T. Kampfrath, et al., *Terahertz-Driven Nonlinear Spin Response of Antiferromagnetic Nickel Oxide*, Physical Review Letters **117**, 197201 (2016).

[19] M. Porer, U. Leierseder, J.-M. Ménard, H. Dachraoui, L. Mouchliadis, I. E. Perakis, U. Heinzmann, J. Demsar, K. Rossnagel, and R. Huber, *Non-thermal separation of electronic and structural orders in a persisting charge density wave*, Nature Materials **13**, 857 (2014).

[20] R. Shimano and N. Tsuji, *Higgs Mode in Superconductors*, Annual Review of Condensed Matter Physics **11**, 103 (2020).

[21] I. Ilyakov, A. Brataas, T. V. A. G. de Oliveira, A. Ponomaryov, J.-C. Deinert, O. Hellwig, J. Faßbender, J. Lindner, R. Salikhov, and S. Kovalev, *Efficient ultrafast field-driven spin current generation for spintronic terahertz frequency conversion*, Nature Communications **14**, (2023).

[22] A. Mayer and F. Keilmann, *Far-infrared nonlinear optics. I. $\chi^{(2)}$ near ionic resonance*, Physical Review B **33**, 6954 (1986).

[23] D. Guidotti and T. A. Driscoll, *Second-harmonic generation in centro-symmetric semiconductors*, Il Nuovo Cimento D **8**, 385 (1986).

[24] U. R. Meza, B. S. Mendoza, and W. L. Mochán, *Second-harmonic generation in nanostructured metamaterials*, Physical Review B **99**, 125408 (2019).

[25] J. Stensberg, X. Han, Z. Ni, X. Yao, X. Yuan, D. Mallick, A. Gandhi, S. Oh, and L. Wu, *Observation of terahertz second harmonic generation from Dirac surface states in the topological insulator Bi2Se3*, Physical Review B **109**, 245112 (2024).

[26] C. Vaswani, M. Mootz, C. Sundahl, D. H. Mudiyanselage, J. H. Kang, X. Yang, D. Cheng, C. Huang, R. H. J. Kim, Z. Liu, et al., *Terahertz Second-Harmonic Generation from Lightwave Acceleration of Symmetry-Breaking Nonlinear Supercurrents*, Physical Review Letters **124**, 207003 (2020).

[27] S. D. Ganichev, E. L. Ivchenko, V. V. Bel'kov, S. A. Tarasenko, M. Sollinger, D. Weiss, W. Wegscheider, and W. Prettl, *Spin-galvanic effect*, Nature **417**, 153 (2002).

[28] Y. Liu, C. Zhang, X. Yuan, T. Lei, C. Wang, D. Di Sante, A. Narayan, L. He, S. Picozzi, S. Sanvito, et al., *Gate-Tunable Quantum Oscillations in Ambipolar Cd_3As_2 Thin Films*, NPG Asia Materials **7**, e221 (2015).

[29] J. Maysonnave, S. Huppert, F. Wang, S. Maero, C. Berger, W. de Heer, T. B. Norris, L. A. D. Vaulchier, S. Dhillon, J. Tignon, et al., *Terahertz Generation by Dynamical Photon Drag Effect in Graphene Excited by Femtosecond Optical Pulses*, Nano Letters **14**, 5797 (2014).

[30] K. Takahashi, T. Kanno, A. Sakai, H. Tamaki, H. Kusada, and Y. Yamada, *Terahertz Radiation via Ultrafast Manipulation of Thermoelectric Conversion in Thermoelectric Thin Films*, Advanced Optical Materials **2**, 428 (2014).

[31] W. Lu, Z. Fan, Y. Yang, J. Ma, J. Lai, X. Song, X. Zhuo, Z. Xu, J. Liu, X. Hu, et al., *Ultrafast Photothermoelectric Effect in Dirac Semimetallic Cd_3As_2 Revealed by Terahertz Emission*, Nature Communications **13**, 1623 (2022).

[32] I. Crassee, R. Sankar, W.-L. Lee, A. Akrap, and M. Orlita, *3D Dirac Semimetal Cd_3As_2 : A Review of Material Properties*, Physical Review Materials **2**, (2018).

[33] Z. Jia, C. Li, X. Li, J. Shi, Z. Liao, D. Yu, and X. Wu, *Thermoelectric Signature of the Chiral Anomaly in Cd_3As_2*, Nature Communications **7**, 13013 (2016).

[34] B. Green, S. Kovalev, V. Asgekar, G. Geloni, U. Lehnert, T. Golz, M. Kuntzsch, C. Bauer, J. Hauser, J. Voigtlaender, et al., *High-Field High-Repetition-Rate Sources for the Coherent THz Control of Matter*, Scientific Reports **6**, (2016).

[35] Q. Wu and X.-C. Zhang, *Free-space electro-optic sampling of terahertz beams*, Applied Physics Letters **67**, 3523 (1995).

[36] Y. Liu, C. Zhang, X. Yuan, T. Lei, C. Wang, D. Di Sante, A. Narayan, L. He, S. Picozzi, S. Sanvito, et al., *Gate-Tunable Quantum Oscillations in Ambipolar Cd_3As_2 Thin Films*, NPG Asia Materials **7**, e221 (2015).

[37] S. Germanskiy, R. M. A. Dantas, S. Kovalev, C. Reinhoffer, E. A. Mashkovich, P. H. M. van Loosdrecht, Y. Yang, F. Xiu, P. Surówka, R. Moessner, et al., *Ellipticity Control of Terahertz High-Harmonic Generation in a Dirac Semimetal*, Physical Review B **106**, L81127 (2022).

[38] L. Hou, Y. Yang, A. Li, Q. Wang, Q. Li, M. Wu, P. Ji, Y. Zhang, Y. Xiao, W. Xu, et al., *Temperature-dependent terahertz properties of carriers and phonons in the topological Dirac semimetal Cd_3As_2*, Physical Review B **108**, 115416 (2023).

[39] Z. Dai, M. Manjappa, Y. Yang, T. C. W. Tan, B. Qiang, S. Han, L. J. Wong, F. Xiu, W. Liu, and R. Singh, *High Mobility 3D Dirac Semimetal (Cd_3As_2) for Ultrafast Photoactive Terahertz Photonics*, Advanced Functional Materials **31**, 2011011 (2021).

[40] J. Singhal and D. Jena, *Unified Ballistic Transport Relation for Anisotropic Dispersions and Generalized Dimensions*, Physical Review Research **2**, 43413 (2020).

[41] J. Sólyom, *Fundamentals of the Physics of Solids Volume 2: Electronic Properties* (Springer Berlin Heidelberg, 2009).

[42] E. V. Gorbar, V. A. Miransky, and I. A. Shovkovy, *Engineering Weyl Nodes in Dirac Semimetals by a Magnetic Field*, Physical Review B **88**, 165105 (2013).

[43] R. Lundgren, P. Laurell, and G. A. Fiete, *Thermoelectric Properties of Weyl and Dirac Semimetals*, Physical Review B **90**, 165115 (2014).

[44] T. Liang, J. Lin, Q. Gibson, T. Gao, M. Hirschberger, M. Liu, R. J. Cava, and N. P. Ong, *Anomalous Nernst Effect in the Dirac Semimetal Cd_3As_2*, Physical Review Letters **118**, 136601 (2017).

[45] M. Goyal, L. Galletti, S. Salmani-Rezaie, T. Schumann, D. A. Kealhofer, and S. Stemmer, *Thickness Dependence of the Quantum Hall Effect in Films of the Three-Dimensional Dirac Semimetal Cd_3As_2*, APL Materials **6**, 26105 (2018).

[46] S. Germanskiy, C. Reinhoffer, S. Kovalev, J.-C. Deinert, N. Awari, M. Chen, I. Ilyakov, T. V. A. G. De Oliveira, A. Ponomaryov, Y. Yang, et al., *Data for "Terahertz Second Harmonic Generation by Transient Thermoelectric Currents in Centrosymmetric Cd_3As_2"*, (2024).

[47] S. Borisenko, Q. Gibson, D. Evtushinsky, V. Zabolotnyy, B. Büchner, and R. J. Cava, *Experimental Realization of a Three-Dimensional Dirac Semimetal, Cd_3As_2*, Physical Review Letters **113**, (2014).

Chapter VI
Terahertz induced electro-optical Kerr effect in Cd_3As_2

1. Introduction

In previous chapters, it was discussed how Dirac fermions are driven into a nonlinear regime by intense terahertz (THz) pulses, leading to the ultrafast Seebeck effect. However, whether the material's symmetry can be modified and thus controlled remains an open question. Due to the presence of the Seebeck effect and the thickness variation in the sample, second-harmonic generation, as a possible probe for symmetry changes, proves unreliable for the sample, and other methods sensitive to induced symmetry changes are necessary. One such method is a THz pump–optical probe experiment, where a THz field excites the material and its response is probed by a separate optical beam. If the terahertz pump modifies the dielectric function of the material, this change will reflect as a modulation of the polarization of the optical probe.

Such modulation of the polarization can be understood in terms of nonlinear optics. Two major effects contribute to polarization changes: the Pockels effect and the electro-optical Kerr effect. The Pockels effect requires a non-zero second-order nonlinearity $\chi^{(2)}$ in the material and serves as the physical mechanism behind electro-optical sampling. Because centrosymmetric materials exhibit $\chi^{(2)} \equiv 0$, the Pockels effect in Cd_3As_2 should be prohibited, leaving only the Kerr effect. If the symmetry of Cd_3As_2 is broken by a strong THz field, this would be observed through the presence of the Pockels effect in addition to the electro-optical Kerr effect.

The Kerr effect is a higher-order nonlinear effect, relying on the $\chi^{(3)}$ tensor, which reflects the material's symmetry. This effect is allowed in many materials, and it has been shown that it can be driven by THz fields, as demonstrated in [1–3]. For example, in gases, molecules tend to align along the THz electric field, becoming anisotropic for a short period. Theoretically, a higher-order nonlinearity $\chi^{(5)}$ should also contribute to polarization changes; however, observing such contributions would require THz fields several orders of magnitude higher than those accessible in this work. Instead, an increase in the optical fluence of the probe could amplify this effect.

Surprisingly, no experimental reports were found in the literature regarding the electro-optical Kerr effect in 3D Dirac materials, with only a few reports available for

graphene[4,5]. There are theoretical works, however, in which nonlinear conductivities for Dirac/Weyl systems have been calculated[6,7]. This chapter aims to address this experimental gap by providing measurements of the THz-induced electro-optical Kerr effect in Cd_3As_2. Additionally, higher-order effects at increased probe power are studied and described.

2. Experimental setup

To observe the electro-optical Kerr effect, THz pump-optical probe measurements in Cd_3As_2 are performed, where the optical probe has an 800 nm wavelength. Induced changes in the probe polarization are monitored by simultaneously detecting Stokes parameters S_1 and S_2 (see Figure 1). The terahertz pump polarization is fixed by a polarizer along the $\boldsymbol{y}$ axis ($\vec{E}_{\mathrm{THz}} \parallel \boldsymbol{y}$). The sample orientation is kept fixed for all measurements; however, the in-plane orientation of the crystal is unknown.

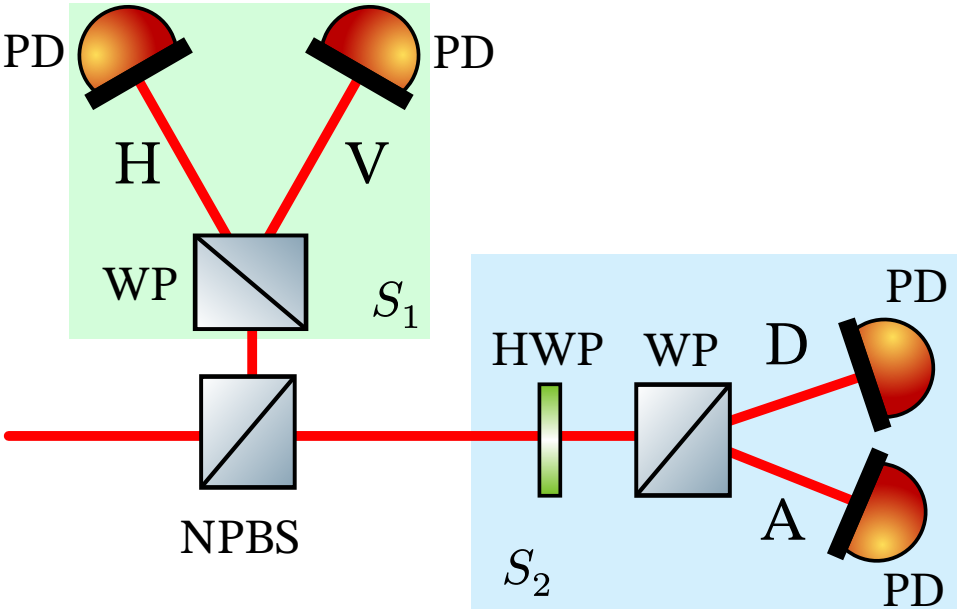

Figure 1: Setup for simultaneous detection of both S_1 and S_2 parameters. WP - Wollaston prism; NPBS - nonpolarizing beam splitter; HWP - half-wave plate; PD - photodiode; H, V, D, A - horizontal, vertical, diagonal, and antidiagonal components of the linear polarization.

The probe is linearly polarized, and its polarization plane is controlled by a half-wave plate. The probe beam is split using a *non-polarizing* beam splitter (*NPBS*) after the sample, and each part is detected individually. A pair of photodiodes (*PD*) is set to detect one of the two Stokes parameters, S_1 or S_2. Each pair uses a typical balanced detection scheme, where a Wollaston prism (*WP*) splits the beam into two orthogonal polarization components. For S_1 detection, these components are horizontal (*H*) and vertical (*V*), corresponding to the lab frame axes $\boldsymbol{x}$ and $\boldsymbol{y}$, respectively. To detect S_2, an additional

half-wave plate (*HWP*) is required to rotate the basis so that the diodes detect diagonal (D) and antidiagonal (A) polarization components after the *WP*.

The output of the diodes is fed into a data acquisition card capable of resolving individual laser pulses. THz pump pulses have a repetition rate half that of the optical probe pulses, allowing not only tracking of pump-induced changes but also measurement of the probe state without the pump. The latter helps in monitoring potential changes induced in the probe by the sample itself.

This approach for measuring Stokes parameters is chosen due to its integration simplicity within the existing setup and because it allows simultaneous measurement of three out of four Stokes parameters: S_0, S_1, and S_2. The S_0 Stokes parameter is obtained as the summed output of all four diodes used in detection. Consequently, the S_3 parameter can also be extracted as $|S_3| = \sqrt{S_0^2 - S_1^2 - S_2^2}$, although its sign information is lost. As it was discussed in Chapter I, the Stokes parameters are then used to calculate the polarization angle θ, ellipticity ξ, and probe intensity I following equations

$$\begin{aligned} \theta &= \frac{1}{2}\arctan\left(\frac{S_2}{S_1}\right), \\ \xi &= \tan\left(\frac{1}{2}\arcsin\left(\frac{S_3}{S_0}\right)\right). \end{aligned} \tag{1}$$

Since the polarization state is measured for each separate probe pulse, induced changes in polarization parameters are obtained by subtracting the values of the probe pulse with the pump from those of the probe pulse without the pump.

An example of measured changes in S_i is shown in Figure 2. The left side represents raw curves for ΔS_0, ΔS_1, ΔS_2, and the calculated ΔS_3. Without normalization to S_0, the remaining Stokes parameters partially follow the probe beam's intensity changes. Normalization to S_0 reveals the dynamics of the induced changes more clearly. This normalization naturally occurs in the calculation of θ and ξ. Calculated changes $\Delta\theta$, $\Delta\xi$, and $\Delta I/I$ are shown in Figure 3. Further details concerning the measured signals are discussed later.

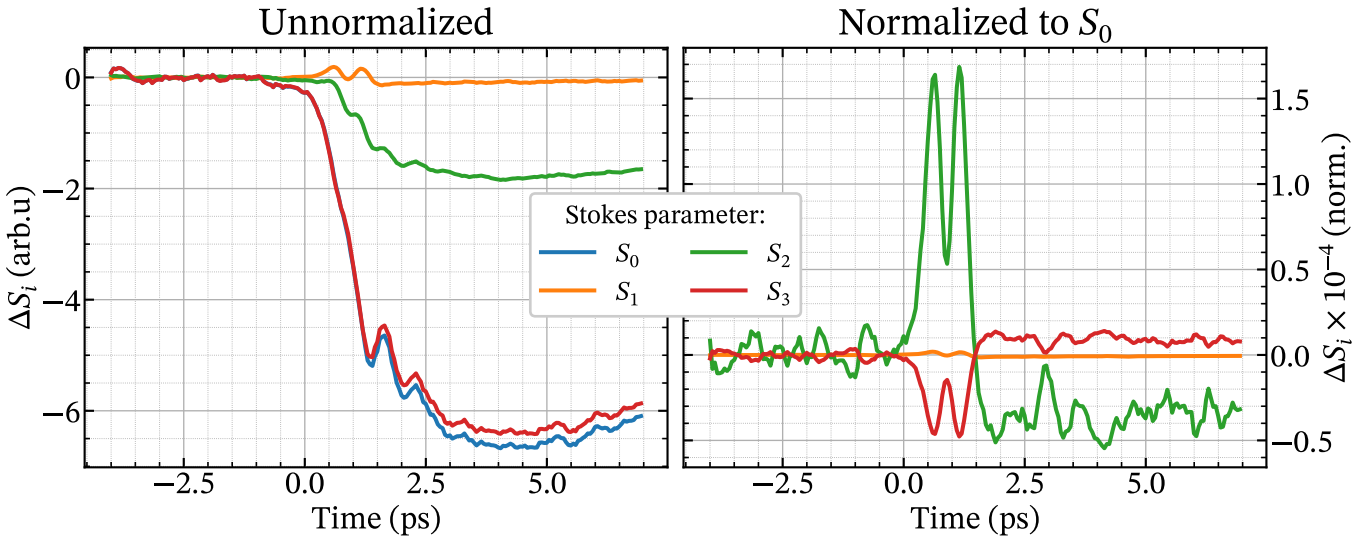

Figure 2: Induced changes in Stokes parameters ΔS_i without (left) and with (right) normalization to S_0.

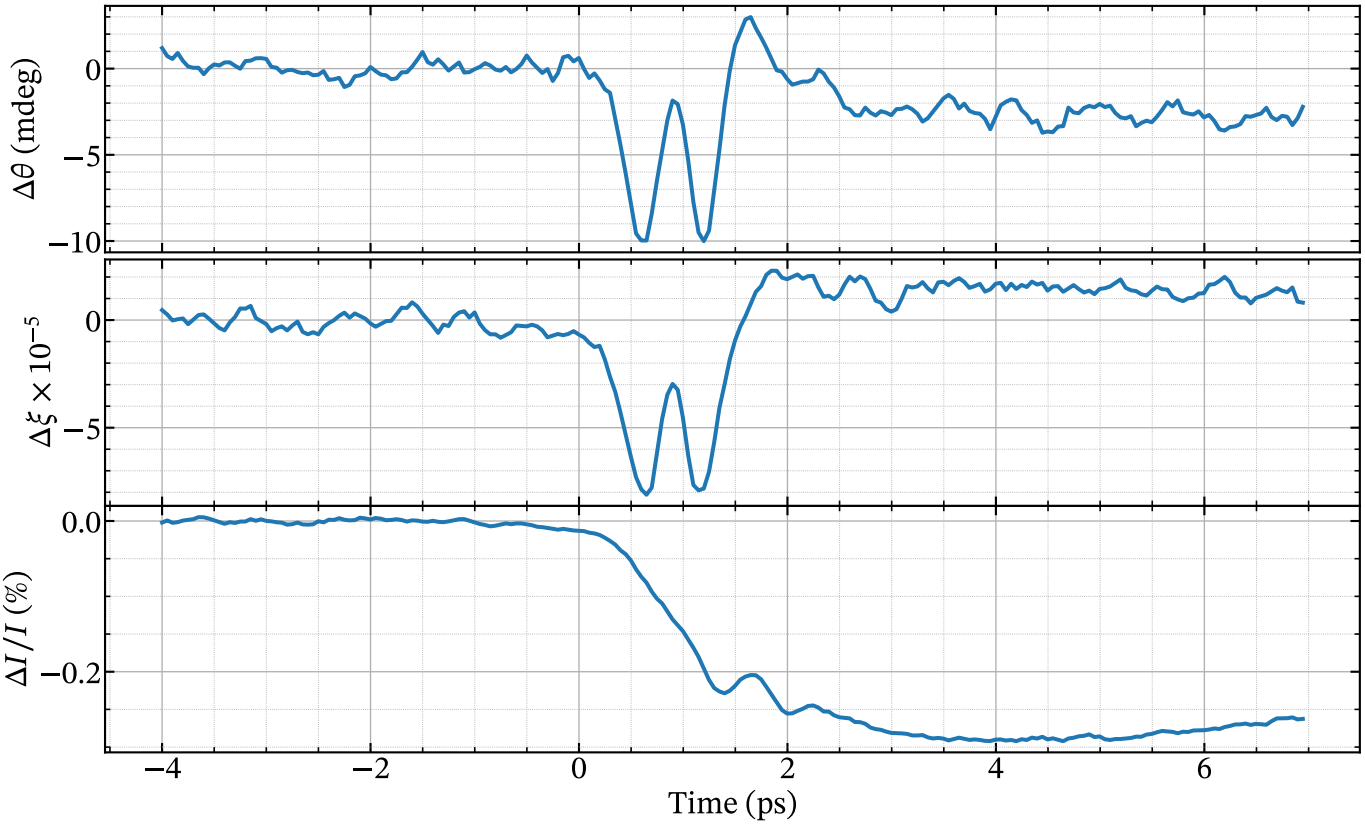

Figure 3: Extracted values of $\Delta\theta$, $\Delta\xi$, and $\Delta I/I$ from measurement.

These changes in the probe beam polarization reflect induced changes in the material. To link polarization changes with alterations in material properties, some theoretical derivations are required.

3. Theoretical description of the electro-optical Kerr effect

In this experiment, the THz field can be treated as a quasi-DC field compared to the optical probe beam, so the theory of the DC Kerr effect is applicable. However, because Cd_3As_2 has non-negligible absorption at the probe frequency, the absorption coefficient can also be modified by the pump field. The complex refractive index $\hat{n} = n' + in''$ of a material under a strong pump can be expressed as:

$$\hat{n} = \hat{n}^0 + \Delta\hat{n}\big(E_{\text{pump}}\big), \tag{2}$$

where $\hat{n}^0$ is the unperturbed complex refractive index, E_{pump} is the electric field of the pump pulse, and $\Delta\hat{n} = \Delta n' + i\Delta n''$ represents the induced complex change in the complex refractive index. This change is assumed to be small, with $\Delta n' \ll n'$ and $\Delta n'' \ll n''$. For simplicity, only the change caused by the THz pump will be taken into account. This induced change in the refractive index alters the polarization state of the probe beam, which is detected in the experiment.

The induced change in the dielectric function can be expressed in terms of nonlinear optics. The nonlinear polarization for such a process is:

$$P^{\text{NL}}(\omega) \sim \hat{\chi}^{(3)}(\omega = \omega + \Omega - \Omega; \Omega, \Omega, \omega)|E(\Omega)|^2 E(\omega) + ..., \tag{3}$$

where ω is a frequency of the probe and Ω is the frequency of the pump. The dots represent higher-order contributions. These contributions usually have the next order of smallness and are thus ignored. In experiments where $\Omega \ll \omega$, P^{NL} will include additional terms proportional to $\omega \pm 2\Omega$, unless contributions at frequencies ω and $\omega \pm 2\Omega$ can be spectrally separated.

Nonlinear contributions can be generalized and are marked as $\hat{\chi}^{\text{NL}}(E(\Omega))$, so:

$$P^{\text{NL}}(\omega) = \varepsilon_0 \hat{\chi}^{\text{NL}}(\omega; \Omega, E(\Omega))E(\omega). \tag{4}$$

In the most general case, χ^{NL} depends not only on the pump field but also on the probe field, sample temperature, applied pressure, etc. Moreover, the tensor nature of $\hat{\chi}^{\text{NL}}$ has to be taken into account to adequately describe the response.

To simplify derivations, the case of an isotropic material will be assumed. Such an assumption is valid for the sample of Cd_3As_2 used in this work, as it was discussed in Chapter V. To reflect experimental conditions, the presence of interfaces between the mica substrate and Cd_3As_2, as well as between Cd_3As_2 and air, will be taken into account. The coordinate frame is chosen to be a laboratory frame, with the z axis matching the

wavevector $\vec{k}$ of the probe beam. To match the experimental layout, normal incidence is considered.

As the material is assumed to be isotropic, the dielectric function in the absence of the pump can be written as:

$$\varepsilon_{ij} = 1 + \chi^0 = \varepsilon^0 \delta_{ij}, \tag{5}$$

where $i, j = \{x, y\}$. Induced nonlinear polarization contributes to the dielectric tensor:

$$\varepsilon_{ij} = 1 + \chi_{ij} = 1 + \chi^0 + \chi_{ij}^{\mathrm{NL}} = \varepsilon^0 \delta_{ij} + \chi_{ij}^{\mathrm{NL}}. \tag{6}$$

The refractive index then becomes:

$$\begin{aligned} n^2 = \varepsilon^0 + \frac{\chi_{xx}^{\mathrm{NL}} + \chi_{yy}^{\mathrm{NL}}}{2} \pm \frac{\sqrt{\left(\chi_{xx}^{\mathrm{NL}} - \chi_{yy}^{\mathrm{NL}}\right)^2 + 4\left(\chi_{xy}^{\mathrm{NL}}\right)^2}}{2} = \\ = \varepsilon^0 + \chi^{\mathrm{avg}} \pm \sqrt{\Delta\chi^2 + \left(\chi_{xy}^{\mathrm{NL}}\right)^2}, \end{aligned} \tag{7}$$

where $\chi^{\mathrm{avg}} = \frac{\chi_{xx}^{\mathrm{NL}} + \chi_{yy}^{\mathrm{NL}}}{2}$ and $\Delta\chi = \frac{\chi_{xx}^{\mathrm{NL}} - \chi_{yy}^{\mathrm{NL}}}{2}$.

By using (2) and ignoring second-order small terms Δn^2, one can write: $n^2 = n^{0^2} + 2n^0\Delta n$. Substituting this into the result above allows the induced change in the refractive index to be written as:

$$\Delta n_{\pm} = \frac{\chi^{\mathrm{avg}}}{2n^0} \pm \frac{\sqrt{\Delta\chi^2 + \left(\chi_{xy}^{\mathrm{NL}}\right)^2}}{2n^0}. \tag{8}$$

For future derivations, let's define the matrix ΔN as:

$$\Delta N = \begin{pmatrix} \Delta n_- & 0 \\ 0 & \Delta n_+ \end{pmatrix}. \tag{9}$$

Plane waves propagating along the z direction in the perturbed media can be written as:

$$\vec{E}(z) = E_- e^{i\frac{\omega}{c}(n^0 + \Delta n_-)z - i\omega t}\hat{\boldsymbol{e}}_- + E_+ e^{i\frac{\omega}{c}(n^0 + \Delta n_+)z - i\omega t}\hat{\boldsymbol{e}}_+, \tag{10}$$

where $\hat{\boldsymbol{e}}_{\pm}$ are the eigenvectors corresponding to the values of $n_{\pm} = n^0 \pm \Delta n_{\pm}$, and $E_{\pm}$ are the corresponding field amplitudes. In the laboratory basis $(\hat{\boldsymbol{x}}, \hat{\boldsymbol{y}})$, eigenvectors are:

$$\begin{aligned}\hat{\boldsymbol{e}}_- &= \frac{1}{\sqrt{K_+}}\hat{\boldsymbol{x}} \quad + \frac{1}{\sqrt{K_-}}\hat{\boldsymbol{y}},\\ \hat{\boldsymbol{e}}_+ &= -\frac{1}{\sqrt{K_-}}\hat{\boldsymbol{x}} + \frac{1}{\sqrt{K_+}}\hat{\boldsymbol{y}},\end{aligned} \tag{11}$$

where $\hat{\boldsymbol{x}}$ and $\hat{\boldsymbol{y}}$ are laboratory basis vectors, and $K_\pm$ are normalization constants such that $\hat{\boldsymbol{e}}_\pm = 1$:

$$K_\pm = 1 + \frac{\left(\Delta\chi \pm \sqrt{\Delta\chi^2 + \left(\chi_{xy}^{\mathrm{NL}}\right)^2}\right)^2}{\left(\chi_{xy}^{\mathrm{NL}}\right)^2}. \tag{12}$$

The transformation matrix T from the basis $(\hat{\boldsymbol{x}}, \hat{\boldsymbol{y}})$ to $(\hat{\boldsymbol{e}}_-, \hat{\boldsymbol{e}}_+)$ is:

$$T = \begin{pmatrix} \frac{1}{\sqrt{K_+}} & \frac{1}{\sqrt{K_-}} \\ -\frac{1}{\sqrt{K_-}} & \frac{1}{\sqrt{K_+}} \end{pmatrix}. \tag{13}$$

Propagation through the material can be represented as the matrix $P(z)$ in the basis $(\hat{\boldsymbol{e}}_-, \hat{\boldsymbol{e}}_+)$:

$$\vec{E}(z) = P(z)\vec{E}(0) = \begin{pmatrix} e^{i\frac{\omega}{c}(n^0+\Delta n_-)z} & 0 \\ 0 & e^{i\frac{\omega}{c}(n^0+\Delta n_+)z} \end{pmatrix}\vec{E}(0), \tag{14}$$

where $\vec{E}(0)$ is the initial probe's electric field. To determine how the polarization changes depend on the initial probe's polarization angle and its ellipticity, $\vec{E}(0)$ is defined as:

$$\vec{E}(0) = \frac{E_0}{\sqrt{2}}e^{-i\omega t}\begin{pmatrix} e^{i\psi}\cos\left(\theta+\frac{\pi}{4}\right) + e^{-i\psi}\sin\left(\theta+\frac{\pi}{4}\right) \\ e^{i\psi}\sin\left(\theta+\frac{\pi}{4}\right) - e^{-i\psi}\cos\left(\theta+\frac{\pi}{4}\right) \end{pmatrix} = \frac{1}{\sqrt{2}}\begin{pmatrix} E_x \\ E_y \end{pmatrix}, \tag{15}$$

where θ is the angle between the $\boldsymbol{x}$ lab axis and the main ellipse axis of the polarization ellipse, and ψ defines the ellipticity of the probe via $\tan(\psi) = \xi$.

Stokes parameters are well-defined in the lab frame, so it is convenient to transform $\vec{E}(z)$ back to the laboratory frame. At the same time, the transformation matrix allows the inclusion of Fresnel transmission matrices F in a diagonal form. In matrix form, this set of transformations is:

$$\vec{E}^{\text{lab}}(z) = T^{-1} F^{\text{out}} P(z) F^{\text{in}} T \vec{E}(0). \tag{16}$$

Fresnel matrices F describe interfaces mica $\rightarrow$ Cd_3As_2 (marked as *in*) and $Cd_3As_2 \rightarrow$ air (marked as *out*). Even though mica is birefringent, the difference between refractive indices in different directions is small compared to the refractive index itself $|n_e - n_o| \approx 5 \cdot 10^{-4}$[8], and thus mica will be assumed to be isotropic for calculations of Fresnel coefficients. With these assumptions, in the $(\hat{e}_-, \hat{e}_+)$ basis, the Fresnel matrix is:

$$F^j = \begin{pmatrix} t_-^j & 0 \\ 0 & t_+^j \end{pmatrix}, \tag{17}$$

where j is either *in* or *out* and $t_\pm^j$ is the corresponding transmission coefficient. For the interface mica$\rightarrow$$Cd_3As_2$, the perturbed transmission coefficient is:

$$t_\pm^{\text{in}} = \frac{2n_{\text{mica}}}{n_{\text{mica}} + n^0 + \Delta n_\pm} \approx t_0^{\text{in}} + \frac{\Delta n_\pm}{n_{\text{mica}} + n^0} t_0^{\text{in}}, \tag{18}$$

where $t_0^{\text{in}} = \frac{2n_{\text{mica}}}{n_{\text{mica}}+n^0}$ is the transmission coefficient without the pump.

For the $Cd_3As_2$$\rightarrow$air interface:

$$t_\pm^{\text{out}} = \frac{2(n^0 + \Delta n_\pm)}{1 + n^0 + \Delta n_\pm} \approx t_0^{\text{out}} + \frac{\Delta n_\pm}{n^0(n^0+1)} t_0^{\text{out}}, \tag{19}$$

where $t_0^{\text{out}} = \frac{2n^0}{n^0+1}$. As a result, the Fresnel transmission matrix can be expressed as:

$$F^j = t_0^k (I + \Delta F^j), \tag{20}$$

where $\Delta F^{\text{in}} = \frac{1}{n_{\text{mica}}+n^0} \Delta N$ and $\Delta F^{\text{out}} = \frac{1}{n^0(n^0+1)} \Delta N$.

The propagation matrix can be significantly simplified, with assumptions made for Δn in (2), by expanding the exponents into a series:

$$e^{i\frac{\omega}{c}(n^0+\Delta n)z} \approx e^{i\frac{\omega}{c}n^0 z}\left(1 + i\frac{\omega}{c}\Delta n z\right). \tag{21}$$

This yields:

$$P(z) \approx e^{i\frac{\omega}{c}n^0 z}\left(I + i\frac{\omega}{c} z \Delta N\right) = p^0(z)(I + \Delta P(z)), \tag{22}$$

where $p^0(z) = e^{i\frac{\omega}{c}n^0 z}$ corresponds to the accumulated phase in the absence of the pump. Dependence on z will not be explicitly written further to keep equations simpler but will be assumed.

By substituting (20) and (22) into (16), the induced change in the electric field vector in the lab frame can be found:

$$\vec{E} = T^{-1}t_0^{\text{out}}(I + \Delta F^{\text{out}})p^0(I + \Delta P)t_0^{\text{out}}(I + \Delta F^{\text{in}})T\vec{E}(0) = \vec{E}^0 + \Delta\vec{E}, \quad (23)$$

where:

$$\vec{E}^0 = t_0^{\text{out}}p^0 t_0^{\text{in}}\vec{E}(0) \quad (24)$$

and:

$$\begin{aligned}\Delta\vec{E} = T^{-1}t_0^{\text{out}}(\Delta F^{\text{out}} + \Delta P + \Delta F^{\text{in}})Tp^0 t_0^{\text{in}}\vec{E}(0) = \\ = t_0^{\text{out}}p^0 t_0^{\text{in}} f T^{-1}\Delta N T\vec{E}(0),\end{aligned} \quad (25)$$

where f is a material constant and is written as:

$$f = \frac{1}{n^0(n^0+1)} + i\frac{\omega}{c}z + \frac{1}{n_{\text{mica}} + n^0}. \quad (26)$$

For Cd_3As_2 terms in f are of the same order for the given material thickness of 80 nm and the 800 nm wavelength of the probe, so neither of them can be ignored.

The term $T^{-1}\Delta N T$ can be directly calculated and yields:

$$T^{-1}\Delta N T = \begin{pmatrix} \frac{\Delta n_-}{K_+} + \frac{\Delta n_+}{K_-} & \frac{\Delta n_- - \Delta n_+}{\sqrt{K_+K_-}} \\ \frac{\Delta n_- - \Delta n_+}{\sqrt{K_+K_-}} & \frac{\Delta n_-}{K_-} + \frac{\Delta n_+}{K_+} \end{pmatrix} = \begin{pmatrix} \Delta N_{xx} & \Delta N_{xy} \\ \Delta N_{xy} & \Delta N_{yy} \end{pmatrix}. \quad (27)$$

The induced change in the electric field is:

$$\Delta\vec{E} = f\begin{pmatrix} \Delta N_{xx} & \Delta N_{xy} \\ \Delta N_{xy} & \Delta N_{yy} \end{pmatrix} t_0^{\text{out}}p^0 t_0^{\text{in}}\vec{E}(0). \quad (28)$$

Knowledge of the induced change in the electric field allows the calculation of induced changes in the Stokes parameters. As the changes are small, all terms of second-order smallness are ignored. Recalling the equations for Stokes parameters:

$$
\begin{aligned}
S_0 &= |E_x|^2 + |E_y|^2 = |E_x^0|^2 + |E_y^0|^2 + 2\,\mathrm{Re}\big(E_x^{0*}\Delta E_x + E_y^{0*}\Delta E_y\big),\\
S_1 &= |E_x|^2 - |E_y|^2 = |E_x^0|^2 - |E_y^0|^2 + 2\,\mathrm{Re}\big(E_x^{0*}\Delta E_x - E_y^{0*}\Delta E_y\big),\\
S_2 &= 2\,\mathrm{Re}\big(E_x^* E_y\big) = 2\,\mathrm{Re}\big(E_x^{0*}E_y^0\big) + 2\,\mathrm{Re}\big(\Delta E_x^* E_y^0 + E_x^{0*}\Delta E_y\big),\\
S_3 &= 2\,\mathrm{Im}\big(E_x^* E_y\big) = 2\,\mathrm{Im}\big(E_x^{0*}E_y^0\big) + 2\,\mathrm{Im}\big(\Delta E_x^* E_y^0 + E_x^{0*}\Delta E_y\big).
\end{aligned}
\tag{29}
$$

All Stokes parameters can now be written as $S_i = S_i^0 + \Delta S_i$.

For the initial electric field $\vec{E}^0$, the Stokes parameters are:

$$
\begin{aligned}
S_0^0 &= \big|t_0^{\mathrm{out}} p^0 t_0^{\mathrm{in}}\big|^2 E_0^2,\\
S_1^0 &= \big|t_0^{\mathrm{out}} p^0 t_0^{\mathrm{in}}\big|^2 E_0^2 \cos(2\theta)\cos(2\psi),\\
S_2^0 &= \big|t_0^{\mathrm{out}} p^0 t_0^{\mathrm{in}}\big|^2 E_0^2 \sin(2\theta)\cos(2\psi),\\
S_3^0 &= \big|t_0^{\mathrm{out}} p^0 t_0^{\mathrm{in}}\big|^2 E_0^2 \sin(2\psi).
\end{aligned}
\tag{30}
$$

Induced changes in the Stokes parameters are:

$$
\begin{aligned}
\Delta S_0 = \big|t_0^{\mathrm{out}} p^0 t_0^{\mathrm{in}}\big|^2 E_0^2 \big(&\mathrm{Re}\big(f\big(\Delta N_{xx} + \Delta N_{yy}\big)\big)\cos(2\psi) +\\
&+\big(\mathrm{Re}\big(f\big(\Delta N_{xx} - \Delta N_{yy}\big)\big) - 2\,\mathrm{Im}\big(\Delta N_{xy}\big)\sin(2\psi)\big)\cos(2\theta) +\\
&+\big(2\,\mathrm{Re}\big(f\Delta N_{xy}\big) + \mathrm{Im}\big(f\big(\Delta N_{xx} - \Delta N_{yy}\big)\big)\sin(2\psi)\big)\sin(2\theta)\big),\\
\Delta S_1 = \big|t_0^{\mathrm{out}} p^0 t_0^{\mathrm{in}}\big|^2 E_0^2 \big(&\mathrm{Re}\big(f\big(\Delta N_{xx} + \Delta N_{yy}\big)\big)\cos(2\theta) +\\
&+\mathrm{Re}\big(f\big(\Delta N_{xx} - \Delta N_{yy}\big)\big)\cos(2\psi) +\\
&+\mathrm{Im}\big(f\big(\Delta N_{xx} + \Delta N_{yy}\big)\big)\sin(2\psi)\sin(2\theta)\big),\\
\Delta S_2 = \big|t_0^{\mathrm{out}} p^0 t_0^{\mathrm{in}}\big|^2 E_0^2 \big(&2\,\mathrm{Re}\big(f\Delta N_{xy}\big) + \mathrm{Im}\big(f\big(\Delta N_{xx} - \Delta N_{yy}\big)\big)\sin(2\psi) +\\
&+\mathrm{Re}\big(f\big(\Delta N_{xx} + \Delta N_{yy}\big)\big)\cos(2\psi)\sin(2\theta)\big),\\
\Delta S_3 = \big|t_0^{\mathrm{out}} p^0 t_0^{\mathrm{in}}\big|^2 E_0^2 \big(&\mathrm{Re}\big(f\big(\Delta N_{xx} + \Delta N_{yy}\big)\big)\sin(2\psi) -\\
&-\mathrm{Im}\big(f\big(\Delta N_{xx} - \Delta N_{yy}\big)\big)\cos(2\psi)\sin(2\theta) +\\
&+2\,\mathrm{Im}\big(f\Delta N_{xy}\big)\cos(2\psi)\cos(2\theta)\big).
\end{aligned}
\tag{31}
$$

The rotation angle with the induced change $\Delta\theta$ is:

$$\tan(2(\theta+\Delta\theta)) = \frac{S_2}{S_1} = \frac{S_2^0+\Delta S_2}{S_1^0+\Delta S_1} = \frac{S_2^0}{S_1^0} + \frac{\Delta S_2}{S_2^0}\frac{S_2^0}{S_1^0} - \frac{\Delta S_1}{S_1^0}\frac{S_2^0}{S_1^0}. \tag{32}$$

Analogously, $\Delta\psi$ is:

$$\sin(2(\psi+\Delta\psi)) = \frac{S_3}{S_0} = \frac{S_3^0}{S_0^0} + \frac{\Delta S_3}{S_3^0}\frac{S_3^0}{S_0^0} - \frac{\Delta S_0}{S_0^0}\frac{S_3^0}{S_0^0}. \tag{33}$$

On the other hand, due to $\Delta\theta \ll \theta$ and $\Delta\psi \ll \psi$:

$$\begin{gathered}\tan(2(\theta+\Delta\theta)) = \tan(2\theta) + 2\Delta\theta(\tan^2(2\theta)+1) = \tan(2\theta) + \frac{2\Delta\theta}{\cos^2(2\theta)}, \\ \sin(2(\psi+\Delta\psi)) = \sin(2\psi) + 2\Delta\psi\cos(2\psi).\end{gathered} \tag{34}$$

This allows $\Delta\theta$ and $\Delta\psi$ to be expressed in terms of Stokes parameters:

$$\begin{aligned}\Delta\theta &= \frac{\cos^2(2\theta)}{2}\left(\frac{\Delta S_2}{S_2^0}\frac{S_2^0}{S_1^0} - \frac{\Delta S_1}{S_1^0}\frac{S_2^0}{S_1^0}\right), \\ \Delta\psi &= \frac{1}{2\cos(2\psi)}\left(\frac{\Delta S_3}{S_3^0}\frac{S_3^0}{S_0^0} - \frac{\Delta S_0}{S_0^0}\frac{S_3^0}{S_0^0}\right).\end{aligned} \tag{35}$$

Ellipticity ξ and its change $\Delta\xi$ are more illustrative than ψ:

$$\xi + \Delta\xi = \tan(\psi+\Delta\psi) = \tan(\psi) + \Delta\psi(\tan^2(\psi)+1) = \xi + \Delta\psi(\xi^2+1). \tag{36}$$

This, along with the simple fact that $\cos(2\psi) = \frac{1-\tan^2(\psi)}{1+\tan^2(\psi)}$, yields the induced change in ellipticity in terms of Stokes parameters:

$$\Delta\xi = \frac{\Delta\psi}{\xi^2+1} = \frac{1}{2(1-\xi^2)}\left(\frac{\Delta S_3}{S_3^0}\frac{S_3^0}{S_0^0} - \frac{\Delta S_0}{S_0^0}\frac{S_3^0}{S_0^0}\right). \tag{37}$$

The induced change in the intensity I of a probe pulse is trivial:

$$\frac{\Delta I}{I} = \frac{\Delta S_0}{S_0^0}. \tag{38}$$

After substituting expressions for ΔS_i's and then ΔN's, Δn's, and $K_\pm$ with the corresponding expressions from (31), (27), (8), and (12), all three values $\Delta\theta, \Delta\xi$ and $\Delta I/I$ produce relatively simple equations:

$$\Delta\theta = \frac{1}{2(\xi^2-1)}(A\sin(2\theta) + B\cos(2\theta) + C\sin(4\theta) + D\cos(4\theta) + E), \tag{39}$$

$$\Delta\xi = \frac{1}{2(\xi^4-1)(\xi^2+1)}(A\sin(2\theta) + B\cos(2\theta) + E), \tag{40}$$

$$\Delta I/I = (A\sin(2\theta) + B\cos(2\theta) + E), \tag{41}$$

where the corresponding coefficients $A - E$ are shown in Table 1.

	$\Delta\theta$	$\Delta\xi$	$\Delta I/I$
A	$(1-\xi^2)\,\mathrm{Re}\left(\frac{f}{n^0}\Delta\chi\right)$	$-2\xi(1+\xi^2)\,\mathrm{Re}\left(\frac{f}{n^0}\chi_{xy}\right) +$ $+(1+4\xi^2-\xi^4)\,\mathrm{Im}\left(\frac{f}{n^0}\Delta\chi\right)$	$-\mathrm{Re}\left(\frac{f}{n^0}\chi_{xy}\right) +$ $\frac{2\xi}{1+\xi^2}\,\mathrm{Im}\left(\frac{f}{n^0}\Delta\chi\right)$
B	$-2\xi\,\mathrm{Im}\left(\frac{f}{n^0}\Delta\chi\right) +$ $+(1+\xi^2)\,\mathrm{Re}\left(\frac{f}{n^0}\chi_{xy}\right)$	$2\xi(1+\xi^2)\,\mathrm{Re}\left(\frac{f}{n^0}\Delta\chi\right) +$ $+(1+4\xi^2-\xi^4)\,\mathrm{Im}\left(\frac{f}{n^0}\chi_{xy}\right)$	$\mathrm{Re}\left(\frac{f}{n^0}\Delta\chi\right) +$ $\frac{2\xi}{1+\xi^2}\,\mathrm{Im}\left(\frac{f}{n^0}\chi_{xy}\right)$
C	$\xi^2\,\mathrm{Re}\left(\frac{f}{n^0}\chi_{\mathrm{avg}}\right)$	—	—
D	$-\xi\,\mathrm{Im}\left(\frac{f}{n^0}\chi_{\mathrm{avg}}\right)$	—	—
E	$\xi\,\mathrm{Im}\left(\frac{f}{n^0}\chi_{\mathrm{avg}}\right)$	$-4\xi^3\,\mathrm{Re}\left(\frac{f}{n^0}\chi_{\mathrm{avg}}\right)$	$\frac{1-\xi^2}{1+\xi^2}\,\mathrm{Re}\left(\frac{f}{n^0}\chi_{\mathrm{avg}}\right)$

Table 1: Trigonometric amplitudes for $\Delta\theta$, $\Delta\xi$ and $\Delta I/I$.

There are three unknown complex values $\chi_{\mathrm{avg}}, \Delta\chi$ and χ^{NL}_{xy}, so to fully reconstruct them from the experiment, the angular dependence of all three values $\Delta\theta, \Delta\xi$ and $\Delta I/I$ has to be measured. After that, simultaneous fitting can be performed to extract the values of $\chi_{\mathrm{avg}}, \Delta\chi$ and χ^{NL}_{xy}, and thus the values for the diagonal components of the tensor χ^{NL}_{xx} and χ^{NL}_{yy}, when materials constants in f are known.

A particular case of linear probe polarization ($\xi = 0$), non-absorbing media ($\mathrm{Im}(n^0) = 0$), and absence of interfaces ($f = i\frac{\omega}{c}z$) significantly simplifies the equations, which allows for a better understanding of the physics causing the change in polarization. Under such conditions, (39), (40) and (41) become:

$$\begin{aligned}\Delta\theta &= \frac{\omega z}{2n^0 c}\big(\mathrm{Im}(\Delta\chi)\sin(2\theta) + \mathrm{Im}\big(\chi_{xy}\big)\cos(2\theta)\big),\\ \Delta\xi &= -\frac{\omega z}{2n^0 c}\big(\mathrm{Re}(\Delta\chi)\sin(2\theta) + \mathrm{Re}\big(\chi_{xy}\big)\cos(2\theta)\big),\\ \Delta I/I &= \frac{\omega z}{n^0 c}\big(\mathrm{Im}\big(\chi_{xy}\big)\sin(2\theta) - \mathrm{Im}(\Delta\chi)\cos(2\theta) - \mathrm{Im}\big(\chi_{\mathrm{avg}}\big)\big).\end{aligned} \tag{42}$$

These equations reveal that induced rotation is only possible when the imaginary parts of nonlinear susceptibility are present. For non-absorbing media, this means induced absorption by the external pump field. The real part only induces the ellipticity change in the probe polarization. Additionally, it is impossible to recover the real part of χ_{avg} and thus to fully extract the values of χ^{NL}_{xx} and χ^{NL}_{yy}.

Since the equations were derived for general nonlinearity, they should match textbook examples with corresponding simplifications. In [9], the induced rotation for isotropic non-absorbing media of thickness L is given by the equation:

$$\Delta\theta = \frac{1}{2}\Delta n\frac{\omega}{c}L, \tag{43}$$

where L is the propagation distance and $\Delta n \equiv n_+ - n_-$ is the difference in refractive index for **circular waves**. To compare this equation with the obtained result, it should be written in a linear basis. The refractive index is defined as $n_\pm = n^0 + \frac{\chi_\pm}{2n^0}$, which means $\Delta n = \frac{1}{2n^0}(\chi_+ - \chi_-) = \frac{\Delta\chi}{2n^0}$. Substituting Δn with $\Delta\chi$ in (43) gives:

$$\Delta\theta = \frac{1}{4n^0}\Delta\chi\frac{\omega}{c}L. \tag{44}$$

This equation matches the obtained result for $\Delta\theta$ in (42) for the case of a medium without absorption $\mathrm{Im}(n^0) = 0$ and for polarization at $\theta = 45°$ to the $\boldsymbol{x}$ axis:

$$\Delta\theta = \frac{\omega L}{2n^0 c}\,\mathrm{Im}(\Delta\chi) = \frac{1}{4n^0}\,\mathrm{Im}\big(\chi^{\mathrm{NL}}_{xx} - \chi^{\mathrm{NL}}_{yy}\big)\frac{\omega}{c}L. \tag{45}$$

The presence of only the imaginary part of $\Delta\chi$ in (45) conflicts with the purely real $\Delta\chi$ in (44). This mismatch arises due to the different bases used in both equations. To see how $\Delta\chi_{\mathrm{circular}}$ transforms to $\Delta\chi_{\mathrm{linear}}$, a transformation of the basis has to be done.

The linear and circular bases are linked when polarization is rotated by angle θ, as shown in [9]:

$$\begin{aligned}\hat{\boldsymbol{\sigma}}_{\pm} &= \frac{\hat{\boldsymbol{x}'} \pm i\hat{\boldsymbol{y}'}}{\sqrt{2}} e^{\pm i\theta},\\ \hat{\boldsymbol{x}'} &= \hat{\boldsymbol{x}}\cos(\theta) + \hat{\boldsymbol{y}}\sin(\theta),\\ \hat{\boldsymbol{y}'} &= \hat{\boldsymbol{y}}\cos(\theta) - \hat{\boldsymbol{x}}\sin(\theta).\end{aligned} \tag{46}$$

By using χ_{xx} and χ_{yy} as $\hat{\boldsymbol{x}}$ and $\hat{\boldsymbol{y}}$ components, and $\chi_{\pm}$ as $\hat{\boldsymbol{\sigma}}_{\pm}$, the difference of the nonlinear polarization is derived as:

$$\begin{aligned}&\chi_+ - \chi_- = \\ &= \sqrt{2}\big((\mathrm{Im}(\chi_{xx}) - i\,\mathrm{Re}(\chi_{xx}))\sin(2\theta) - \big(\mathrm{Im}\big(\chi_{yy}\big) - i\,\mathrm{Re}\big(\chi_{yy}\big)\big)\cos(2\theta)\big).\end{aligned} \tag{47}$$

This means that only the imaginary parts of χ_{xx} and χ_{yy} have to be taken into account to keep the rotation angle real. Here, χ_{ij} is some *effective* value, which does not match χ_{ij}^{NL} used above. This is only an illustrative demonstration, as only diagonal terms are taken into account. With the mismatch explained, the obtained equation matches the textbook example, which additionally supports the correctness of the theoretical findings.

4. Experimental observation of the Kerr effect in Cd_3As_2

Before discussing the experimental results, it is important to summarize what is expected for the electro-optical Kerr effect in Cd_3As_2. As all three values $\Delta\theta$, $\Delta\xi$, and $\Delta I/I$ are linear in $\hat{\chi}^{\mathrm{NL}}$, the fluence dependence of these values will reflect the fluence dependence of $\hat{\chi}^{\mathrm{NL}}$. For the electro-optical Kerr effect, according to (3), this fluence dependence is expected to be parabolic, meaning that $(\Delta\theta, \Delta\xi, \Delta I/I) \propto E_{\mathrm{THz}}^2$. In the case of broken inversion symmetry, the Pockels effect appears as a linear fluence dependence on the THz field $(\Delta\theta, \Delta\xi, \Delta I/I) \propto E_{\mathrm{THz}}$. From equations (39) – (41), it is clear that the angular dependence is expected to show either 4 or 8 peaks, depending on the material parameters. This angular dependence also allows extraction of both the real and imaginary parts of χ_{ij}^{NL}. Once extracted, the value of the nonlinear refractive index n_2[9] can be estimated and compared with other materials.

4.1. Mica effect on probe's polarization

The ability to monitor S_3 and, consequently, the ellipticity of the probe beam is essential for the experiment. The substrate used, mica, has a monoclinic structure[10] and thus is birefringent. The absorption coefficient at 800 nm is estimated to be 6.3 cm^{-1}[11], which means a transmission of 95% in the probe's intensity. The sample is oriented so that the optical beam passes first through the substrate and then reaches Cd_3As_2. Such geometry produces a higher signal compared to when the sample faces the THz beam directly. Since the substrate has a lower refractive index and nearly no absorption ($n \approx 2.5, \kappa \approx 0$

[12]) in the THz range compared to Cd_3As_2 (estimated as $n \approx 23$, $\kappa \approx 38$[13]), there are fewer losses at the air–mica–Cd_3As_2 interface than at the air–Cd_3As_2 interface alone. Improvement in coupling is estimated to be around 2, meaning that the THz field inside Cd_3As_2 is twice as high with mica before the sample than without. Such enhancement is critical for the observation of nonlinear processes.

However, this geometry also changes the polarization state of the probe, which must be taken into account to accurately extract the induced change in susceptibility. This is addressed by monitoring the probe pulse in the absence of the pump pulse. The effect caused by the presence of the substrate is shown in Figure 4. Due to its natural birefringence, mica acts as an arbitrary wave plate for the 800 nm probe beam, causing clear modulations in both the rotation and ellipticity of the probe beam. The peak-to-peak change in ellipticity is about 0.1, which corresponds to a 10% deviation from the mean value of 0.58. Deviations in the polarization angle are approximately $\pm 8°$. Both the angle and ellipticity also show additional modulation, potentially caused by the substrate cut or slight misalignment of the sample.

Due to the detection method, these deviations are internally corrected when the Stokes parameters ΔS_i are calculated. However, for angular dependence and accurate extraction of χ_{ij}^{NL}, it is crucial to use these values of the polarization angle and ellipticity.

During the experiments, mica did not exhibit any induced contributions to the probe's polarization changes under the THz pump.

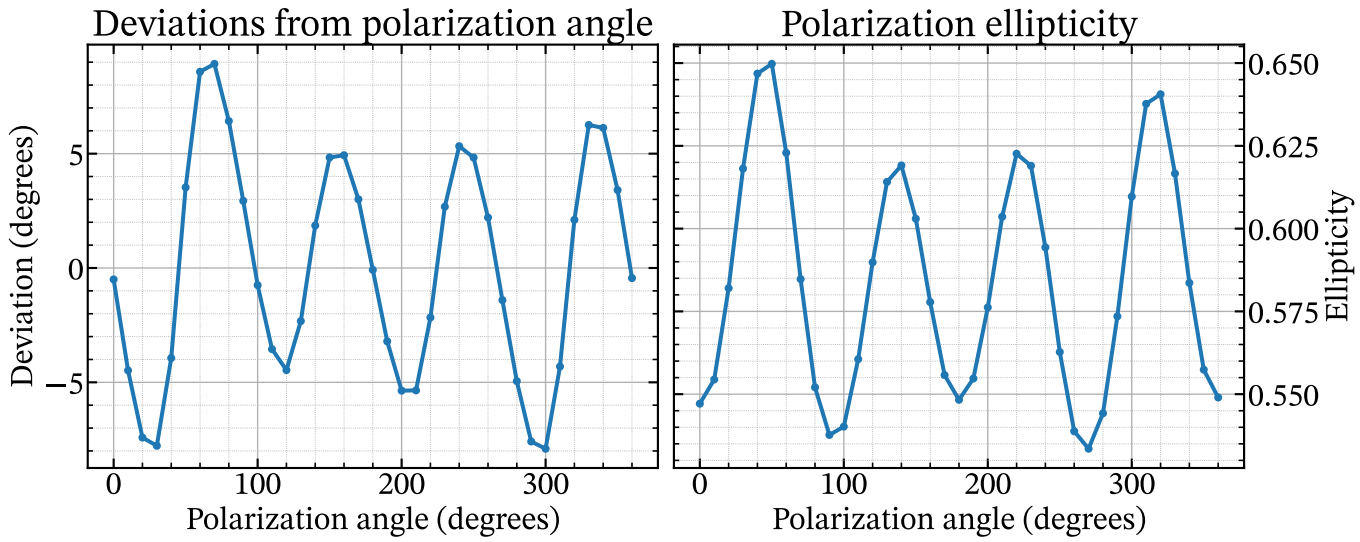

Figure 4: Deviations in the polarization angle of the probe (left) and ellipticity of the probe (right) after the substrate.

4.2. Kerr effect

Measured values of Kerr rotation $\Delta\theta$, induced ellipticity $\Delta\xi$, and transmission change $\Delta I/I$ are shown in Figure 5. Data were acquired at a polarization angle of $45°$ and at room temperature. The squared THz field indicates the time when the external drive is present. The peak THz field used in the experiment is estimated to be ~ 700 kV/cm in free space.

Several features are present in the measured signals. First, two peaks appear in $\Delta\theta$ and $\Delta\xi$, matching in time with the peaks of the THz field. These peaks can be attributed to the instantaneous response of the material, typically due to electronic polarization[9]. Interestingly, the second peak in $\Delta\theta$ and $\Delta\xi$ has the same amplitude as the first, despite the THz field's second peak being approximately 1.5 times stronger (2.5 times in intensity). This may be related to the second main feature in the measured signals: long-term dynamics. The presence of such dynamics in the electro-optical Kerr signal is nothing new; a slow response related to molecular realignment has been demonstrated, for example, in CS_2[3]. In Cd_3As_2, this dynamic could be caused by accumulated energy in the electronic subsystem, which takes time to dissipate via electron-phonon interactions, Seebeck current generation, etc.

All three signals exhibit this behavior. In polarization rotation and ellipticity, the rise time of the long-term dynamics is unclear, whereas in intensity change, it is clearly about 3 ps. This duration is longer than the THz pump pulse, suggesting that the THz field alters Cd_3As_2 properties, which appear as long-term dynamics in polarization changes. Oscillations in $\Delta I/I$ after 1 ps have a period of ~ 0.6 ps (~ 0.17 THz), close to the frequency of the lowest energy optical phonon[14]. The changes in Cd_3As_2 properties may reduce the amplitude of the response in $\Delta\theta$ and $\Delta\xi$, potentially explaining why the second peak has a similar amplitude, while the THz field is higher at the second peak.

To decouple these two dynamics and study their properties separately, two time points are considered. The first, a "fast" response, is taken at 0.6 ps, where the signal reaches its peak and the instantaneous response dominates. As discussed above, the second peak appears affected by long-term changes in the material and is thus excluded from analysis. The second time point, capturing long-term changes (or "slow" response), is taken at 4 ps. At this time, the THz pump has ended, so no instantaneous material response is present. While in $\Delta\theta$ and $\Delta\xi$, the long-term signal is nearly constant, in $\Delta I/I$, there is a clear decay for later times.

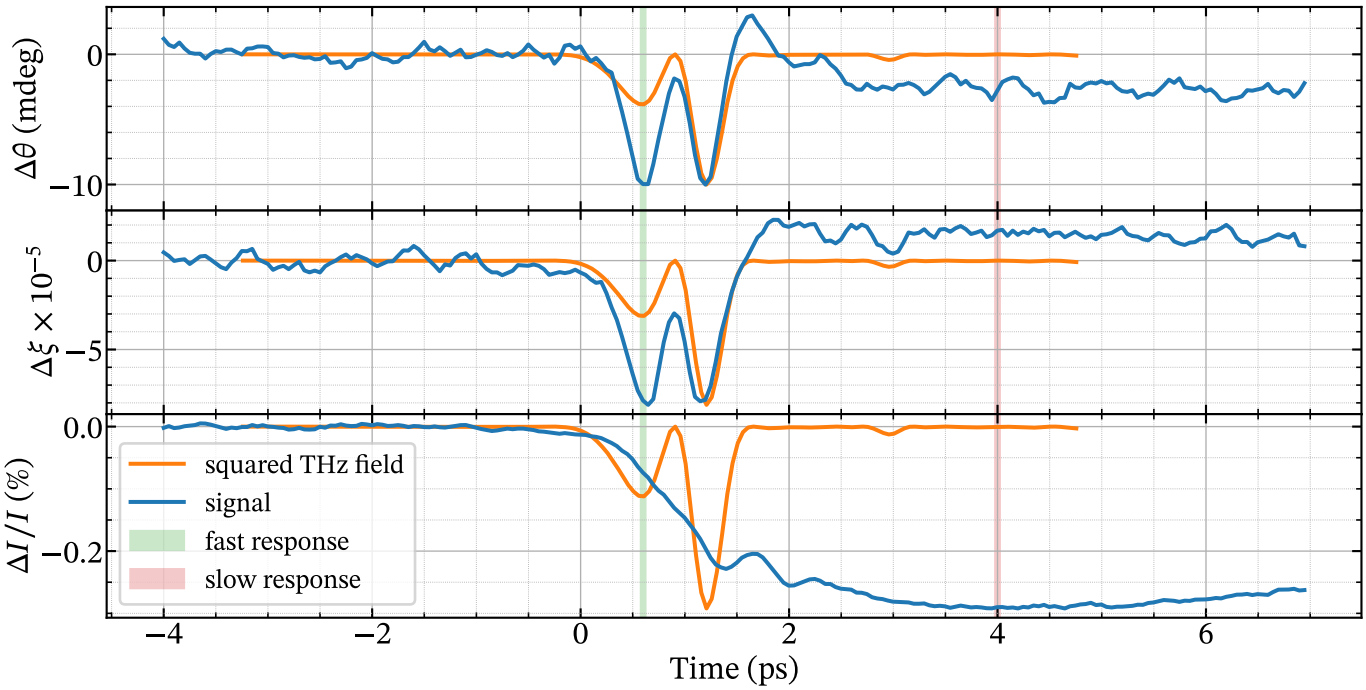

Figure 5: Induced changes in polarization rotation (top), ellipticity (middle), and transmission (bottom) of the probe pulse. The orange line is a scaled square of the terahertz field. Colored areas indicate the time points for further signal analysis.

4.3. Fluence dependence

As was discussed above, in Cd_3As_2 only the Kerr effect is expected, while the Pockels effect should be prohibited by the material's symmetry. In the fluence dependence, this should result in signals being proportional to the square of the pump field. However, if the Pockels effect is present due to symmetry breaking, a linear term in fluence dependence should appear.

The measured fluence dependence, shown in Figure 6, demonstrates that all measured values are proportional to the square of the pump field in both time ranges. Linear contributions are zero within the error for all fits in the "fast" response. For "slow" responses, this is less clear, as the fit indicates larger linear contributions.

Another way to verify if the signals depend on the square of the pump field is through measurements with the THz pump phase shifted by 180°. As seen in Figure 7, all three signals remain unchanged. Due to alignment, there is a constant offset in THz pump energies for 0° and 180°. To account for this, $\Delta\theta$, $\Delta\xi$, and $\Delta I/I$ related to the 180° phase of the THz were scaled by the ratio $\left(E^{0°}_{\mathrm{THz}}/E^{180°}_{\mathrm{THz}}\right)^2$, and the THz trace was scaled by a factor proportional to $E^{0°}_{\mathrm{THz}}/E^{180°}_{\mathrm{THz}}$.

All of this suggests that there are no contributions from the Pockels effect to the observed signals, indicating that the THz field itself does not break inversion symmetry in Cd_3As_2, which is necessary for the Pockels effect.

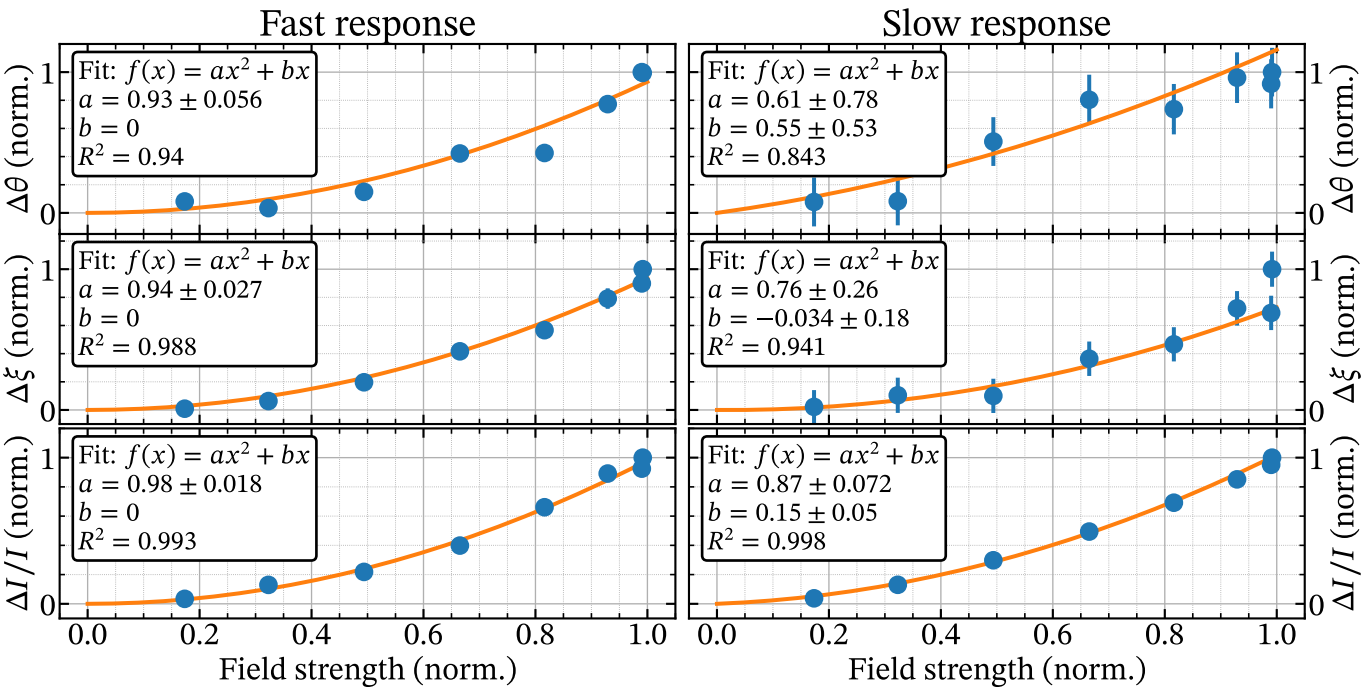

Figure 6: Dependence of $\Delta\theta$, $\Delta\xi$, and $\Delta I/I$ on the THz pump field for fast and slow response regions. Both signal and field strength are normalized to their maximum absolute values.

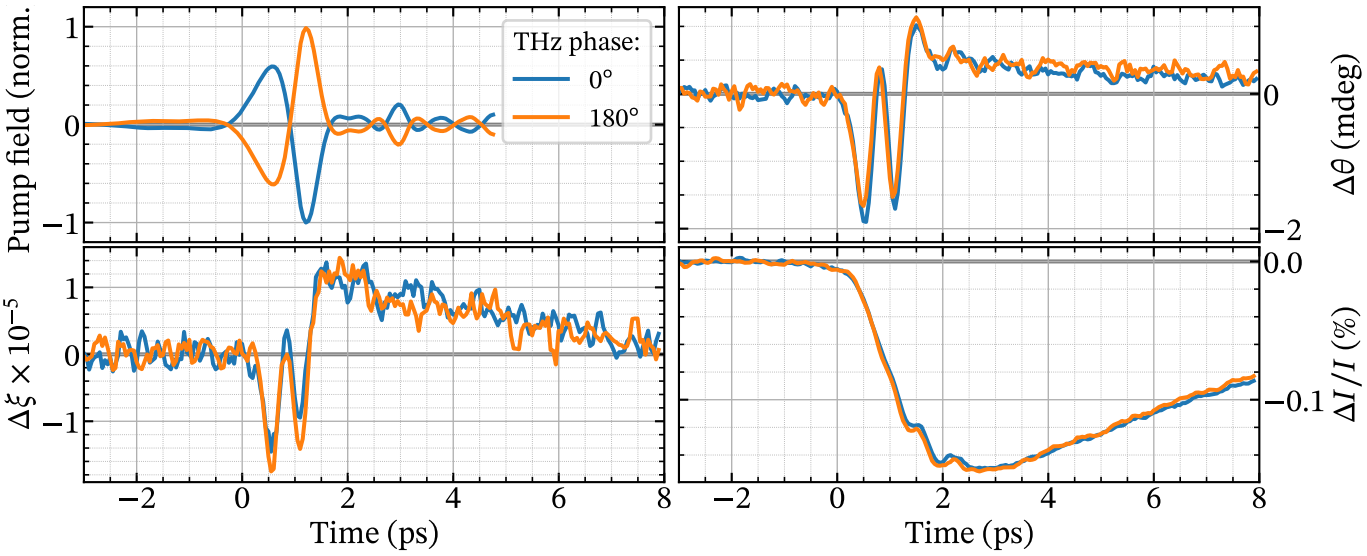

Figure 7: Pump field (top left) and induced changes in polarization at different phases of the THz pump. Terahertz fields have opposite phases, while all other signals remain unchanged. Data related to 180° has been corrected to compensate for the difference in THz pulse energy.

4.4. Angular dependence

By rotating the probe polarization, the angular dependence of $\Delta\theta$, $\Delta\xi$, and $\Delta I/I$ is measured. Only the probe beam polarization angle was changed (using a half-wave plate); the sample and THz pump orientations were kept fixed. This set of measurements was conducted at a maximum THz field of 700 kV/cm. The theoretically derived equations, (39), (40), and (41), were used to fit the experimental data and extract the values of χ_{ij}^{NL}. However, (41) does not accurately reflect the signal measured in the experiment and thus does not fit the data. This discrepancy arises because, for simplicity, only changes related to induced birefringence were considered in Fresnel coefficients, while isotropic changes in Cd_3As_2's refractive index were ignored. To account for the isotropic change, a phenomenological coefficient, Δt, is introduced as an additional term, $\Delta I/I + \Delta t$. This term represents isotropic changes in both components of the complex refractive index, which affect both propagation and transmission through interfaces.

Measured results and corresponding *simultaneous* fits are shown in Figure 8, and extracted fit values are provided in Table 2. It is clear that while $\Delta\theta$ and $\Delta I/I$ align well with the derived equations, $\Delta\xi$ does not show as good a fit. A possible reason is that the theoretical equation in (40) may not fully apply. The issue with the equation lies in its limitations for high ellipticities, as it diverges for values close to 1. Given that the average probe ellipticity is about 0.6 according to Figure 4, second-order terms for the $\Delta\psi$ expansion in (34) may need to be included.

	$\mathrm{Re}(\chi_{xx}^{\mathrm{NL}})$	$\mathrm{Im}(\chi_{xx}^{\mathrm{NL}})$	$\mathrm{Re}(\chi_{yy}^{\mathrm{NL}})$	$\mathrm{Im}(\chi_{yy}^{\mathrm{NL}})$	$\mathrm{Re}(\chi_{xy}^{\mathrm{NL}})$	$\mathrm{Im}(\chi_{xy}^{\mathrm{NL}})$	Δt
fast response	13 ± 4	-23 ± 4	-37 ± 4	37 ± 4	-22 ± 3	-12 ± 3	-7.9 ± 0.2
slow response	4 ± 3	-2 ± 3	2 ± 3	-4 ± 3	1 ± 3	-2 ± 3	-30.3 ± 0.1

Table 2: Fit results for two response regimes. All values have a 10^{-4} multiplier.

Since a full time trace was measured for each polarization angle, the fit described above can be applied to *each time point*. This allows the extraction of the time dependence of χ_{ij}^{NL}, which could subsequently be used to derive the time dependence and values of the third-order susceptibility. This time-resolved fit is shown in Figure 9. According to this fit, oscillations in $\Delta I/I$, observed in Figure 5, result from isotropic changes in the material rather than birefringent ones.

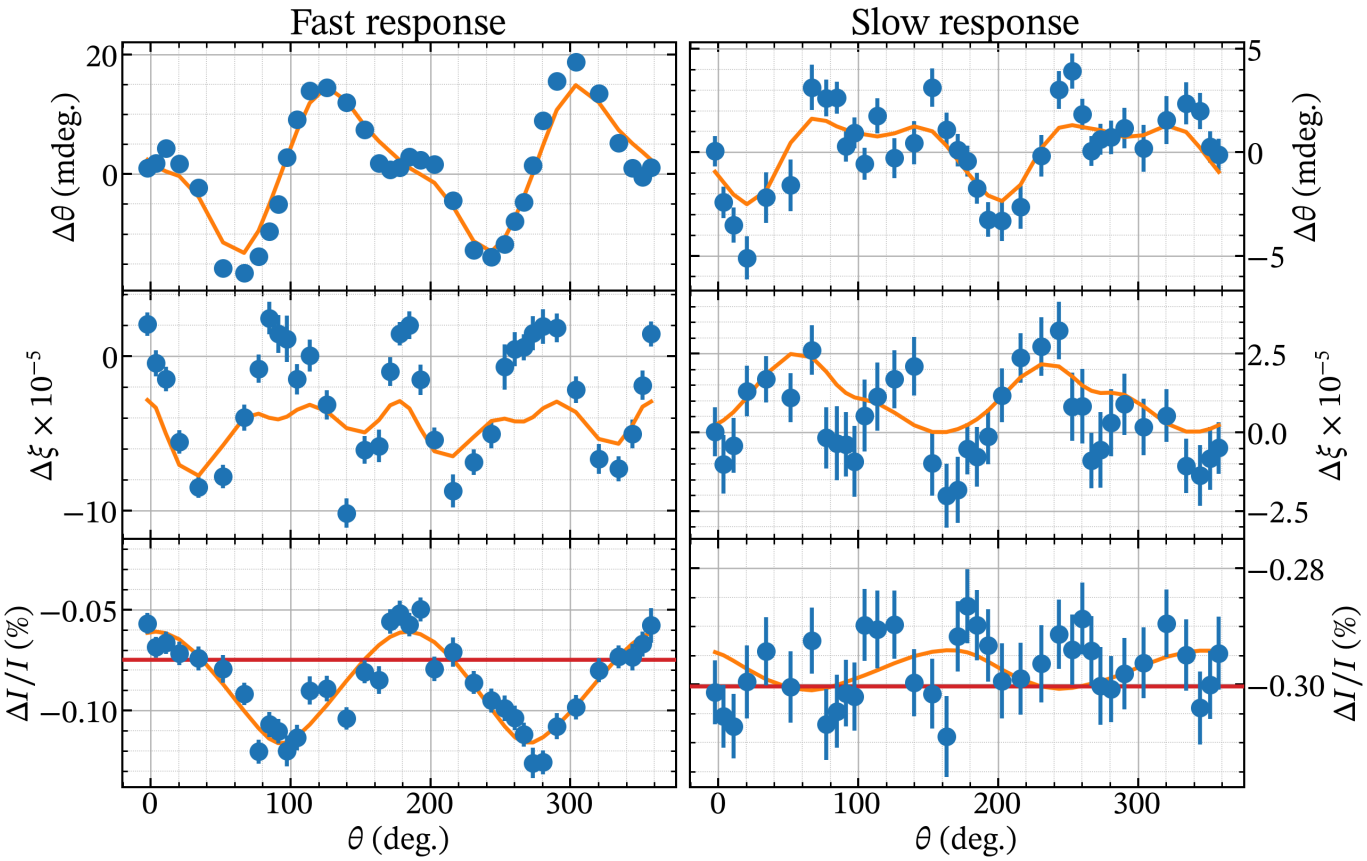

Figure 8: Experimental data and corresponding fits for induced changes in the probe beam for two time regions. The red line for $\Delta I/I$ shows the contribution of the induced Fresnel coefficient Δt.

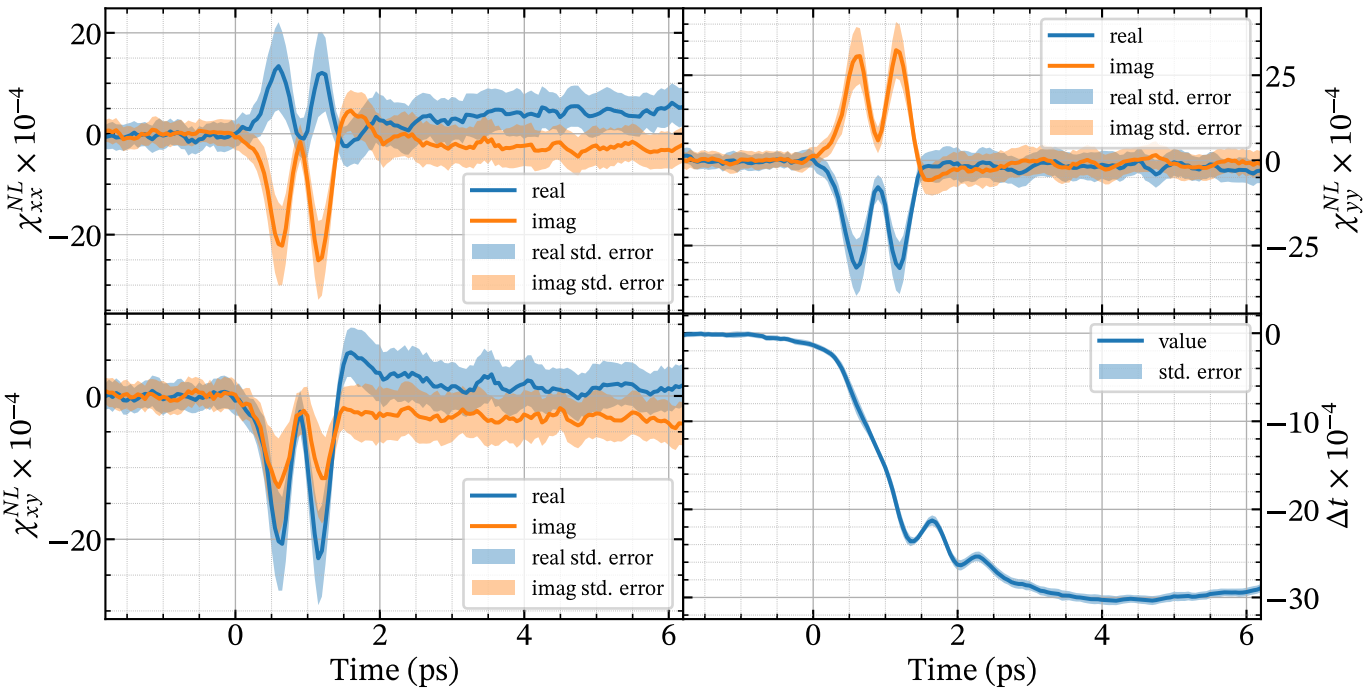

Figure 9: Extracted time dependence of the components of χ^{NL}_{ij} and Δt. The shaded area represents the 3σ uncertainty, obtained from the fit procedure.

The fitted value of χ_{ij}^{NL} for the fast response allows estimation of the peak value of $n_2\left(\frac{\mathrm{cm}^2}{\mathrm{W}}\right)$ achieved in the experiment. To estimate this value accurately, the THz field inside Cd_3As_2 must first be estimated. The electric field inside Cd_3As_2 will be:

$$E_{\mathrm{THz}}^{\mathrm{in}} = t_{\mathrm{mica}} t_0^{\mathrm{in}} E_{\mathrm{THz}}^{\mathrm{out}}, \tag{48}$$

where $t_{\mathrm{mica}} = \frac{2}{n_{\mathrm{mica}}+1}$ represents transmission at the air→mica interface, and t_0^{in} is as defined in (18). Using values for mica ($n \approx 2.5, \kappa \approx 0$[12]) in the THz range and Cd_3As_2 (estimated as $n \approx 23, \kappa \approx 38$[13]), the field inside the sample is estimated to be $\left|E_{\mathrm{THz}}^{\mathrm{in}}\right| \approx$ 44 kV/cm for a free-space field of 700 kV/cm. According to [9], the value of n_2 can be expressed as:

$$n_2 = \frac{\bar{n_2}}{n^0 \varepsilon_0 c}, \tag{49}$$

where $\bar{n_2} = \Delta n_{\pm} / \left|E_{\mathrm{THz}}^{\mathrm{in}}\right|^2$ for the peak field, and ε_0 is the vacuum permittivity. Using (8) and fitted values for the fast response from Table 2, two values of n_2 are estimated:

$$\begin{aligned} n_2 &\approx (16 + 7i) \cdot 10^{-14} \frac{\mathrm{cm}^2}{\mathrm{W}} \text{ for } \Delta n_-, \\ n_2 &\approx -(8 + i) \cdot 10^{-14} \frac{\mathrm{cm}^2}{\mathrm{W}} \text{ for } \Delta n_+. \end{aligned} \tag{50}$$

These estimated values are significantly lower than those observed in graphene ($\sim 10^{-8} - 10^{-7} \frac{\mathrm{cm}^2}{\mathrm{W}}$)[4,5], on par with quasi-2D semiconductor $MnPS_3$[15] or semiconductors like CdTe or GaAs[16], and significantly higher than in dielectrics[17].

5. Effect of probe fluence on the Kerr effect in Cd_3As_2

During the experiments, it was observed that the Kerr signal is affected by the fluence of the probe beam. This is puzzling because, in theory, the induced rotation $\Delta\theta$ should not depend on the probe beam intensity. Such a dependence suggests that additional nonlinear interactions between the pump and probe beams occur in the material, for example, effects related to $\chi^{(5)}$ terms. The first results of the investigation into how the intensity of the probe affects the Kerr effect in Cd_3As_2 are presented here.

5.1. Effect of high fluence of the probe

Figure 10 shows how the induced changes in the polarization state of the probe beam are affected by probe intensity. The most obvious difference occurs in intensity transmission, where not only the amplitude of the effect changes but also the shape of the response. Compared to the data from the previous subchapter, the sign of $\Delta\theta$ has

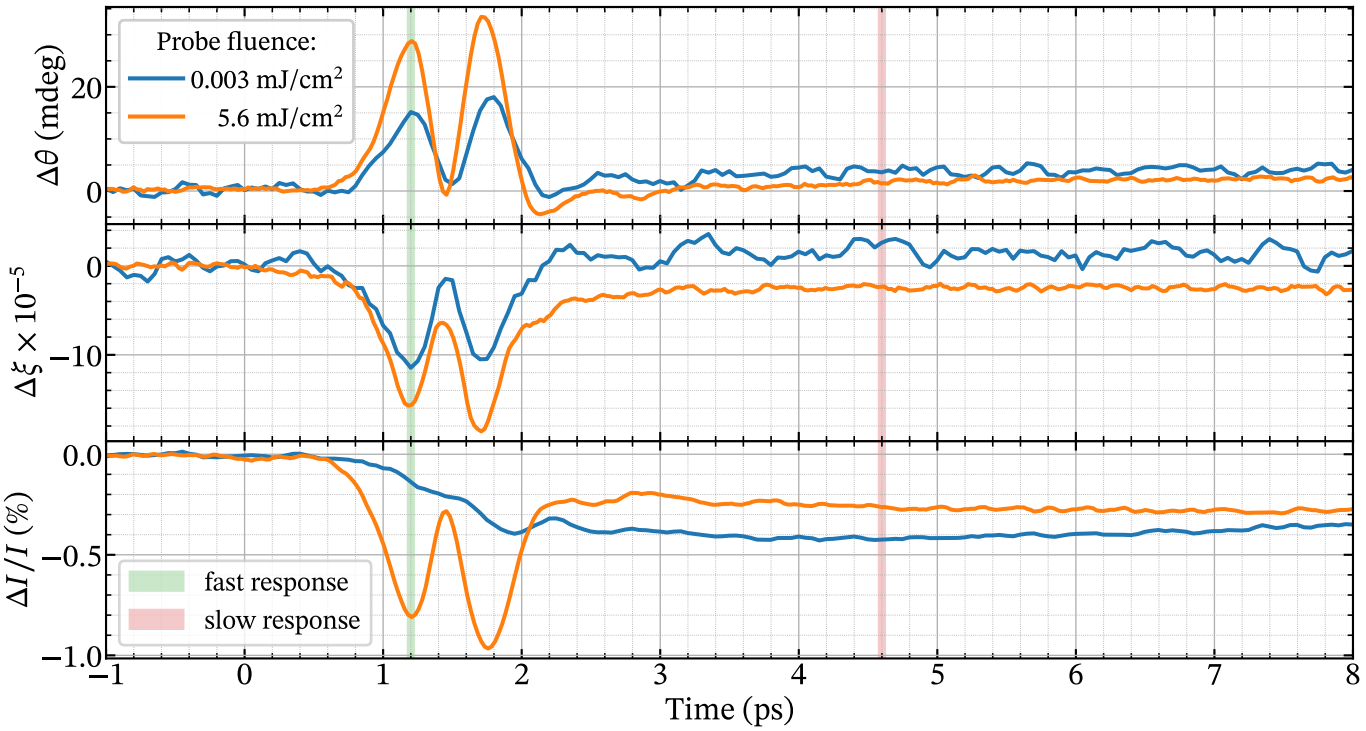

Figure 10: Induced changes in the probe beam's polarization state at different probe intensities.

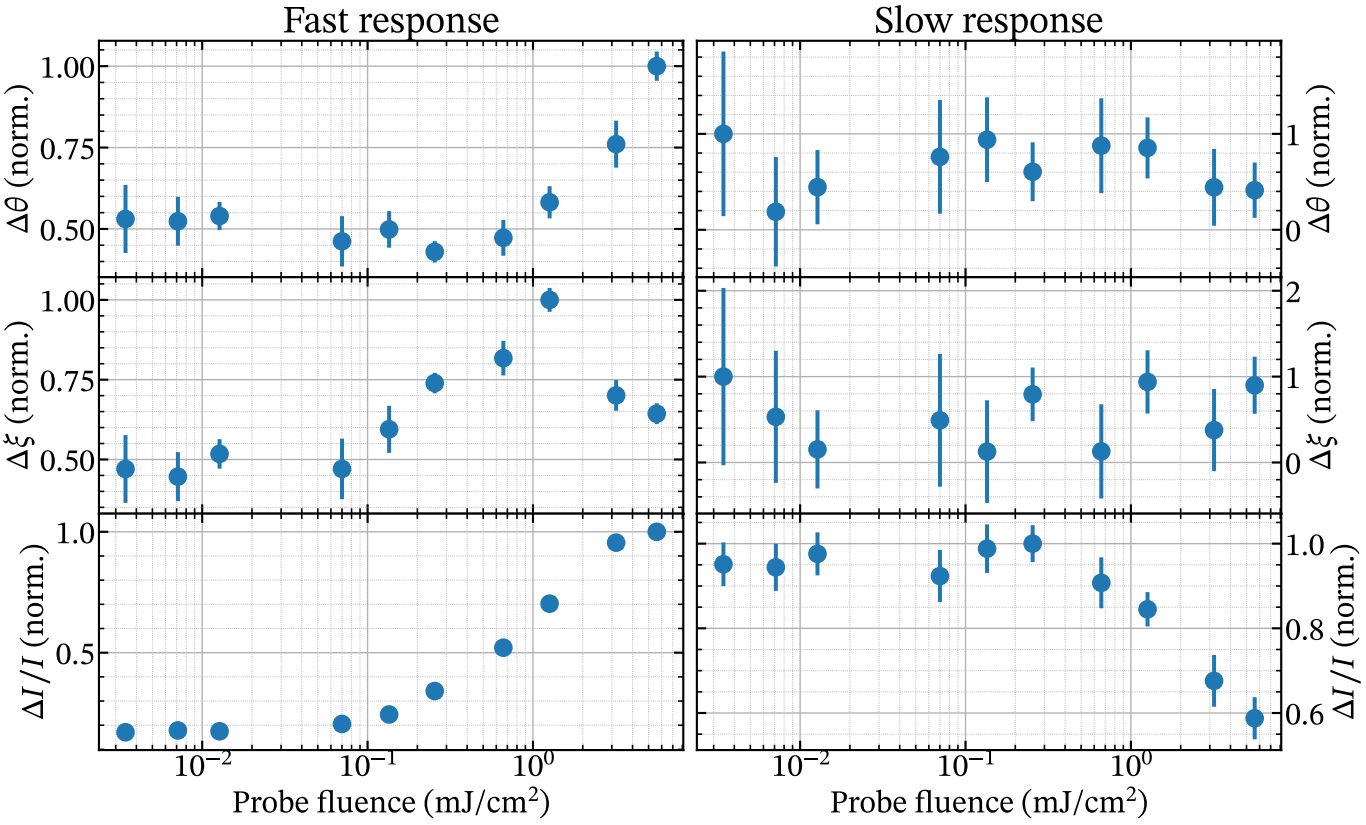

Figure 11: Dependence of changes in the probe beam's polarization on probe power. All values are normalized to their maximum *absolute* value.

flipped, although the experimental conditions remained the same. Since these were two different series of experiments, the change could have been caused by a misalignment of the *HWP* in detection, which effectively changes the sign of the S_2 Stokes parameter. To study the material response, the same two "fast" and "slow" time points approach is used as before. The positions of the time points are 1.2 ps and 4.6 ps, respectively.

The probe fluence dependence for $\Delta\theta$, $\Delta\xi$, and $\Delta I/I$ is shown in Figure 11. Several interesting observations can be made here. For the fast response, there is a possible sign of saturation in $\Delta I/I$ and $\Delta\xi$, but $\Delta\theta$ clearly does not show this. What $\Delta\theta$ does show is a signal decrease at medium powers, whereas the other two signals do not demonstrate this behavior. In the slow response, $\Delta\theta$ and $\Delta\xi$ do not depend on probe intensity, and $\Delta I/I$ only shows changes at relatively high probe powers.

5.2. Angular dependence

Angular dependence can reveal symmetries of the studied material and, as shown earlier, can be used to extract values of induced polarization. It can demonstrate the difference in sensitivity of two different regimes to the symmetries of the system. Figure 12 shows polar plots for the Kerr effect, discussed earlier, and for a higher-intensity probe. The probe power was 1.3 mJ/cm^2 for these measurements.

For the fast response, both fluences in $\Delta\theta$ show similar fourfold symmetry, typical for isotropic materials (for example, see Fig. 7 in [18]); however, there is an angular offset between the two regimes. At higher fluence, there are signs of additional features at 0°, 90°, 180°, and 270°. The most drastic changes are observed in $\Delta I/I$ in the signal value. Ellipticity changes have higher amplitude at higher fluence and exhibit similar symmetry to those at lower fluence. Compared to lower fluence, lobes at $45°$—$225°$ are larger than those at $150°$—$330°$, whereas at lower fluence, all lobes have similar values.

In the slow response, however, the opposite occurs, and the signals of $\Delta\theta$ and $\Delta\xi$ become more structured. The improved signal-to-noise ratio reveals a sixfold structure in induced rotation $\Delta\theta$ and a fourfold structure in $\Delta\xi$, which are not seen in low-fluence measurements. Induced intensity does not show significant changes in the symmetry of the signal.

5.3. Pump fluence dependence

As the angular dependence demonstrates, high probe fluence affects the symmetry of the processes. Because of this, it is important to perform a THz pump fluence dependence study to observe whether higher probe power causes any changes compared to lower ones. Figure 13 demonstrates such fluence dependence for all three values, $\Delta\theta$, $\Delta\xi$, and $\Delta I/I$, for both fast and slow responses. While the data were fitted with a

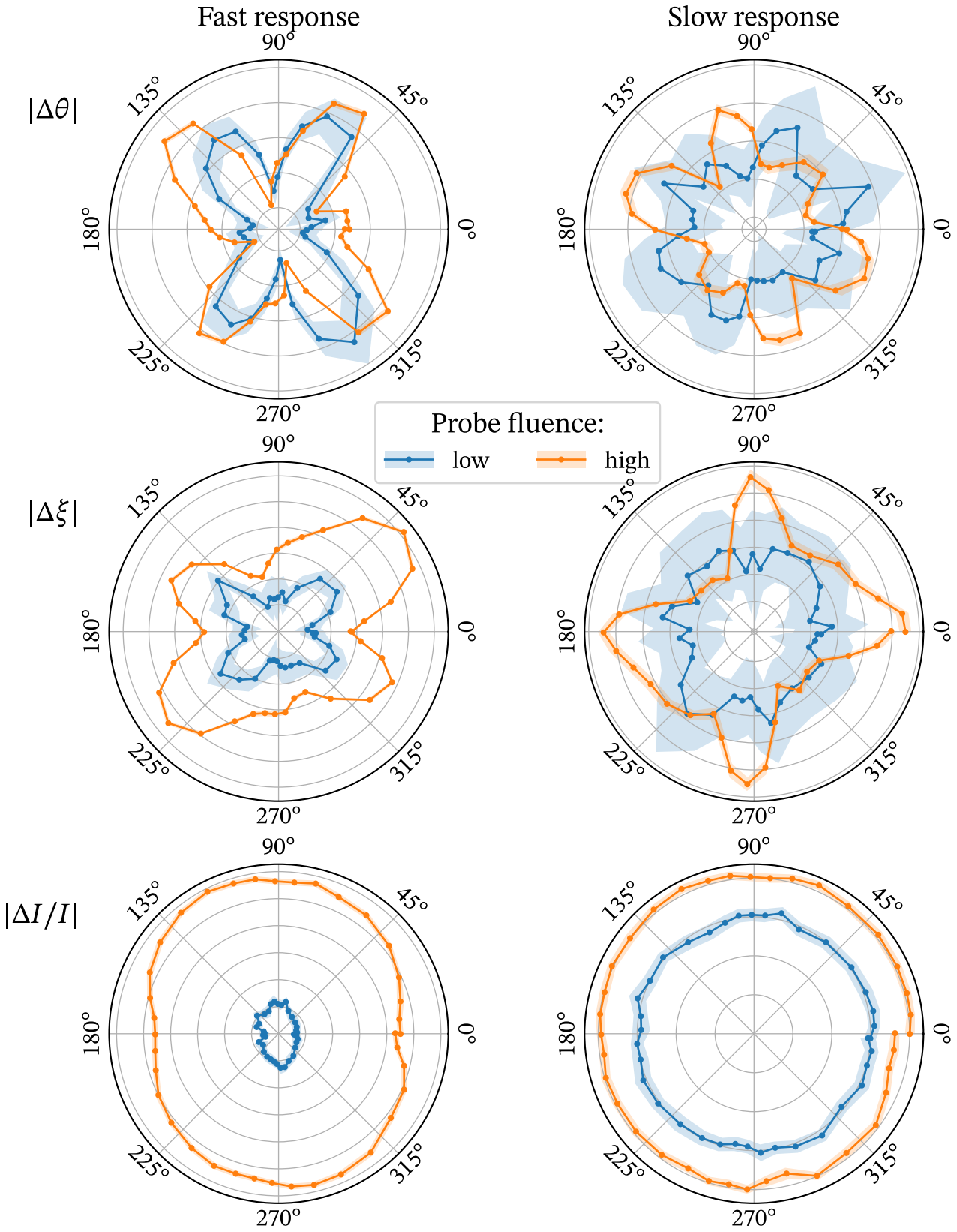

Figure 12: Polar plots of induced changes in the probe's polarization state for two fluences. Low-fluence data corresponds to the Kerr measurements discussed earlier. High-fluence data was obtained with 1.3 mJ/cm^2 probe power. Shaded areas represent standard error.

polynomial function of 4th order, it was also fitted with a parabolic function for comparison with the low probe fluence regime. The reasons for choosing the 4th order will be discussed in the next section.

The difference between the two regimes is immediately obvious, as it is not possible to fit the data with a parabolic function, unlike the low probe fluence case. While $\Delta\xi$ and $\Delta I/I$ show similar behavior, where an additional linear term is needed to fit the data, $\Delta\theta$ exhibits completely different fluence dependence. In the fast response, it shows a significant contribution of E^4_{THz} in addition to the quadratic term, while in the slow response, it has a more complex structure with possible saturation at high THz fields. It is worth noting, however, that $\Delta\theta$ data can also be fitted by a cubic function. The C_3

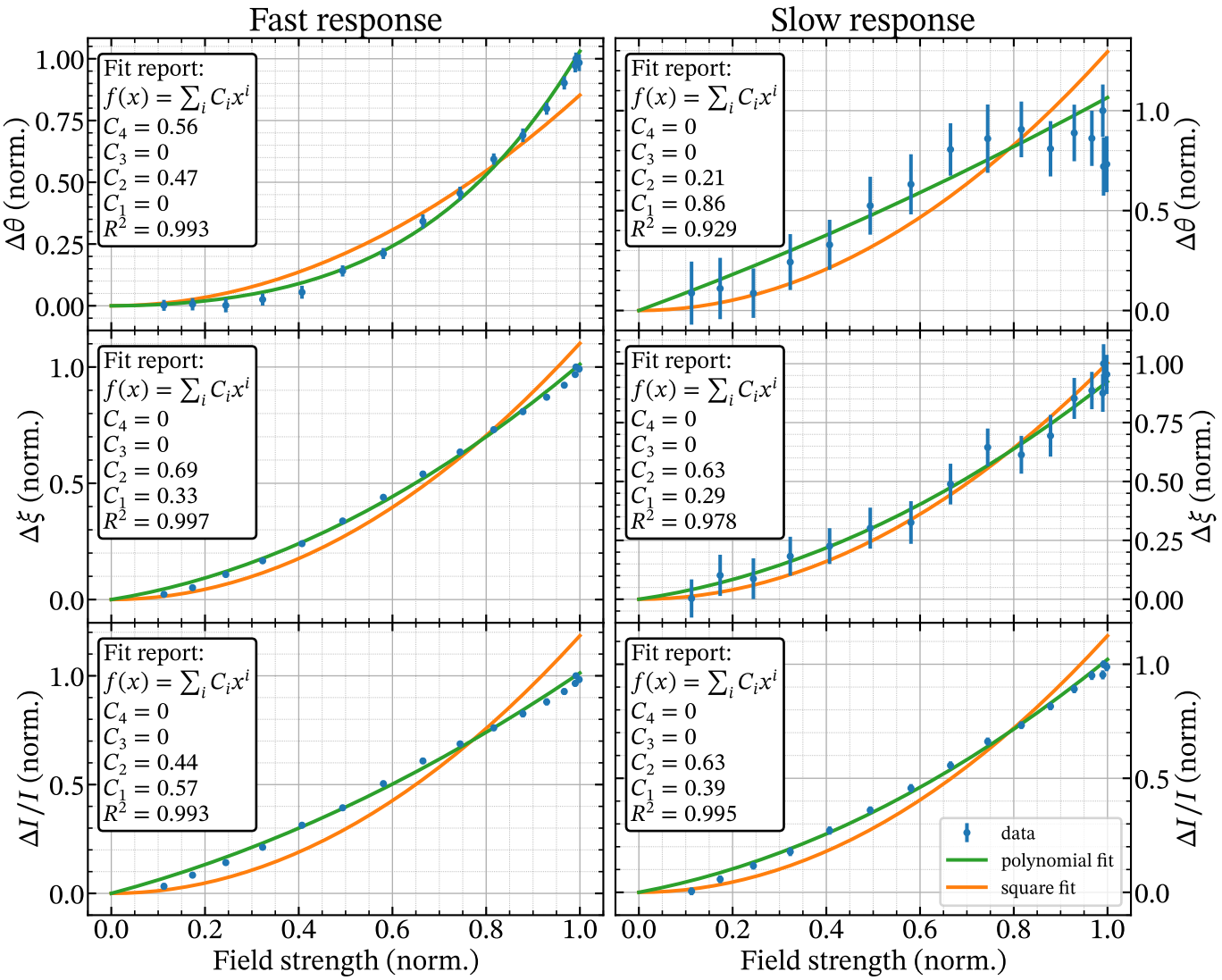

Figure 13: Dependence of induced polarization changes on the THz pump field. The data were fitted with two functions: a parabolic function x^2 and a 4th-order polynomial. Measurements were taken at $\theta = 45°$ and with a probe fluence of 1.3 mJ/cm^2. The two points at the highest fields were excluded from the fitting procedure.

parameter was manually fixed to 0 in this case. Reasons for such a decision are discussed in the next section.

5.4. Discussion

The results presented above clearly show the differences between the cases of low and high probe beam fluence. It is evident that a beam with sufficiently high intensity alters the material properties or nonlinearly mixes with the THz pump pulse, depending on the delay between the pump and probe pulses. While there is no clear answer as to which specific physical mechanism leads to the observed responses, there are some ideas about potential causes.

A logical step would be to consider the susceptibility of higher orders for the induced χ^{NL}:

$$\chi^{\mathrm{NL}} = \chi^{(3)}\left|E_{\mathrm{pump}}\right|^2 + \chi^{(5)}\left(\left|E_{\mathrm{pump}}\right|^2\left|E_{\mathrm{probe}}\right|^2 + \left|E_{\mathrm{pump}}\right|^4\right). \tag{51}$$

This could explain the THz fluence dependence for $\Delta\theta$ in the fast response. However, the same should be true for Kerr measurements, as the term $\chi^{(5)}\left|E_{\mathrm{pump}}\right|^4$ does not depend on E_{probe}. The term $\chi^{(5)}\left|E_{\mathrm{pump}}\right|^2\left|E_{\mathrm{probe}}\right|^2$ will have the same parabolic fluence dependence as the Kerr effect but with an increased signal. Equation (51) also demonstrates the absence of E^3_{pump} terms, which is why the C_3 term in the fluence dependence fit was zeroed. Self-induced changes in the probe are excluded from the equation here.

Since the Kerr data show perfect parabolic behavior, the only conclusion is a scaling of susceptibility with the probe. Additionally, the probe-induced changes in $\chi^{(i)}$ could explain the observed drop in $\Delta\theta$ shown in Figure 11, as an interplay between the decreasing contribution of $\chi^{(3)}$ and the increasing contribution of $\chi^{(5)}$. Such a decrease in $\chi^{(3)}$ was observed in [19], where the efficiency of third harmonic generation in the THz range dropped under the fluence of an 800 nm pump. Simultaneously, the pump seems to introduce a $\chi^{(3)}$ of different microscopic origin, which participates in harmonic generation.

The presence of a linear contribution in $\Delta\xi$ and $\Delta I/I$ does not fit with equation (51) and likely has a different origin. One effect not accounted for is THz-induced second harmonic generation[20]. Nonlinear polarization for such an effect is $P^{\mathrm{NL}}(2\omega) \sim \chi^{(3)}E^2_{\mathrm{probe}}E_{\mathrm{pump}}$, which is clearly linear in the THz field. Since only the fundamental frequency of the probe was detected in the experiment, second harmonic generation becomes an additional channel for the probe's energy dissipation. Because SHG scales quadratically, its effect is stronger at high fluences than at lower ones. Since

$\Delta\xi$ is calculated, such energy dissipation indirectly affects the fluence dependence of $\Delta\xi$. This means that $\Delta\xi$ data strongly correlate with $\Delta I/I$ data and reflect the properties of both induced ellipticity changes and induced second harmonic generation. This problem could be addressed either by directly measuring $\Delta\xi$ with an additional pair of photodiodes and a quarter-wave plate or by measuring the intensity of the induced SHG and using it for $\Delta\xi$ calculations.

Another effect that likely plays a role in the experiment is two-photon absorption (TPA) of the probe beam. According to Boyd in [21], TPA contributes to the imaginary part of $\chi^{(3)}$ and affects the transmitted intensity as:

$$I(z) = \frac{I(0)}{1 + \beta I(0) z}, \tag{52}$$

where $\beta \propto \omega \,\mathrm{Im}\left(\chi^{(3)}\right)$ is the TPA coefficient and z is the distance traveled. According to [22], Cd_3As_2 has absorption at the doubled probe frequency, which makes TPA possible. As this effect contributes to $\chi^{(3)}$, it could cause interaction between the THz and optical fields, which is observed in this work.

6. Summary

As a result of the work done in this chapter, analytical expressions for the induced changes caused by the Kerr effect in the polarization state and intensity of the probe beam have been derived. These derived expressions extend the existing literature to include the presence of absorption in isotropic media with a complex nonlinear susceptibility tensor. Moreover, the equations describe the dependence of the Kerr signal on the probe polarization angle and probe ellipticity (for small ellipticities). Simplified equations for a linearly polarized probe reveal that induced rotation can be caused only by the imaginary part of the nonlinear tensor, which corresponds to induced anisotropic absorption. Induced ellipticity, on the other hand, is caused by the real part of the tensor, representing induced anisotropy in the medium. For an elliptically polarized probe, however, both the real and imaginary parts contribute to both induced rotation and ellipticity. Since no specific assumptions were made about the nonlinear part of the susceptibility tensor, the theory should be applicable to a broader range of processes that modify the probe polarization state via nonlinear polarization.

The electro-optical Kerr effect in Cd_3As_2 was studied, and components of the nonlinear susceptibility tensor χ^{NL} were extracted from the measurements using theoretical derivations. The extracted χ^{NL} was used to estimate values of the nonlinear refractive index n_2. The estimated $n_2 \sim 10^{-14}\,\frac{\mathrm{cm}^2}{\mathrm{W}}$ is comparable to those observed in semiconductors but

much smaller than in graphene. The scaling of signals with the THz field was confirmed to be parabolic, as expected for the usual Kerr effect. No signs of the Pockels effect were observed in fluence or phase flip measurements, indicating that there is no THz-induced symmetry breaking leading to $\chi^{(2)}$ in this experiment.

The experimental observations prompted an investigation into how probe power affects the electro-optical Kerr effect in Cd_3As_2. While the experiment was not ideally suited for studying such interactions, it was shown that high probe fluences completely change the Kerr response. The symmetries of the signals differ for high fluences compared to lower ones, and the fluence dependence on the THz pump is no longer parabolic. Such deviations from the parabolic law cannot be explained within a perturbative regime and therefore require more sophisticated theoretical models of the process.

Overall, the experiment performed is not ideal for studying a Kerr-like response at high probe intensities. A more robust approach would involve performing a THz pump–optical pump–optical probe experiment, which would allow for greater control over experimental parameters, such as pump power or time delays between the two pumps. This approach would also resolve the problem of induced SHG in the probe beam, as the probe intensity would be low enough to neglect this effect. Such an experimental design, combined with more sophisticated theoretical models, would significantly enhance the understanding of the underlying processes.

For the reader's convenience, all time traces used for data evaluation are presented in the Appendix.

7. Appendix. Raw time traces

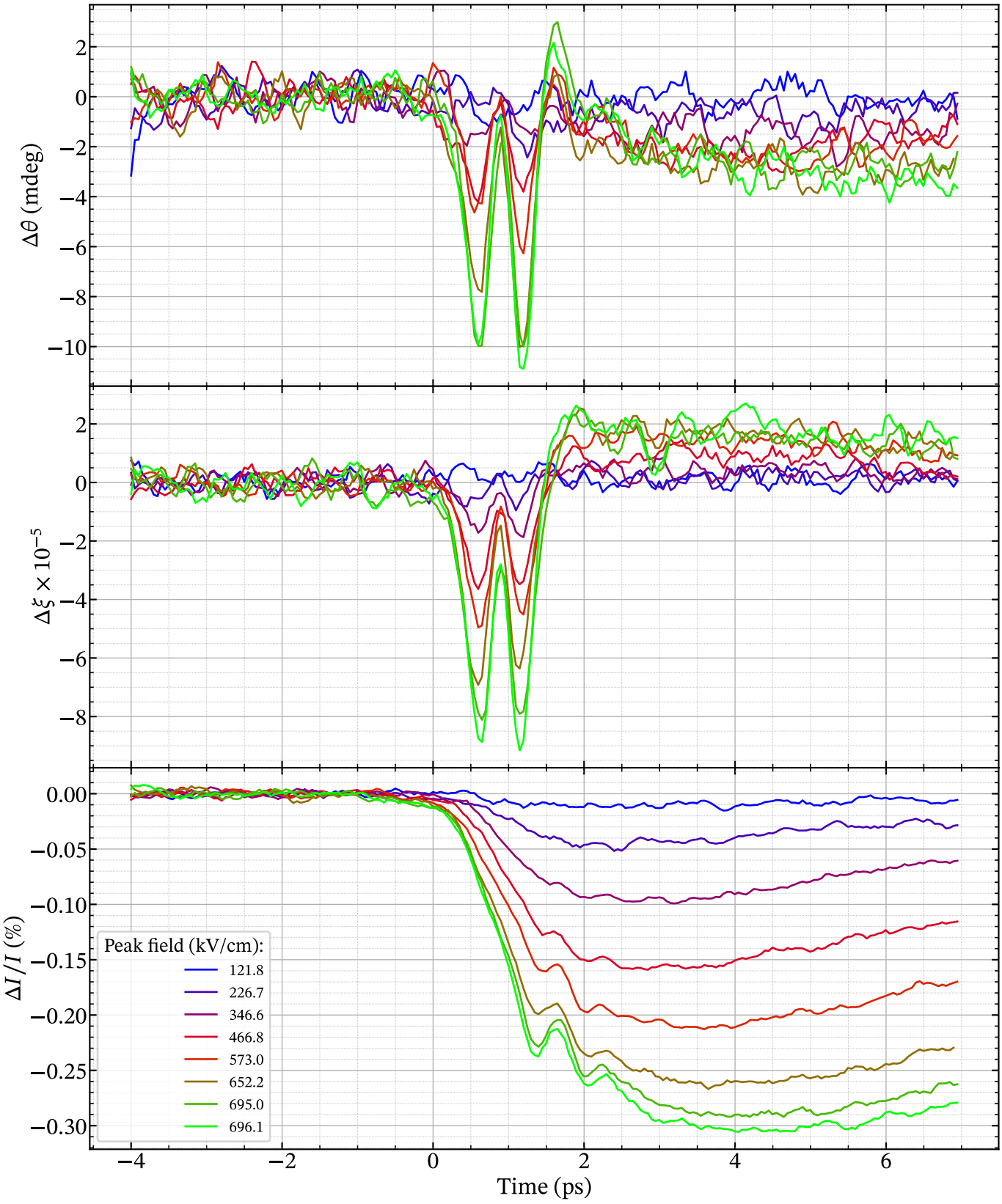

Figure 14: Time traces for fluence dependence of the Kerr effect.

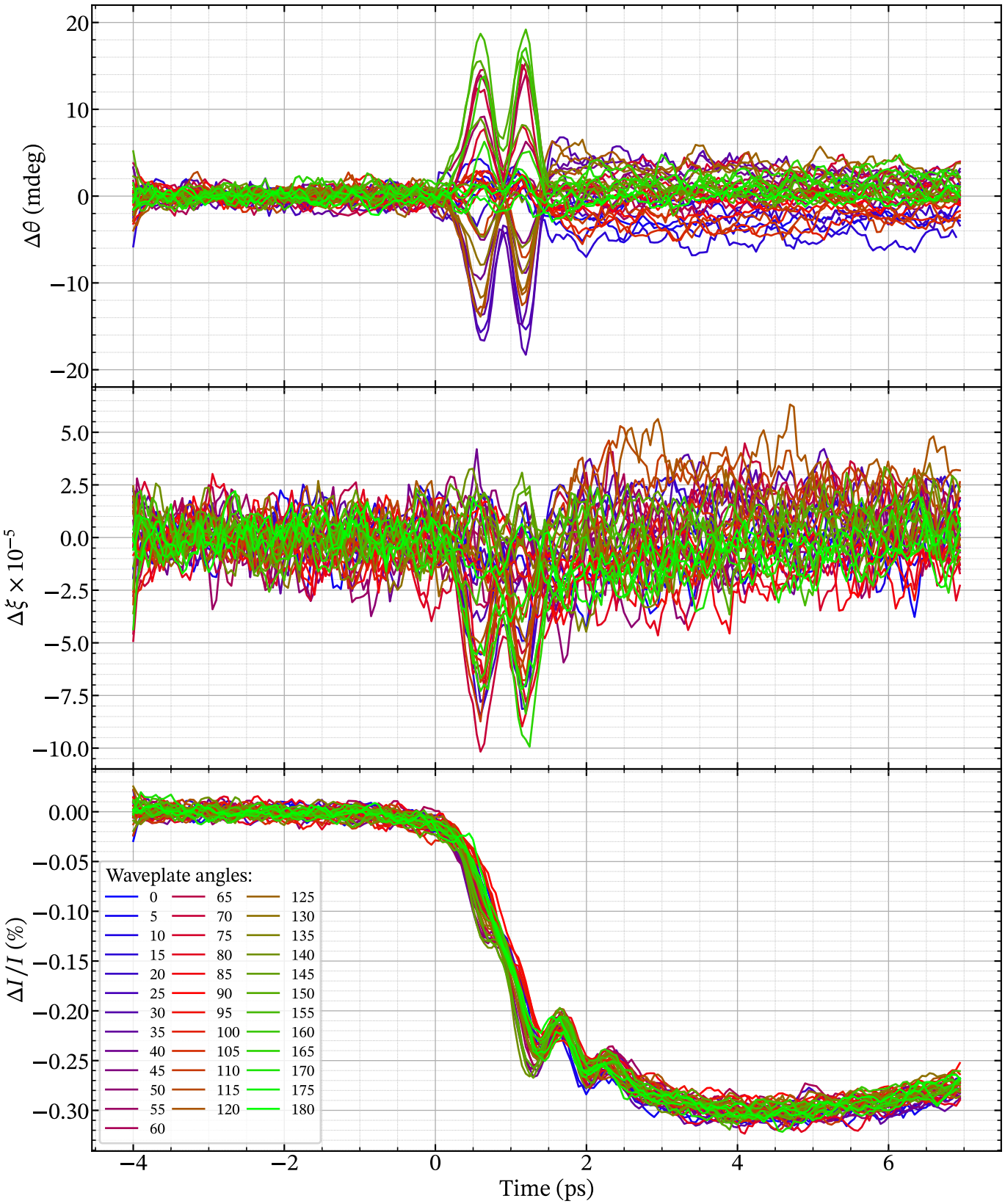

Figure 15: Time traces for angular dependence of the Kerr effect.

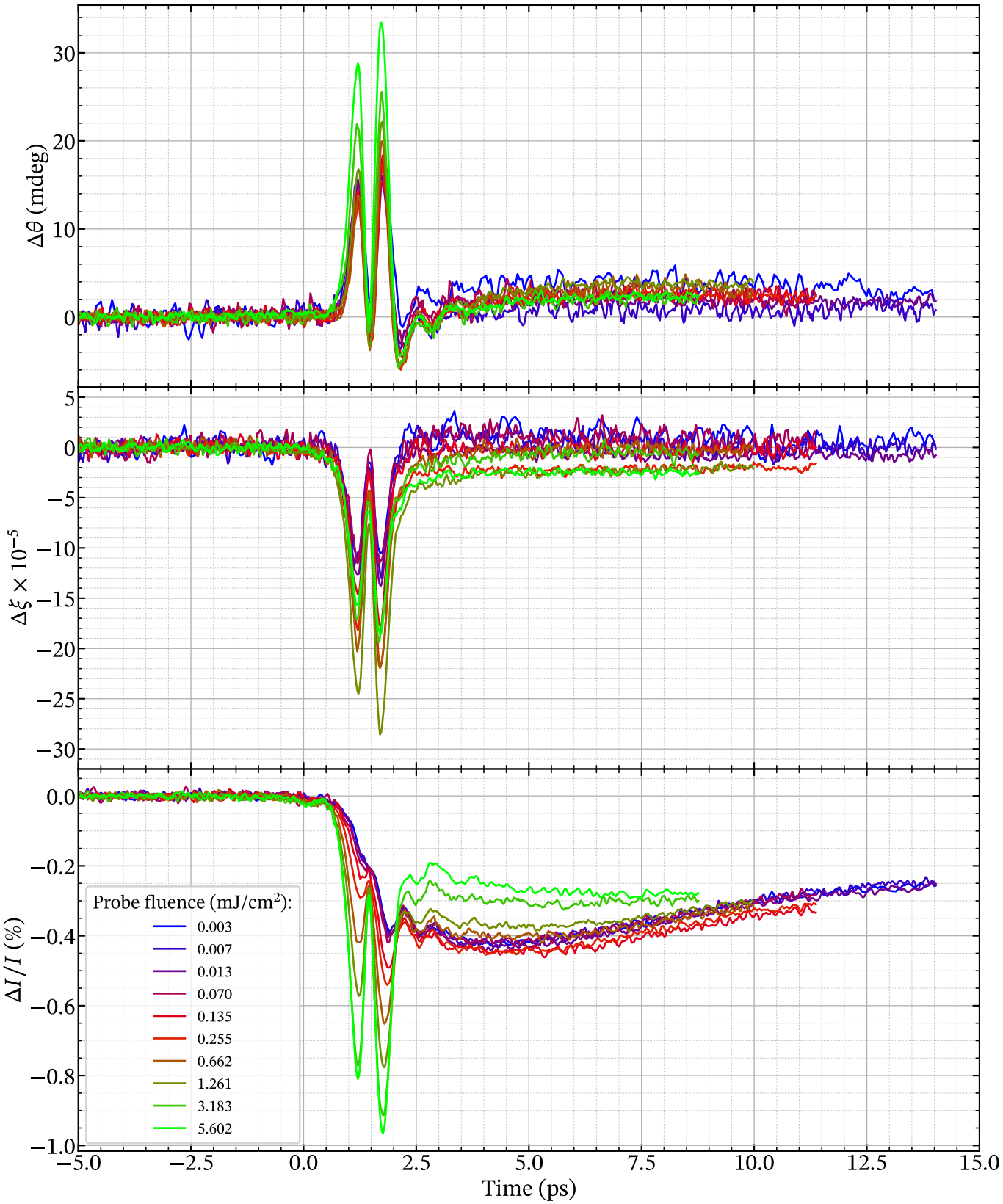

Figure 16: Time traces for fluence dependence of the probe in the high fluence regime.

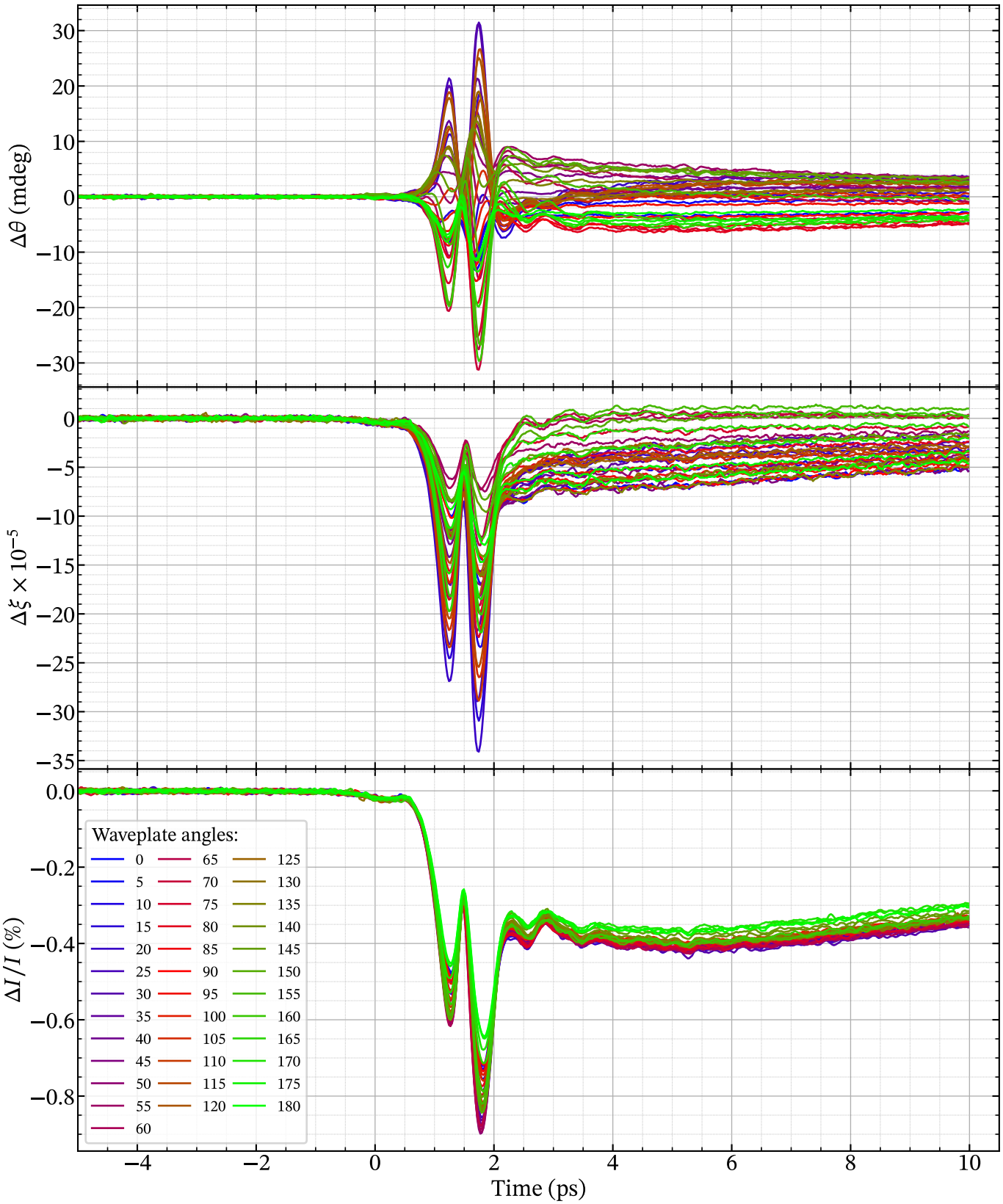

Figure 17: Time traces for angular dependence in the high fluence regime.

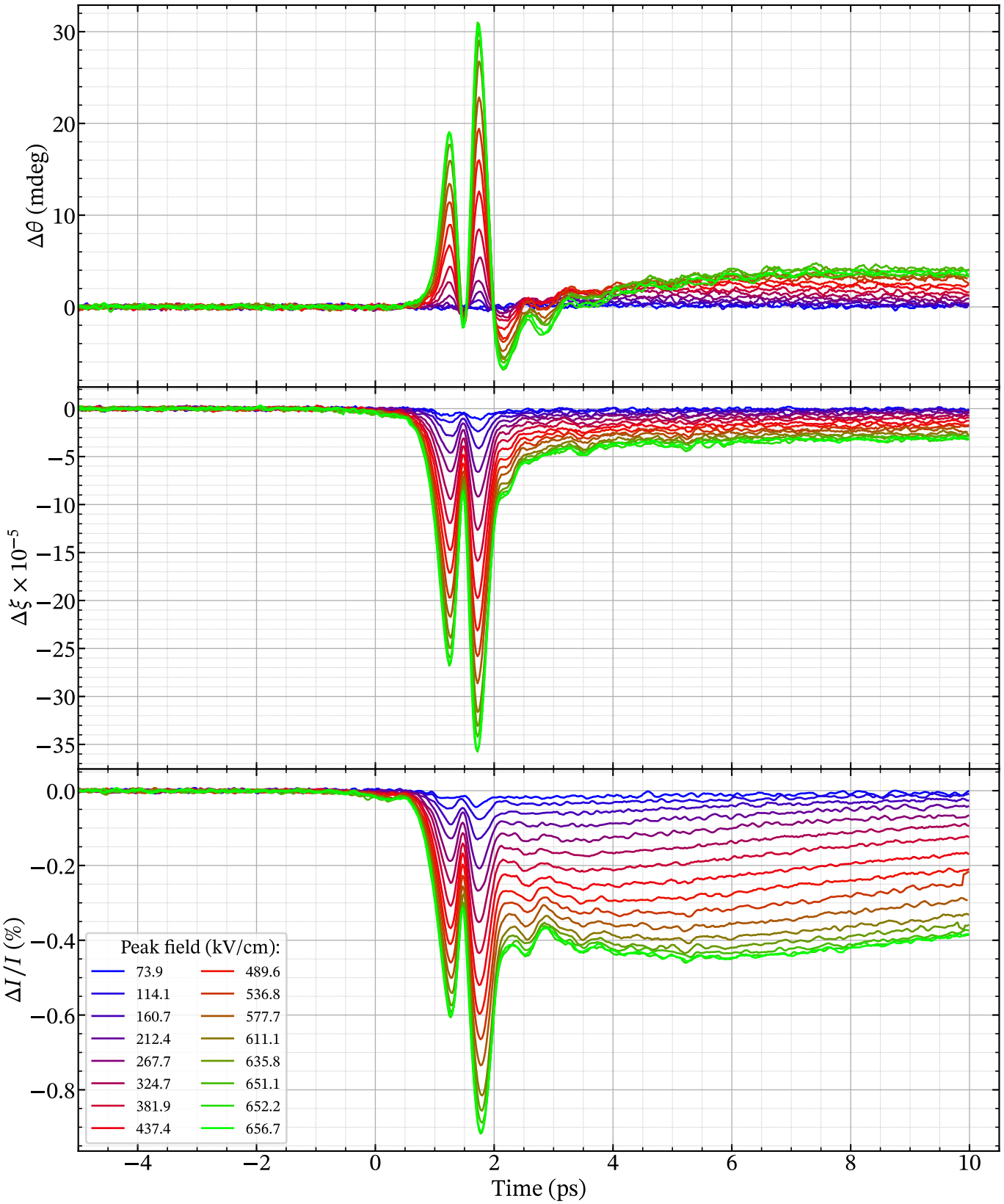

Figure 18: Time traces for THz fluence dependence in the high fluence regime.

8. References

[1] M. Sajadi, M. Wolf, and T. Kampfrath, *Terahertz-Field-Induced Optical Birefringence in Common Window and Substrate Materials*, Optics Express **23**, 28985 (2015).

[2] S. Bodrov, Y. Sergeev, A. Murzanev, and A. Stepanov, *Terahertz Induced Optical Birefringence in Polar and Nonpolar Liquids*, The Journal of Chemical Physics **147**, 84507 (2017).

[3] M. C. Hoffmann, N. C. Brandt, H. Y. Hwang, K.-L. Yeh, and K. A. Nelson, *Terahertz Kerr Effect*, Applied Physics Letters **95**, 231105 (2009).

[4] E. Dremetsika, B. Dlubak, S.-P. Gorza, C. Ciret, M.-B. Martin, S. Hofmann, P. Seneor, D. Dolfi, S. Massar, P. Emplit, et al., *Measuring the Nonlinear Refractive Index of Graphene Using the Optical Kerr Effect Method*, Optics Letters **41**, 3281 (2016).

[5] H. Zhang, S. Virally, Q. Bao, L. K. Ping, S. Massar, N. Godbout, and P. Kockaert, *Z-Scan Measurement of the Nonlinear Refractive Index of Graphene*, Optics Letters **37**, 1856 (2012).

[6] J. L. Cheng, J. E. Sipe, and S. W. Wu, *Third-Order Optical Nonlinearity of Three-Dimensional Massless Dirac Fermions*, ACS Photonics **7**, 2515 (2020).

[7] T. Zhang, K. J. A. Ooi, W. Chen, L. K. Ang, and Y. Sin Ang, *Optical Kerr Effect and Third Harmonic Generation in Topological Dirac/Weyl Semimetal*, Optics Express **27**, 38270 (2019).

[8] M. S. El-Bahrawi, N. N. Nagib, S. A. Khodier, and H. M. Sidki, *Birefringence of Muscovite Mica*, Optics & Laser Technology **30**, 411 (1998).

[9] R. W. Boyd, *Nonlinear Optics*, Fourth edition (Academic Press, an imprint of Elsevier, London, United Kingdom ; San Diego, CA, 2020).

[10] S. M. Richardson and J. W. Richardson Jr, *Crystal Structure of a Pink Muscovite from Archer's Post, Kenya: Implications for Reverse Pleochroism in Dioctahedral Micas*, American Mineralogist **67**, 69 (1982).

[11] R. Nitsche and T. Fritz, *Precise Determination of the Complex Optical Constant of Mica*, Applied Optics **43**, 3263 (2004).

[12] M. Janek, I. Bugár, D. Lorenc, V. Szöcs, D. Velič, and D. Chorvát, *Terahertz Time-Domain Spectroscopy of Selected Layered Silicates*, Clays and Clay Minerals **57**, 416 (2009).

[13] L. Hou, Y. Yang, A. Li, Q. Wang, Q. Li, M. Wu, P. Ji, Y. Zhang, Y. Xiao, W. Xu, et al., *Temperature-Dependent Terahertz Properties of Carriers and Phonons in the Topological Dirac Semimetal Cd_3As_2*, Physical Review B **108**, 115416 (2023).

[14] S. Yue, H. T. Chorsi, M. Goyal, T. Schumann, R. Yang, T. Xu, B. Deng, S. Stemmer, J. A. Schuller, and B. Liao, *Soft Phonons and Ultralow Lattice Thermal Conductivity in the Dirac Semimetal Cd_3As_2*, Physical Review Research **1**, 33101 (2019).

[15] L. Cheng, F. Formisano, K. A. Grishunin, S. D. Gorelov, P. H. M. van Loosdrecht, J. Yan, X. Luo, Z. Sheng, and E. A. Mashkovich, *Nonlinear Terahertz Kerr Effect in Quasi-2D $MnPS_3$*, Optics Letters **47**, 4052 (2022).

[16] M. J. Weber, *Handbook of Optical Materials* (Chapman and Hall/CRC, Boca Raton, 2018).

[17] M. Sajadi, M. Wolf, and T. Kampfrath, *Terahertz-Field-Induced Optical Birefringence in Common Window and Substrate Materials*, Optics Express **23**, 28985 (2015).

[18] M. G. Kuzyk, R. A. Norwood, J. W. Wu, and A. F. Garito, *Frequency Dependence of the Optical Kerr Effect and Third-Order Electronic Nonlinear-Optical Processes of Organic Liquids*, Journal of the Optical Society of America B **6**, 154 (1989).

[19] C. Zhu, P. Pilch, R. M. A. Dantas, A. Reinold, Y. Yang, F. Xiu, A. Bedoya-Pinto, S. S. P. Parkin, R. Moessner, and Z. Wang, *Population Inversion and Ultrafast Terahertz Nonlinearity of Transient Dirac Fermions in Cd_3As_2*, Physical Review B **109**, L201111 (2024).

[20] D. J. Cook, J. X. Chen, E. A. Morlino, and R. M. Hochstrasser, *Terahertz-Field-Induced Second-Harmonic Generation Measurements of Liquid Dynamics*, Chemical Physics Letters **309**, 221 (1999).

[21] R. W. Boyd, A. L. Gaeta, and E. Giese, *Nonlinear Optics*, in *Springer Handbook of Atomic, Molecular, And Optical Physics*, edited by G. W. F. Drake (Springer International Publishing, Cham, 2023), pp. 1097–1110.

[22] K. Karnicka-Moscicka, A. Kisiel, and L. Zdanowicz, *Fundamental Reflectivity Spectra of Monocrystalline and Polycrystalline Bulk Cd_3As_2*, Solid State Communications **44**, 373 (1982).

Conclusions and outlook

We have demonstrated that Cd_3As_2 exhibits significant nonlinearity in the THz frequency range, which originates from the presence of Dirac fermions. This observation has been validated through first-principles calculations using the Boltzmann transport equations, confirming the theoretical understanding of the nonlinear behavior.

Our study further explored the relationship between third harmonic generation and the polarization state of the pump beam. In the case of linear polarization, the response is isotropic. With increasing ellipticity of the pump, we found that the efficiency of harmonic generation decreases. Also, the ellipticity of the generated harmonic follows that of the pump, and this behavior is successfully explained by the same theoretical model used in the linear case. This consistency in the model highlights the reliability of our approach.

In a surprising finding, we observed that Cd_3As_2 is capable of generating second harmonics despite being a centrosymmetric material. This phenomenon can be attributed to a combination of thermoelectric currents and uneven sample thickness, which disrupt the overall centrosymmetry. Additionally, the application of a magnetic field introduces the Nernst effect, which plays an additional role in this process. These effects complicate the observation of possible intrinsic symmetry breaking via second harmonic generation under the influence of THz pump and magnetic fields, which makes this effect parasitic in some sense.

We also attempted to use the polarization state of an optical probe beam as a tool to investigate material symmetries through the electro-optical Kerr effect. In this experiment, we observed a THz-induced Kerr effect in the sample, which closely follows theoretical predictions. No traces of the Pockels effect are found, which could be a sign of broken symmetry in the material. Moreover, we found that the Kerr signal depends on probe fluence, causing significant changes in the symmetry of the observed signal.

Of course, the work done in the thesis is by no means finished. The main goal of the project has not been achieved, but now we know the possible problems for such an experiment. First, the quality of the film surface has to be perfect, as any thickness variations will lead to the rise of Seebeck currents. Second, the quality of the THz pump beam is similarly critical, as it will lead to similar effects. Another important topic is the THz field penetration into the sample. Cd_3As_2 has very high conductance and reflects THz radiation very well. As we found during experiments, the substrate

acts as an antireflection coating, improving the penetration of pump radiation into the sample. The presence of such an antireflection coating is a great help, as for weak but nonlinear effects it simply makes the effects observable. This is especially important for bulk crystals, as they usually do not have a substrate that could improve the penetration depth of the THz. Ideally, the sample should be a sandwich structure, with a film of Cd_3As_2 covered by THz transparent material on both sides. This should also improve the yield of harmonics signals.

Another possible experiment, not described in the thesis, is the detection of optical second harmonic generation. In theory, bulk SHG should be prohibited and should appear under THz pump or external magnetic field. However, for a thin film sample, a substrate is required, which is also isotropic. Unfortunately, mica is non-centrosymmetric and produces significant second harmonic by itself. In the case of a THz pump, a TFISH effect[1] will act as a parasitic one. In theory, TFISH is unavoidable as it is a $\chi^{(3)}$ related effect. Here, Kerr measurements will be useful, as they provide information about components of the $\chi^{(3)}$ tensor in Cd_3As_2. This will allow for the comparison of TFISH signals under different experimental conditions: with or without a magnetic field and for different pump ellipticities. Another sign of processes additional to TFISH can be a deviation from linear THz fluence dependence, typical for the TFISH process ($P^{\mathrm{TFISH}} = \chi^{(3)} E^2_{\mathrm{probe}} E_{\mathrm{THz}}$).

Further studies of electron dynamics in Cd_3As_2 require more sophisticated experimental setups, such as optical pump – THz pump – optical probe experiments to reveal how two-photon absorption affects optical Kerr effects or TFISH processes. Tunable probe frequency would be a plus, as it would allow for control over the strength of TPA in Cd_3As_2.

Finally, the same experimental techniques could be used to study other quantum materials with linear electron dispersion, like Weyl and line-node semimetals. $Co_3Sn_2S_2$, an established Weyl semimetal[2], hosts an interesting combination of Weyl nodes, magnetism[3], and reported spin excitations[4]. This intriguing combination of material properties could affect harmonic generation in unexpected ways, but it has yet to be studied.

However, Weyl materials are especially complicated for harmonic generation studies due to their high conductivity and the resulting low coupling between the THz pump and the material at the air-sample interface. This could explain the absence of experimental works on such materials in the field of nonlinear THz spectroscopy.

References

[1] D. J. Cook, J. X. Chen, E. A. Morlino, and R. M. Hochstrasser, *Terahertz-Field-Induced Second-Harmonic Generation Measurements of Liquid Dynamics*, Chemical Physics Letters **309**, 221 (1999).

[2] D. F. Liu, A. J. Liang, E. K. Liu, Q. N. Xu, Y. W. Li, C. Chen, D. Pei, W. J. Shi, S. K. Mo, P. Dudin, et al., *Magnetic Weyl Semimetal Phase in a Kagomé Crystal*, Science **365**, 1282 (2019).

[3] Y. Okamura, S. Minami, Y. Kato, Y. Fujishiro, Y. Kaneko, J. Ikeda, J. Muramoto, R. Kaneko, K. Ueda, V. Kocsis, et al., *Giant Magneto-Optical Responses in Magnetic Weyl Semimetal $Co_3Sn_2S_2$*, Nature Communications **11**, (2020).

[4] C. Liu, J. Shen, J. Gao, C. Yi, D. Liu, T. Xie, L. Yang, S. Danilkin, G. Deng, W. Wang, et al., *Spin Excitations and Spin Wave Gap in the Ferromagnetic Weyl Semimetal $Co_3Sn_2S_2$*, Science China Physics, Mechanics & Astronomy **64**, (2020).

Acknowledgement

This manuscript is a result of many years of work. After being a PhD student from February 2016 in my alma matter and after more than 8 years the work finally comes to end in University of Cologne. During this time, I visited many places, performed many experiments and met many peoples. We have witness historical events. A global pandemic paused all our work for months and forced us to be isolated at homes. A war in Europe started and it is still going, while this lines are being written. Without support this work would never be finished.

My dear parents you are the main reason why I started a PhD after graduation. You convinced me that it was worth to try and supported me throughout all these years. And you always patiently listened to complex physics topics, which are difficult to understand even when you study them.

Beloved Sofia, you have been with me for the last two years of my PhD, but probably most complicated ones. Your love and support are priceless. I love you, and my greatest luck is that I have met you.

Paul, you are the one who was able to guide me to the end of this work. You give your students a lot of freedom, which is quite unique but also challenging for a student. And while it makes the PhD process more complicated, the final result feels more like my own. There's an old joke from the Russian academic world, which is hilariously difficult to translate properly. I will try, but I will also include the original here:

– Почему написать докторскую сложнее, чем кандидатскую?	*– Why is writing of doctor's[1] dissertation more difficult than candidate's[1] one?*
– Потому что кандидатскую пишет доктор, а докторскую – кандидат.	*– Because the candidate's one is written by a doctor, but the doctor's one is written by a candidate.*

I really enjoy to talk with you about physics and not only. Thank you for your advice and help during my years in Cologne.

Also I want to thank Chris for his help with my adaptation in the University in the first years and for many useful discussions we had about experiments and results. You took care of the lab during move and planned it, which was incredibly important. It was a

[1]https://en.wikipedia.org/wiki/Doctor_of_Sciences
[2]https://en.wikipedia.org/wiki/Candidate_of_Sciences

pleasure to work and speak with you. And I am proud, that setup we planned and built together contributed significantly to your results.

I would like to thank Evgeniy for his supervision and discussions during this work. You help with paper and the thesis are really valuable.

Robin, Lukas, Phillip, Omar, Anuja, Julian it was always a pleasure to spend time and talk with you, feel free to contact me in the future. Labs move was a special kind of fun.

Also I would like to thank Jens, who provided us technical support all this time and all other colleagues in Institute of Physics II.

Dear Zhe, you are the one who brought me to Cologne from Dresden as your student and offered me a dissertation topic. Thank you for your trust in me and for believing I could be useful as an experimentalist. It is unfortunate that we had to part ways after a long time of you being my supervisor and colleague in Dresden. I was happy to help with your new lab in Dortmund and will be delighted to hear about exciting new results from your group, professor!

In Dresden, where I spent first two years in Germany, I learned a lot about high field THz generation and nonlinear THz spectroscopy. TELBE group played significant role for my thesis, as place where I learned and collected data later for two papers and parts of the thesis. I would like to especially thanks Sergey Kovalev for his help and experimental knowledge, which he shared with me. He also helped me to find position in Dresden. During shifts at beamline we spent a lot of hours speaking and working together. Jan, Igor, Thales, Min, Nielesh, Bert you were my colleagues during my work at TELBE and I will always remember this time. Sometimes I miss our group “meetings” in Biergarten at the bank of Elbe.

Despite being a long time ago, I remember my time in Moscow while studying physics as a student and time I spent as postgraduate. My special thank go to Prof. G. Kh. Kitaeva, who opened world of terahertz radiation for me and led my first steps as a scientist. And also I would like to thank all members of SPDC Lab, with whom I worked back in the day. My warm greetings go to people of the department of quantum electronics, which became almost a second home. I hope, one day I will visit you again.

What is a live without friends, huh? Артемий, когда-то мы были первокурсниками, которые познакомились в университете. Сегодня мы оба заканчиваем долгий, полный трудностей путь на дороге к званию доктора философии. Я безумно рад, что все эти годы мы общались, делили забавные и не очень Германия-моменты и смогли пережить исторические моменты, которые выпали нам в аспирантское

время. Твоя дружба неоценима, а проводить время в твоей компании всегда приятно!

Народ из ОБД, спасибо вам за кучу веселья и общения. Без вас было бы определенно сложнее сделать эту работу. Всегда рад почитать свежие сообщения, хехе!

Cologne, 2024

List of publications

15. **Germanskiy, S.**, Dantas, R. M. A., Kovalev, S., Reinhoffer, C., Mashkovich, E. A., Loosdrecht, P. H. M. van, Yang, Y., Xiu, F., Surówka, P., Moessner, R., Oka, T., Wang, Z.,. *Ellipticity Control of Terahertz High-Harmonic Generation in a Dirac Semimetal*. Physical Review B 106, L81127 (2022). https://doi.org/10.1103/PhysRevB.106.L081127
14. Kovalev, S., Hafez, H. A., Tielrooij, K.-J., Deinert, J.-C., Ilyakov, I., Awari, N., Alcaraz, D., Soundarapandian, K., Saleta, D., **Germanskiy, S.**, Chen, M., Bawatna, M., Green, B., Koppens, F. H. L., Mittendorff, M., Bonn, M., Gensch, M., Turchinovich, D.,. *Electrical Tunability of Terahertz Nonlinearity in Graphene*. Science Advances 7, eabf9809 (2021). https://doi.org/10.1126/sciadv.abf9809
13. Reinhoffer, C., Mukai, Y., **Germanskiy, S.**, Bliesener, A., Lippertz, G., Uday, A., Taskin, A. A., Ando, Y., Wang, Z., Loosdrecht, P. H. M. van,. *Relaxation Dynamics of the Optically Driven Nonequilibrium States in the Electron- and Hole-Doped Topological-Insulator Materials* $(Bi_{1-x}Sb_x)_2Te_3$. Physical Review Materials 4 (2020). https://doi.org/10.1103/physrevmaterials.4.124201
12. Kovalev, S., Dong, T., Shi, L.-Y., Reinhoffer, C., Xu, T.-Q., Wang, H.-Z., Wang, Y., Gan, Z.-Z., **Germanskiy, S.**, Deinert, J.-C., Ilyakov, I., Van Loosdrecht, P. H. M., Wu, D., Wang, N.-L., Demsar, J., Wang, Z.,. *Band-Selective Third-Harmonic Generation in Superconducting MgB 2 : Possible Evidence for the Higgs Amplitude Mode in the Dirty Limit*. Physical Review B 104, L140505 (2021). https://doi.org/10.1103/PhysRevB.104.L140505
11. Kovalev, S., Dantas, R. M. A., **Germanskiy, S.**, Deinert, J.-C., Green, B., Ilyakov, I., Awari, N., Chen, M., Bawatna, M., Ling, J., Xiu, F., Loosdrecht, P. H. M. van, Surówka, P., Oka, T., Wang, Z.,. *Non-Perturbative Terahertz High-Harmonic Generation in the Three-Dimensional Dirac Semimetal* Cd_3As_2. Nature Communications 11 (2020). https://doi.org/10.1038/s41467-020-16133-8
10. Deinert, J.-C., Iranzo, D. A., Pérez, R., Jia, X., Hafez, H. A., Ilyakov, I., Awari, N., Chen, M., Bawatna, M., Ponomaryov, A. N., **Germanskiy, S.**, Bonn, M., Koppens, F. H., Turchinovich, D., Gensch, M., Kovalev, S., Tielrooij, K.-J.,. *Grating-Graphene Metamaterial as a Platform for Terahertz Nonlinear Photonics*. ACS Nano 15, 1145–1154 (2020). https://doi.org/10.1021/acsnano.0c08106
9. Chu, H., Kim, M.-J., Katsumi, K., Kovalev, S., Dawson, R. D., Schwarz, L., Yoshikawa, N., Kim, G., Putzky, D., Li, Z. Z., Raffy, H., **Germanskiy, S.**, Deinert, J.-C., Awari, N., Ilyakov, I., Green, B., Chen, M., Bawatna, M., Cristiani, G., Logvenov,

G., Gallais, Y., Boris, A. V., Keimer, B., Schnyder, A. P., Manske, D., Gensch, M., Wang, Z., Shimano, R., Kaiser, S.,. *Phase-Resolved Higgs Response in Superconducting Cuprates*. Nature Communications 11, 1793 (2020). https://doi.org/10.1038/s41467-020-15613-1

8. Chen, M., Deinert, J.-C., Green, B., Wang, Z., Ilyakov, I., Awari, N., Bawatna, M., **Germanskiy, S.**, Oliveira, T. V. A. G. de, Geloni, G., Tanikawa, T., Gensch, M., Kovalev, S.,. *Pulse- and Field-Resolved THz-diagnostics at 4th Generation Lightsources*. Optics Express 27, 32360 (2019). https://doi.org/10.1364/oe.27.032360
7. Wang, Z., Kovalev, S., Awari, N., Chen, M., S. Germanskiy, Green, B., Deinert, J.-C., Kampfrath, T., Milano, J., Gensch, M.,. *Magnetic Field Dependence of Antiferromagnetic Resonance in NiO*. Applied Physics Letters 112, 252404 (2018). https://doi.org/10.1063/1.5031213
6. Kovalev, S., Wang, Z., Deinert, J.-C., Awari, N., Chen, M., Green, B., **Germanskiy, S.**, Oliveira, T. V. A. G. de, Lee, J. S., Deac, A., Turchinovich, D., Stojanovic, N., Eisebitt, S., Radu, I., Bonetti, S., Kampfrath, T., Gensch, M.,. *Selective THz Control of Magnetic Order: New Opportunities from Superradiant Undulator Sources*. Journal of Physics D: Applied Physics 51, 114007 (2018). https://doi.org/10.1088/1361-6463/aaac75
5. Hafez, H. A., Kovalev, S., Deinert, J.-C., Mics, Z., Green, B., Awari, N., Chen, M., **Germanskiy, S.**, Lehnert, U., Teichert, J., Wang, Z., Tielrooij, K.-J., Liu, Z., Chen, Z., Narita, A., Mullen, K., Bonn, M., Gensch, M., Turchinovich, D.,. *Extremely Efficient Terahertz High-Harmonic Generation in Graphene by Hot Dirac Fermions*. Nature 561, 507–511 (2018). https://doi.org/10.1038/s41586-018-0508-1
4. Chen, M., Kovalev, S., Awari, N., Wang, Z., **Germanskiy, S.**, Green, B., Deinert, J.-C., Gensch, M.,. *Towards Femtosecond-Level Intrinsic Laser Synchronization at Fourth Generation Light Sources*. Optics Letters 43, 2213 (2018). https://doi.org/10.1364/OL.43.002213
3. Chekhova, M. V., **Germanskiy, S.**, Horoshko, D. B., Kitaeva, G. K., Kolobov, M. I., Leuchs, G., Phillips, C. R., Prudkovskii, P. A.,. *Broadband Bright Twin Beams and Their Upconversion*. Optics Letters 43, 375 (2018). https://doi.org/10.1364/OL.43.000375
2. Kuznetsov, K. A., Kitaeva, G. K., Kovalev, S. P., **Germansky, S. A.**, Buryakov, A. M., Tuchak, A. N., Penin, A. N.,. *Complex Extraordinary Dielectric Function of Mg-doped Lithium Niobate Crystals at Terahertz Frequencies*. Applied Physics B 122 (2016). https://doi.org/10.1007/s00340-016-6498-5
1. Kornienko, V. V., **Germanskiy, S. A.**, Kitaeva, G. K., Penin, A. N.,. *Generation of Optical-Terahertz Biphoton Pairs via Spontaneous Parametric down-Conversion*.

International Journal of Quantum Information 12, 1560023 (2014). https://doi.org/10.1142/s0219749915600230

Data availability

The data and the code used for producing this dissertation are published with Zenodo and can be found as:

Germanskiy, S.,. *Data and Code for Thesis "Nonlinear Terahertz Spectroscopy of the 3D Dirac Material Cd_3As_2"* (2025). https://doi.org/10.5281/zenodo.15230531

Erklärung zur Dissertation

Hiermit versichere ich an Eides statt, dass ich die vorliegende Dissertation selbstständig und ohne die Benutzung anderer als der angegebenen Hilfsmittel und Literatur angefertigt habe. Alle Stellen, die wörtlich oder sinngemäß aus veröffentlichten und nicht veröffentlichten Werken dem Wortlaut oder dem Sinn nach entnommen wurden, sind als solche kenntlich gemacht. Ich versichere an Eides statt, dass diese Dissertation noch keiner anderen Fakultät oder Universität zur Prüfung vorgelegen hat; dass sie - abgesehen von unten angegebenen Teilpublikationen und eingebundenen Artikeln und Manuskripten - noch nicht veröffentlicht worden ist sowie, dass ich eine Veröffentlichung der Dissertation vor Abschluss der Promotion nicht ohne Genehmigung des Promotionsausschusses vornehmen werde. Die Bestimmungen dieser Ordnung sind mir bekannt. Darüber hinaus erkläre ich hiermit, dass ich die Ordnung zur Sicherung guter wissenschaftlicher Praxis und zum Umgang mit wissenschaftlichem Fehlverhalten der Universität zu Köln gelesen und sie bei der Durchführung der Dissertation zugrundeliegenden Arbeiten und der schriftlich verfassten Dissertation beachtet habe und verpflichte mich hiermit, die dort genannten Vorgaben bei allen wissenschaftlichen Tätigkeiten zu beachten und umzusetzen. Ich versichere, dass die eingereichte elektronische Fassung der eingereichten Druckfassung vollständig entspricht.

Teilpublikationen:

- Kovalev, S., Dantas, R. M. A., **Germanskiy, S.**, Deinert, J.-C., Green, B., Ilyakov, I., Awari, N., Chen, M., Bawatna, M., Ling, J., Xiu, F., Loosdrecht, P. H. M. van, Surówka, P., Oka, T., Wang, Z.,. *Non-Perturbative Terahertz High-Harmonic Generation in the Three-Dimensional Dirac Semimetal Cd_3As_2*. Nature Communications 11 (2020). https://doi.org/10.1038/s41467-020-16133-8
- **Germanskiy, S.**, Dantas, R. M. A., Kovalev, S., Reinhoffer, C., Mashkovich, E. A., Loosdrecht, P. H. M. van, Yang, Y., Xiu, F., Surówka, P., Moessner, R., Oka, T., Wang, Z.,. *Ellipticity Control of Terahertz High-Harmonic Generation in a Dirac Semimetal*. Physical Review B 106, L81127 (2022). https://doi.org/10.1103/PhysRevB.106.L081127

Manuskripte:

- **Germanskiy, S.**, Reinhoffer, C., Kovalev, S., Deinert, J.-C., Awari, N., Chen, M., Ilyakov, I., de Oliveira, T., Ponomaryov, A., Yang, Y., Xiu, F., Zhu, C., Pilch, P., Reinold, A., Mashkovich, E.A., van Loosdrecht, P.H.M. Terahertz second harmonic generation by transient thermoelectric currents in centrosymmetric Cd_3As_2, *manuscript in preparation*

Köln, den 01.12.2024 Semen Germanskiy